Aix Marseille Université

NNT : 2025AIXM0000

THÈSE DE DOCTORAT

Soutenue à Aix-Marseille Université
le 5 Février 2025 par

Nesrin AKEL

Experimental and numerical investigation of a PVC geomembrane under different tensile modes

Discipline
Sciences pour l'ingénieur

Spécialité
Mécanique des solides

École doctorale
Ecole doctorale 353 – Sciences pour l'ingénieur : Mécanique, Physique, Micro et Nano-électronique

Laboratoire/Partenaires de recherche
INRAE, Aix-en-Provence, UR RECOVER

Composition du jury

Lucien Laiarinandrasana DR, Mines Paristech	**Rapporteur**
Katerina Ioannidou CR, LMGC	**Rapporteuse**
Jean-Luc Bouvard PR, CEMEF MINES ParisTech	**Examinateur**
Pascal Villard PR, Université Grenoble Alpes	**Président du jury**
Nathalie Touze ICPEF, INRAE	**Directrice de thèse**
François Nicot PR, USMB	**Co-directeur de thèse**
Guillaume Stoltz IR, INRAE	**Co-encadrant**
Antoine Wautier ICPEF, INRAE	**Membre invité**

INRAE Région PACA Galopin Génie étanchéité

Affidavit

I, undersigned, Nesrin AKEL, hereby declare that the work presented in this manuscript is my own work, carried out under the scientific supervision of Nathalie TOUZE, thesis director and Francois NICOT co-thesis director, in accordance with the principles of honesty, integrity and responsibility inherent to the research mission. The research work and the writing of this manuscript have been carried out in compliance with both the French national charter for Research Integrity and the Aix-Marseille University charter on the fight against plagiarism.

This work has not been submitted previously either in this country or in another country in the same or in a similar version to any other examination body.

Place Aix-en-Provence, France, date 20 novembre 2024



Cette œuvre est mise à disposition selon les termes de la Licence Creative Commons Attribution - Pas d'Utilisation Commerciale - Pas de Modification 4.0 International.

Liste de publications et/ou brevets et participation aux conférences

1) Liste des publications réalisées dans le cadre du projet de thèse :
    1. Akel, N., A. Wautier, G. Stoltz, N. Touze, and F. Nicot. "A micromechanical model of PVC geomembranes using discrete element method." In Geosynthetics: Leading the Way to a Resilient Planet, pp. 2165-2172. CRC Press, 2023. 10.1201/9781003386889-292ff. hal04366575. (Published). Related to Chapter 3.
    2. Akel, Nesrin, Guillaume Stoltz, Antoine Wautier, François Nicot, et Nathalie Touze. 2025. « Rate-dependent tensile response of Polyvinyl Chloride geomembranes ». Geotextiles and Geomembranes 53 (1): 445-56. https://doi.org/10.1016/j.geotexmem.2024.11.004. (Published). Related to Chapter 4.
    3. Nesrin Akel, Antoine Wautier, François Nicot, Guillaume Stoltz, Nathalie Touze. "Multiscale modeling of PVC geomembrane using Discrete Element Method (DEM)." (In preparation). Related to Chapter 3 and 5.
    4. Nesrin Akel, Laurent Josseaume, Guillaume Stoltz, Antoine Wautier, François Nicot, Guillaume Stoltz, Nathalie Touze. «Experimental investigation of a PVC geomembrane response to different tensile loading modes». (Conference paper submitted to EuroGeo8). Related to Chapter 4.
2) Participation aux conférences au cours de la période de thèse :
    1. 12th International Conference of Geosynthetics (12ICG), Sep 2023, Roma, Italy (oral presentation). Related to Chapter 3.
    2. Particles 2023, Oct 2023, Milan, Italy (oral presentation). Related to Chapter 3.
    3. EMI 2024 IC – ASCE Engineering Mechanics Institute 2024 International Conference, Sep 2024, Vienna, Austria (oral presentation). Related to Chapter 3.
    4. EuroGeo8, Sept 2025, Lille, France. (Accepted abstract for oral presentation). Related to Chapter 4.
    5. Participation à la journée des doctorants –Recover INRAE, Juin2022, Aix-En-Provence, France (Poster). Related to Chapter 3 and 4.
    6. Participation à la journée des doctorants –Recover INRAE, Juin2023, Aix-En-Provence, France (Poster). Related to Chapter 3 and 4.
    7. Participation à la journée des doctorants –Recover INRAE, Juin2024, Aix-En-Provence, France (Poster). Related to Chapter 3 and 4.
    8. Participation à la journée des doctorant – ED353, Université Aix-Marseille, Mai 2024, Marseille, France (Poster). Related to Chapter 3 and 4.
    9. Participation à ALERT Geomaterials workshop – 30 Sept 2024, Aussois, France (Poster). Related to Chapter 3 and 4.

"Nothing in life is to be feared, it is only to be understood.
Now is the time to understand more, so that we may fear less."
– Marie Curie



Résumé

Face aux changement climatiques qui représentent une menace pour les ressources en eau, les géomembranes (GMB) jouent un rôle essentiel dans la conservation durable de l'eau en limitant les pertes d'eau au sein des ouvrages hydrauliques. Les GMBs en PVC sont privilégiées pour les barrages et les canaux en raison de leur flexibilité et leur grands déformabilité.

Bien qu'elles ne soient pas conçues pour supporter des charges mécaniques, elles restent vulnérables à des contraintes de traction imprévues, lors de l'installation ou au cours de leur durée de vie, ce qui peut dégrader leurs propriétés d'étanchéité et entraîner des défaillances prématurées.

Cette étude examine leur réponse mécanique pour une large gamme de vitesses de sollicitation via des essais de traction uniaxiale, afin de traiter les écarts entre les conditions in situ et en laboratoire. Les résultats montrent une dépendence marquée à la vitesse de traction, principalement au temps court. cette dépendance disparaît après environ 4 heures de relaxation sous deformation constante. L'historique de précharge, incluant la durée d'exposition et le poids, affecte la récupération de déformation, et les propriétés à long terme peuvent être déduites d'essais à court terme dans des conditions constantes.

En complément, un modèle micromécanique multi-échelle novateur, basé sur la méthode des éléments discrets, a été développé, intégrant des paramètres microstructuraux comme la cristallinité et la densité de la zone amorphe. Ce modèle relie la microstructure au comportement macroscopique, en identifiant les points de défaillance.

Mots-clés : géomembrane PVC, traction, dépendance vitesse, dépendance temps, modélisation multi-échelle, DEM.

Abstract

Faced with climate change, which poses a significant threat to water resources, geomembrane (GM) plays a vital role in sustainable water conservation strategies by preventing water loss in hydraulic structures. PVC GMs are preferred in dams and canals thanks to their flexibility and large deformability.

Although not designed to bear mechanical loads, they remain vulnerable to face unexpected tensile stresses, during installation and over their lifespan, potentially degrading the waterproofing barrier properties through premature failure.

Thus, the mechanical properties of PVC GM are vital considerations for engineers when designing long-lasting waterproofing systems.

This study investigates the rate-dependent mechanical response of PVC GMs through uniaxial tensile loading, addressing discrepancies between in-situ and laboratory conditions. Results reveal that lower tensile rates reduce rigidity, strength, and strain at failure, while the dependency on the initial loading rate diminishes after $\sim$4 hours of constant strain relaxation. Preloading history, including exposure time and weight, impacts strain recovery, and long-term properties can be deduced from short-term tests under consistent conditions.

To complement experiments, an original multiscale micromechanical model using the Discrete Element Method (DEM) accounts for microstructural features like amorphous phase density, chain tortuosity, and crystallinity. This model links microstructural elements to macroscopic behavior, enabling the detection of failure points and their effects on overall performance.

Keywords: PVC GM, tensile testing, rate-dependency, time-dependency, multiscale modeling, DEM, microstructural features.

Remerciements

Je ne saurai débuter ce manuscrit sans exprimer mes profonds remerciements à mes encadrants Guillaume Stoltz et Antoine Wautier, INRAE Aix-en-Provence, qui, par leurs idées constructives, leurs conseils avisés, et nos fréquentes discussions, ont grandement contribué au progrès de cette thèse. Leur soutien, leur gentillesse et leur supervision continue ont été d'une grande aide tout au long de ce projet. La patience dont ils ont fait preuve à mon égard a été importante pour atteindre le succès que nous célébrons aujourd'hui… Ils ont été bien plus que des guides; ils ont constitué deux fondations solides dans l'édifice de cette thèse, que nous avons érigé ensemble au cours de ces trois années.

J'adresse également mes vifs remerciements à ma directrice de thèse Nathalie Touze, Présidente du centre INRAE Ile-de-France – Jouy-en-Josas – Antony, ainsi qu'à mon co-directeur de thèse François Nicot, Professor à l'Université Savoie Mont Blanc, Chambéry. Leur expertise approfondie et leur orientation scientifique ont été essentielles tout au long de cette recherche, enrichissant considérablement le développement de ce travail. Je leur suis également reconnaissant pour leur soutien constant, leurs encouragements réguliers et leur disponibilité, malgré leurs grandes responsabilités.

Je voudrais aussi remercier chaleureusement Paul Guinard, Jérôme Douriez, Franck Bourrier, Alexis Roulet, Loïc Laure, Nicolas Durville pour leur participation à mon comité de thèse et leur intérêt soutenu pour mes recherches. Leur présence a enrichi ce comité par une diversité précieuse de perspectives, combinant expertise industrielle et connaissances en mécanique. Je leur suis reconnaissant pour le temps précieux qu'ils ont consacré à l'évaluation de mon travail, ainsi que pour la qualité de leurs critiques constructives.

Aussi, voudrais-je remercier sincèrement les membres du jury pour l'intérêt qu'ils ont porté à ce sujet de thèse. Un remerciement tout particulier aux rapporteurs Lucien Laiarinandrasana et Katerina Ioannidou pour avoir examiné le manuscrit avec attention, ainsi que aux examinateurs Pascal Villard et Jean-Luc Bouvard, dont les précieux commentaires et évaluations m'ont permis d'enrichir et d'améliorer ce travail.

Bien sûr, Je ne peux pas oublier INRAE et la Région PACA, qui ont contribué au financement de ce projet de thèse, ainsi que Galopin, qui a fourni un soutien financier supplémentaire pour les budgets opérationnels.

La famille INRAE-RECOVER, je tiens à leur adresser mes sincères remerciements pour leur gentillesse et leur bienveillance. Je suis profondément reconnaissante d'avoir pu évoluer au sein d'une unité aussi dynamique, enrichie par des activités telles que la journée de la famille, la Fête de la Science, les journées des doctorants et la journée de la diversité, qui ont toutes contribué à rendre cette expérience plus enrichissante et conviviale.

À mes amis…

Je tiens à remercier mes amis pour leur soutien indéfectible. Je souhaite exprimer une gratitude particulière au groupe Saint-Charles (ma famille marseillaise), qui a toujours été

à mes côtés, m'aidant à recharger mon énergie pour faire avancer sur mon projet. Un remerciement tout spécial à Abbas, qui n'a pas seulement été un collègue de travail, mais aussi un frère de vie, ainsi qu'à Zeinab, Rouba et Ahmad, qui m'ont accompagnée dans tous les hauts et les bas de ce parcours.

Je voudrais également adresser un remerciement tout particulier à mes proches amies au Liban, Pascal et Manar. Nos appels réguliers et votre soutien inestimable ont été une véritable bouffée d'air frais. Grâce à vos encouragements et à vos messages, même à distance, vous avez réussi à me faire sourire, à recharger mon esprit et à croire en moi. Votre présence dans ma vie est un véritable cadeau.

À ma famille…

Avant tout, je suis profondément reconnaissante envers ma famille, qui m'a soutenue tout au long de mes études.

Maman et Papa, merci infiniment pour votre soutien quotidien et vos encouragements chaleureux, qui ont été une source constante de motivation. Votre amour et vos conseils avisés ont éclairé mon chemin et m'ont permis de surmonter tous les défis.

À mes deux frères, Khoder et Wassef, merci d'avoir résisté et d'avoir attendu mon retour comme si c'était la chose la plus précieuse au monde.

Sans vous, je ne serais certainement pas arrivée là où j'en suis aujourd'hui !

Contents

Affidavit **2**
Liste de publications et/ou brevets et participation aux conférences **3**
Résumé **5**
Abstract **6**
Remerciements **7**
Contents **9**
Chapter 1: Introduction **13**
1.1. Geomembranes from an industrial point of view 13
1.1.1. The evolution and importance of geomembranes in modern engineering 13
1.1.2. The different geomembrane materials with a focus on PVC 14
1.1.3. Unexpected mechanical loads affecting the hydraulic barrier function of geomembranes 14
1.1.4. Standardized tensile tests for evaluating geomembrane mechanical properties 16
1.2. From engineer to scientific challenges 16
1.3. Methodology and structure of the present work 17
Chapter 2: State of the art **19**
2.1. Microstructural characteristics and environmental effects on PVC GMs 19
2.1.1. PVC resin microstructure 19
2.1.2. PVC geomembrane manufacturing 20
2.1.3. Partial crystallization and plasticizer impact on the PVC microstructure 21
2.1.4. From physical properties to PVC characteristics 22
2.1.5. Effect of temperature on PVC mechanical characteristics 23
2.1.6. PVC geomembrane aging and degradation 24
2.2. Modeling approaches for polymeric material at different scale 27
2.2.1. Quantum scale ($\sim 10-10\ \mathbf{m}, \sim 10-12\ \mathbf{sec}$) 27
2.2.2. Atomistic scale ($\sim 10-9\ \mathbf{m}, \sim 10-9-10-6\ \mathbf{sec}$) 28
2.2.3. Mesoscale ($\sim 10-6\ \mathbf{m}, \sim 10-6-10-3\ \mathbf{sec}$) 29
2.2.4. Macroscale ($\sim 10-3\ \mathbf{m}, \sim 1\ \mathbf{sec}$) 31
2.2.5. Multiscale modeling of polymeric materials 32
2.3. The specific case of geomembranes 34
2.3.1. Phenomenological models for GM's behavior investigation 34
2.3.2. Geomembrane modeling approach 37
2.4. Discrete Element Method (DEM) 40
2.5. YADE: a DEM platform 42

2.5.1. YADE simulation overview 42
2.5.2. DEM contact laws implemented in YADE 42
2.5.3. Modeling of deformable structure in YADE framework 45
2.5.4. Time integration and Motion calculation 49
2.5.5. Computational Challenges and Efficiency Considerations in DEM Simulations 50
Chapter 3: Construction of a numerical model at mesoscale for investigating the mechanical response of PVC geomembranes 53
3.1. Discretization of PVC microstructure in the DEM framework 54
3.1.1. Polymer fiber modeling 54
3.1.2. Crystallites modelling and distribution 55
3.1.3. Amorphous region modeling 57
3.2. Integration of the plasticizer into the model 60
3.3. Sensitivity of microstructure morphology to geometrical parameters 63
3.4. Simplification of model's mechanical parameters 65
3.5. Modeling assumptions 66
3.5.1. Contact-based mechanics 66
3.5.2. Micro-inertial effects and their role 66
3.5.3. Numerical damping 67
3.6. Setting numerical uniaxial tensile tests 67
3.6.1. Boundary conditions setting 68
3.6.2. Chain's strength calibration 70
3.7. Summary 71
Chapter 4: Towards calibrating the model: Experimental Investigation of PVC Geomembrane Response to Tensile Forces 73
4.1. Materials and Experimental devices 74
4.1.1. Materials 74
4.1.2. Apparatus and data acquisition 74
4.1.3. Specimens preparation 75
4.2. Experimental methods 76
4.2.1. Methodology of uniaxial tensile tests at various loading rates 77
4.2.2. Methodology of relaxation tests 82
4.2.3. Methodology of creep tests 84
4.2.4. Methodology of strain recovery tests 84
4.3. Results and discussions 87
4.3.1. Rate-dependency effect at short term 87
4.3.2. Rate-dependency effect on the long term 93
4.3.3. Time-dependency response 98
4.3.4. Failure threshold 108
4.4. Conclusions 110
Chapter 5: Multiscale analysis of PVC GMs: From microstructural features to macroscopic behavior 112

5.1. Mechanical behavior of a simple two-crystallites system 113
5.1.1. Microstructural evolution 113
5.1.2. Force distribution 114
5.1.3. Stress-strain response 117
5.2. Model calibration: defining a reference sample 121
5.2.1. Reference parameters 121
5.2.2. Macroscopic stress-strain response 122
5.2.3. Stress distribution in specimen microstructure 125
5.2.4. Comparison with experimental data 133
5.3. Impact of EV sizes on the stress distribution 135
5.3.1. Macroscopic stress-strain behavior for different EV sizes 135
5.3.2. Linking macroscopic behavior to microstructural analysis 137
5.3.3. Comparison with experimental data 143
5.4. Impact of the number of chains per crystallite 145
5.4.1. Stress-strain curves at different chain number per crystallite 145
5.4.2. Force Distribution Maps at Different Chain Densities 146
5.4.3. Stress uniformity across the specimen 151
5.5. Impact of the chain's length on the model results 152
5.5.1. Impact of chain's length on the stress-strain curve 153
5.5.2. Microstructural analysis and force distribution 154
5.5.3. Stress uniformity across the specimen 160
5.6. Tensile strain rate and micro-inertial dynamics effects 163
5.6.1. Stress-strain response with different tensile rates 163
5.6.2. Energy balance 168
5.7. Simulation of non-plasticized PVC material 169
5.8. Main findings 172
Chapter 6: General conclusions and perspectives 174
6.1. Objective of this work 174
6.2. Major contributions of this work 174
6.2.1. Rate-dependent behavior 174
6.2.2. Time-dependent response 175
6.2.3. Failure criteria under tensile forces 175
6.2.4. Relation between mesoscale deformation and macroscale behavior 175
6.3. Perspectives and future work 175
6.3.1. Future studies on REV size and selection 176
6.3.2. Towards more exploration and model enhancements 176
6.3.3. Evaluation of material behavior through cyclic loading-unloading-reloading tests 177
References 178
List of figures 187
List des tables 195

APPENDIX A **196**
A. Key Concepts of DEM Formulation in YADE 196
a. YADE code structure 196
b. Collision detection between bodies in YADE 196
c. Interaction detection and computation in YADE 196

Chapter 1: Introduction

1.1. Geomembranes from an industrial point of view

1.1.1. The evolution and importance of geomembranes in modern engineering

Waterproofing has been essential for human civilizations for millennia. Early approaches used natural materials like clay, bitumen, and plant fibers to resist water infiltration. The advent of geosynthetics in the mid-20th century marked a significant milestone in waterproofing technology.

According to (ISO/DIS 10318-1, 2015), a polymeric geosynthetic barrier is defined as a *"factory-assembled structure of geosynthetic materials in the form of a sheet in which the barrier function is essentially fulfilled by polymers".* The barrier function, in this context, refers to the ability of the polymeric geosynthetic to prevent or limit fluids migration through structures, ensuring effective containment. This type of polymeric geosynthetic is commonly referred to as a *geomembrane*.

Initially developed for canal linings, geomembranes quickly gained popularity in the 1960s, particularly in dam construction, due to their outstanding impermeability compared to traditional materials like clay, concrete, or asphalt concrete. The first recorded use of geomembranes in dams dates back to 1959 at the Contrada Sabetta fill dam in Italy (Scuero and Vaschetti 2017), where they served to provide a water barrier for a new embankments dam. Over time, different systems were developed to rehabilitate existing dams, and waterproof all types of new dams (Touze et al. 2021).

The importance of geomembrane has grown year by year, aligning the growing concern towards sustainable development and resource management. This rise in importance is driven by the urgent need for new adaptation strategies to address worldwide challenges (i.e., Climate change, pollution, and drought crises), resulting from population increase and industrialization (Dixon et al. 2017; Touze et al. 2021). They are preferred over common barrier materials like compacted clay liners (CCL) and concrete for their extra advantages, which include impermeability, cost-effectiveness, ease of construction, and durability (Cazzuffi and Gioffrè 2023).

Today, geomembranes (GMs) are becoming indispensable for waterproofing all types of hydraulic and geotechnical structures worldwide, including canals, hydraulic tunnels, traffic tunnels, surge shafts, reservoirs, underground tanks, landfills (in waste management for municipal, industrial, hazardous, and low level radioactive solid waste), and different type of dams (concrete gravity dams, arch dams, rockfill dams, earthfill dams, tailing dams, RCC dams)(Dammyr et al. 2014; Rowe et al. 2019).

1.1.2. The different geomembrane materials with a focus on PVC

The selection of geomembrane materials varies by application. They include principally polyvinyl chloride (PVC), high-density polyethylene (HDPE), linear low-density polyethylene (LLDPE), ethylene propylene diene monomer (EPDM), polypropylene (PP), and bituminous geomembranes (BGM). Given its widespread use and proven performance in hydraulic applications, this research focuses specifically on PVC geomembranes.

PVC geomembranes, are preferred in dams and underground tunnels due to their flexibility during installation and ability to accommodate large deformation (Bekoin 2016; Cazzuffi and Gioffrè 2018, 2023; Krauskopf 1993). As in 2016, it is estimated that around 400 large dams in the world are lined with geomembranes, mainly made of PVC (Scuero and Vaschetti 2017). In embankments dams specifically, PVC geomembranes are used in approximately 48.5% of dams, while polyethylene geomembranes (LLDPE, HDPE, CSPE, CPE) are employed in nearly 30% of dams, and bituminous geomembranes constitute waterproofing about 12% of embankment dams (Cazzuffi and Gioffrè 2023). Additionally, PVC geomembranes have been employed in over 92% of lined tunnels all over the world, according to the ITA - International Tunnelling Association (Cazzuffi et al. 2023).

1.1.3. Unexpected mechanical loads affecting the hydraulic barrier function of geomembranes

According to Cazzuffi and Gioffrè (2023), geomembranes in embankment dams, for example, are typically located on the upstream face of the structure. This could expose it to a variety of detrimental actions, including damage by ice, floating debris, boats, falling rocks, animals, waves, fluctuations in water level and exposure to environmental agents (Oxygen, UV, heat). Therefore, cover layers are frequently used to protect the geomembranes.

Based on the ICOLD database, 70% of the geomembranes used on the upstream face of embankment dams are protected by a cover layer made of heavy materials such as cement concrete, or soil. Examples of in-situ casting include Contrada Sabetta (1959), Italy; Codole (1983), Corsica, France; Figari (1993), Corsica, France; Bovilla (1996), Albania; Ortolo (2000), Corsica, France; and La Galaube (2000), France. Examples of using concrete blocks include Mas d'Armand, France (1981) and Mauriac, France (1989) (Cazzuffi et al. 2011).

However, during construction, in-situ casting, the placement of concrete blocks, or even soil can lead to unexpected mechanical actions that may damage the geomembrane (Cazzuffi and Gioffrè 2023; Rowe 1998). To mitigate these operational problems, geomembranes are typically combined with a needle-punched nonwoven geotextile. Similarly, in concrete and masonry dams, a geomembrane-geotextile geocomposite is applied to the upstream face. The geotextile component serves to protect the geomembrane from mechanical damage caused by irregularities in the dam face,

additionally, to reinforce it, thereby minimizing the risk of creeping or sagging along the quasi-vertical dam face (Cazzuffi and Gioffrè 2020; Giroud 2006).

Despite protective measures, geomembranes remain vulnerable to unexpected mechanical actions, such as earthquakes, improper installation (see Figure 1.1), and contact with angular solids in the case of a malfunctioning of the protective layer (see Figure 1.2). In reservoirs, the subgrade beneath the geomembrane can become softened in some areas, potentially resulting in differential settlements and localized tensile stress when the weight of stored fluid is applied (Cen et al. 2018; Eldesouky and Brachman 2020; Hornsey and Wishaw 2012; Marcotte and Fleming 2019, 2021; Rowe et al. 2019). Additionally, down-drag forces on side slopes and gravitational stresses in high quasi-vertical dams during installation can lead to persistent tensile stresses on geomembranes, causing potentially significant indentations, punctures, or even holes and tears. This results in various severe consequences ranging from loss of stored fluid to structural failure (Abdelaal et al. 2014; Frost et al. 2012; Hornsey and Wishaw 2012; Luciani and Peila 2019; Müller and Wöhlecke 2019; Rowe et al. 2019). Therefore, the distribution of these tensile stresses within the geomembrane, and consequently, the ability of a geomembrane to elongate without failing is strongly important, to resist puncturing, bridge cracks, and perform well at interface interactions with rigid surfaces. Thus, beside its waterproofing properties, the mechanical properties of geomembrane are essential considerations for engineers when designing waterproofing systems.

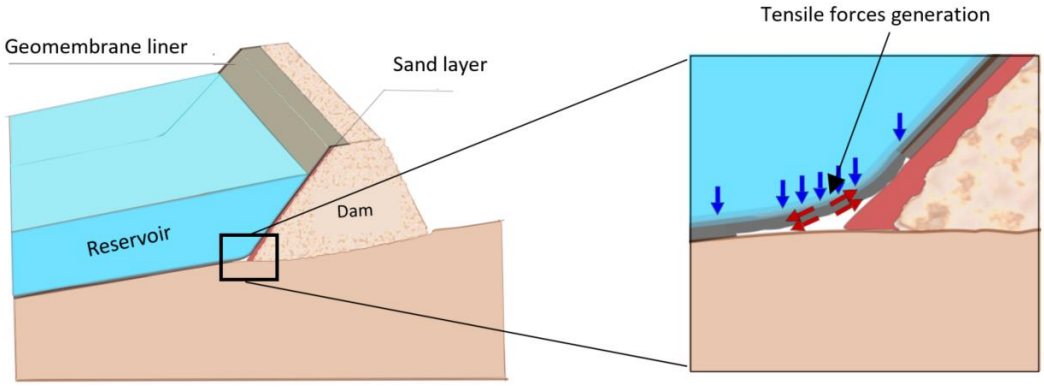


Figure 1.1: Traction forces generated inside improperly installed geomembrane under water loading.

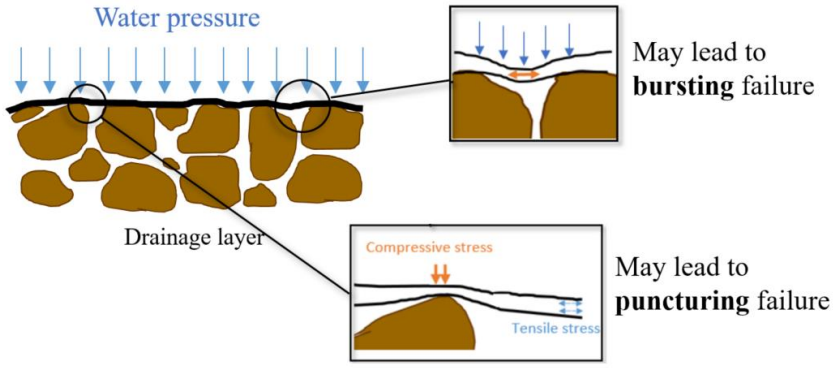


Figure 1.2: Direct contact of the geomembrane with drainage layer.

1.1.4. Standardized tensile tests for evaluating geomembrane mechanical properties

Several regulations and standardized tensile tests have been put in place to evaluate the mechanical properties of the geomembrane (GM). There are two main types of tests to determine the tensile characteristics of a geomembrane: the uniaxial tensile test and the multiaxial tensile test. The latter, performed according to the European standard NF EN 14151 (AFNOR 2010), involves applying hydraulic pressure under a circular GM specimen until it ruptures. For the characterization of GMs, the uniaxial tensile test is systematically used. It involves subjecting a GM specimen to tensile stress at a constant deformation rate until failure (i.e., separation of the specimen into two pieces). Regarding tests on geomembranes, we can cite the European standards NF EN 12311-2 (AFNOR 2013), and the international standard NF EN ISO 527-1, 3, 4 (AFNOR 2018, 2019a, 2023), and ASTM D4885 (ASTM D4885 2018).

1.2. From engineer to scientific challenges

A major engineering challenge is to extrapolate fast laboratory test results (minutes or hours) to design waterproofing systems that will protect the environment and public health over years or decades. Therefore, it is worth to consider the disparity in tensile speeds between laboratory tests and in situ scenarios. The actual tensile speed in-situ conditions does not necessarily match the speeds used in standard laboratory tests, such as those specified by the European standard EN12311(AFNOR 2013), which recommends a displacement rate of 100 mm/min, or the ASTM D4885 (ASTM D4885 2018), which recommends a displacement rate of 10 mm/min.

Merry and Bray (1997) focused on characterizing the time-dependent mechanical behavior of high-density polyethylene (HDPE) geomembranes used in landfills. Strain-controlled multiaxial tension tests were performed on HDPE specimens 1.0 and 1.5 mm thick from two different manufacturers. The strain rates used in this study varied from 10% per minute to about 0.0004% per minute. It has been demonstrated that as the strain rate decreases, both the maximum stress and the initial moduli decrease. Therefore, the mechanical properties at a single strain rate fail to meet the actual needs of engineering.

Consequently, studying the effect of tensile speed is of paramount importance for accurately determining the mechanical response and resistance of the GM (Cazzuffi and Gioffrè 2023; Merry and Bray 1997).

Indeed, numerous factors can influence the mechanical performance of GMs (mentioned in section 2.1), prompting researchers to employ numerical modeling methods to account for this diversity and its implications. To date, the Finite Element Method (FEM), the Material Point Method (MPM), and the Discrete Element Method have been prominently used for GMs modeling. However, these methods typically assume homogeneous behavior in GMs, excluding the ability to replicate localized issues related to internal features that control macroscopic mechanical behavior and failure modes.

Therefore, to better understand this subject, it is essential to first explain the fundamental mechanisms that govern the observed macroscopic mechanical behavior of the material. This requires studying the behavior at a mesoscale level, focusing on the microstructure to reveal the material's elementary deformation mechanisms. Such an investigation is highly relevant, as it provides critical insights into tensile stress distribution and failure mechanisms. Additionally, investigation on the structural evolution during tensile deformation of semi-crystalline polymers is of importance for correlating the microstructure with ultimate properties. Thus, it is important to develop a fundamental understanding of the effects of microscale variability on material properties and response, such as the Young's modulus, stress/strain distribution and damage initiation mechanisms.

1.3. Methodology and structure of the present work

The present work provides a comprehensive investigation aimed at understanding the mechanical behavior of PVC GMs under tensile loading. Tensile actions represent the most critical mechanical stresses, as their occurrence can lead to severe consequences, such as puncturing and tearing that affect the integrity and long-term performance of the geomembrane. To address this, the research, carried out over three years, combines experimental work (chapter 4) and advanced modeling techniques (chapters 3 and 5) to uncover key insights into material behavior under uniaxial tensile loading.

This thesis manuscript is organized into five chapters:

- **Chapter 2** presents a **comprehensive overview** of the essential concepts and numerical tools necessary to the following work. It begins by detailing the main characteristics of the PVC GM adopted in this study, including its composition, structure, and mechanical properties. The chapter then presents a brief review of modeling approaches used for polymeric materials across different scales. Hereinafter, a particular attention is given to phenomenological models and numerical techniques relevant to geomembranes, highlighting that, to the best of our knowledge, no study investigates the localized issues stemming from internal features, which play a critical role in shaping the macroscopic behavior of geomembranes.

- By taking advantage of the discretization of the DEM, this study replicates the microstructure of PVC geomembranes, composed of a semi-crystalline assembly of polymer chains embedded within a matrix of plasticizers. Thus, **Chapter 3** details the step-by-step construction of a DEM-based model of PVC GMs accounting for their semi-crystalline structure over an elementary volume of a few tens of nanometers. The chapter details the geometrical construction of the model, and discusses the sensitivity of microstructural morphology to geometrical parameters. It concludes by setting up a numerical uniaxial tensile tests and calibrating the mechanical parameters.
- **Chapter 4** presents an extensive experimental campaign proposed to investigate the GM's mechanical response to uniaxial tensile loading, focusing on both rate-dependent and time-dependent behaviors. The campaign includes short-term tests (rate-dependent tensile tests) and long-term tests, such as relaxation, creep, and strain recovery experiments. Moreover, these experimental efforts provide critical data for understanding, calibrating, and validating the DEM-based model introduced in Chapter 3.
- **Chapter 5** investigates the capability of the model to predict the macroscopic mechanical behavior, while bridging the gap between the elementary deformation mechanisms within the semi-crystalline polymer and the observed macroscopic responses. Additionally, it presents a comprehensive parametric study, examining the influence of microstructural features on shaping the material's overall mechanical performance.
- Finally, **Chapter 6** presents the general conclusions and perspectives of this work.

Chapter 2: State of the art

The objective of this chapter is to provide a concise overview of the current state of the art and introduce the essential concepts and numerical tools necessary for understanding the methodology presented in the following chapters. In the first section, we clarify the main characteristics of PVC geomembranes and explore the environmental effects on their performance. Following this, we briefly explain the numerical modeling techniques used for polymers at different time and length scales. Subsequently, we review the methods employed in modeling geomembranes, involving numerical approaches, and provide a justification for the choice of the Discrete Element Method (DEM) in our modeling. Finally, the last sections offer details about the numerical methods used in this study and the key concepts borrowed from the open-source software YADE.

2.1. Microstructural characteristics and environmental effects on PVC GMs

The mechanical properties and durability of geomembranes are influenced by their weathering resistance and ability to withstand unexpected external loads. It is important to note that not all geomembranes exhibit the same behavior due to differences in their chemistry, basic ingredients, and manufacturing processes. This research focuses specifically on plasticized-PVC-type geomembranes (PVC GMs). In the following sections, we will discuss the manufacturing process, the nature of the microstructure, and the various effects of environmental agents and internal features on the properties of PVC GMs.

2.1.1. PVC resin microstructure

Polyvinyl chloride (PVC) is a synthetic polymer made from vinyl chloride monomers (C_2H_3Cl). During the polymerization process, these molecules undergo a chemical transformation in which their double bonds open, allowing carbon atoms to link together sequentially, forming a very long chain-like molecule called polymer. This process yields a powder with a grain size of around 100μm, where the morphology of the powder's grain consists of agglomerates of primary particles, examined by electron microscopy (Gilbert 1994). A smaller, microdomain structure is observed by small-angle x-ray scattering as density fluctuations at about 0.01 microns spacing, which have been related to PVC crystallite spacing (Gilbert 1994; Summers 1981; Wenig 1978). Crystallites consist of well-aligned PVC chains that arrange into a specific shape. Therefore, the structure of PVC primary particle would be such as the crystallites are tied together by a three dimensional network of tie molecules (Summers 1981), with the crystalline content comprising approximately 5-10% (see Figure 2.1 (a)). Wenig (1978) has determined PVC crystal sizes using wide angle X-ray scattering line widths in the Scherrer equation. The average crystallite size is illustrated in Figure 2.1 (b), as reported by Summers (1981). This

indicates that at low temperatures, primary particles are weakly interacting due to their internal three-dimensional network structure, which prevents interaction with other primary particles.

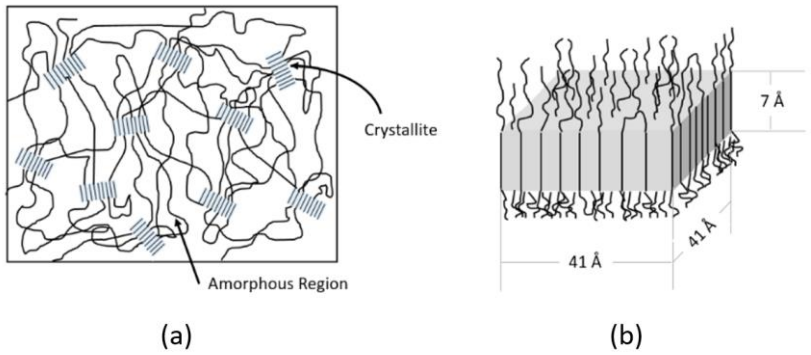


Figure 2.1 : The micro-domain structure of PVC. (Right) Average crystallite size of PVC. Inspired from Summers (1981).

2.1.2. PVC geomembrane manufacturing

Flexible PVC is produced by mixing the PVC particles resin with additives. In the case of PVC used for geomembranes, plasticizers make up 25 to 35% of the material (Cazzuffi and Gioffrè 2020). Additional additives can be included to provide various functions, such as UV stabilizers (e.g., Carbon black), heat stabilizers, fire-resistant additives, filler and pigments for specific colors. While these additives primarily serve to prevent degradation and enhance durability, they generally do not significantly alter the mechanical properties of the PVC geomembranes (Lodi et al. 2008).

The production of PVC membranes involves several steps. Initially, a sufficient "mechanical work" is required to break the initial hierarchical structure of PVC grains into micronic primary particles, as shown in Figure 2.2 (1) (Fillot et al. 2006). The mix is then heated to a temperature between 185 and 200 °C, causing partial melting of some crystallites and increasing interaction between primary particles at their boundaries, although the primary particle structure is not entirely destroyed (see Figure 2.2 (2)). This process, known as gelation, is followed by extrusion and calendaring, which is a process to let the polymers pass through rollers to stretch, compress and cool (Rollin et al. 2002). A schematic representation of the process is illustrated in Figure 2.3. Upon cooling, secondary crystals form not only within the primary particles but also at their interfaces, as seen in Figure 2.2 (3). Consequently, the initial morphological shape of primary particles has partially vanished and been replaced by a network of entangled molecules and newly arranged crystallites (Fillot et al. 2006; Summers 1981).

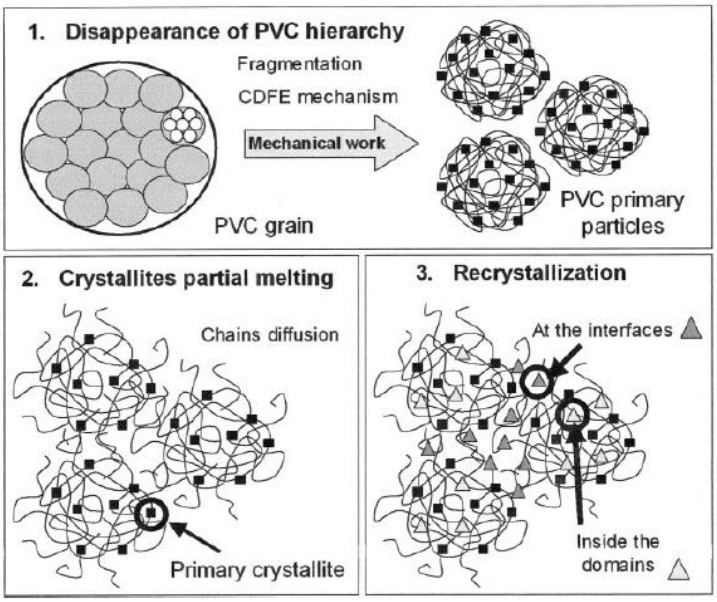


Figure 2.2 : Gelation process described by Summers's model. Disappearance of the PVC primary particle structure and development of a macromolecular network (Illustration taken from (Fillot et al. 2006))

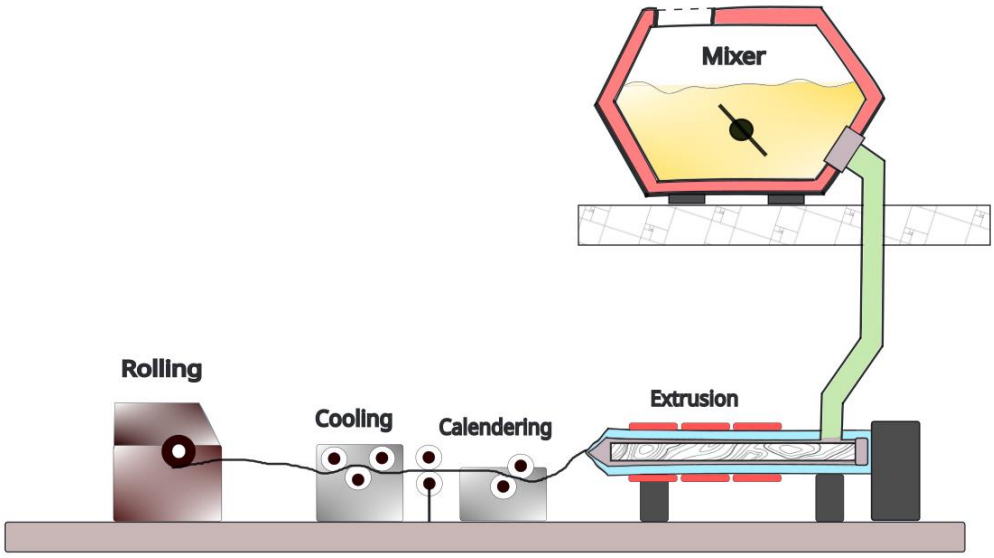


Figure 2.3 : PVC GM manufacturing. Inspired from (Rollin et al. 2002).

2.1.3. Partial crystallization and plasticizer impact on the PVC microstructure

Two morphological forms of crystallinity exist. First, the crystals are comprised up of a set of polymer chains that are well-aligned in parallel, forming crystallized regions (see Figure 2.4 (a)). The second type consists of polymer chains that fold onto themselves, forming plate-like structures known as lamellae (see Figure 2.4 (b)).

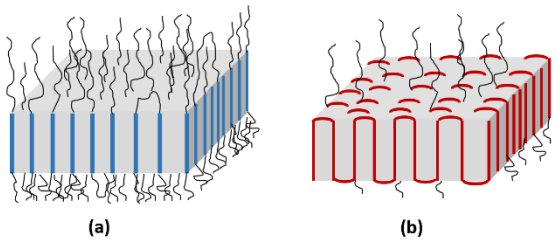


Figure 2.4 : Two crystallinity-types are shown here. (a) The crystals is made up of a series of parallel polymer chains. (b) The lamella-shaped crystal is being formed by molecular chains that fold onto themselves. Adapted from (Gilbert 1994).

Lebedev et al. (1972) discovered a sudden morphological change in crystallites as the molecular weight increases. They concluded that crystallites in high molecular weight polymers contain short syndiotactic segment from different chains, without chain folding, corresponding to the first type of crystallite structure (Figure 2.4(a)). According to Summers (1981), these crystallites typically consist of bundles of 8 molecules arranged laterally and spanning 3 monomer units along the chain direction.

Gilbert (1994) has mentioned that the presence of up to 50% plasticizer in the PVC had little effect on its crystallinity. Additionally, Summers (1981) has investigated the impact of plasticizers on the micro-domain. He revealed that the addition of plasticizer affects the crystallite spacing, which increases due to swelling in the amorphous regions. This swelling is limited by the crystallites, which act as an interlocking network. Consequently, the morphology of the PVC GM consists of arranged small crystal domains connected by a network of entangled molecules, where the crystallites are not destroyed by the plasticizer.

2.1.4. From physical properties to PVC characteristics

The predominant intermolecular interactions in PVC are the Van Der Waals and the Dipole-Dipole interactions. This later consists of electrostatic attractions of a chlorine atom in one molecule to a hydrogen atom in another molecule. The hydrogen interactions are rarely present. These considerable intermolecular attractions between polymer chains make PVC a fairly strong material. Additionally, those interactions forces are the primary interactions that help maintain the alignment of the polymer chains within the crystallites of PVC. When adding the plasticizer, it fits in between the polymer chains in the amorphous region (Gilbert 1994), resulting in their separation, and consequently weakening the intermolecular forces between them (Figure 2.5). Therefore, products made from PVC only are rigid. They are suitable in building construction for items such as pipes. Introducing plasticizers in PVC alters its physical properties, transforming it from a rigid material to a flexible one.

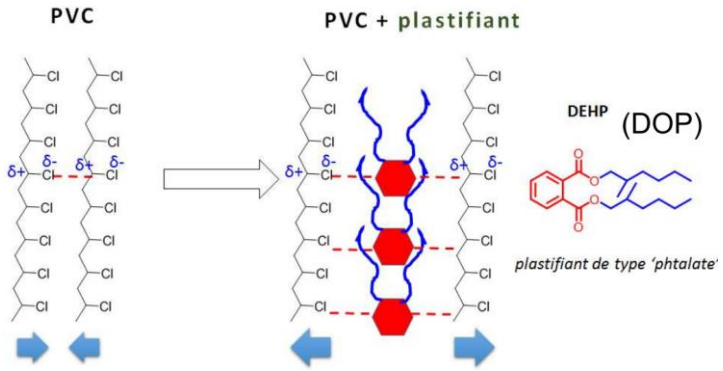


Figure 2.5 : Integration of plasticizer between the polymer chains (Personal communication from Alexis Roulet).

Polymers can be exposed to many processing stages that may affect their characteristics and the product quality. For instance, during extrusion -- the primary industrial process used for PVC geomembranes manufacturing -- the material is subjected to high shear stresses and elevated temperatures (Lamri et al. 2020). This process can alter the polymer's molecular orientation and crystalline structure, ultimately influencing its mechanical and physical properties.

Additionally, the physical properties of polymers, including molecular weight, density, degree of polymerization, and crystallinity of material, significantly affects the material's properties and performance. The degree of polymerization in a polymer molecule is defined as the number of repeating units in the polymer chain. Thus, the molecular weight of a polymer molecule is determined by the product of the degree of polymerization and the molecular weight of the repeated unit.

As mentioned in (Gilbert 1994), the polymerization conditions, and subsequently the molecular weight induce morphology change in crystallite, as with high molecular weight the crystallite consists of well-aligned parallel segments from different polymer chains without folding. As molecular weight increases, the structure contains more entanglements, thereby giving higher material's strength (Balani et al. 2014).

The degree of crystallinity within the material enhances the strength as well, as intermolecular bonding is more significant in the crystalline phase. Additionally, the crystallites act as crosslinks, as noted by Summers (1981), which further contributes to the material's increased strength and Young's modulus (Gilbert 1994; Patterson et al. 1982).

Patterson et al. (1982) have demonstrated that the increased chain length between crosslinks (i.e., crystallites and entanglements) with increasing quantity of plasticizer is attributed to the disentanglements of the non-crystalline network (i.e., entanglements). This results in a more flexible PVC material.

2.1.5. Effect of temperature on PVC mechanical characteristics

Mechanical properties are significantly impacted by temperature. At lower temperature, in the amorphous region of the polymer, the molecules are in a frozen state, where they can vibrate slightly but are not able to move significantly. This state is referred as the

glassy state, where the behavior of polymer is brittle, hard and rigid. Conversely, when the material is heated, the chains' ability to move and wriggle around each other is improved, resulting in soft, flexible behaviors (i.e., Rubbery state) (Balani et al. 2014). The transition temperature between the two states (i.e., rubbery to glassy state) is called the glass transition temperature T_g.

It is worth mentioning that the crystalline region is not affected at the glass transition temperature. The melting of crystallites, a first-order transition, occurs at the melting point temperature T_m higher than T_g.

Indeed, the value of T_g depends on several factors (Balani et al. 2014; Landel and Nielsen 1993). Strong intermolecular forces cause higher T_g. Additionally, a higher degree of crosslinks (i.e., crystallites and entanglements) between the chains restricts rotational mobility, leading to a higher T_g. Plasticizers, which penetrate between the chains, reduce the intermolecular cohesive forces (i.e., dipole-dipole interactions), thereby decreasing T_g (Hsuan et al. 2008; Stark et al. 2004). Moreover, chain stiffness has an effect too; stiffer bonds in the backbone of the chain reduce its flexibility, resulting in a higher T_g. Finally, a higher molecular weight of polymer can increase T_g, as described by the Fox_Flory Equation (2.1):

$$T_g = T_{g,\infty} - \frac{K}{M_n} \tag{2.1}$$

Where $T_{g,\infty}$ is the glass transition temperature at infinite molecular weight, K is the empirical Fox-Flory parameter.

The glass transition temperature for PVC material used for GM is around +87°C. The addition of plasticizers significantly reduces this T_g (Cazzuffi and Gioffrè 2018).

At ambient temperature, Hsuan et al. (2008) have found that the flexibility of PVC GM decreased and the brittleness increased at low temperatures. According to Cazzuffi and Gioffrè (2020), high temperatures lead to a reduction in the tensile modulus and an increase in elongation compared to low temperatures. Zhang et al. (2021) have studied the response of mechanical properties of PVC GM to ambient temperature subjected to axial tension. They revealed that the temperature significantly affects the stress-strain curve of PVC GM. As temperature increases, the material exhibits lower stress for the same strain level. Thus, they concluded that evaluating mechanical properties at a single temperature is insufficient to fully assess GM quality. Instead, properties should be evaluated by considering the full range of ambient temperatures experienced during operation.

2.1.6. PVC geomembrane aging and degradation

The degradation of geomembranes can be attributed to both internal and external factors. Internal factors are related to the intrinsic characteristics of the geomembrane, including the composition of PVC, the quality of its additives, and the thickness of the geomembrane. External factors are influenced by site conditions that are more difficult to manage, such

as environmental factors (e.g., temperature, UV radiation, dry-wet cycles, chemical and biological attacks) and unexpected loads (e.g., gravity, puncture, waves, earthquakes).

PVC degradation primarily occurs due to dehydrochlorination, a chemical process in which hydrogen chloride (HCl) is eliminated from the polymer chain (Cazzuffi et al. 2023; Lodi et al. 2013). This leads to the creation of double bonds that propagate along the polymer backbone, contributing to the degradation of the geomembrane. Several factors promote the dehydraochlorination: UV radiation initiates the process (UV degradation), elevated temperatures accelerate the loss of HCl (thermal degradation), and certain chemicals can catalyze the removal of HCl from PVC (Vivek G. Bhartu 2017). This process significantly impacts PVC GM properties, such as reduced flexibility, decreased elongation at failure, and increased rigidity (Lodi et al. 2008). The first visible sign of the dehydrochlorination is typically discoloration, turning the material to yellow or brown due to the formation of conjugated double bonds.

After dehydrochlorination, oxidative degradation can occur in PVC geomembranes. This process involves UV radiation breaking chemical bonds within PVC, generating free radicals (Hsuan et al. 2008). These highly reactive radicals then interact with oxygen (Usman and Galler 2014). This reaction weakens the polymer's structure and leads to degradation of its mechanical properties. UV degradation can be mitigated by adding antioxidants and carbon black, or by keeping a minimum layer of 15 cm of soil or gravel to block light penetration (Koerner 1998; Reddy and Butul 1999).

The temperature is an important parameter in the aging process due to its capability to influence mechanical properties (Lodi et al. 2006; Zhang et al. 2021). Higher temperatures can result in decreased bending stiffness in the polymer chain, reduced resistance to chemicals, and accelerated thermo-oxidative degradation processes. (Karademir and Frost 2021) found that the behavior of the interface shear strength in a geotextile–geomembrane system is highly dependent on the temperature.

Microbial attack also affects the durability of PVC GM , as fungi degrade plasticizers, resulting in a stiffer material with higher tensile strength (Cazzuffi et al. 2023; Usman and Galler 2014).

Plasticizer loss is the most common symptoms of aging of PVC GMs, occurring through contact with air, liquids, or absorbent solid materials (Hsuan et al. 2008; Stark et al. 2004). Both external and internal factors influence plasticizer retention. External or environmental factors include temperature, frequent freeze-thaw cycles, ice actions, chemicals, microorganisms, and the nature of the contact material, such as air, liquid, or solid. Internal factors are related to the molecular weight and linearity of the plasticizer.

In the air, plasticizer can evaporate through two major transfer processes, firstly diffusion from inside to the surface, then evaporation from the surface. This kind of loss plays an important role in PVC GM liner systems without a protective layer. Additionally, even in the case of covered GMs, this loss cannot be neglected if the protective layer contains moisture and provides enough free air for evaporation. Researchers (Blanco et al. 2017; Giroud 1984; Krauskopf 1993) suggest that increasing the plasticizer molecular weight or decreasing the degree of branching imparts significant reduction in plasticizer volatility.

Plasticizer migration into liquids typically occurs in pond liners below the water line. This can happen through two mechanisms. The main mechanism occurs where the solvent diffuses into the plasticized PVC, dissolves the plasticizer, and diffuses out to the surface(Stark et al. 2004). This mechanism depends strongly on the compatibility of the plasticizer and the solvent. The second-type of mechanism occurs when the molecular size of the solvent molecules is too large to penetrate inside the GM (Stark et al. 2004). In such a case, the migration of plasticizer can only occur when the plasticizer diffuses to the surface of the GM, and then partitions in the solvent (Rowe et al. 2023). Here, the retention of plasticizers is influenced by molecular weight and diffusion coefficients of the plasticizer.

Additionally, plasticizer can migrate into another polymeric material, with this migration increasing as the plasticizer's molecular weight decreases and its linearity (i.e., degree of branched molecule) increases (Wilson 1995). Blanco (2006) has found that when a PVC GM was covered with a protective sheet made of the same material (plasticized PVC), the GM's plasticizer content increased due to its migration from the protective sheet. This improves the mechanical properties of the PVC GM after eight-and-a-half-year period (Blanco et al. 2017).

Therefore, Stark et al. (2004) recommends a minimum average plasticizer molecular weight of 400 to ensure excellent long-term performance of the GM (Blanco et al. 2017).

Plasticizer play a critical role in terms of variation in mechanical properties of the PVC GM (Blanco et al. 2010, 2017, 2018; Koerner et al. 2016; Krauskopf 1993). Cazzuffi and Gioffrè (2020) observed that PVC GMs installed without a protective layer on the upstream face of six Italian dams over 25 years showed a consistent decrease in plasticizer content and a reduction in nominal thickness. Mechanical testing indicated increased stiffness, higher tensile strength, and reduced strain, with a slight decrease in water permeability coefficient measured thanks to vapor transmission test (AFNOR 2000).

The lifetime assessment of the exposed PVC GM is strongly dependent of the plasticizer content. However, it is worth mentioning that the minimum quantity of plasticizer admissible to ensure durability of the GMs rely on the applied external actions on the GMs (e.g., external environment, type of application, and design of the barrier system), as well as, on the type of plasticizer used. (Cazzuffi and Gioffrè 2020; Giroud 2021) suggest that a loss of 30 % of the initial quantity of plasticizer indicates the non-workability of the geomembrane. Rowe et al. (2009) argue that the degradation of a GM involves the reduction of up to 50 % in its properties compared to the values required in normative. Blanco et al. (2018) found that even with a loss of greater than 70% of the plasticizer in reinforced PVC geomembranes, the mechanical characteristics have remained well preserved over time. Thus, they suggest that current loss of plasticizers durability criteria need to be discussed.

Gilbert (1994) reported that mechanical properties can evolve over time even when the plasticizer content remains stable. This is attributed to the change in internal structure arising from reduction in free volume, or due to the development of secondary crystallization when T_g is below the room temperature.

Consequently, the durability of the GM depends on its weathering properties and resistance to external unexpected loads. To evaluate the performance and durability of geomembranes, various tests are conducted to ensure they meet the necessary standards and specifications for their intended applications. Among these tests are the plasticizer extraction test EN ISO 6427 (AFNOR 2014) , Normal thickness test EN1849-2 (AFNOR 2019b), Volumic mass EN ISO 1183-1 (AFNOR 2019c), Tensile properties NF EN 12311-1 and 2 (AFNOR 2013) or the international standard NF EN ISO 527-1, 3, 4 (AFNOR 2018, 2019a, 2023), water vapor permeability EN 1931(AFNOR 2000).

In Chapter 4, we investigate the tensile properties of PVC GMs when subjected to unexpected loading, which influence both their short-term performance during installation and their long-term durability in service. A range of several loading speed is employed to encompass several scenarios that may occur under in situ conditions, in order to help engineers in predicting and assessing the GM behavior, thereby significantly lower the risk of failure.

2.2. Modeling approaches for polymeric material at different scale

As seen in Section 2.1, polymeric materials exhibit a remarkable array of characteristics across different scales, from the angstrom level of individual bonds to tens of nanometers (e.g., chains, crystallites, and entanglements), to micrometers and millimeters (i.e., laboratory tests), and even larger scales (i.e., in situ inspections, blends, solutions, and melts).

At the molecular scale, polymers are characterized by their morphological structure and intermolecular interactions, which are responsible of the fundamental properties such as flexibility, strength, strain, and chemical reactivity. These molecular arrangements give rise to mesoscale phenomena such as polymer crystallization, and chain entanglements, which in turn influence the material's mechanical response at the macroscopic scale. This has driven researchers to develop and employ computational methods to design, predict and optimize the structures and properties of the materials.

This section presents the modeling approach and used tools associated with different length and times scales.

2.2.1. Quantum scale ($\sim 10^{-10}$ m, $\sim 10^{-12}$ sec)

Starting from the quantum scale, the modeling at this scale is used to study the physical phenomena at the scale of subatomic particles, including formation and rupture of chemical bonds and the changes in electrons configurations. Thus, classical Newtonian physics no longer accurately describes phenomena, and instead, quantum mechanics provides a convenient framework. However, these simulations are very computationally expensive; thus, this modeling technique is restricted to small number of atoms. Among the QM methods used, we cite “Ab Initio Quantum Mechanical Methods” (Hageman et al. 1997; Serra et al. 2000), “Semi-Emperical Quantum Mechanical Methods” and “ Density Functional Theory DFT” (Bouvard et al. 2009; Gooneie et al. 2017; Kohn and Sham 1965).

2.2.2. Atomistic scale ($\sim 10^{-9}$ m, $\sim 10^{-9} - 10^{-6}$ sec)

The atomistic scale is the right scale to study phenomena and properties related to groups of atoms. Here, atomistic modeling typically treats each atom as a distinct particle, which interact with others through interatomic potentials. The typical interactions include the bonded interactions, for atoms chemically bonded to one another, and the non-bonded interactions, for the interactions not chemically bonded to one another (e.g., Van Der Waals, Electrostatic, dipole-dipole, Hydrogen bonds). This technique is not limited to single atom-atom interactions but can be extended to molecule-molecule interactions.

Among the models adopting the atomistic approach, we cite the Molecular dynamics (MD) and the Mont-Carlo (MC) simulations. This latter help scientists understand how atoms interact and behave under different conditions by running many random experiments and analyzing the results statistically (Gooneie et al. 2017). This method has been used to investigate a variety of phenomena in polymeric material, such as Polymer melt elasticity (Mavrantzas and Öttinger 2002), Polymer dynamics (Mavrantzas 2021), polymer degradation (Adema et al. 2015; Makki et al. 2014).

The Molecular Dynamics method is a deterministic simulation, which use a single particle to describe the motion of the atom. Then, atomic potentials are employed to describe the interactions between particles. These interaction potentials define how particles influence each other through interaction forces. The forces f_i on each particle are derived from the potential, as given in Equation 2.2.

$$f_i = \frac{\partial E}{\partial r_i} \tag{2.2}$$

where E is the system potential energy, and r_i is the position vector of the particle.

Hereinafter, the motion of the collection of particles are determined through Newton's equations of motions. The most common used numerical integration schemes in MD are the Verlet (Verlet 1967), and the Gear velocity operator method which consists of a predictor-corrector algorithm (Brooks 1989). LAMMPS (Large-scale Atomic/Molecular Massively Parallel Simulator) is widely used software package for MD simulations, that includes a comprehensive set of interaction potentials (Plimpton 1995). Applications of MD is used to treat various topics in polymeric materials (Bouvard et al. 2009), such as molecular dynamics, crystal structure, diffusion phenomena, crack propagation, and polymer membrane (Neyertz and Brown 2013).

For instance, Neyertz and Brown (2013) conducted large-scale MD simulations to investigate CO_2 in a fully atomistic 50,000-atom fluorinated 6FDA–6FpDA polyimide membrane, as seen in Figure 2.6. They modeled the interface of the glassy polymer membrane, focusing on the interactions between CO_2 molecules and the polymer structure. The objective of this study is to examine the CO_2 sorption, diffusion, and its plasticizing effects on the polymer. The simulations used appropriate force fields to describe atomic interactions and periodic boundary conditions to represent an infinite membrane surface. CO_2 molecules were modeled as individual molecules with explicit

representation of each atom bounded rigidly. This approach enables the study of plasticization effects and the molecular-level mechanisms of gas transport through the membrane.

It is worth mentioning that these simulations require significant computational time. For instance, using 128 processors at Mississippi State University's Center for Advanced Vehicular Systems to simulate 10^6 atoms for one nanosecond took 72 hours with LAMMPS (Bouvard et al. 2009).

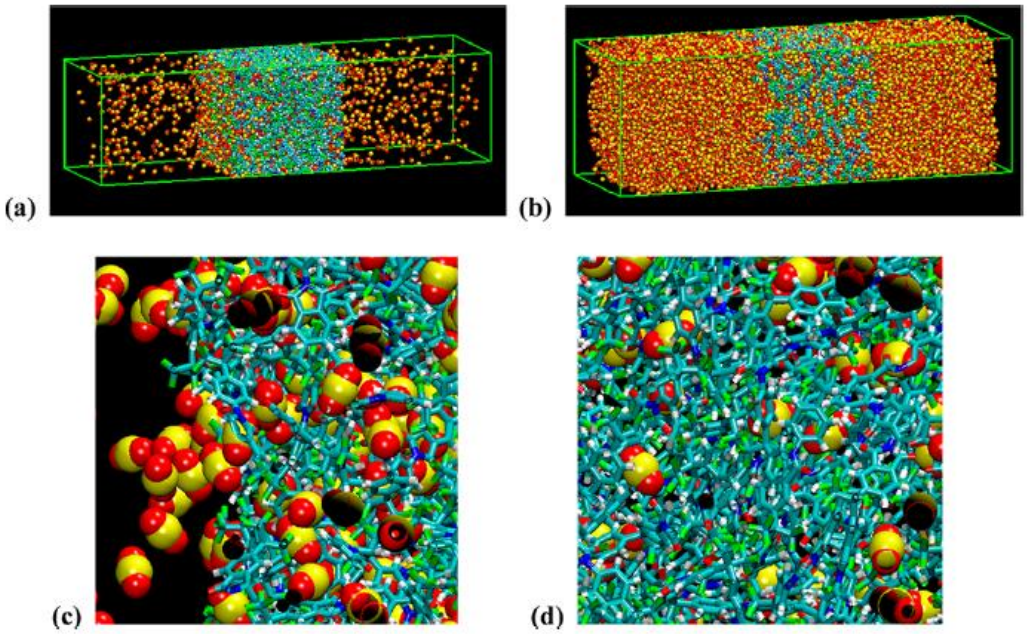


Figure 2.6 : The polymer and the CO_2 penetrants displayed along the x-direction in space-filling models with the VMD software. Extracted from (Neyertz and Brown 2013)

2.2.3. Mesoscale ($\sim 10^{-6}$ m, $\sim 10^{-6} - 10^{-3}$ sec)

Atomistic simulations of complex systems, such as polymeric materials, offer detailed insights into component interactions and conformational dynamics. However, this level of detail is typically absent in macroscale models due to the high computational cost at the atomic scale. Therefore, to bridge these two scales, mesoscale methods have been developed.

One prominent mesoscale approach is the coarse-grained modeling. This method increases the length scales studied using MD but remains constrained by time scaling. It involves representing a number of atoms by a single super-atom (i.e., bead), as seen in Figure 2.7, significantly reducing computational costs while preserving essential molecular interactions (Bouvard et al. 2009).

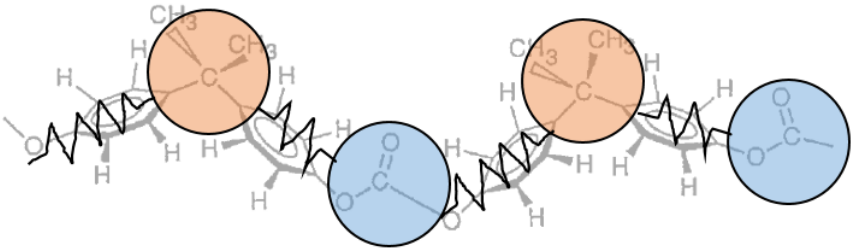


Figure 2.7 : A polycarbonate chain was represented using a two beadspring coarse-grain model, where the interaction potentials were derived from distribution functions proportional to the Boltzmann factors of generalized intrachain interactions. Subsequently, a standard molecular dynamics simulation scheme was applied for each considered temperature. Adapted from (Tschöp et al. 1998).

Another mesoscale method is Dissipative Particle Dynamics (DPD), introduced by Hoogerbrugge and Koelman (1992). DPD incorporates hydrodynamic interactions and thermal fluctuations to simulate soft matter systems with improved accuracy over purely particle-based models, where each bead represents the dynamic behavior of several atoms or molecules. The motion of each bead is governed by three types of forces: conservative force, dissipative force and random dissipative force from other neighboring beads. The velocity-Verlet algorithm is commonly used to update bead positions and velocities during simulation. This method have been successfully applied to simulate various complex systems, including blood rheology, lipid bilayers, and surfactant aggregation, and polymer/clay nanocomposites (Gooneie et al. 2017). For instance, Gooneie et al. (2016) developed DPD models to simulate the orientation of weakly-interacting anisometric silicate particles in a polymer matrix. The polymer chains are modeled as linear flexible chains of 50 beads connected together by harmonic springs (see Figure 2.8). The semi-flexible silicate is modeled with a 21×21 beads connected together by a harmonic springs with a stiffness constant higher than that of the chains. The dynamics of these beads is governed by Newton's law supplemented by friction and random forces to provide the thermostat of the system.

It is worth to mention that the Discrete Element Method (DEM) has grown in popularity for evaluating force networks and addressing localized challenges with granular assemblies at the mesoscale. This technique has been extensively used to investigate granular materials, rock materials, and other particle systems, providing critical insights into the microscopic mechanisms that plays a significant role in their overall constitutive behavior and interaction under various conditions (Lin et al. 2021; Nicot et al. 2005; Scholtès et al. 2009; Shi et al. 2015; Wautier et al. 2019).

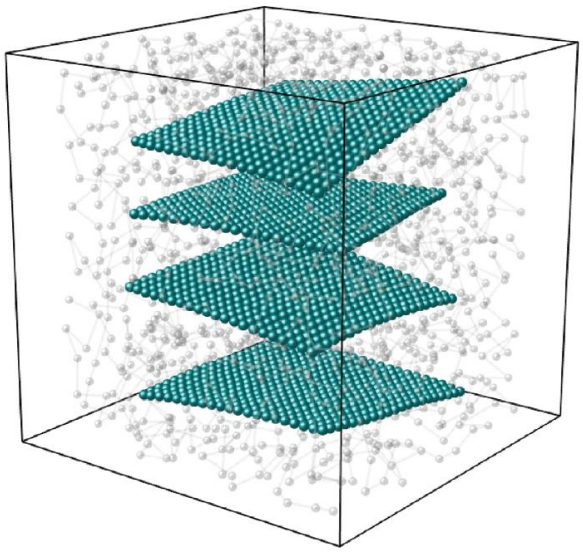


Figure 2.8 : Four semi-flexible silicate embedded between polymer chains (Gooneie et al. 2016).

2.2.4. Macroscale ($\sim 10^{-3}$ m, $\sim$ 1 sec)

At this scale, quantum, molecular, and atomistic theories become computationally expensive for solving engineering boundary value problems. Consequently, the fundamental approach at this scale involves replacing a heterogeneous material (comprising atoms, molecules, and chains) with an equivalent homogeneous model.

This scale is often referred to the continuum scale, where physical properties are defined as continuous functions of space and time. Constitutive laws, ranging from simple (e.g., Hooke's law for linear elastic materials) to complex (e.g., viscoelastic, or elastoplastic models), accompanied with conservation laws (including mass conservation, linear momentum balance, angular momentum balance, energy conservation), govern the behavior of materials to simulate various phenomena. Numerical methods such as the Finite Difference Method (FDM), Finite Element Method (FEM), Finite Volume Method (FVM), and Material Point Method (MPM) are employed at the continuum scale, each serving as a suitable approach to solve complex problems. While the finite method provides advantages in high simulation efficiency to model polymers, it cannot be used to model heterogeneous microstructure where discontinuities make the FE approach inappropriate.

Recently, DEM is being increasingly used to model continuous materials by treating them as assemblies of bonded particles, which interact through predefined contact law. This later can be calibrated to simulate a macroscopic behavior (Effeindzourou et al. 2016; Feng et al. 2018; Meidani et al. 2016). This method is practically useful for simulating processes like deformation, fracture, failure, where traditional continuum-based methods may struggle.

It should be noted that there are other macroscale methods designed for granular materials such as Smoothed Particle Hydrodynamics (SPH), and Smoothed Dissipative Particle Dynamics (SDPD) that used particle based methods to represent the system.

These methods are often employed for viscoelastic flows (Ellero et al. 2003; Gooneie et al. 2017; Vázquez-Quesada et al. 2009).

2.2.5. Multiscale modeling of polymeric materials

Polymeric materials exhibit behaviours at one scale that requires detailed understanding of behaviours at a smaller scale. Therefore, no single method can adequately describe a multiscale system on its own.

For instance, the reptation, or snakelike motion of the polymer chain is one of the fundamental concepts of polymer dynamics in entangled polymer systems, which is responsible of the majority of the viscoelastic-plastic properties of the polymeric material (Brinson and Brinson 2008). This phenomenon consists of the movement of the polymer molecule as a snake along its axis due to the restriction of its lateral motion by the surrounding molecules (see Figure 2.9). de Gennes (1971) proposed that a polymer chain is confined to a tube-like region formed by surrounding chains, and can only move along this tube, similar to a snake slithering through grass. By this means, the single-polymer dynamics in an entangled solution is reduced to the curvilinear Brownian motion of its center of mass along the long axis of the tube (Sperling 1986). The reptation is considered a mesoscale phenomenon, at the origin of the movement of polymer chains within a network of entangled chains.

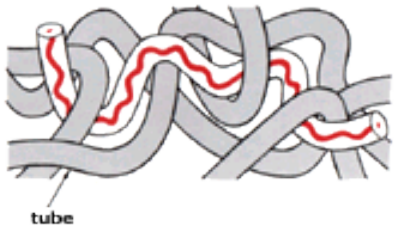


Figure 2.9 : A schematic of the reptation model. In a crowded and entangled polymer environment, a long and linear polymer chain (red) is located in a virtual tube (red), which traces the chain trajectory. Surrounding polymers are shown in gray. Extracted from (de Gennes 1971; “The Nobel Prize in Physics 1991” 1991).

Additionally, the length scales associated with a single polymer chain can range from the atomistic scale, such as the length of a single covalent bond, to the mesoscale, such as the persistence length. Each of these scales plays a crucial role in determining the material's behavior. The persistence length, also known as the Kuhn segment length, measures the chain's flexibility (Sperling 1986; Talamini et al. 2017). The polymer chain is divided into specified lengths called Kuhn segments (denoted b), that contains a number of monomers, which act as rigid units with orientations independent of each other, or deformable due to deformation of the constituent bonds, as illustrated in the Figure 2.10. For polyvinyl chloride (PVC) polymers, the Kuhn segment length is highly dependent on factors such as temperature, the incorporation of plasticizers, and molecular weight. It decreases with increasing temperature and with the addition of plasticizers, both of which enhance the flexibility of the polymer chain.

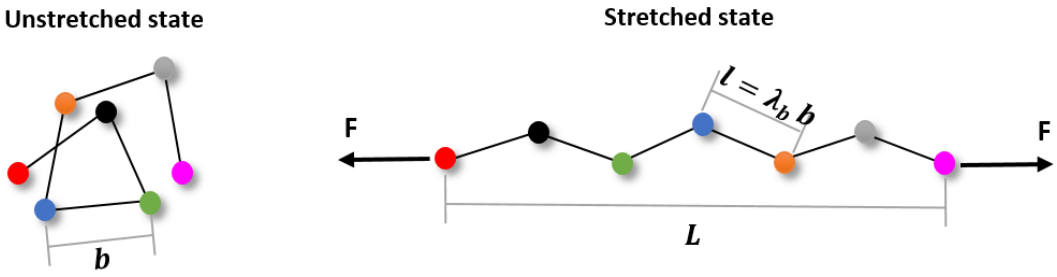


Figure 2.10 : The Kuhn segment in the unstretched state is b. Upon stretching, the polymer chain deformed under two types: alignment of the Kuhn segments, then, stretching due to the deformation of the consistent molecular bonds, with $\lambda_b$is dimensionless stretch constant referred to the bond deformation stretch. Referred to (Leelaprachakul et al. 2023; Talamini et al. 2017).

Given the complexity and interconnected nature of phenomena at different scales in polymeric materials, a multiscale approach is crucial for a comprehensive understanding and accurate modeling of their behavior.

Three main categories of multiscale approaches exist: Sequential multiscale approach, concurrent multiscale approach, and adaptive resolution schemes (Gooneie et al. 2017). The Sequential approach involve simulations that operate on different scale sequentially (Gooneie et al. 2016; de Pablo and Curtin 2011; Suter et al. 2015). In here, the information at one-length scale methods is used to inform a coarser-scale model, and vice versa. The concurrent multiscale approach consists of integrating multiple scale-models within a single simulation, where different regions of the system are modeled at different scales simultaneously (Brooks 1989; Broughton et al. 1999; Nakano et al. 2001; Rudd and Broughton 2000; Shilkrot et al. 2002; Tadmor et al. 1996). They often use a "handshaking" procedure to pass information between each other seamlessly. The third category is similar to the concurrent multiscale approach. However, this method dynamically changes the resolution of the system during the simulation, which promotes the accuracy when needed, and provides the required precision.

The study of (Zhang et al. 2015) is an example of the sequential approach, where the researchers developed a model for epoxy based-material, that bridges different length scales, from nanoscale (MD) to macroscale (FEM) (see Figure 2.11). Firstly, a series of MD simulations were performed using LAMMPS. They created 500 Representative Elementary Volumes (REVs), each containing a random distribution of epoxy resin, hardener, and smart material molecules. Then, a static spring-bead based network model was developed based on the MD simulation results. It consists of interconnected springs and beads, where the spring represents the elastic mechanical response of bonds cluster, and the bead represents the mass of bond clusters. At the macroscale, a coupled network and the FE model is constructed to represent the mechanical response in the structure.

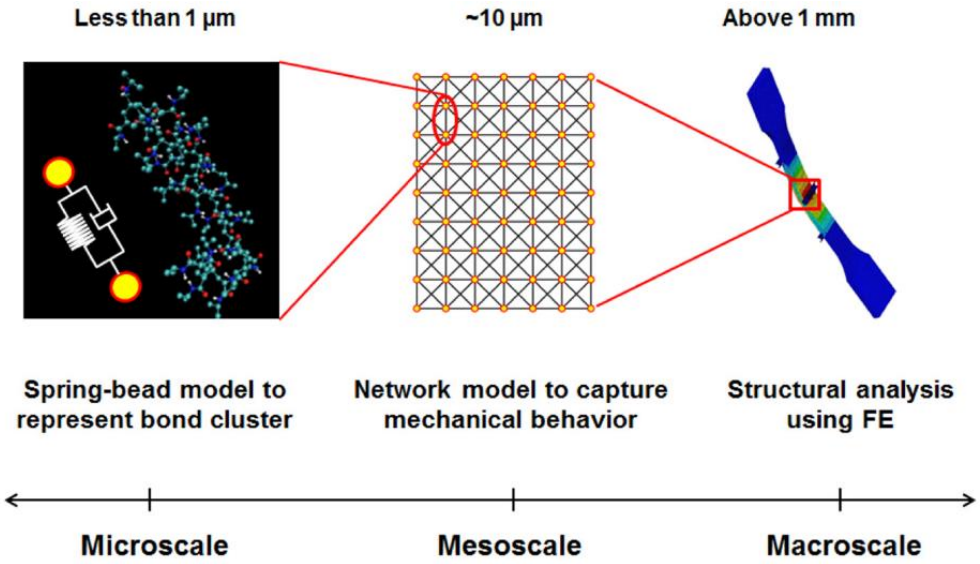


Figure 2.11 : Multiscale modeling of epoxy material. Extracted from (Zhang et al. 2015).

2.3. The specific case of geomembranes

Section 2.2 discusses the modeling approach at several scales, as well as the resolution of each length and time scale. In this section, we shift our focus to GM modeling approaches and how they have evolved over the decades.

The behavior of GMs has been traditionally investigated using phenomenological models, which provide useful macroscopic descriptions but often oversimplify the material's response. As research advances, the need of understanding the behavior under diverse environmental conditions, and complex loading scenarios is raised. This has driven researchers for numerical modeling to simulate a broader range of scenarios. To the best of our knowledge, these models have largely been limited to represent the geomembranes as continuous systems at the macroscale.

In the first subsection, the phenomenological models, that have been used to understand GM behavior over the years, will be discussed. The second subsection will concentrate on the numerical models used to investigate GMs, emphasizing their advantages in overcoming the constraints encountered in the empirical and mathematical approaches.

2.3.1. Phenomenological models for GM's behavior investigation

Modeling geomembranes over the years has been based on various techniques. Many empirical approaches have been developed to understand the behavior of geomembranes through laboratory tests (Müller 2006). Additionally, mathematical models have been developed to describe the stress-strain curves of the GM under uniaxial tensile loading using n-Order Parabola (Giroud 1994; Wesseloo et al. 2004).

Moreover, understanding the mechanical response of geomembranes has been studied through constitutive models. In 1D conditions, the simplest mechanical models for viscoelastic behavior consist of two elements: a spring to represent the elastic behavior and a damper (or dashpot) to represent the viscous behavior. Among these models,

Maxwell's model consists of a linear spring and a linear viscous damper in series (see Figure 2.12 (a)). Equation 2.3 drives the constitutive equation of the Maxwell's model. Equation 2.4 describes creep behavior, and Equation 2.5 depicts relaxation behavior, as shown in Figure 2.12 (b) and (c). While the model effectively describes relaxation behavior under constant stress conditions, it does not accurately depict creep, as it implies that strain will increase linearly with time.

$$\sigma + \frac{\eta}{E}\dot{\sigma} = \eta\dot{\varepsilon} \tag{2.3}$$

where E is the stiffness modulus of the spring, and η is the viscosity coefficient.

$$\varepsilon_{(t)} = \sigma_0 \left(\frac{1}{E} + \frac{t}{\eta}\right) \tag{2.4}$$

where σ_0 is the constant applied stress.

$$\sigma_{(t)} = \varepsilon_0 E e^{-\frac{t}{\tau}} \tag{2.5}$$

where ε_0 is the applied constant strain, τ is the relaxation time equal to the ratio $\frac{\eta}{E}$.

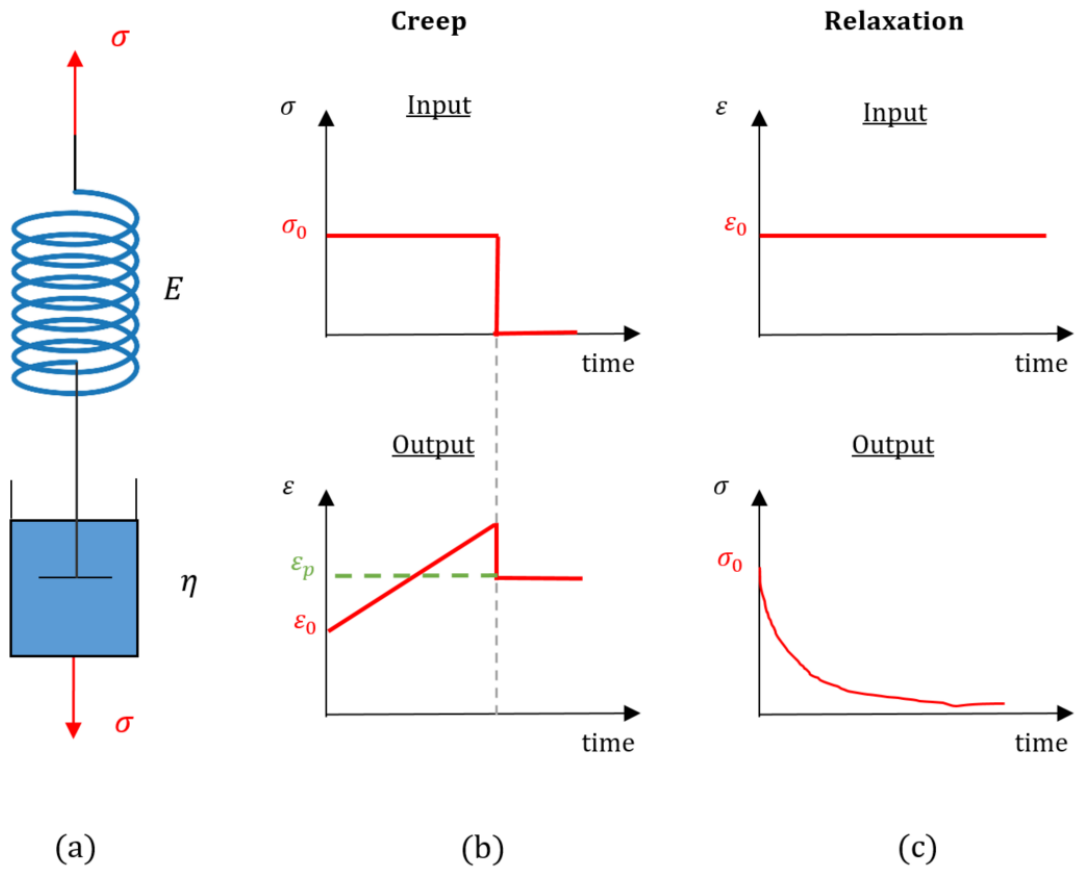


Figure 2.12 : Maxwell's model. (a) Rheological model, (b) the creep behavior, and (c) the relaxation behavior.

In contrast, Kelvin's model consists of a linear spring and a linear viscous damper arranged in parallel (refer to Figure 2.13 (a)). Equations (2.6), (2.7), and (2.8) represent, respectively, the constitutive equation, the creep response and the relaxation response. Therefore, Kelvin's model is not effective for stress relaxation but more suitable for describing creep behavior realistically.

$$\sigma = E\varepsilon + \eta\dot{\varepsilon} \tag{2.6}$$

where E is the stiffness modulus of the spring, and η is the viscosity coefficient.

$$\varepsilon_{(t)} = \frac{\sigma_0}{E}\left(1 - e^{-\frac{t}{\tau}}\right) \tag{2.7}$$

$$\sigma_{(t)} = E\varepsilon_0 = \sigma_0 \tag{2.8}$$

where ε_0 is the applied constant strain.

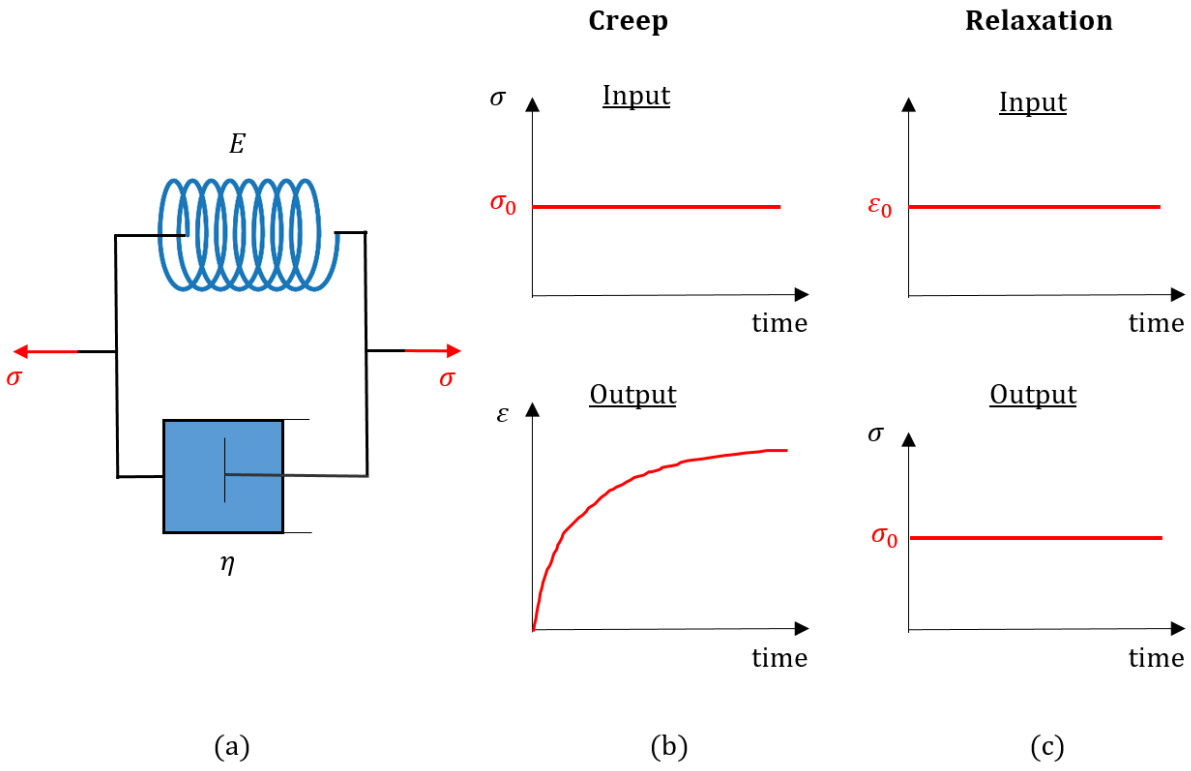


Figure 2.13 : Kelvin's model. (a) Rheological model, (b) the creep behavior, and (c) the relaxation behavior.

These aforementioned rheological models represent the backbone of various advanced models used in describing the mechanical behavior of viscoelastic and viscoplastic materials. Therefore, the combination of spring and damper elements in various configurations allows for simulating diverse viscoelastic responses. Considerable research has been dedicated to formulating a constitutive model for theoretically capturing the mechanical behavior of Polymeric material (Ghafar Chehab and Moore 2006; Kongkitkul et al. 2014; Kuhl et al. 2016; Yin et al. 2019).

2.3.2. Geomembrane modeling approach

As the understanding of GM behavior has advanced, the limitations of purely empirical and simple analytical models have become apparent. Numerous factors, such as material microstructure, environmental conditions, and complex loading scenarios, can significantly influence the mechanical performance of geomembranes. These complexities have driven researchers to adopt numerical modeling methods that can account for the diversity of influencing factors and their interactions.

Finite Element Method (FEM) and Material Point Method (MPM) have been prominently used for geosynthetics modeling. These methods rely on the constitutive models described earlier (Section 2.3.1) to define the material's response under various loading conditions. Hamad et al. (2014) have used the MPM to model a tensile membrane using two-dimensional triangular elements. The study focuses on two-geotechnical application aspect: the release of a geocontainer from a split barge, and the stability of a reinforced embankment using a geotextile. Meidani et al. (2017) have developed a

coupled finite-discrete framework to investigate the behavior of a gravel drainage layer located above HDPE GM sheet and subjected to moderate to high normal stress conditions. The GM is modelled using FEM whereas the drainage layer and the underlying foundation are modelled using discrete elements (DEM). Vasiluta et al. (2017) have developed predictive virtual models based on FEM to simulate the behavior of the geomembranes used in ecological landfills. Numerous other studies have also contributed to this field, including those by (Almeida et al. 2013; Eldesouky and Brachman 2020). Chen et al. (2021) have coupled the Finite Difference Method (FDM) for the GM with the DEM for the sand particles to examine the complex interactions at the geomembrane-sand interface at the microscale level.

DEM (presented in details in the next section) has gained popularity in granular soil-geosynthetics interaction modeling (Bhandari and Han 2010; Chareyre and Villard 2005; Chen et al. 2012; Effeindzourou et al. 2016; Feng et al. 2018; Frost et al. 2012; Hou et al. 2021; Meidani et al. 2016). (Meidani et al. 2016) propose a calibration procedure to model the HDPE GM using DEM. This involves representing the GM as an assembly of rigid, locally deformable spherical particles wherein the bonds are defined by shear and normal tensile strength (see Figure 2.14). In the study of (Feng et al. 2018), an effective method for simulating the surface features of the geomembranes is established, by using bonded particles with overlap, as shown in Figure 2.15. (Effeindzourou et al. 2016) have extended the DEM method to model deformable structures, such as geomembranes, employing the P-facet structure, as seen in Figure 2.16. These studies have shown how efficient the DEM is in capturing the intricate soil-geosynthetic interaction mechanisms, which is rather out of reach using conventional continuum-based methods.

However, the significant drawback of all the aforementioned numerical models lies in their assumption of homogeneous GMs, which prevents the replication of localized issues stemming from internal features (e.g., chain length, chain flexibility, degree of crystallinity, degree of polymerization, plasticizer quantity) that govern its macroscopic mechanical behavior. Therefore, explicitly accounting for local geometry and bridging the gap between scales through homogenization techniques becomes crucial.

Moreover, DEM is commonly employed to investigate soil-geomembrane interactions, offering valuable insights into how interface features and external loading conditions affect the overall mechanical performance and failure characteristics of geomembranes. Therefore, by taking advantage of the discretization of the DEM, this significantly enhances our understanding by tracking the mechanisms within geomembrane, capturing the microstructural details at the mesoscale level, and effectively simulating interface interactions.

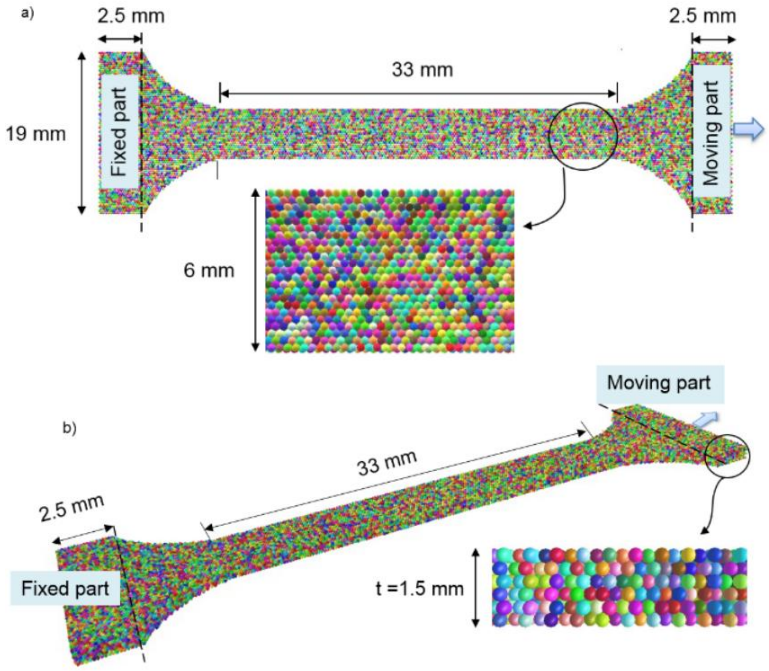


Figure 2.14 : (a) Top view of the GM specimen made of particles arranged in a dumbbell-shape. (b) A 3D view of the specimen. Extracted from (Meidani et al. 2016).

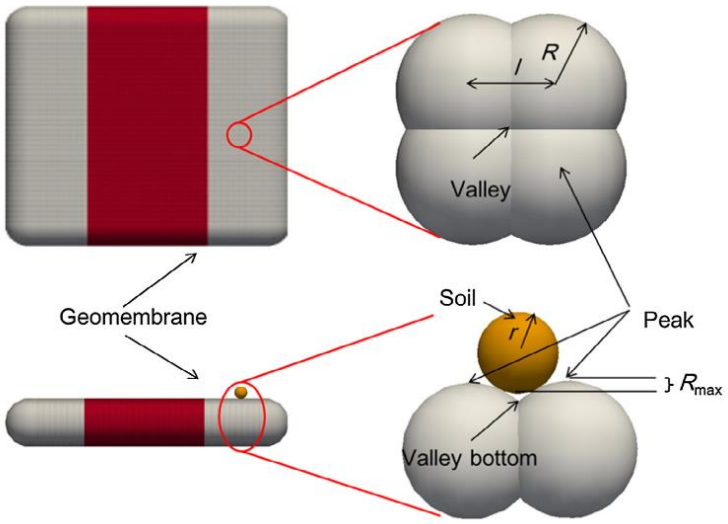


Figure 2.15 : Modeling the GM using bounded particles with overlap to reasonably simulate the surface characteristics of the geomembrane. Extracted from (Feng et al. 2018).

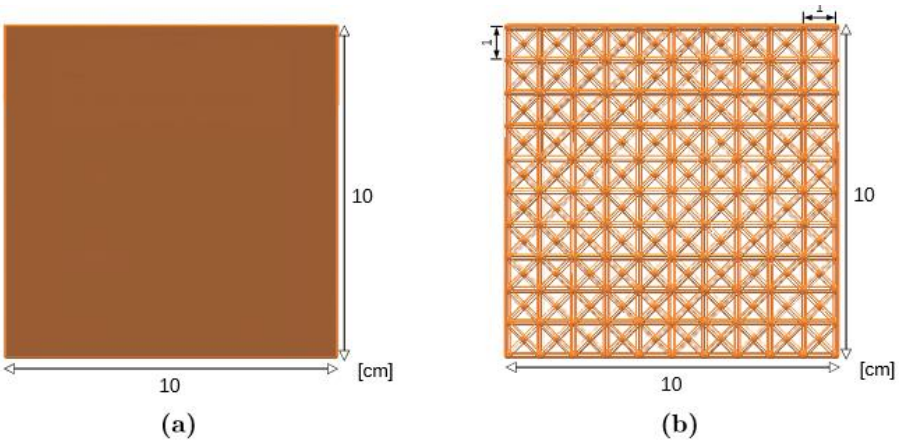


Figure 2.16 : Geomembrane modeling. (a) Membrane view. (b) Membrane modeling using cylinders and nodes indicating the mesh. Derived from (Effeindzourou et al. 2016).

2.4. Discrete Element Method (DEM)

Motivated by the necessity for microstructural characterization of the underlying mechanisms governing the mechanical behavior of PVC GMs, this study develops an original multiscale modeling technique. This approach employs the capabilities of the DEM to generate a micromechanical model of PVC GMs, that bridges the existing research gap by examining the mechanical behavior and elucidating the internal mechanisms controlling the macroscopic behavior.

Since the research question is closely built upon a specific numerical method, the DEM, this section provides a brief review of the DEM classical framework.

The Discrete Element Method (DEM) is a dynamic Lagrangian technique that tracks the positions of specific material particles over time. Initially stemming from molecular dynamics (MD), which simulates atomic and molecular behavior at the atomistic scale with consideration of interaction potentials, DEM has evolved into a specialized method for modeling granular materials. This evolution focuses on capturing discrete interactions between individual particles in contact. Originally developed by (Cundall 1971) in pioneering studies and later with (Cundall and Strack 1979), DEM was first applied to investigate challenges within rock mechanics.

Among the discrete numerical methods that have been developed, two distinct families of models can be identified based on the computation of the contact force (Dubois et al. 2018). The first family simulate perfectly rigid bodies, so the inter-penetration between bodies are not allowed. This approach is known as non-smooth contact modeling or Contact Dynamic approach, where contact forces are computed based on the mechanical problem. This approach relies on an implicit numerical scheme, and consequently a high time step can be integrated. The main drawbacks of this approach are the complexity to implement algorithms that handle abrupt changes in velocities and forces at contact, requiring careful consideration of numerical stability and accuracy in the coding process. Additionally, each time step is computationally more expensive. An example of software that adopts the non-smooth contact approach is LMGC90, developed in Montpellier,

France. On the contrary, the second family use soft bodies where the inter-penetration is allowed, and the contact forces are generally defined as functions of these overlaps. Such an approach is referred to as smooth contact approach, or Molecular Dynamic-like approach, which rely on an explicit numerical scheme. Thus, this necessitates a sufficiently small time step to satisfy the Courant-Friedrichs-Lewy (CFL) condition, ensuring stability and accuracy, and consequently, the simulation can be computationally expensive. To achieve equilibrium effectively, numerical damping techniques are often employed to mitigate high-frequency oscillations. Examples of software that implement smooth contact dynamics include LAMMPS, YADE, Particle Flow Code (PFC), BlazeDEM, Rocky DEM.

This thesis focuses on employing a smooth-contact dynamic approach, using YADE (Yet Another Dynamic Engine) as the chosen tool for supporting discrete modeling. YADE[1] is an extensible open-source software framework for DEM, developed at 3SR lab in Grenoble, France. This selection is driven primarily by its robust code base and the flexibility to implement algorithms and functions with complete control over the source code. Moreover, it is chosen for its capability to model deformable structures such as cylindrical bodies, developed by (Bourrier et al. 2013; Chareyre and Villard 2005).

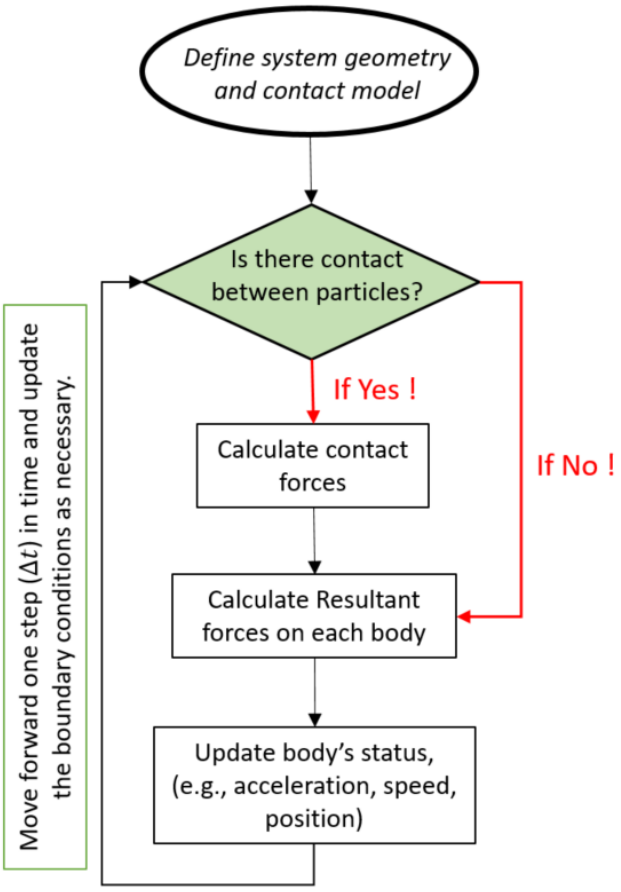


Figure 2.17 : The sequence of typical DEM simulation.

[1] The open-source code is available at : <https://yade-dem.org/>

The DEM consists of defining the material as an assembly of rigid bodies obeing to Newton's law and interacting through contact laws. By applying boundary conditions, perturbations propagate to these bodies, inducing individual particle movements.

The simulation cycle is described in the Figure 2.17.

2.5. YADE: a DEM platform

This section details a typical simulation cycle in YADE, including key steps and processes involved. Additionally, it delves into the essential tools and methodologies that will be employed throughout this research. The discussion extends to considerations of computational efficiency, highlighting strategies to optimize performance.

2.5.1. YADE simulation overview

YADE is extensively utilized by researchers worldwide, supported by a large, active, and growing community that contributes to code development and user support through the Launchpad communication platform. The software is written in C++ language and has a Python interface for direct simulation, scripting, and post-processing of results. It is primarily used on Linux-based operating systems and is available in the official repositories of popular distributions such as Ubuntu and Debian. The source code is freely accessible on GitHub under the GPL2 open-source license.

Simulations can be described as iterative processes that typically run multiple times or in time steps, involving cycles of actions defined by engines and functions. A typical simulation involves several key steps: detecting contacts between (Appendix A—Section b) particles, computing contact parameters (Appendix A—Section c), calculating contact forces (Section 2.5.2), determining bodies' accelerations using Newton's second law (Section 2.5.4), and updating their velocities and positions according to the discretization of Newton's equations (Section 2.5.4). Before each time increment that marks the final action of the simulation cycle, additional algorithms can be incorporated into the model to perform specific desired actions, such as data collection functions. Section a (Appendix A) provides detailed information about the code structure.

2.5.2. DEM contact laws implemented in YADE

Today, a wide range of contact laws have been developed and implemented in DEM computation codes (Smilauer et al. 2011). One of the most commonly used laws in DEM formulations is the one proposed by (Cundall and Strack 1979). This constitutive law models non-cohesive elastic behavior with Coulomb-type friction and is implemented in the YADE C++ class Law2_ScGeom_FrictPhys_CundallStrack. According to this law, contact between two particles is assumed to occur when they overlap. The two contacting bodies are then modeled as being connected by two virtual linear springs and a slider, as depicted in Figure 2.18.

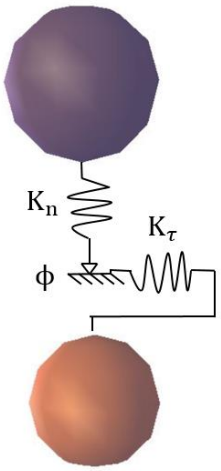


Figure 2.18 : Simplified representation of the elasto-frictional law used in DEM simulations

For this simple case, the YADE C++ class Ip2_FrictMat_FrictMat_FrictPhys creates a new FrictPhys instance that defines normal K_n, shear stiffness K_τ, and a friction angle ϕ as a function of a material stiffness rigidity misnamed "Young's modulus" in YADE and a stiffness ratio misnamed "Poisson's ratio" in YADE. Thus, in the case of two spherical particles, the contact normal stiffness is proportional to the stiffness rigidity and the harmonic average of the two particles radii R_i and R_j, as described in Equation 2.9. The shear stiffness K_τ of the contact is a specific fraction α of the computed K_n, as described in Equation 2.10.

$$K_n = E\frac{2R_iR_j}{R_i + R_j} \tag{2.9}$$

$$K_\tau = \alpha\, K_n \tag{2.10}$$

At each time step, displacement change (i.e., overlapping distance) u_n^t generates normal force F_n^t and tangential force F_τ^t. The normal force F_n^t is proportional to the overlapping distance u_n^t via the contact stiffness K_n, as outlined in Equation 2.11. However, the tangential force F_τ^t is not solely a function of the current geometrical configuration; it also depends on the loading history and the accumulated shear displacement u_τ^t at time *t*.

$$F_n^t = \begin{cases} K_n\, u_n^t\, \vec{n}^t & ,if\ contact \\ 0 & ,otherwise \end{cases} \tag{2.11}$$

where,

$$u_n^t = R_i + R_j - \left\| x_j^t - x_i^t \right\| \tag{2.12}$$

where x_i^t, x_j^t represent respectively the positions of the center of mass of particles *i* and *j*. And,

$$\vec{n}^t = \frac{x_j^t - x_i^t}{\left\| x_j^t - x_i^t \right\|} \tag{2.13}$$

While u_n^t is easily determined by calculating the overlapping distance between two particles (Equation 2.12), the incremental shear displacement u_τ^t, characterized by the displacement perpendicular to the interaction axis, is more complex. Based on the combination of two shapes (*e.g. two spherical particles*), an instance IGeom (e.g., Yade C++ class yade.wrapper.ScGeom in the case of two spherical particles) is responsible of calculating shear component using specified incremental algorithm (Luding 2008). This process involves updating u_{τ^t} to account for both global movements and mutual interactions between the spheres.

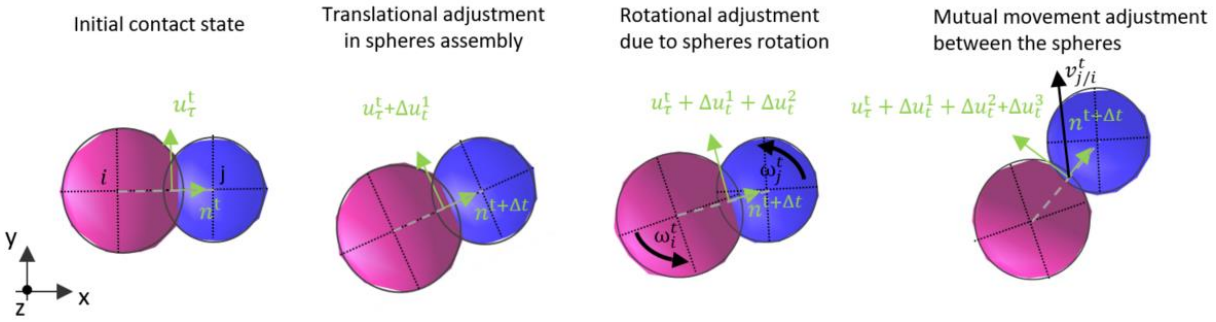


Figure 2.19 : Illustration of incremental update of the shear displacement

Initially, at time t, two spheres are in contact, with their contact point C and normal vector $\vec{n}^t$ defined (see Figure 2.19). The total shear displacement at $t + \Delta t$ is composed of three incremental terms:

- First term: As the particles move and rotate, the contact point C and normal vector n evolve spatially. Thus, the shear displacement u_τ^t at time t, initially perpendicular to $\vec{n}^t$, must be adjusted to remain perpendicular to the updated normal vector $\vec{n}^{t+\Delta t}$.

$$\Delta u_\tau^1 = (-u_\tau^t \times n^t) \times n^{t+\Delta t} \tag{2.14}$$

- Second term: This is an adjustment related to the rotational contribution due to the rotation of the spheres around their own centers ($\omega_{(i)}^t$ and $\omega_{(j)}^t$, where i and j are the particles index). This adjustment ensures that u_τ^t, initially perpendicular to $\vec{n}^t$, remains perpendicular to the updated normal vector $\vec{n}^{t+\Delta t}$. It is worth to mention that Δu_τ^1 and Δu_τ^2 do not alter the magnitude of the shear displacement u_τ^t.

$$\Delta u_\tau^2 = -u_\tau^t \times \left(\frac{1}{2}\left(\omega_i^t + \omega_j^t\right).\Delta t.n^{t+\Delta t}\right).\ n^{t+\Delta t} \tag{2.15}$$

- Third term: this term includes the shear displacement increment resulting from the relative motion (i.e., velocity) between the two particles $v_{j/i}^t$.

$$v_{j/i}^t = \left[v_j^t + \omega_j^t \times \left(x_C^t - x_j^t\right)\right] - \left[v_i^t + \omega_i^t \times (x_C^t - x_i^t)\right] \tag{2.16}$$

where x_C^t represents the position of the contact point C.

Thus, the increment in shear displacement is calculated by Equation 2.17.

$$\Delta u_\tau^3 = \Delta t\left[v_{j/i}^t - (v_{j/i}^t \,.\, n^{t+\Delta t})\, n^{t+\Delta t}\right] \tag{2.17}$$

Consequently, Equation 2.18 gives the total shear displacement at $t + \Delta t$.

$$u_\tau^{t+\Delta t} = u_\tau^t + \Delta u_\tau^1 + \Delta u_\tau^2 + \Delta u_\tau^3 \tag{2.18}$$

The tangential force F_τ^t, at time t, is then represented by Equation 2.19:

$$F_\tau^t = K_\tau\, u_\tau^t \tag{2.19}$$

This formulation holds true as long as there is no sliding at the contact. However, if sliding occurs, the tangential force F_τ^t cannot exceed the maximum static friction force. In such cases, F_τ^t is expressed as a threshold value determined by Coulomb-type friction:

$$F_\tau^t = \begin{cases} K_\tau\, u_\tau^t & ,if\ \|F_\tau^t\| < F_n^t \tan(\phi) \\ \tan(\phi)\, F_n^t\, \dfrac{u_\tau^t}{\|u_\tau^t\|} & ,otherwise \end{cases} \tag{2.20}$$

Accordingly, the total contact force F acting on each element is computed by the sum of the normal and tangential force (i.e., Equations 2.11 and 2.20). This total force, when applied at the contact point C, induces a moment T, detailed in Equations 2.21 and 2.22.

$$T_i^t = -F\,(x_C^t - x_i^t)\,.\,n^t \tag{2.21}$$

and,

$$T_j^t = F\left(x_C^t - x_j^t\right).\,n^t \tag{2.22}$$

2.5.3. Modeling of deformable structure in YADE framework

In YADE, the concept of deformable structures has been proposed in recent years to produce more realistic particles for the discretization of solid elements. This advancement aims to provide a more accurate representation of the mechanical response of materials compared to using less realistic particle shapes.

Cylinder-shape deformable particles have been developed firstly by Bourrier et al. (2013) and Chareyre and Villard (2005) and then extended by Effeindzourou et al. (2016). Each cylinder topology is created by applying the Minkowski sum of a sphere and a segment. Consequently, each cylinder is composed of two GridNodes joined by a GridConnection, as illustrated in Figure 2.20.

The interaction between these nodes is governed by the same set of equations introduced for the sphere-sphere contact model, as detailed in Section 2.5.2. Specifically, the YADE C++ class Ig2_Sphere_Sphere_ScGeom creates a new IGeom instance that manages the geometrical interactions. Accordingly, the deformation of the cylinder elements is defined by the positions and orientations of their two nodes. The positions of the nodes provide a basis for calculating the longitudinal deformation, while their orientations are crucial for determining the rotational deformation.

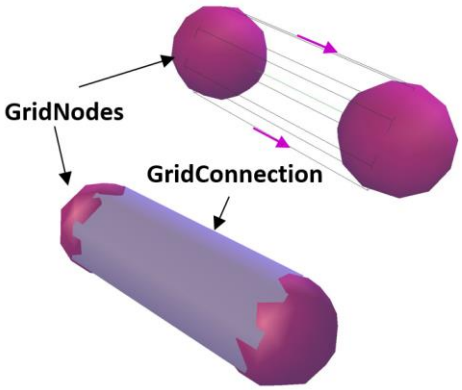


Figure 2.20: Cylinder Element created by employing the Minkowski sum.

Internal parameters of the cylinder control its mechanical behavior. Hence, a cohesive-frictional material CohFrictMat, characterized by contact friction and cohesion, is specified using the YADE C++ class yade.wrapper.CohFrictMat and applied to the GridNodes. The set of parameters includes the elastic modulus, density ρ, Coefficient equivalent to Poisson's ratio ν, normal σ_n and shear σ_s strength of the connection.

The physical interaction parameters between the two nodes is defined to exhibit a beam-like behavior, using the YADE C++ class yade.wrapper.CohFrictPhys. Therefore, this class enables the cylinder to withstand normal (i.e., tensile and compressive), shearing, bending, and twisting loading. To accurately define the contact stiffnesses for the cylinder, the same principles to those used for beam mechanics are applied. These stiffnesses are derived based on the mechanical and geometrical properties of the GridNodes, as described in Equations 2.23, 2.24, 2.25, and 2.26 or can be defined individually by the user.

$$K_n = \frac{E\ (\pi\ R^2)}{L} \tag{2.23}$$

$$K_s = \frac{12\ E\left(\frac{\pi R^4}{4}\right)}{L^3} \tag{2.24}$$

$$K_b = \frac{E\left(\frac{\pi R^4}{4}\right)}{L} \tag{2.25}$$

$$K_{tw} = \frac{G\left(\frac{\pi R^4}{2}\right)}{L} \tag{2.26}$$

where K_n , K_s, K_b, and K_{tw} are respectively the normal, shear, bending and torsional stiffness. R and L denote the radius and the length of the cylinder, respectively. E is the elastic modulus. G is the shear modulus calculated by: $E/[2(1+\nu)]$.

The constitutive contact law, implemented in the YADE C++ class Law2 ScGeom6D_CohFrictPhys_CohesionMoment (Smilauer et al. 2011), allows for the precise calculation of internal forces and moments. This law is similar to the law proposed by (Cundall and Strack 1979) (i.e., Law2_ScGeom_FrictPhys_CundallStrack) (refer to Section 2.5.2), but incorporates adhesion as well as bending and twisting moments. Internal forces are derived from the relative displacements between the GridNodes, while internal moments are similarly obtained using linear laws that account for the relative rotations of the element nodes, as described by the following Equations (2.27-30).

$$F_n = K_n\, u_n \tag{2.27}$$

$$F_\tau = K_\tau\, u_\tau \tag{2.28}$$

$$M_b = K_b\, \Omega_b \tag{2.29}$$

$$M_{tw} = K_{tw}\, \Omega_{tw} \tag{2.30}$$

where F_n and F_τ are respectively the normal and shear force. M_b and M_{tw} are the bending and twisting moments, respectively. u_n represents the relative displacement between the two GridNodes, while u_τ denotes the shear displacement. Additionally, $\Omega_b$and Ω_{tw} correspond to the relative rotations associated with bending and twisting.

Bending and twisting interactions between the GridNodes can be disregarded by setting the Boolean parameter `yade.wrapper.CohFrictMat::momentRotationLaw` or `yade.wrapper.Law2_ScGeom6D_CohFrictPhys_CohesionMoment::momentRotationLaw` to True.

The elastic limits for internal forces and moments are defined using the normal and shear strengths, denoted as $\sigma_n$and σ_s, respectively[1]. The equations governing these limits are as follows:

- The normal force is only limited in tension; it is assumed that compression at the contact is purely elastic. The normal force limit is determined by the tensile strength and is calculated as:

$$a_n = \sigma_n . R^2 \tag{2.31}$$

[1] Note that in the latest version of YADE (third edition, July 2024), users can define the maximum bending and twisting moments directly using newly incorporated parameters: `yade.wrapper.Ip2_CohFrictMat_CohFrictMat_CohFrictPhys::rollingCohesion` and `yade.wrapper.Ip2_CohFrictMat_CohFrictMat_CohFrictPhys::twistingCohesion`.

- The shear force limit includes both the contribution from the coulomb friction limit and the shear strength. This can be expressed as:

$$a_s = F_n.\tan\phi + \sigma_s.R^2 \tag{2.32}$$

  Coulomb friction contribution can be ignored if `yade.wrapper.CohFrictPhys::cohesionDisablesFriction` is set to True, where $a_s = \sigma_s.R^2$.
- The bending moment limit is given by:

$$a_b = \frac{\sigma_n R^3}{4} \tag{2.33}$$

- The torsional moment limit is described by:

$$a_{tw} = \frac{\sigma_s R^3}{2} \tag{2.34}$$

Two failure scenarios can occur when the limit normal or shear force is reached, governed by the parameter `yade.wrapper.CohFrictMat::fragile` or `yade.wrapper.CohFrictPhys::fragile`. If fragile is set to True, the cohesive links break and, the normal and shear strength are set to zero. In this scenario, internal interactions are lost, leading to a brittle failure. Conversely, if fragile is set to False, the material exhibits a ductile behavior, modeled as perfect plasticity. This means that, despite continued loading, the internal forces and moments remain constant.

Viscous behavior is incorporated in this law, specifically for the shear and twisting components. The viscosity for each component can be independently activated using the Boolean parameters:

- `yade.wrapper.Law2_ScGeom6D_CohFrictPhys_CohesionMoment::shear_creep` (True/False)

and,

- `yade.wrapper.Law2_ScGeom6D_CohFrictPhys_CohesionMoment::twist_creep` (True/False).

The viscosity coefficient for these components is defined through `yade.wrapper.Law2_ScGeom6D_CohFrictPhys_CohesionMoment::creep_viscosity`. Thus, the evolution of the elastic part of the shear displacement and twisting rotation is described by the following equations:

$$\frac{du_{s,e}}{dt} = -\frac{F_s}{v_s} \tag{2.35}$$

$$\frac{d\,\Omega_{tw,e}}{dt} = -\frac{M_{tw}}{\nu_{tw}} \tag{2.36}$$

where ν_s and ν_{tw} are the viscosity coefficients for the shear and twisting components, respectively. F_s is the shear force, and M_{tw} is the twisting moment.

External interactions between polymer chains are modeled as interactions between two spheres. A virtual sphere is introduced, with its center positioned at the projection of the contact point—this contact could be between a cylinder and other particles, such as spheres, or another cylinder, as illustrated in Figure 2.21. Contact laws can then be inherited at the contact point, with the translational and rotational velocities of the virtual sphere being interpolated linearly between the two nodes of the cylinder. Subsequently, the forces and moments are distributed to the nodes of the cylinder, as detailed by (Effeindzourou et al. 2016).

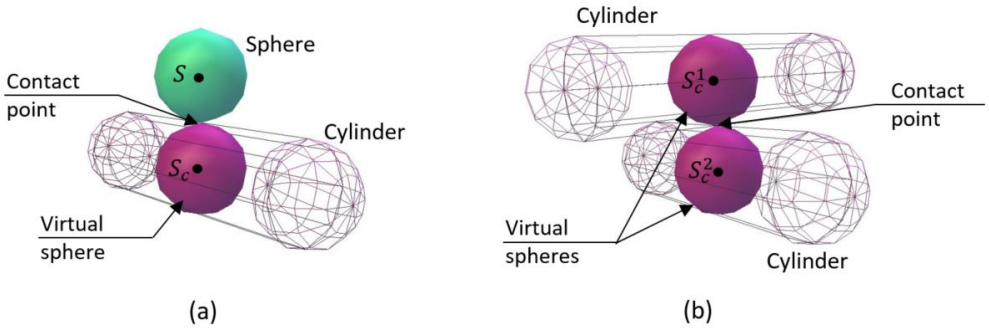


Figure 2.21: Schematic views of external interactions. (a) Sphere-cylinder interaction. (b) Cylinder-cylinder interaction.

2.5.4. Time integration and Motion calculation

Regardless of the design of the interaction laws, all external forces (e.g., including imposed forces and contact forces) are determined for each particle. By applying Newton's second law, the acceleration $\overrightarrow{a_i}^t$ of each particle can be calculated through force balance equation, based on its mass m_i and the total applied force $\overrightarrow{F_{/i}}^t$ (Equation 2.37). Additionally, the angular acceleration $\dot{\omega_i^t}$ is determined via momentum balance equation (Equation 2.38).

$$\frac{d^2x_i}{dt^2} = \overrightarrow{a_i}^t = \frac{F_{/i}^t}{m_i} \tag{2.37}$$

$$\frac{d\omega_i}{dt} = \dot{\omega_i^t} = \frac{T_i}{J_i} \tag{2.38}$$

where J_i is the moment of inertia, given by $J_i = \frac{2}{5} m\, R_i^2$ for spherical particles.

For time-domain numerical integration, YADE applies the leapfrog scheme (Fincham 1992). Leapfrog reveals the concept that derivatives calculated at midpoint intervals offer a more accurate approximation compared to those computed at the extreme points. This characteristic allows for the determination of position and orientation derivatives at full-step intervals, while velocity derivatives are calculated at mid-step intervals, in a

sequence of calculation steps (See Figure 2.22). This algorithm is implemented in the YADE C++ class yade.wrapper.NewtonIntegrator (Smilauer et al. 2011).

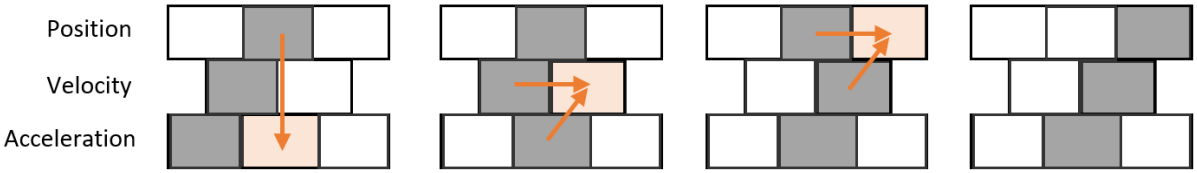


Figure 2.22 : Leapfrog integration. Velocities are known at time $t + \frac{\Delta t}{2}$, while positions and accelerations are known at time t.

Accordingly, for the time increment Δt, the discretization of the Equations 2.37 and 2.38 give the velocities and the angular rotation, as described in Equations 2.39 and 2.40.

$$\left.\frac{dx_i}{dt}\right|_{t+\frac{\Delta t}{2}} = \left.\frac{dx_i}{dt}\right|_{t-\frac{\Delta t}{2}} + \left.\frac{d^2x_i}{dt^2}\right|_t \Delta t \tag{2.39}$$

and,

$$\omega_i^{\,t+\frac{\Delta t}{2}} = \omega_i^{\,t-\frac{\Delta t}{2}} + \left.\frac{d\omega_i}{dt}\right|_t \Delta t \tag{2.40}$$

Thus, the position at time t can be determined by the dicretization of Equation 2.41.

$$x_i^{t+\Delta t} = x_i^t + \left.\frac{dx_i}{dt}\right|_{t+\frac{\Delta t}{2}} \Delta t \tag{2.41}$$

Updating the particle orientation q is analogous to updating the position, using angular acceleration and torque, and employing quaternion algebra for efficient computation (Smilauer et al. 2011).

2.5.5. Computational Challenges and Efficiency Considerations in DEM Simulations

As previously mentioned, in explicit integration schemes, an important numerical parameter is the time step Δt. As an image, consider a scenario where a particle, traveling at a high velocity, can pass through another particle within a single time step without the detection and the computation of the interactions. As the numerical information travels faster than the physical information, this usually leads to instability that compromises the accurate capture of the essential modeling features affecting the macroscopic behavior. Therefore, to avoid this situation, a time step Δt should be selected to be smaller than a critical value Δt_c, which depends on the wave propagation velocity in the medium.

Considering the spring contact model described above (i.e. mass-spring system), the characteristic oscillation period T is equal to $2\pi\sqrt{m/k}$ with m the particle m and k the spring stiffness. For an assembly of mass-spring systems, the critical time step is defined as the minimum oscillation period over the whole assembly:

$$\Delta t_c = \min(2\pi \sqrt{\frac{m_i}{k_i}}) \tag{2.42}$$

In systems with six degrees of freedom (i.e., in translation and rotation), the generalized mass and stiffness matrices M and K replace the fractions m_i/k_i with the eigenvalues of $.K^{-1}$. To improve computational efficiency, the engine, implemented in YADE C++class yade.wrapper.GlobalStiffnessTimeStepper, simplifies this process by focusing only on the translational components of the stiffness matrix, which are typically the limiting factors, and thus estimates eigenvalues solely from the diagonal terms. The time step Δt_c is dependent on the contact stiffness, which can lead to Δt_c tending to infinite in the absence of contact. To avoid numerical inaccuracies under these conditions, the GlobalStiffnessTimeStepper engine preemptively estimates stiffness based on anticipated future interactions.

Since most of the contact laws do not include any velocity-based damping, an artificial (i.e., numerical damping) may be required to achieve an equilibrium or a steady state solution. The basic idea is to decrease forces, which increase the particle velocities and vice versa by comparing the acceleration direction with respect to the velocity direction. Therefore, the force decrement is defined in the Equation 2.43. This damping is clearly non-physical, since it is not invariant to rotation in a coordinate system.

$$\frac{\Delta F_d^i}{F^i} = -\lambda_d \, sign\left[F^i . \left(\left.\frac{dx_i}{dt}\right|_{t-\frac{\Delta t}{2}} + \left.\frac{d^2 x_i}{dt^2}\right|_t \frac{\Delta t}{2}\right)\right] \tag{2.43}$$

where,

ΔF_d^i = the force decrement component;

F^i = the total force acting on the particle i;

λ_d = dimensionless non-physical damping coefficient.

Numerous computational optimizations have been implemented in YADE, notably the application of numerical damping to expedite the attainment of equilibrium states, and the efficient detection of neighbors and contacts. The computational cost of this later is highly dependent on the number of particles involved in the simulation. To address this challenge, the sweep and prune algorithm is used. This algorithm significantly reduces the complexity of collision detection by sorting and sweeping the bounding volumes of objects. In fact, collision detection typically exhibits a time complexity of $\mathcal{O}(n2)$, where n is the number of objects. However, the sweep and prune algorithm improves this complexity to approximately $\mathcal{O}(n \log n)$.

Additionally, many DEM codes use parallel processing to boost computational speed. However, if there are too many tasks to handle, the efficiency of parallelization can decrease because of the extra communication needed between CPU cores. Additionally,

the collision detection algorithms are run on a single core regardless of the number of cores used for the simulation. This can result in higher computational costs. Therefore, it is important to optimize both the number of CPU cores and the allocated processing CPU time before starting simulation.

Chapter 3: Construction of a numerical model at mesoscale for investigating the mechanical response of PVC geomembranes

Polymers are characterized at the molecular level by their chemical composition and morphological structure, which together determine key properties such as flexibility, strength, and strain. The molecular configurations result in mesoscale phenomena such as polymer crystallization, chain entanglements, and reptation, all of which have a significant impact on the material's macroscopic mechanical response. PVC GMs, the focus of this study, are made of polymeric materials and have a mechanical behavior that is impacted by chain rearrangements and reorientations.

In this chapter, following the definition recalled in Section 2.2.5, we propose a sequential multiscale approach for bridging the gap between observable macroscale behavior and mesoscale phenomena. Mesoscale simulations are fed by macroscale information stemming from macroscale experimental tests (*e.g. Boundary conditions, mechanical parameters*). To enhance simulation efficiency and reduce the complexity of the problem, additional material properties such as thermal and chemical characteristics are neglected.

The discrete nature of the microstructure of PVC geomembranes, composed of a semi-crystalline assembly of polymer chains embedded within a matrix of plasticizers, makes the Discrete Element Method (DEM) a well-suited approach for this type of structured material. Additionally, studies by Bourrier et al. (2013) and Chareyre and Villard (2005) have demonstrated the capability of the DEM to model deformable elements, such as flexible inclusions and structures. They have developed new specific discrete elements representing flexible cylinders that can potentially be connected to create a complete inclusion architecture. This cylinder-based approach enables the simulation of the individual polymer chains and their interactions, as well as the inclusion of plasticizers and other additives within the geomembrane matrix.

This chapter is structured as follows: Section 3.1 details the creation and modeling of the PVC microstructure using cylindrical elements (i.e., GridNodes, and GridConnections). The integration of the plasticizer between the chains—which employs spherical particles as placeholders—is described in Section 3.2. Section 3.3 discusses the sensitivity of microstructure morphology to geometrical parameters. Section 3.4 presents the model's mechanical parameters. Section 3.5 summarizes the model's assumptions. Finally, the sample preparation and boundary condition definition are discussed in Section 3.6.

3.1. Discretization of PVC microstructure in the DEM framework

As previously mentioned in the State of the Art (Section 2.1), PVC GM is primarily made up of PVC resin, plasticizers, and other additives. In this work, we only consider GM materials composed of PVC resin and plasticizer as other additives have little impact on mechanical behavior (Lodi et al. 2008). The morphological microstructure of this type of GMs is described in Sections 2.1.1, 2.1.2, and 2.1.3.

This section presents the modeling of the morphological microstructure of PVC material, starting from individual polymer chain to the whole microstructure using cylinders. Detailed information about the formulation of the cylinders is provided in the Appendix A.

In the following subsections, we will discuss the step-by-step process of constructing the model.

3.1.1. Polymer fiber modeling

The PVC polymer comprises numerous C-C principal bonds, along with branched bonds such as C-H and C-Cl. In this context, a polymer chain can be represented as a set of connected cylinders that can only deform longitudinally. Each cylinder does not correspond to a single C-C bond but rather represents a segment of the polymer chain, with its axis aligned with the C-C bonds to model the overall structural alignment of the polymer. This representation is analogous to the Kuhn segment in polymer science, which simplifies the polymer chain into a series of flexible segments that capture its essential mechanical and structural properties (Sperling 1986; Talamini et al. 2017). The radius of the cylinder is then determined as the average between the bond lengths of C-H and C-Cl. Here, a bond length is defined as the distance between the centers of two atoms bonded covalently, where electrons are shared between the atoms. This bond length is influenced by the electronegativity of each atom, which represents its ability to attract a shared electron. The following empirical equation was proposed by (Schomaker and Stevenson 1941) to calculate bond length:

$$d_{(A-B)} = r_A + r_B - 0.09|x_A - x_B| \tag{3.1}$$

where $d_{(A-B)}$ is bond distance between two atoms A and B; r_A and r_B are the covalent radii of A and B; and $(x_A - x_B)$ is the electronegativity difference between A and B. Accordingly, the C-Cl and C-H bond are respectively 173.94 pm and 105.96 pm long. Consequently, the radius of the polymer chains is estimated equal to 140 pm.

In the DEM framework of YADE, each cylinder consists of two GridNodes (i.e., spheres) linked together by a connection known as the GridConnection, as shown in Figure 3.1. This connection corresponds to an internal cohesive contact law implemented (Law2 ScGeom6D_CohFrictPhys_CohesionMoment as presented in Section 2.5.3) (Smilauer et al. 2011). This class governs the deformation of the cylinder through the internal cohesive contact law. Consequently, the mechanical behavior of the polymer chains is dictated by

internal parameters including the elastic stiffness E, the density ρ, normal C_n and shear C_s strengths, as detailed in the Appendix A.

In order to obtain fiber-like behavior, the cylinders are allowed to support only tensile forces. Consequently, bending and twisting moments between GridNodes are disregarded.

From the elastic stiffness E, the normal rigidity between two successive GridNodes is computed according to Equation 2.23 (Section 2.5.3).

Internal forces are computed based on the relative displacements of the two GridNodes (see Figure 3.1). The cylinder is considered to have an elastic brittle behavior with a maximal force given by $a_{n_polymerChain}$.

This maximum normal force $a_{n_polymerChain}$ is computed based on the normal strength specified in the material, according to Equation 3.2:

$$a_{n_{polymerChain}} = C_n . R_c^2 \tag{3.2}$$

where C_n is the normal strength, and R_c is the cylinder's radius.

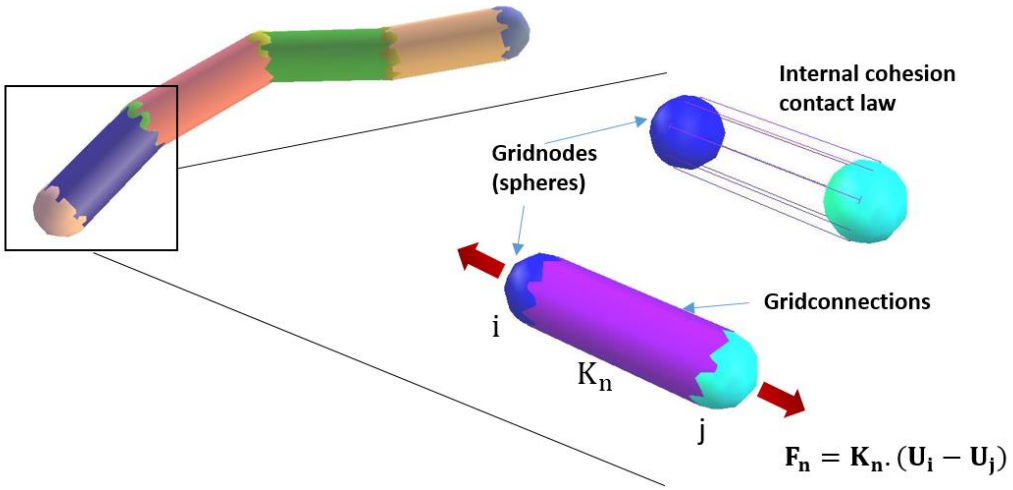


Figure 3.1 : Polymer chains modeling using connected cylinders, where each cylinder element is made up of two GridNodes joined by a GridConnection. The deformation of the cylinder is governed by the relative displacement between the two nodes.

For numerical reasons, the internal shear force cannot be deactivated. Therefore, the maximum shear force limit is set sufficiently high to ensure that failure only occurs due to tensile forces.

3.1.2. Crystallites modelling and distribution

A crystallite is represented as a parallelepiped with the same dimensions as mentioned by (Summers 1981). In DEM, it is modeled as a parallelepiped, using GridNodes connected by GridConnections, as shown in Figure 3.2. Eight vertical components are created laterally, consistently with Summers (1981), with three nodes corresponding to each chain in the chain's direction.

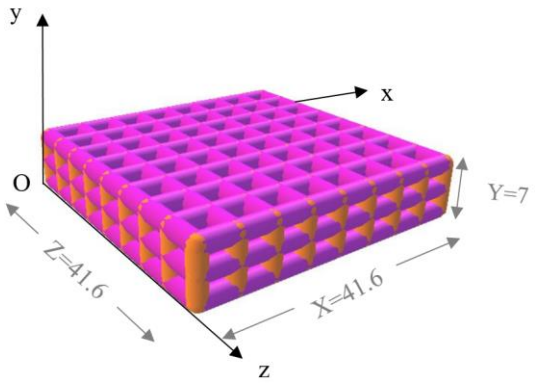


Figure 3.2 : A typical crystallite model.

Between the GridNodes of the crystallites, two types of connections have been modeled: strong links, representing the covalent bonds within the polymer chains, and weak links, corresponding to the intermolecular interaction (e.g., Van Der Waals and dipole-dipole) responsible for the well-aligned polymer chains. As illustrated in Figure 3.2, two materials are used for the GridConnections to represent the cylinder forming the polymer chains (orange cylinders) and weak interactions (pink cylinders).

The bond energy of the weak interactions is considered approximately 10 times smaller than that of the covalent bonds (Niklausa et al. 2006). This energy corresponds to the external work required to break the bond. Therefore, assuming that both bonds experience the same displacement, the ratio of the forces supported by the cylinders (e.g., Cylinders representing Van Der Waals and covalent bonds) is equivalent to the ratio of their bond energies. The maximum normal and shear forces supported by the cylinders representing the weak interactions are determined in Equation 3.3:

$$a_{n_{weak}} = a_{s_{weak}} = 10^{-1}\, a_{n_{polymerChain}} \tag{3.3}$$

where $a_{n_{weak}}$ and $a_{s_{weak}}$ are subsequently the normal and shear adhesion of the cylinders forming the weak interactions.

The crystallites act as physical crosslinks or rigid domains within the overall PVC structure, forming a three-dimensional network spaced of about 0.01 microns (10 nm) for non-plasticized PVC. The addition of the plasticizer induces the swelling of the amorphous phase without destruction of crystallites. This swelling is limited by the length of the polymer chains connecting the crystallites. Therefore, the inter-crystallites distance D increases with the quantity of plasticizer added during manufacturing up to a limiting value.

Numerically, the crystallites are distributed in such a way that the distance between them is controlled via a constant, D. To generate the cloud of crystallites in DEM, each crystallite is first represented by a sphere of diameter D. A random pack of spheres is created and compressed isotropically under periodic boundary conditions using the YADE's engine PeriTriaxContoller (Smilauer et al. 2011), as seen in Figure 3.3. In this

auxiliary simulation, a frictionless contact law is used. Eventually, a randomly oriented crystallite is inserted into each sphere of control, as shown in Figure 3.3.

3.1.3. Amorphous region modeling

In the amorphous region between crystallites, the polymer chains are generated using a random walk algorithm:

- Select randomly a node along a crystallite boundary,
- Create new cylinders until reaching a different node along another crystallite boundary (refer to Figure 3.4), or until reaching sample boundaries.

Each segment of the chain is set to a length of 3.4 Å. This specific length is chosen for technical reasons, allowing for a cross-check with crystallites that have a thickness of 7 Å, which is the double of the length of each chain segment.

The random walk is governed by a random deviation angle, θ, between the directions of consecutive cylinders. The deviation angle is limited by a predefined maximum deviation angle, θ_{max}.

The systematic check for intersections between the polymer chain segments and crystallites is computationally costly, with a complexity of $\mathcal{O}(B.N)$ for B chain's segments and N crystallites. One method used to enhance computation efficiency is to divide the whole sample domain into C cells, where only one crystallite (represented by its barycenter) may stand. This method makes it possible to quickly search for neighbors when a cylinder is being created, avoiding cross-checking with every crystallite in the system, as illustrated in Figure 3.5. Consequently, the intersection check complexity is reduced from $\mathcal{O}(B.N)$ to $\mathcal{O}(B.k)$, where k represents the number of neighboring cells that a cylinder can possibly intersect (in the 3D case, k equals 27).

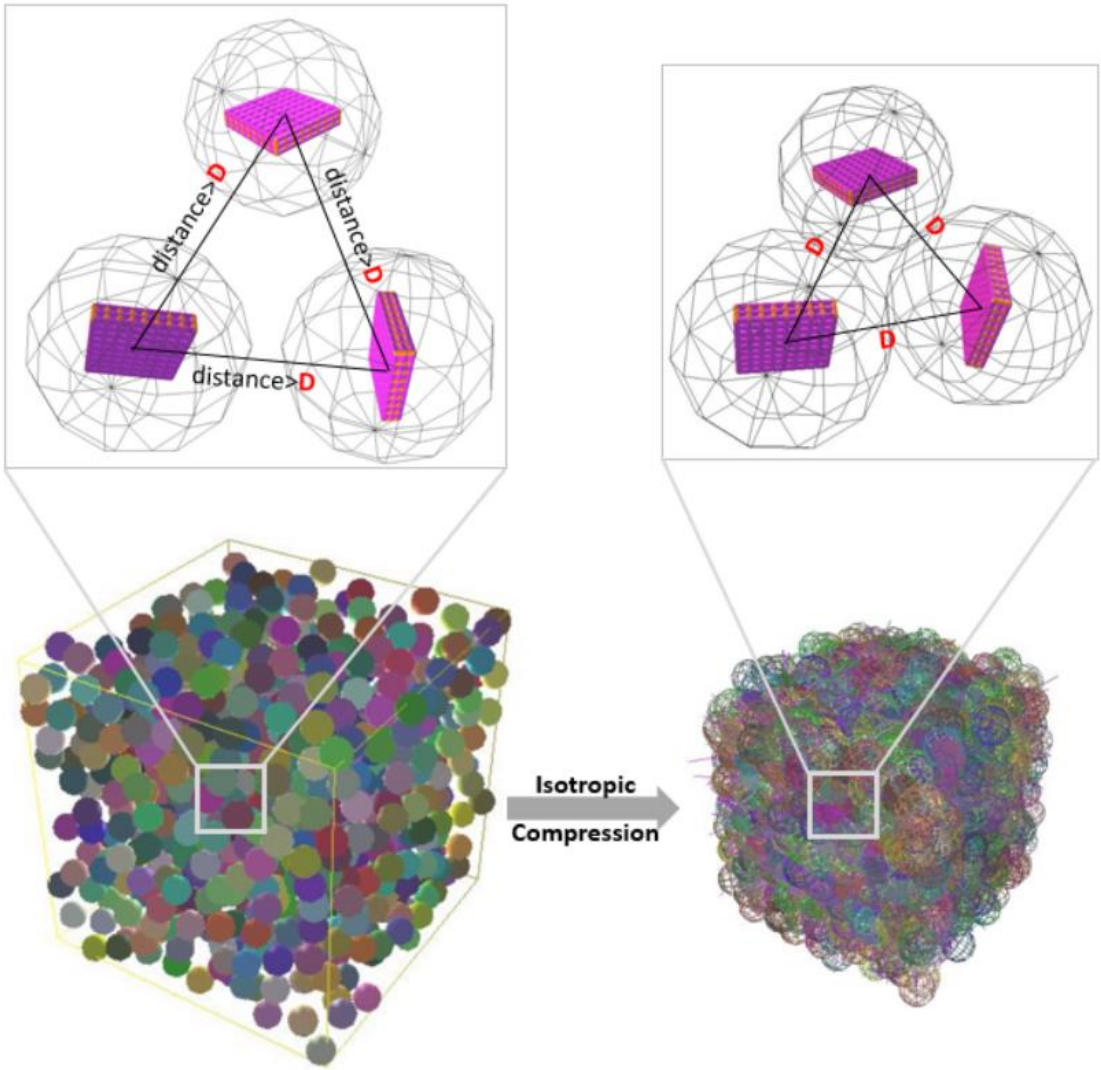


Figure 3.3 : Numerical procedure to control intercrystallite distance thanks to periodic isotropic compression. In such auxiliary simulations, each crystallite is represented by a virtual sphere with radius D.

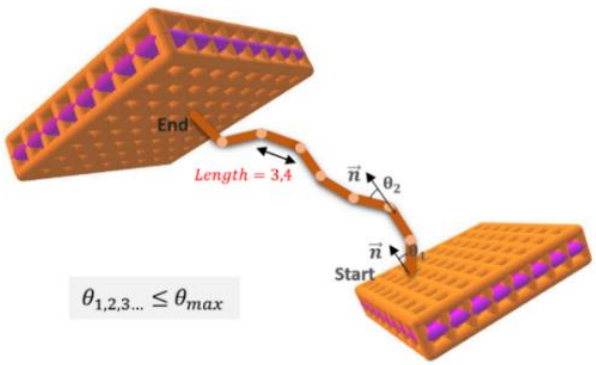


Figure 3.4 : Random walk algorithm to initialize the polymer chains between crystallites.

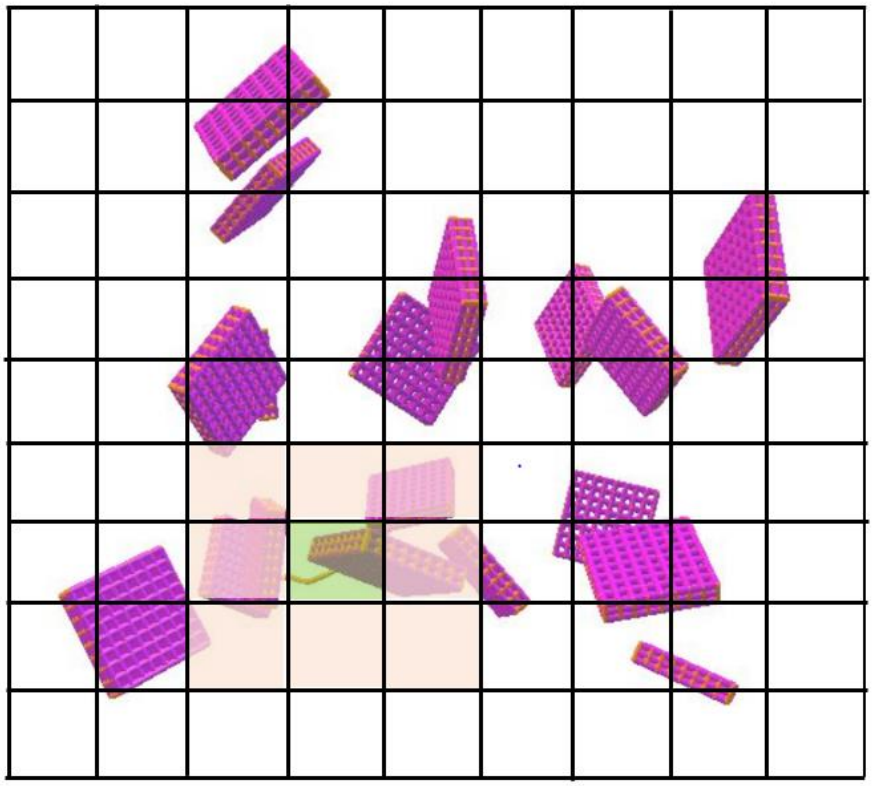


Figure 3.5 : Intersection cross-check of chains in amorphous regions via spatial partitioning of crystallites in cells. Potential crystallite neighbours for the chains' nodes are only searched for in its own cell and in the neighboring cells (light orange and green zones).

The random walk process may cause cylinders to overlap (Figure 3.6). To mitigate this issue, an additional step is employed to separate the overlapped cylinders, ensuring accurate chain interactions while eliminating artifacts caused by overlapping. This method involves activating a repulsive force by increasing the material's stiffness coefficient. This later could increase the repulsive force, and consequently, facilitate the separation of the overlapped cylinders. This procedure iterates until zero overlapping is achieved. The velocity of bodies is frequently reset to zero, in order to maintain GridNodes cohesion and prevent the separation of cylinders. Additionally, for the same reason, the maximum resistance supported by the cylinders is temporarily increased to prevent the cylinders to fail due to these repulsive forces.

Figure 3.7 shows an example of the final configuration obtained to account the PVC microstructure recalled in Section 2.1.1.

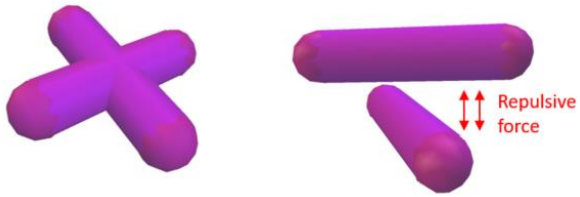


Figure 3.6 : Separation of overlapped cylinders by repulsive forces.

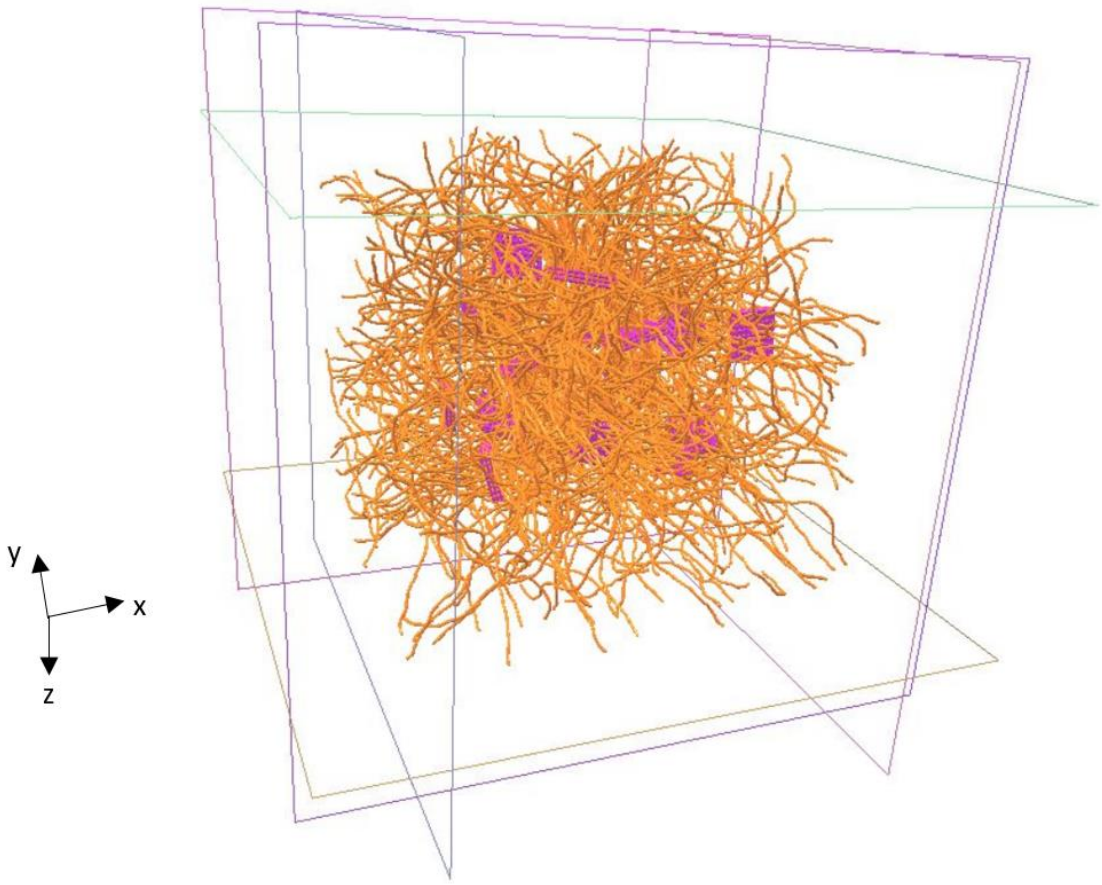


Figure 3.7 : Final 3D configuration of the microstructure of PVC with a characteristic size of 40 nm and $\theta_{max} = 0.1\ \pi$.

3.2. Integration of the plasticizer into the model

As mentioned in Section 3.1.2, the inter-crystallites distance D depends on the quantity of plasticizer added during manufacturing. Technically, the plasticizer is introduced in the model by using spherical particles to fill the pore space between the polymer chains in the amorphous zone. This process is executed through several steps, as depicted in Figure 3.8.

A random distribution of spheres is first generated in an empty box. Then, the spheres that do not overlap with the polymer chains and the crystallite are embedded within the PVC microstructure. For the plasticizer, the particle size distribution by numbers, determined by the spheres' diameters, follows a linear pattern in semi-log space, as shown in Figure 3.9, with D_{60}/D_{10} equals to 3. This value is a trade-off between achieving well-graded packing with minimal porosity and keeping a relatively small number of particles. Eventually, the added spheres are slightly expanded to come into contact with the polymers. This step is added as spheres overlapping with the polymer chains are dismissed.

It should be noted that using a growing factor might cause internal compaction. This expansion is stopped when the stress transmitted to the sample boundaries reaches a specified value determined using a dimensionless parameter known as the stiffness level, κ, which compares material stiffness to the level of loading (Radjai and Dubois 2011).This

parameter is related to the degree of overlap between the interacting rigid bodies within the simulation.

$$\kappa = \frac{K_N}{P\ D} \tag{3.4}$$

Where K_N represents the normal contact stiffness, P the confining pressure, and D the particle diameter.

The normal contact stiffness, K_N, can be estimated between two spheres of the same size and material as expressed in Equation 3.5:

$$K_N = \frac{ED}{2} \tag{3.5}$$

where E is the material's stiffness. Consequently, the confining pressure P can be expressed as:

$$P = \frac{E}{\kappa} \tag{3.6}$$

The value of stiffness level, κ, is chosen to uphold the principle of simulating rigid bodies with smooth contact in DEM, while avoiding significant overlap between the bodies. Serving as a crucial parameter, κ approximates the ratio of the cylinder diameter to the extent of overlap and is set at 3000. In that way, the simulation aims to maintain realistic behavior where bodies interact without too large penetration.

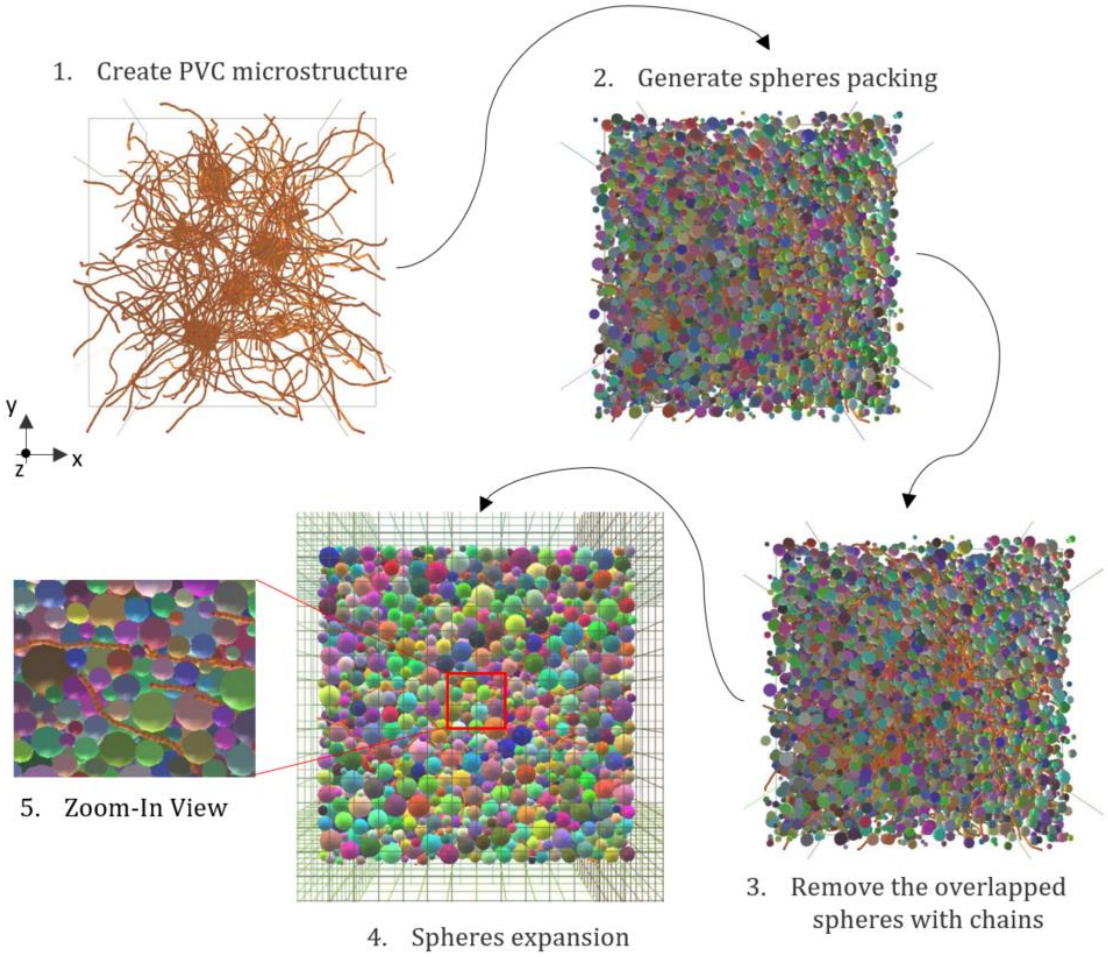


Figure 3.8 : Process of integrating plasticizers using spherical particles. (1) Creation of a randomly distributed sphere pack. (2) Removal of the overlapped spheres with chains' cylinders. (3): Spheres expansion to fill voids between the chains. (4) Zoom-in view of polymer chains embedded between the plasticizer's particles.

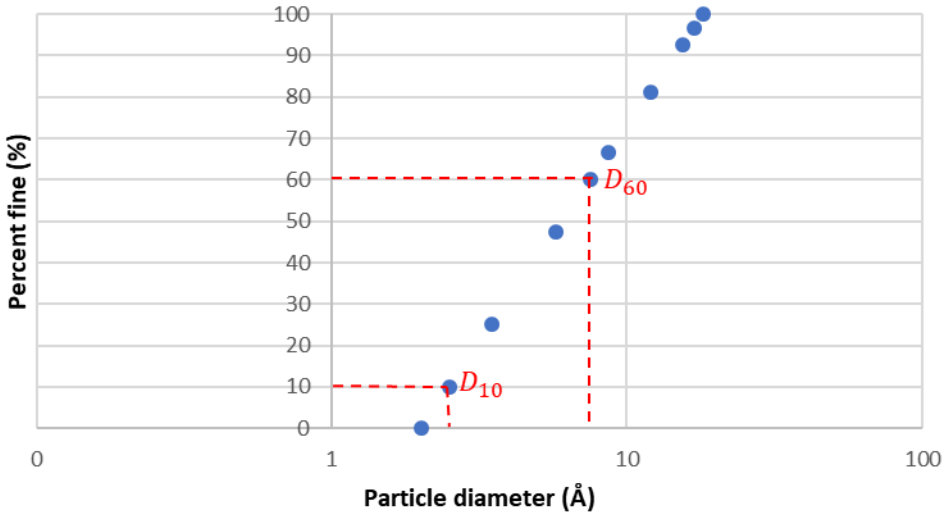


Figure 3.9 : Particle size distribution of spheres according to diameter, with D_{60}/D_{10} equal to 3.

Despite that, internal compaction in the system causes particle overlap, which generates repulsive forces during the mechanical parameter calibration process. As a result, to end the sample preparation in a zero stress state, it is necessary to shift the boundary walls until there is no stress applied on them. However, due to numerical limitations (e.g. high computation time), achieving precisely zero penetration depth and zero stress on the wall have not been possible. Thus, an additional step, consisting of adjusting the chains' position to further reduce the overlap depth, have been employed.

3.3. Sensitivity of microstructure morphology to geometrical parameters

The microstructure in the amorphous zone is created by a random walk method. This procedure is governed a deviation angle, whose definition is illustrated in Figure 3.4. The microstructure configuration is determined by the largest value of this angle, θ_{max}. Thus, increasing θ_{max} can result in longer polymer chains and more entanglement (i.e., crosslinks), providing a denser and more intricate network within the microstructure. This is illustrated in Figure 3.10 where the density and entanglements of the amorphous phase rise when θ_{max} equals 0.15π rad, whereas for a small number (0.05π rad), the fibers are straighter, which decreases the density.

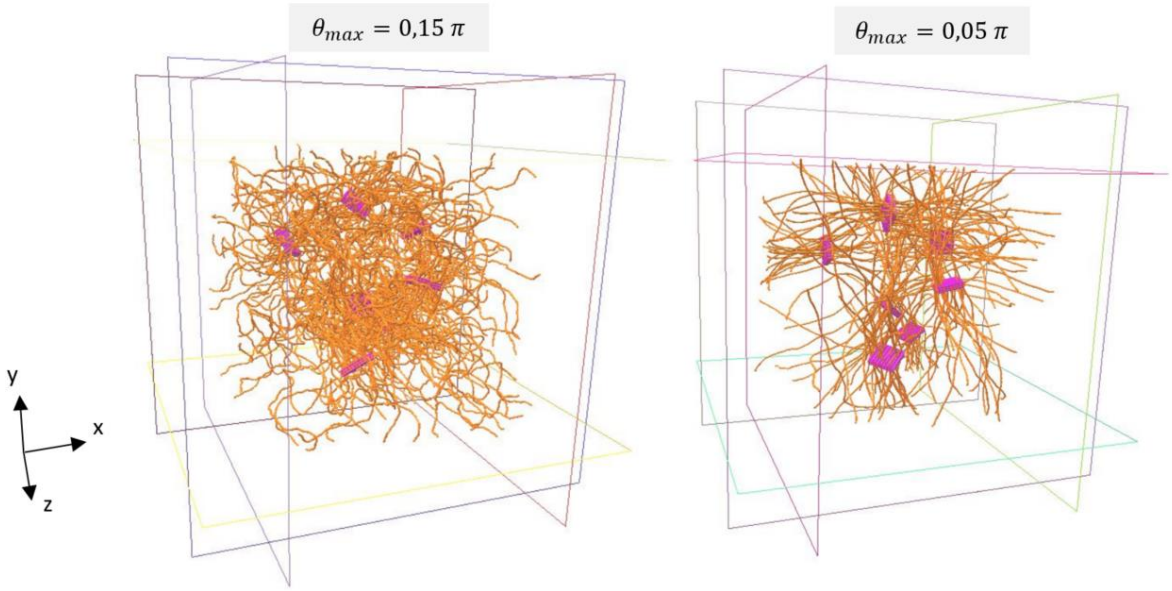


Figure 3.10 : Comparative analysis of 3D configurations: impact of θ_{max}.

Another crucial parameter in selecting the density of the amorphous phase is the number of chains. As mentioned in the random walk algorithm procedure, the chains are initiated from a random node of the crystallite boundaries. This approach allows the model to control the number of chains generated and extended from a crystallite. By systematically increasing the number of chains, the density of the amorphous phase correspondingly increases, as the additional chains occupy more space and reduce the free volume within the amorphous region (see Figure 3.11).

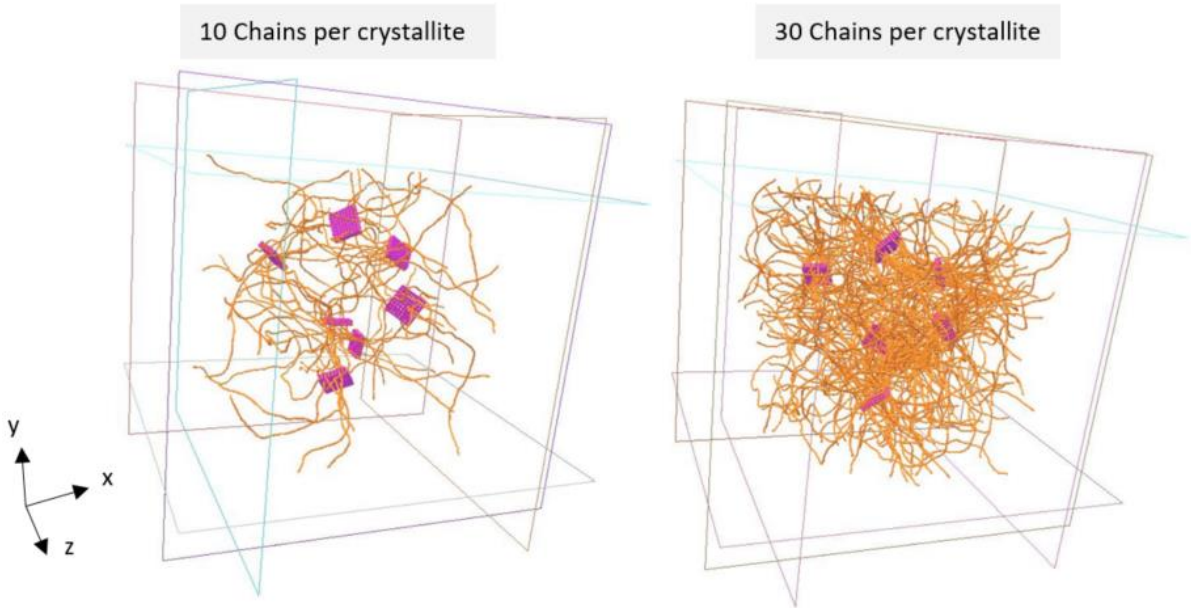


Figure 3.11 : Comparative analysis of 3D configurations: impact of different chain number per crystallite.

This model provides a method for effectively managing the impact of plasticizer amount variations by adjusting the inter-crystallite spacing parameter D. Furthermore, it enables for the simulation of non-plasticized PVC by setting the inter-crystallite distance to D = 10 nm. This modification causes a denser packing of crystallites inside the same volume, increasing the overall crystallinity of the microstructure. Consider a comparison of two microstructures from the same volume, for D = 10 nm, the microstructure has 18 crystallites, whereas raising D to 15 nm results in fewer crystallites and a larger proportion of material in the amorphous zone (see Figure 3.12).

It is important to note that the choice of the sample volume is crucial to account for all the microscopic characteristics that influence the macroscopic behavior and macro properties of the material. However, sample size accessible to DEM simulations are typically about nanometers, making them probably too small to fully capture the material's macroscopic properties and reach a representative elementary volume (REV) size. Therefore, the proposed strategy is to consider multiple elementary volumes (EV) to recover REV conditions through averaging.

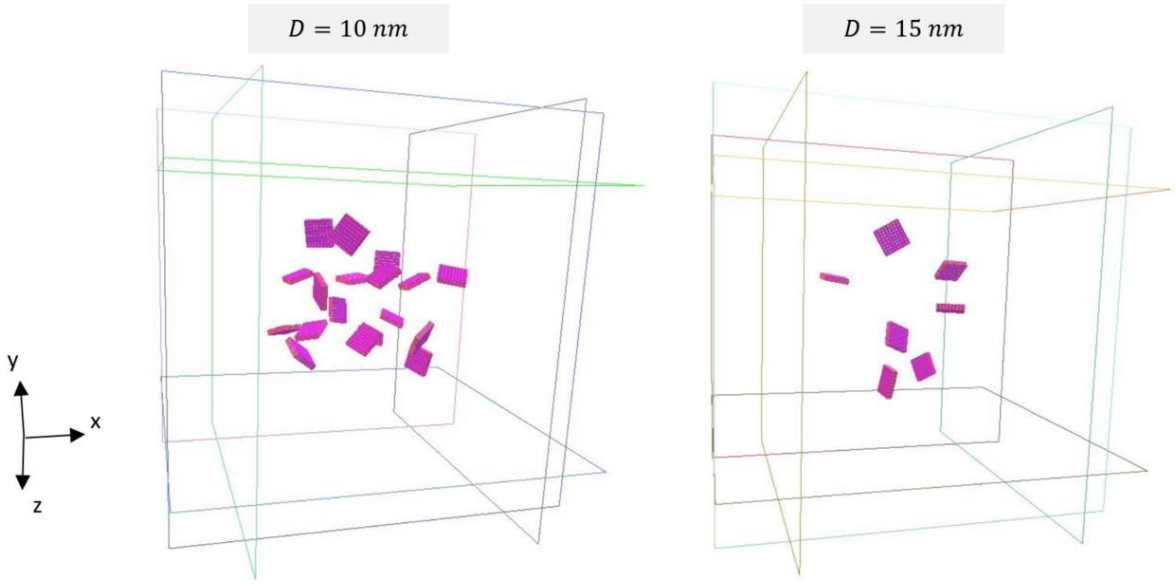


Figure 3.12 : Comparative analysis of 3D configurations: impact of inter-crystallites distance D (For the same elementary volume, 18 Crystallites at D=10 nm vs. 7 Crystallites at D=15 nm).

3.4. Simplification of model's mechanical parameters

The intrinsic properties of the chains, including stiffness, E, density, ρ, and tensile strength, C_n, influence significantly the overall mechanical behavior of the material. The maximum force, F_{max}, a chain segment can withstand before rupture is given by Equation 3.7:

$$F_{max} = C_n \times R_c^2 = K_n \times \varepsilon_{max} \times L_c \tag{3.7}$$

where K_n is the normal stiffness of the segment (Equation 2.23) and ε_{max} is the maximum deformation before rupture (refer to Appendix). Using Equations 3.7 and 2.23 yields:

$$E = \frac{C_n}{\pi \times \varepsilon_{max}} \tag{3.8}$$

The chain's segment length (3.4 Å) is equivalent to approximately three C-C bonds (1.54 Å each). Assuming a maximum deformation ε_{max} of 10%, which corresponds to the deformation of three C-C bonds, the Young's modulus is calculated as:

$$E \approx 3.18\ C_n \tag{3.9}$$

A linear elasto-frictional (and non-cohesive) contact law governs the interactions between particles system (Law2_ScGeom_ FrictPhys_CundallStrack (refer to Chapter 2, Section 2.5.3). According to this law, contact between two particles is assumed to occur when they overlap.

At the molecular scale, the concept of friction lacks physical meaning, thus, friction angle is set to zero in this model. This means that while the system accounts for normal contact forces, tangential forces cannot develop.

For the sake of simplicity, the elastic rigidity and density of plasticizer particles are set to be of the same order of magnitude as those for the polymer chains.

All the remaining geometrical and mechanical parameters influencing the model's responses are summarized in Table 3.1.

Table 3.1: Model's parameters influencing global behavior.

Type	Parameter	Unit	Function
Geometrical	Elementary Volume (EV)	$[m^3]$	Affects the number of independent simulations needed to recover the REV condition
	Number of chains	--	Affects the density in the amorphous phase
	Max orientation angle θ_{max}	$[0.05\pi, 0.15\pi]$ [rad]	Affects the density, the length of the chain, as well as the percentage of entanglements in the amorphous zone
	Inter-crystallites distance D	$\geq 10 \times 10^{-9}$ [m]	Represents the effect of the plasticizer that increase the volume between the crystallites
Mechanical	Material strength C_n	$[N/m^2]$	Sets the max tensile strength of the cylindrical segment chains
	Material modulus E	$[N/m^2]$	Controls the elasticity of the cylinders
	Material density ρ	$[Kg/m^3]$	Controls micro-inertial effects

3.5. Modeling assumptions

For the sake of computation cost, our original approach includes several assumption and simplifications that are listed in this section.

3.5.1. Contact-based mechanics

The focus of this study is to assess the material's elementary mechanisms as well as microstructural deformation, which consists of chains, crystallites, and plasticizers that interact mechanically.

As a result, the model operates without taking into account the intermolecular interactions and the potential energy consideration, while relying on the direct physical contact particles.

3.5.2. Micro-inertial effects and their role

As will be observed from the experimental campaign conducted in chapter 4, the PVC GM exhibits an intricate viscous behavior. This macroscopic viscosity is merely attributed to the resistance force experienced by the PVC polymer chains while moving through the

matrix of plasticizer. Therefore, micro-inertial effects in DEM can account for a macroscopic rate dependency behavior. However, inertial effects are not dissipative. Combined with numerical dissipation, these micro-inertial effects may still serve as a proxy for viscous effects.

However, the resistance force in real PVC is potentially due to intermolecular forces between the system's elements. These forces limit the movement of chains under applied stress leading to energy dissipation. This dissipation can occur via heat generation, or through the rearrangement of chains within the material (Müller 2006).

Additionally, the plasticizer itself plays an important role by weakening the intermolecular forces between polymer chains, which results in an increase in the chain mobility and soften the material. In the developed model, the plasticizer is simplified and represented as spherical particles embedded between the polymer chains. These spherical particles fill the voids and simulate the plasticizer's geometrical effect in swelling the distance between crystallites. While this representation significantly reduces computational complexity—especially compared to more complex non-spherical shapes—it also introduces certain limitations. Real plasticizer molecules, such as phthalates, often have irregular, complex shapes (e.g., a benzene ring with two ester functional groups). This can affect the imbrication of the chains between the plasticizers molecules.

To address the missing contribution of these interactions, a target density considerably exceeding the intrinsic material density of the molecular chains is used. Therefore, the density is increased to 10^{20} kg/m^3, while the real chain density estimated using the molar mass is approximately 5500 kg/m^3.

3.5.3. Numerical damping

In the context of DEM, numerical damping is required to dissipate high frequency oscillation, and consequently achieve the equilibrium state effectively (refer to Section 2.5.5).

In a real system of polymeric material, energy dissipation occurs through molecular rearrangements and heat generation.

Since these effects are not explicitly modeled, this artificial damping, when combined with the micro-inertial effect, can provide a way to replicate some of the dissipative behavior – energy dissipation through heat. Although not physically equivalent, damping serves as a practical means of managing the energy losses in the absence of a more detailed molecular interaction framework. In the model, a numerical damping coefficient of 0.01 is applied (refer to Section 2.5.5 for more details about the artificial damping).

3.6. Setting numerical uniaxial tensile tests

The sample prepared in the previous sections is subjected to a uniaxial tensile loading. To accurately conduct this test, it is essential to determine the mechanical properties of the chain listed above, as well as to apply relevant boundary conditions to the EV.

3.6.1. Boundary conditions setting

In accordance with the homogenization principles, the generated samples define an elementary volume (EV) of PVC GM (i.e., the 3D sample prepared in the previous sections) that should be selected carefully to include enough microstructural details to derive the average macro-properties of the geomembrane.

To link the microscopic properties to the macroscopic behavior under the multiscale approach, Green's formula is employed to calculate the macroscopic stress $\underline{\underline{\Sigma}}$ and strain $\underline{\underline{E}}$ by averaging their microscopic counterparts over the boundary of the EV, ∂V. It can therefore be written:

$$\underline{\underline{E}} = \frac{1}{|V|} \int_{\partial V} \underline{u} \otimes_s \underline{n}\, dS \tag{3.10}$$

Where:

- $\underline{u}$ is the displacement vector on the boundary ∂V,
- $\underline{n}$ is the outward unit normal vector to the boundary ∂V,
- $\otimes_s$ denotes the symmetric tensorial product,
- dS is the surface area,
- V is the volume of the EV

$$\underline{\underline{\Sigma}} = \frac{1}{|V|} \int_{\partial V} [(\underline{\sigma}) \otimes_s \underline{x}]\, dS \tag{3.11}$$

Where:

- $\underline{\sigma}$ is the traction force at a point on the boundary ∂V,
- $\underline{x}$ is the position vector at the boundary point considered.

In the context of homogenization theory, the selection of the boundary conditions is of key importance as they influence the size of the sample necessary to reach the REV condition. In this respect, we use Kinematic Uniform Boundary Conditions (KUBC) instead of directly imposing laboratory uniaxial conditions at the sample scale.

Under KUBC, and in accordance with the material's incompressibility (refer to Chapter **4**, Section 4.2.1), a macroscopic homogeneous strain rate $\underline{\underline{\dot{E}}}$ is imposed along the boundary, using a linear relationship between boundary displacements and macroscopic homogeneous true strain (as expressed by Equation 3.13). Contrary to laboratory conditions, the tangential velocities on the lateral boundaries of the sample are imposed with KUBC.

In the case of uniaxial tensile loading, the macroscopic homogeneous strain rate is expressed as:

$$\underline{\underline{\dot{E}}} = \begin{pmatrix} -\nu\dot{\varepsilon}\,(1+\dot{\varepsilon}t)^{-\nu-1} & 0 & 0 \\ 0 & \dot{\varepsilon} & 0 \\ 0 & 0 & -\nu\dot{\varepsilon}\,(1+\dot{\varepsilon}t)^{-\nu-1} \end{pmatrix} \tag{3.12}$$

where $\dot{\varepsilon}$ represents the applied tensile rate on the specimen, t is the time, and v is a constant equal to 0.5 to respect (this constant is determined later in Section 4.2.1).

Consequently, the applied velocity on the boundary at a point of initial coordinates x can be calculated using:

$$\dot{u}(\underline{x}) = \underline{\underline{\dot{E}}} \,.\, \underline{x} \tag{3.13}$$

For the simulation, uniaxial loading is applied to the specimen through the boundaries, specifically targeting the wall and the GridNodes' boundaries. Equation 3.13 based on the KUBC approach determines the velocity distribution on the boundary, illustrated in Figure 3.13 and Figure 3.14. These velocities are applied to the boundary nodes and wall, with the bottom boundary fixed to serve as a stable reference point. To maintain a consistent strain rate throughout the test, Newton's discretization equations are not applied to the GridNodes on the boundary in the direction of the applied velocity, as shown in Figure 3.14. This can be achieved in practice by setting the Boolean parameter yade.wrapper.State.blockedDOFs to True on all the chains nodes touching the boundaries.

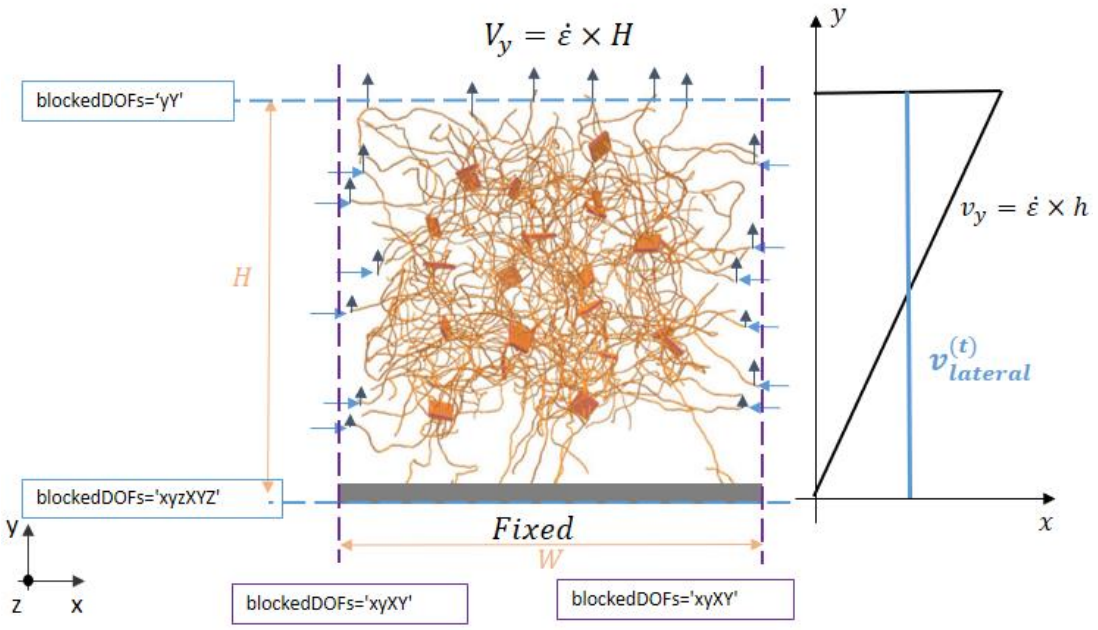


Figure 3.13: Applied velocity distribution on the GridNodes's boundaries with respect to the KUBC approach.

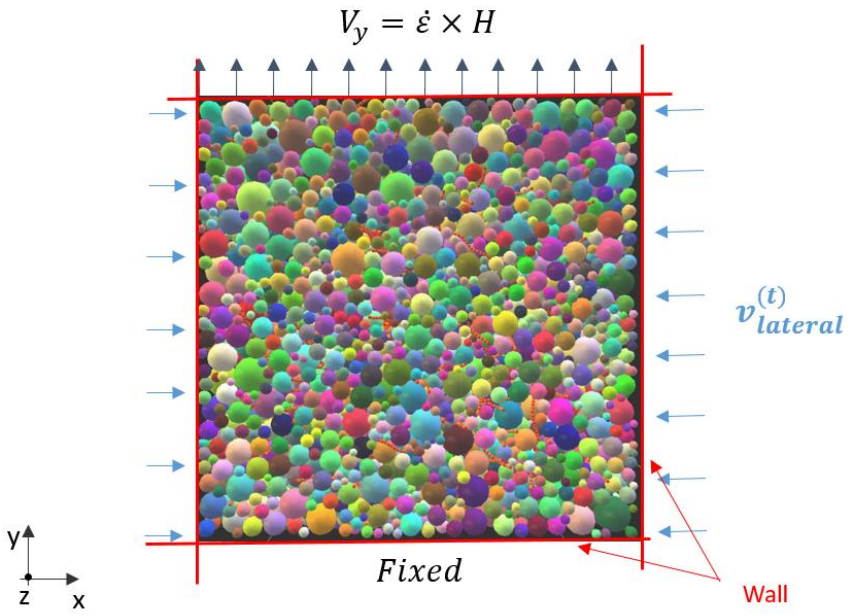


Figure 3.14 : Set of velocities applied on the boundary walls.

3.6.2. Chain's strength calibration

Assuming a uniformly homogeneous distributed stress within the EV, represented by a set of aligned chains oriented in the direction of uniaxial loading at the boundary where the load is applied (i.e., top surface boundary of the EV), each cylindrical segment supports an equal tensile force. Thus, the total force, supported by all the chains located at the top surface of loading, is given by:

$$F_{total} = m \times A_{chain} \times \sigma_{chain} \tag{3.14}$$

Where m is the number of chains at the surface boundary, ∂V^u, on which the loading is applied, and A_{chain} is the cross-section area of the cylinder.

Thus, the vertical component of the macroscopic stress is calculated as follows:

$$\sigma = \frac{F_{total}}{A_{sample}} \tag{3.15}$$

Where A_{sample} is the actual cross-sectional area of the sample.

Substituting the expression F_{total} from Equation 3.15 into Equation 3.14 gives

$$\sigma = \frac{m \times A_{chain} \times \sigma_{chain}}{A_{sample}} \tag{3.16}$$

Combining with Equation 3.9, the microscopic strength of the cylindrical segment C_n of the chains can be related to the macroscopic strength of the material σ_{max}. This relationship gives only the respective orders of magnitude and must be adjusted by a correction coefficient $c > 1$ as chains are not perfectly aligned in the direction of tensile loading (i.e., randomly oriented chains) and not evenly loaded. Thus, the strength of the cylinder is related to the macroscopic tensile strength σ_{max} as follows:

$$C_n = c \times \frac{A^0_{sample} \times \sigma_{max}}{m \times A_{chain}} \tag{3.17}$$

where, c is the correction coefficient, A^0_{sample} is the initial cross-sectional area of the EV, m is the number of chains touching the top boundary, A_{chain} is the cross sectional area of the chain's segment, with $A_{chain} = R_c^2$. The value of σ_{max} is determined based on the experimental campaigns detailed in the following chapter.

3.7. Summary

In this chapter, we have presented a detailed step-by step construction of a 3D model of PVC geomembrane at the mesoscale level. This model takes the complex morphology of the PVC microstructure into account, including polymer sizes, crystallite shape and size, complex amorphous region, all of them embedded within a matrix of plasticizer.

The model is designed to simulate an elementary volume subjected to uniaxial tensile loading, using a homogenization approach to link macro- to mesoscale.

The process of constructing the model, summarized in Figure 3.15, begins with the creation of a 3D complex network of the PVC microstructure. First, the positions of the crystallite barycenter are determined (refer to Section 3.1.2). Crystallites are then formed, followed by the creation of the amorphous chains in the amorphous regions using a random walk algorithm, as detailed in Section 3.1.3. Plasticizer is incorporated next, using spheres as placeholders to fill the spaces between the chains (explained in Section 3.2). Here, the effects of plasticizer are considered in two aspects: first, it increases the distance between the crystallites, which contributes to the material's flexibility; and second, it fills space between the polymer chains, making it harder to reorganize polymer chains. Various geometrical parameters, such as the number of chains, chain tortuosity, crystallinity level, and the dimensions of the EV, affect the configuration generated (see Section 3.3).

A uniaxial tensile numerical test is set up as described in Section 3.6, with KUBC applied on all the boundaries nodes.

The mechanical properties of the polymer chains are simplified into three key parameters: stiffness, E, density, ρ, and tensile strength, C_n (refer to Sections 3.1.1 and 3.4).

The model employs several key assumptions and approaches (refer to Section 3.5):

- Intermolecular interactions, such as van der Waals or dipole-dipole forces, are not explicitly modeled within the amorphous region, and particle interactions are modeled based on frictionless contact interaction laws.
- Micro-inertial effects are introduced by assigning high material density values. Combined with numerical dissipation, it serves as a proxy for viscous behavior.
- The elastic rigidity, E, and material's density, ρ, of the plasticizer particles are set to be of the same order of magnitude as those of the polymer chains.

The model will provide valuable insights into how macroscopic behavior is linked to mesoscale mechanisms. Specifically, it outputs macroscopic response, through axial true stress (Cauchy stress) and true strain (logarithmic strain), where the axial true stress is calculated using Equation 3.18:

$$\sigma_{yy}^{t} = \frac{1}{A_{sample}^{t}} \sum_{i} \overrightarrow{F_i}^{t} . \overrightarrow{e_y} \tag{3.18}$$

Where i represents the chain number at a given section of the specimen, A_{sample}^{t} is the cross-sectional area of the sample at time t, $\overrightarrow{F_i}^{t}$ is the internal force vector within the i -th chain, and $\overrightarrow{e_y}$ is the unit vector along the y-axis, indicating the direction of the applied tensile load.

In the following chapters, we will delve into the analysis of the model's parameters effects on mechanical behavior, and the calibration of certain key parameters will be discussed as well thanks to experimental campaigns. Through this analysis, we aim to demonstrate the model's capability to relate microstructural details to macroscopic mechanical properties.

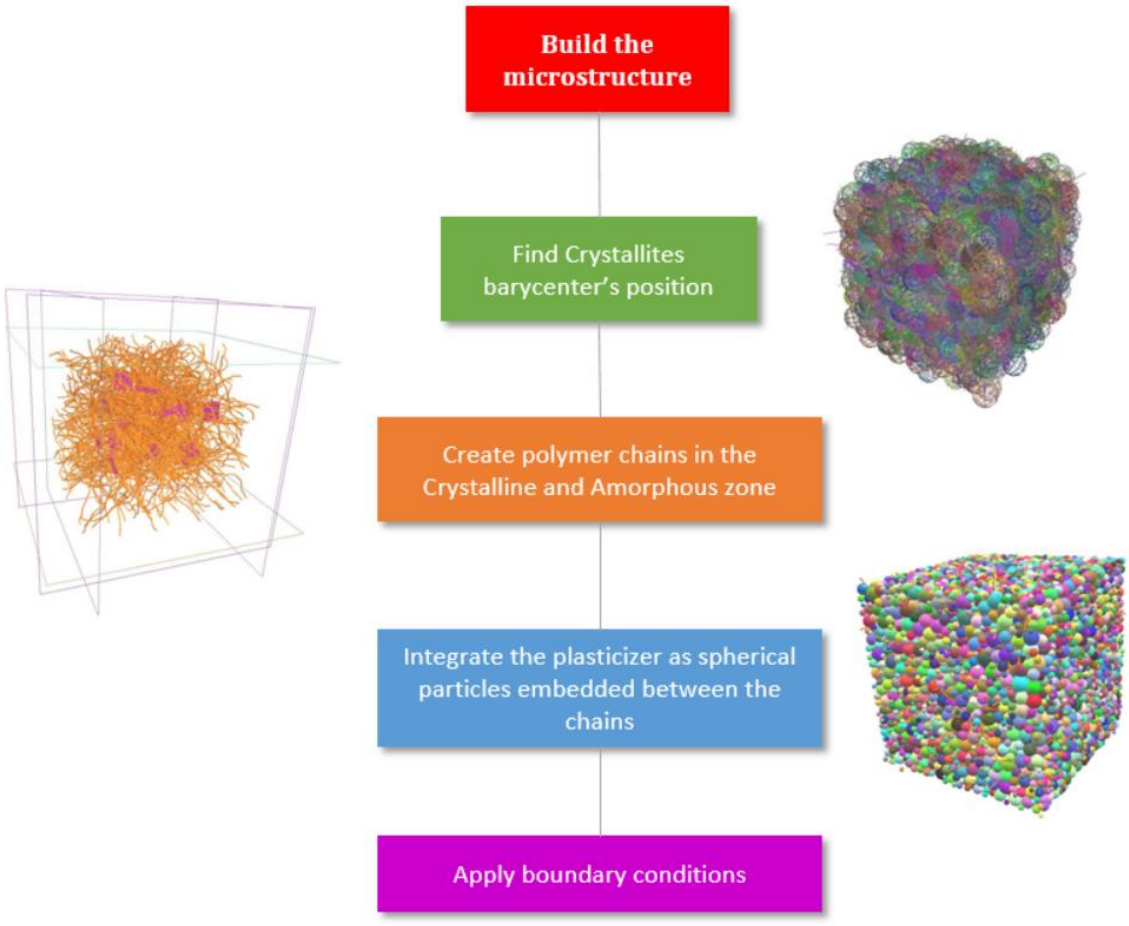


Figure 3.15: Summary of the model's build-up steps.

Chapter 4: Towards calibrating the model: Experimental Investigation of PVC Geomembrane Response to Tensile Forces

Geomembrane systems have a design stress far lower than their stress resistance, however, larger stress concentrations can occur due to unexpected local conditions. Thus, understanding the mechanical behavior of the PVC GM's material under different loading conditions is crucial.

Additionally, a major engineering challenge, associated with designing the waterproofing systems intended for protecting the environment and public health over long periods, is the effective conversion of short-term laboratory test results into long-term performance predictions. Specifically, in the case of PVC GM, the interplay between various factors—such as tensile forces, strain rates and environmental conditions— necessitates a comprehensive understanding to make informed design decisions.

In order to tackle this problem, this study investigates how these forces affects the tensile strength and elongation at failure on the short and long-term performance of the GMs. This chapter presents an experimental campaign, including uniaxial tensile tests, creep tests, and relaxation tests, all aimed at assessing the material's response to varying strain rates, applied stresses, and strains. The key properties evaluated include tensile strength, strain at failure, and both rate- and time-dependent behaviors.

Furthermore, the study also includes an investigation into the strain recovery behavior of PVC geomembranes subjected to different preloading histories. This aspect is crucial for understanding the material's ability to recover from deformation under in-situ conditions.

Moreover, upon developing the micromechanical model in Chapter 3, the primary objective of this chapter and the following chapter is to calibrate and validate the model to gain deeper insights into the material's behavior at the mesoscale level.

This chapter is largely based on our published paper (Akel et al. 2025), which focus on the rate-dependent tensile response of PVC GMs.

Briefly, this chapter will discuss the rate-dependent effect on the material's ultimate properties and rigidity, at short- and long-term performance, by conducting uniaxial tensile and relaxation tests at different loading rates. Afterward, creep tests will be conducted at different loading weights, to examine the effect of loading weights on the creep behavior, and to determine the ultimate properties (i.e., strength and strain at failure) at long term. Finally, strain recovery tests will be performed to evaluate the impact of pre-loading history and time-dependency on the strain recovery process.

The results from these tests provide a complementary comprehensive analysis that helps in understanding the overall mechanical behavior of the geomembrane, offering critical insights into its performance under different conditions.

4.1. Materials and Experimental devices

4.1.1. Materials

The geomembrane, considered in the experimental tests, is a transparent 3 mm thick PVC GM, obtained from a slot extrusion process through two extruders, followed by calendering technology, designed specifically for a tunnel project. The chemical composition comprises PVC resin, plasticizer, and stabilizer.

The selection of this geomembrane type aims to mitigate the influence of antioxidants or any additives, such as fillers, carbon black, and fire retardants, on the research outcomes (Lodi et al. 2008). This choice allows for a more precise examination of the fundamental properties of PVC GMs, and a clearer understanding of their performance, unaffected by the existence of additives.

4.1.2. Apparatus and data acquisition

The test apparatus used for conducting tensile and relaxation tests on PVC GMs is shown in Figure 4.1. This setup comprises a tensile testing machine equipped with upper and lower grips for holding the specimen, and a force sensor with a sufficient loading capacity (at least 2000 N).

The test specimen is to be tightly clamped in the tensile test machine grips, ensuring precise alignment of the longitudinal axis of the test specimen and the axis of grips (see Figure 4.2 (a)). The testing procedure of the uniaxial traction test involves subjecting a PVC GM specimen to continuous stretching at a constant displacement rate.

The displacement rate, or grip separation speed, is adjustable within the range 0.01 to 500 mm/min. According to the European standard EN12311 (AFNOR 2013), which specifies methods for determining the tensile properties of plastic and rubber sheets, a speed of 100 mm/min is recommended. The clear distance between the grips is set at 80 mm, according to the same standard.

A video extensometer is employed to measure the relative displacement between two predefined markers on the specimen. Concurrently, an acquisition system continuously records both the tensile force and the corresponding longitudinal relative displacement in the specimen.

For the creep tests, the setup consists of a newly installed fixed frame that securely holds the geomembrane specimen. The upper part of the specimen is tightly anchored using a screw and a washer. A constant load is then applied by suspending weights gradually from the lower part of the geomembrane specimen via a suspended cable, exerting a constant uniaxial tensile force. The creep test setup is shown in Figure 4.3.

To measure the deformation over time, the relative displacement between the two marked points on the specimen is measured using a caliper.

The tests are conducted at a controlled temperature of 23 ± 2 °C and relative humidity in the range 30% to 70%.

4.1.3. Specimens preparation

The dimensions of the dumbbell-shaped specimens for the GM uniaxial tensile test conform to the specifications mentioned in the European standard EN12311 (Method B). These specimens are randomly extracted from a sample of PVC GM. Using a template, a GM cutter machine was used to cut the specimens into a dumbell-shaped specimen (Figure 4.2 (b)). On the less brilliant side of the specimen, two marker reference points are placed using a template, as shown in Figure 4.2 (c), to measure the relative longitudinal displacement using the extensometer. The specific dimensions are detailed in Figure 4.4.

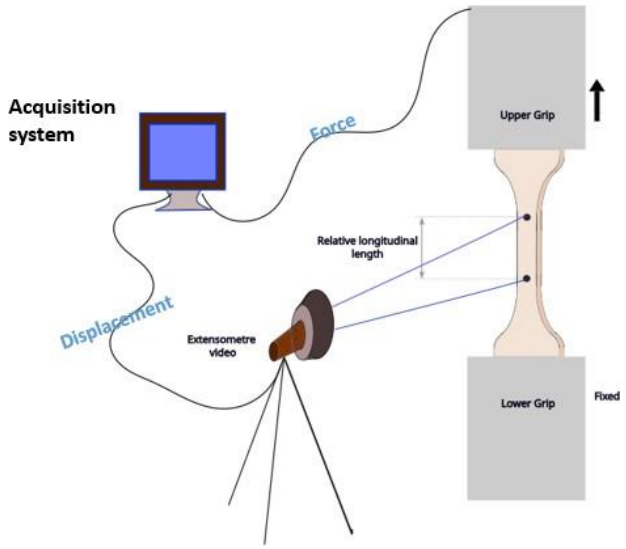


Figure 4.1: Uniaxial tensile test setup.

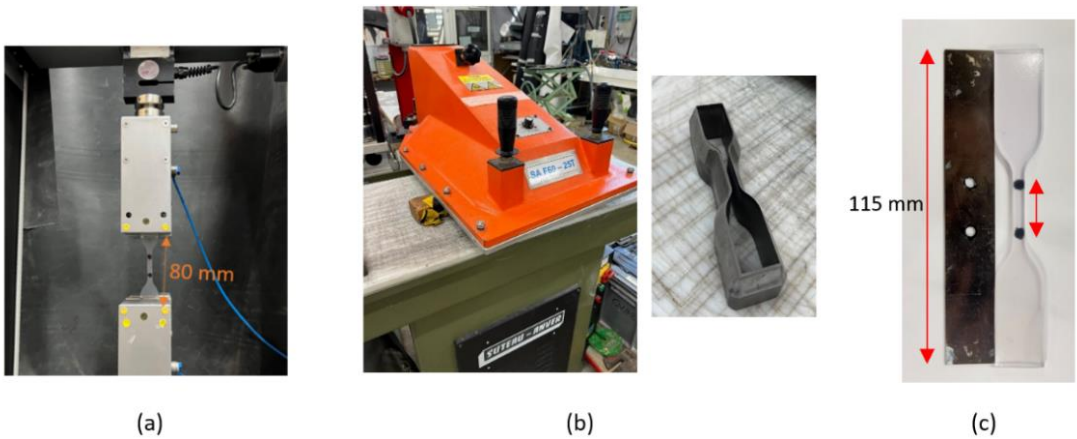


Figure 4.2: (a) Specimen mounted between the clumps of the two grips. (b) Template used for marking the two reference points. (c) The cutter machine and the template used to crop specimens in the form of dumbbell-shape.

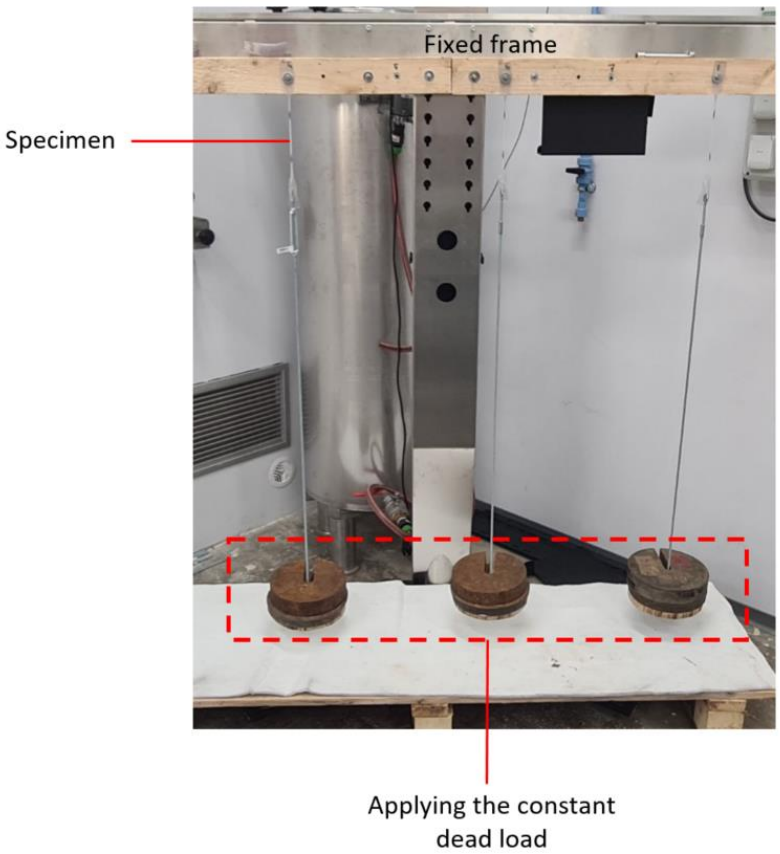


Figure 4.3: Creep Test Frame where several creep tests can be conducted simultaneously.

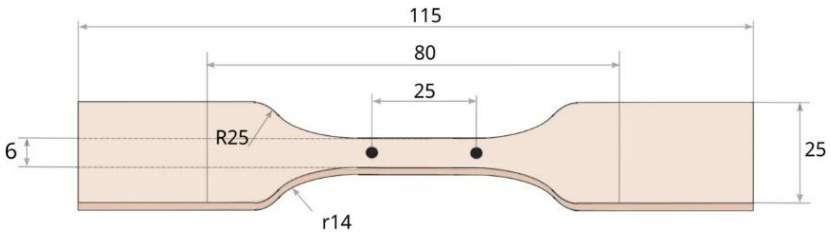


Figure 4.4: Dimensions (in millimeters) of Dumbbell-shaped specimen.

4.2. Experimental methods

Tensile tests, being the most straightforward experimental approach, are used for the determination of the mechanical properties of materials in terms of their stress-strain behavior, stiffness, strength, and strain at failure (i.e., failure point where specimen is separated into two pieces).

The studied PVC GM's variation of the mechanical properties over time are investigated for short-term through strain-rate-dependent tensile tests, and long-term scenarios via relaxation tests, creep tests, and strain-recovery tests.

4.2.1. Methodology of uniaxial tensile tests at various loading rates

It is worth mentioning firstly that the tests conforming to the European standard EN12311 were conducted at a speed of 100 mm/min. However, this study includes a thorough evaluation of the rate dependency effect over a set of tensile speeds (i.e., displacement rate), spanning several orders of magnitude from 0.01 to 500 mm/min (0.01, 0.1, 0.5, 1, 10, 50, 100, 200, and 500).

Speeds exceeding 100 mm/min are included in this study to better understand and assess the material's behavior under extreme loading scenarios, such as impacts and seismic loads (Thusyanthan et al. 2012). For each tensile speed, at least three repeatability tests have been carried out. This range of displacement rates allows for a comprehensive understanding of the material's response to different loading conditions.

The test ends when the failure occurs. Throughout the test, the applied force and the corresponding relative displacement of the specimen are recorded. The outcome of this test is a force-strain curve, wherein the strain represents the engineering strain (i.e., infinitesimal strain) expressed as the ratio of the incremental length to the initial length (Equation 4.1).

$$\varepsilon_{aE} = \frac{\Delta L}{L_0} = \frac{L_f - L_0}{L_0} \tag{4.1}$$

where ε_{aE} is the axial engineering strain or infinitesimal strain, L_0 is the initial relative length between the two predefined marked points on the specimen, and L_f is the final distance between them.

Figure 4.5 shows the typical force-engineering strain curve. As the strain progresses, the force increases, until reaching a maximum value at the rupture point.

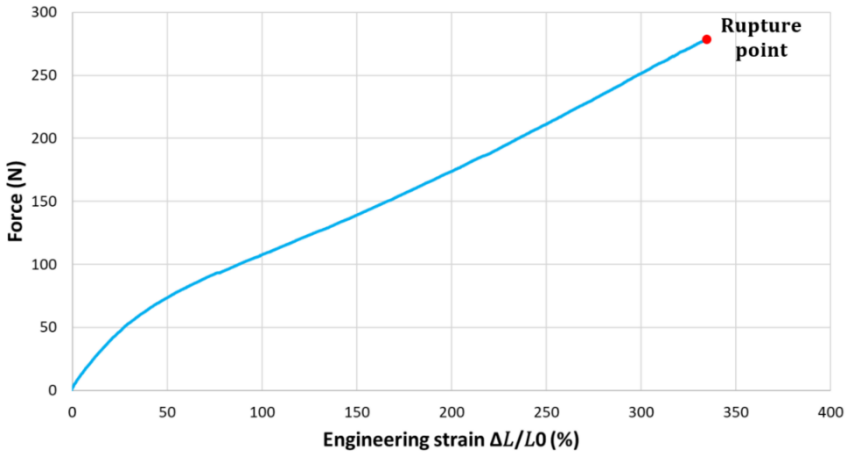


Figure 4.5: Typical force-engineering strain curve in uniaxial tensile tests.

While force-engineering strain curves offer useful and practical insights, a deeper understanding of the mechanical properties of PVC GMs can be gained through the presentation of true stress – true strain curves (Zhang et al. 2022), providing a detailed analysis of key properties of the material, such as the maximum true tensile strength and

strain. Here, axial true stress represents the axial Cauchy stress (see Equation 4.9), while true strain refers to the logarithmic strain.

The true axial strain is defined as the logarithmic strain, as expressed in Equation 4.2:

$$\varepsilon_{aT} = \int_{L_0}^{L_f} \frac{dL}{L} = \ln\left(\frac{L_f}{L_0}\right) = ln\left(\frac{L_0 + \Delta L}{L_0}\right) = \ln(1 + \varepsilon_{aE}) \tag{4.2}$$

Both the width and the thickness of the specimen decrease during the uniaxial tensile test. Hence, similarly, the true strain for width and thickness is respectively defined as:

$$\boldsymbol{\varepsilon_{wT} = \ln(1 + \varepsilon_{wE})} \quad \boldsymbol{and} \quad \boldsymbol{\varepsilon_{tT} = \ln(1 + \varepsilon_{tE})} \tag{4.3}$$

with,

$$\boldsymbol{\varepsilon_{wE} = \frac{\Delta w}{w_0}} \qquad \boldsymbol{and} \qquad \boldsymbol{\varepsilon_{tE} = \frac{\Delta t}{t_0}} \tag{4.4}$$

where ε_{wT} and ε_{tT} are respectively the true strain for width and thickness direction, ε_{wE} and ε_{tE} are respectively the engineering strain in the thickness and width direction, w_0 and t_0 are respectively the initial width and thickness, Δw and Δt are respectively the change in width and thickness.

The relation between the axial and lateral (i.e., width and thickness) true strains is determined by measuring the local (i.e., logarithmic) strains along the three axes of the specimen. To do so, uniaxial tensile tests are conducted at low speed (0.5 mm/min), in order to facilitate the measurements of the thickness and width using a caliper while testing. For this purpose, two specimens, one cut along the machine direction and the second along the cross direction, were employed. In Figure 4.6, the relationship between the lateral true strain and the axial true strain is illustrated.

The results show a linear relationship in both the machine and cross directions, characterized by a slope of around 0.5 up to the point of material failure. This relationship is characterized by a slope of approximately 0.5, with slight fluctuations primarily attributed to measurement errors. Therefore, the tests demonstrate that the material can be considered isotropic and incompressible.

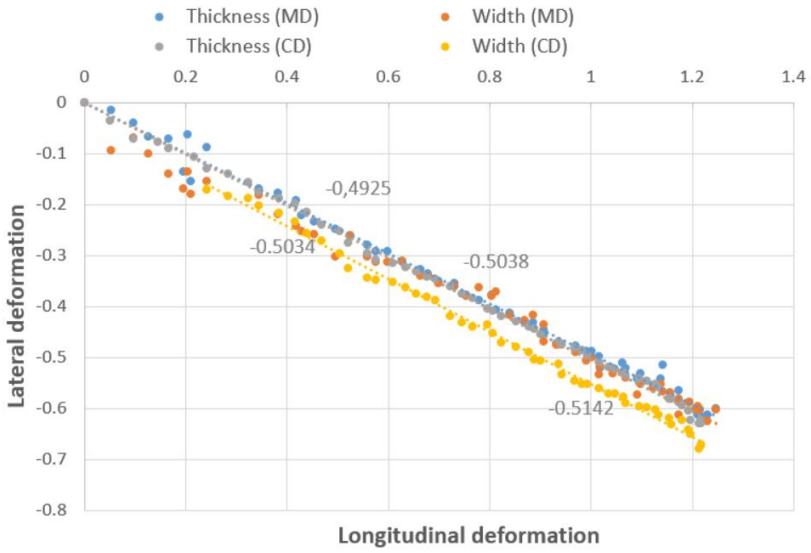


Figure 4.6: Lateral true strain vs. axial true strain in machine (MD) and cross directions (CD) at a uniaxial tensile speed of 0.5mm/min: Slopes of -0.49 (Thickness) and -0.5 (Width) in MD, and -0.5 (Thickness) and -0.51 (Width) in CD.

To explore high-speed conditions, two tensile tests are conducted at 100 and 200 mm/min. For these two tests, width and length are determined by a non-contact optical method using image processing with Fiji_ImageJ software. The procedure of image treatment is illustrated in Figure 4.7. The spatial-temporal evolution of both width and length is determined by tracking pixel values across both dimensions. Remarkably, as seen in Figure 4.8, the results obtained from the high-speed tests reveal an axial true strain, with a slope of around 0.5, with slight deviations due to various factors such as image treatment errors, material heterogeneity, or experimental errors. Interestingly, a complementary investigation was conducted using the video extensometer analysis. The findings confirm a linear relationship between both true lateral and axial strains, with a similar slope of approximately 0.5. This consistency across testing methodologies suggests that the PVC GM under study is incompressible whatever the loading rate. Hence, the relationship between true axial and lateral strains is defined as:

$$\boldsymbol{\varepsilon_{tT} = \varepsilon_{wT} = -\alpha \varepsilon_{aT}} \qquad \mathbf{(4.5)}$$

with a value of α equal to 0.5.

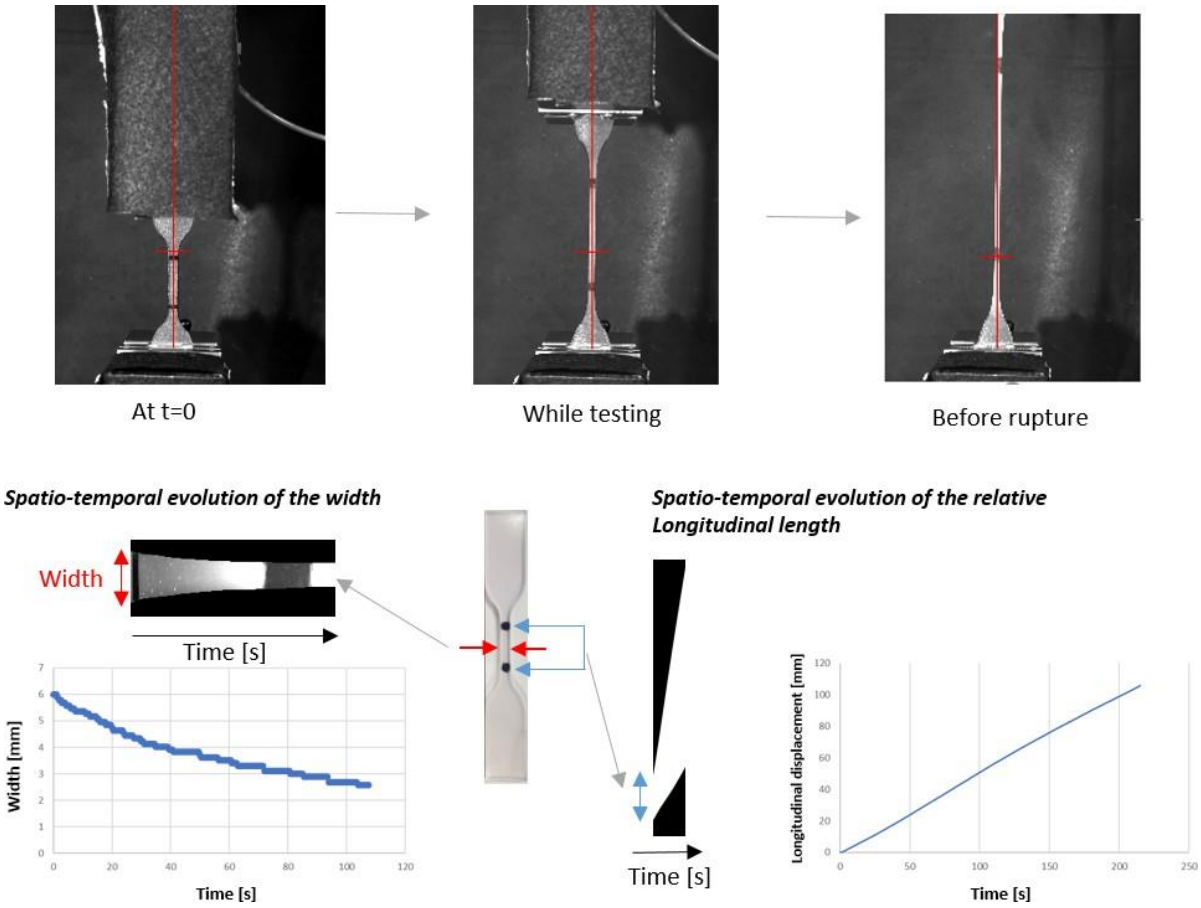


Figure 4.7: Schematic view of the image processing method employed to determine the width and relative longitudinal length during uniaxial tensile testing. The spatial-temporal evolution of both width and length is determined by monitoring pixel values along the width and length using a horizontal and vertical red line, respectively.

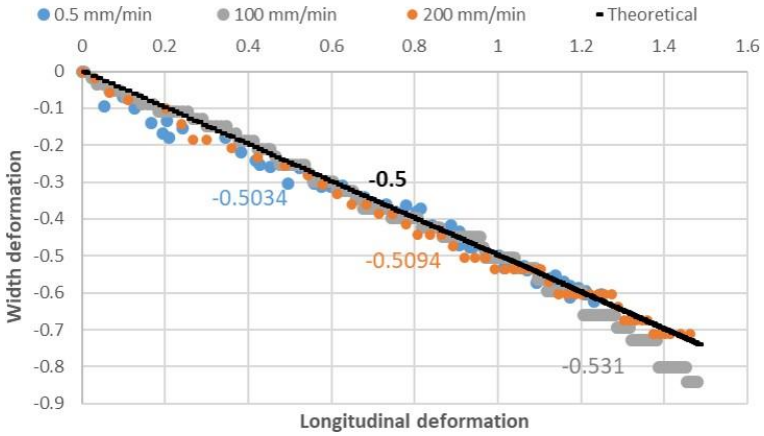


Figure 4.8: Lateral true strain vs. axial true strain at uniaxial tensile speeds of 0.5, 100, and 200 mm/min.

Given the variations in cross-sectional area during testing, it becomes crucial to calculate the actual true stress, represented by the axial Cauchy stress, to accurately assess the material's behavior under applied forces. The axial Cauchy stress is determined by dividing the force acting on the material by its corresponding current cross-sectional area.

Equation 4.6 gives the current cross-sectional area:

$$A = w \times t \tag{4.6}$$

where w and t denote respectively the current width and thickness, derived from Equations 4.3, 4.4 and, 4.5 as:

$$w = w_0 e^{-\alpha \varepsilon_{aT}} \tag{4.7}$$

and,

$$t = t_0 e^{-\alpha \varepsilon_{aT}} \tag{4.8}$$

where w_0 and t_0 are the initial width and thickness.

Thereupon, the axial Cauchy stress, can be calculated as follows:

$$\sigma = \frac{F}{A} = \frac{F}{w_0 t_0 e^{-2\alpha \varepsilon_{aT}}} \tag{4.9}$$

Figure 4.9 shows the typical Cauchy (i.e., axial true) stress- axial true strain curve. One can note that, until approximately 80% of true strain, the PVC GM behaves as a linear elastic solid. After, a nonlinear behavior prevails, underpinning an intricate interplay between elasticity, viscosity, and plasticity.

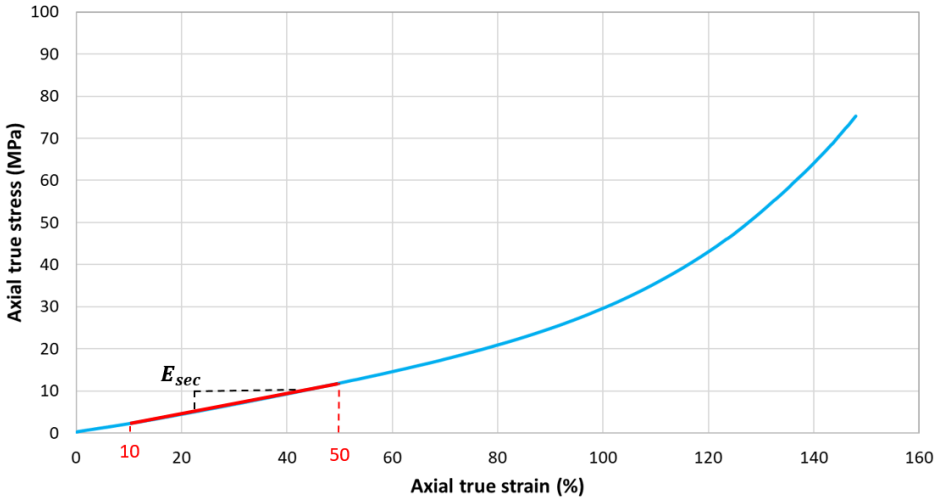


Figure 4.9: Typical axial true stress - axial true strain curves in uniaxial tensile tests. The tensile modulus $\boldsymbol{E_{sec}}$ is determined from the initial secant drawn between 10 % and 50 % true strain.

When examining the rate dependency effect, one important property to be investigated is the young modulus. Due to the non-linear stress-strain behavior of the PVC geomembrane, which lacks a clearly defined yield point, the tensile modulus is used instead of Young's modulus.

As an estimation of the tensile modulus, the initial secant modulus is considered. This is computed by drawing a line from the origin to a specific point on the stress-strain curve, specifically at 50% logarithmic deformation, where the relationship remains approximately linear, as shown in Figure 4.9. To enhance accuracy, the origin point is considered at 10% logarithmic deformation to mitigate the influence of any artifacts-

induced deformations caused by the initial positioning of the specimens, as shown in Figure 4.9.

4.2.2. Methodology of relaxation tests

Investigations through relaxation tests aim to understand the material response to persistent strain over time. To assess the effects of tensile loading rate on stress relaxation properties, seven distinct speeds have been selected: 0.01, 0.1, 0.5, 1, 10, 100, and 500 mm/min. For each speed, two tests are performed, and specimens were stretched up to a 50% axial engineering strain (to stay far away from the failure point).

By maintaining this strain level (i.e., the initial strain at the onset of relaxation) at 50%, the focus is on examining how different strain rates applied during the pre-relaxation phase affect relaxation behavior, thereby assessing the material's long-term performance.

The decision to use engineering strain rather than true strain is driven by practical considerations arising from the testing machine, which permits the application of engineering strain but not true strain. The testing procedure is described in Figure 4.10 and Figure 4.11. Due to technical constraints, achieving precisely 50% of deformation is not possible; the actual deformation levels reached in each test are detailed in Table 4.1. Once the target strain was reached, the strain was kept constant, and the tensile stress was recorded over a duration of 4 days. The typical stress decay with time is shown in Figure 4.11, revealing a notable initial variation of stress. Over time, this variation progressively reduces but no complete stabilizing is observed.

The actual transversal deformation (i.e. width) is assessed during the relaxation test using a non-contact optical method with image processing, using Fiji ImageJ software. The spatial-temporal evolution of the specimen's width, as seen in Figure 4.12, shows no variation in width during stress relaxation. This indicates that the material undergoes isochoric relaxation, maintaining a constant volume throughout the process.

Table 4.1: Level of maximal engineering strain achieved during each relaxation test.

Tensile speed [mm/min]	Level of engineering strain [%]	
	Test 1	Test 2
0.01	57.44	50.64
0.1	49.35	53.31
0.5	46.62	49.92
1	49.97	49.97
10	61	50.06
100	50.09	50.22
500	50.17	49.15

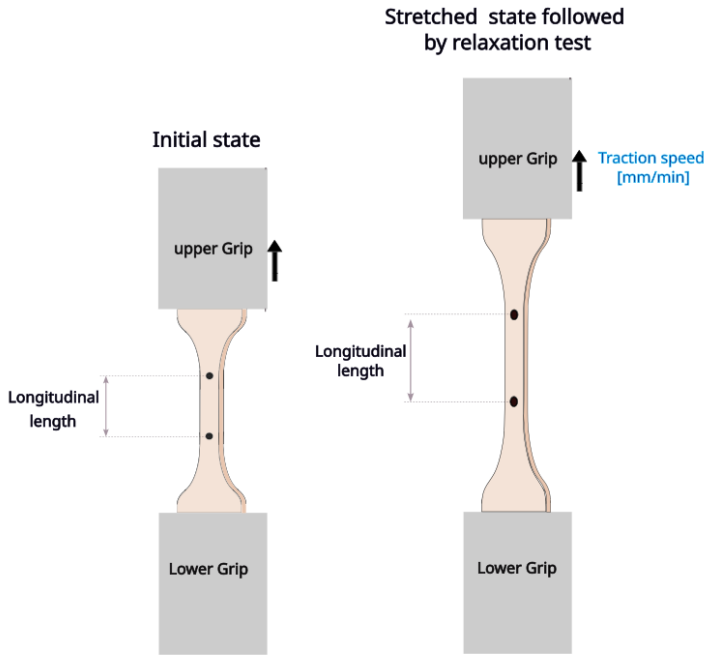


Figure 4.10: Pre-Relaxation Test Procedure: the sample is stretched until it reaches a 50% deformation level. Once this level is reached, the specimen is held in this configuration, and the stress-relaxation phase starts.

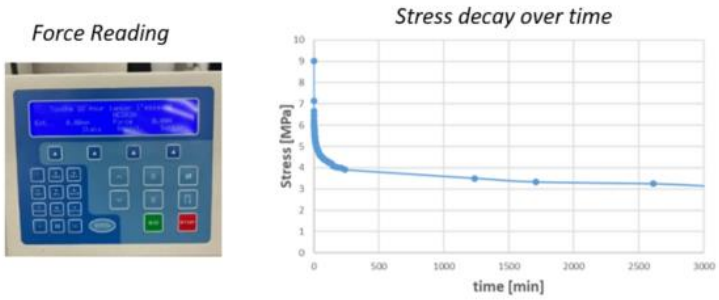


Figure 4.11: Relaxation Test: measuring stress over time at a fixed Deformation level.

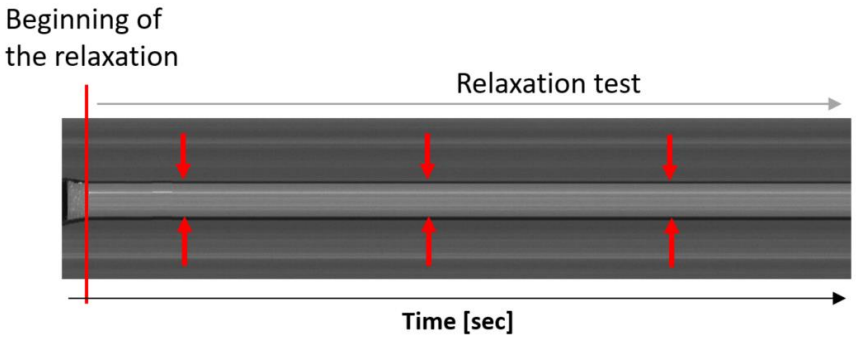


Figure 4.12: Spatial-temporal evolution of width during stress relaxation determined by monitoring pixel values along the width.

4.2.3. Methodology of creep tests

Investigations through creep tests aim to evaluate the long-term characteristics of materials under constant stress. This is particularly important in engineering, as it significantly influences the design and selection of geomembrane.

To explore the creep characteristics of geomembrane under uniaxial tensile stresses, a series of creep tests were carried out at different load levels (100, 110,120,140,150, 200, 250 N)[1].

It is worth to mention that all tests were conducted using specimens from the same sample and performed using the same load frame.

The typical strain variation over time curves is shown in Figure 4.13, revealing that the geomembrane experiences an immediate deformation upon loading. This is f ollowed by a rapid increase in strain during the first stage of creep, where the creep strain rate gradually decelerates with no stable value reached.

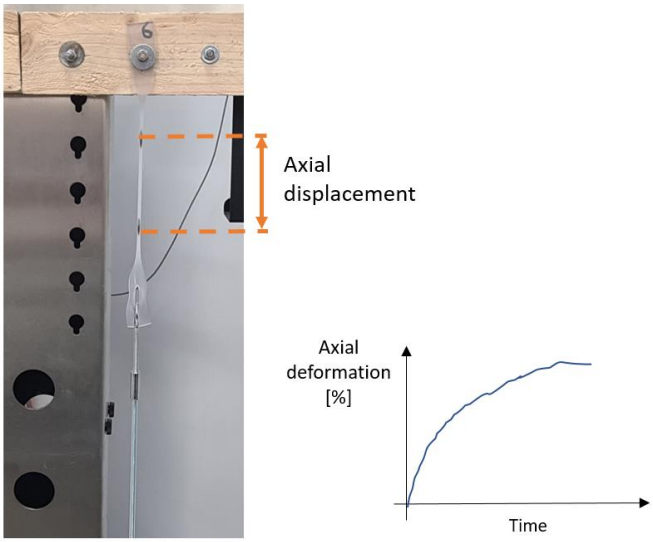


Figure 4.13: Measuring displacement over time at a fixed load level.

4.2.4. Methodology of strain recovery tests

In order to evaluate the reversibility of the strain in the geomembrane, a series of loading and unloading tests have been conducted.

The procedure involves applying a constant displacement rate to the specimen. When the specimen reached 50% of its engineering strain, the load was gradually reduced at the same displacement rate until the force on the specimen reached zero. This unloading phase was then followed by reapplying the load, increasing the strain to 100%, and subsequently continuing with the next cycle. Each cycle involved increasing the deformation by an additional 50% until rupture of the specimen was reached. This

[1] These tests were conducted by the internship student, Laurent Josseaume, as part of this thesis.

method allows for a detailed assessment of the strain recovery characteristics and its mechanical behavior under loading and unloading test.

However, Figure 4.14 reveals a loop-like pattern, which reflects a hysteretic behavior. which may be attributed to the material's viscosity. This is why the strain recovery is not immediate, and may take time to fully occur.

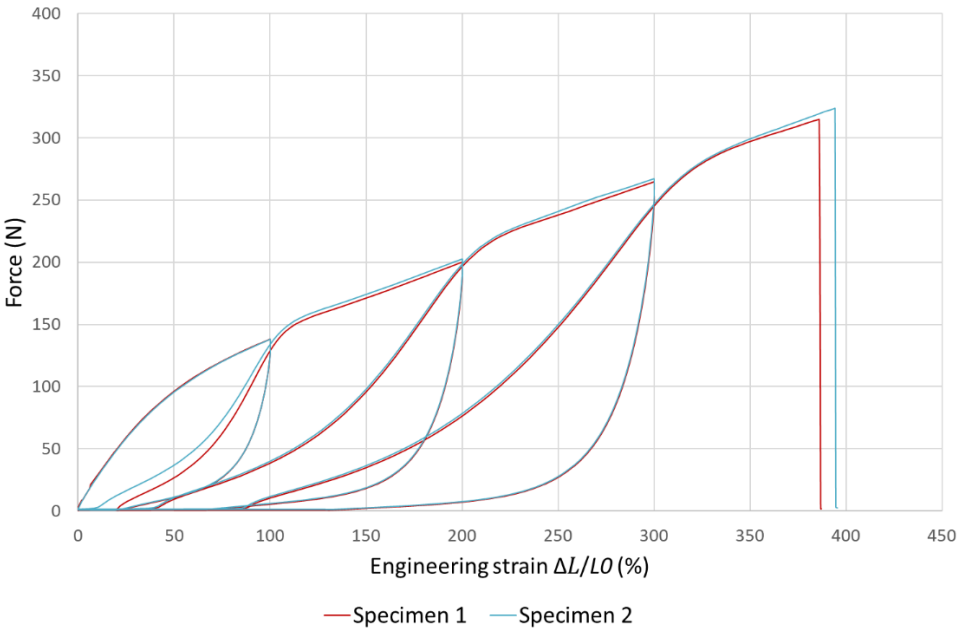


Figure 4.14: Loading and unloading tests conducted on two specimens randomly chosen from the GM sample.

Consequently, a new protocol has been developed to better understand the material's deformation recovery behavior. This protocol involves uniaxially tensile loading the specimen to various predetermined deformation levels at a constant displacement rate. Here, a standard displacement rate of 100 mm/min is chosen. Once a specified level is reached, the loading is stopped and the specimen is removed from the tensile machine. The strain recovery is then measured over a 7 days period; by measuring the relative length between the marked references points using a caliper to capture precise measurements (see Figure 4.15). Nineteen levels of deformation have been considered, ranging between 30% to 300%.

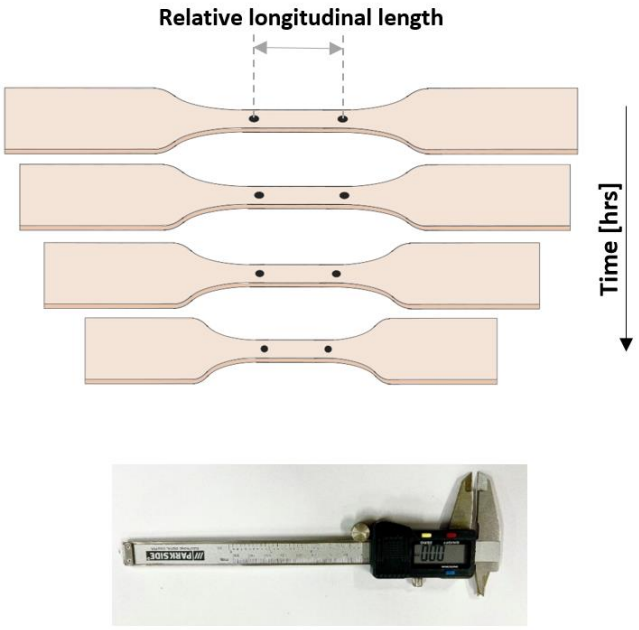


Figure 4.15: strain Recovery Test Procedure: Measuring the length between the two marked points over time.

The impact of loading history and time on strain recovery properties have been also investigated through relaxation and creep tests. The aim of these tests is to assess how the material recovers strain after being subjected to prolonged loading. These tests involved subjecting the geomembrane specimen to either a constant stress (refer to creep test protocol Figure 4.13) or constant strain (refer to relaxation test protocol Figure 4.10 and Figure 4.11) condition for an extended period. Then, the loads are removed, and the strain recovery is measured regularly over the time using a caliper (refer to Figure 4.15). For the creep tests conducted prior to measuring strain recovery, a series of applied constant weights ranging from 10 to 100 N were used[1]. A different extended creep period was chosen for each weight to assess how different loading conditions influence the strain recovery properties. The extended duration under loading for each weight is displayed in Table 4.2. After removing the weights, the engineering strain was measured over time.

For the relaxation tests conducted prior to measuring strain recovery, the procedure involved stretching a specimen until it reached 50% of its engineering strain at a constant displacement rate of 0.01 mm/min. The specimen was then kept clamped in the tensile machine at this strain level for an extended period of 10 days. After this period, the specimen was taken out from the machine, and the evolution of the strain over time (i.e., strain recovery) was measured for an extended period of 80 days.

As this test requires an extended duration (92-days), it was conducted at a single constant displacement rate of 0.01 mm/min.

[1] These tests were conducted by the internship student, Laurent Josseaume, as part of this thesis.

Table 4.2: Extended Loading Durations for Different Applied Weights in Creep Tests.

Applied weight (N)	Duration of Load during creep tests (min)					
	Specimen 1	Specimen 2	Specimen 3	Specimen 4	Specimen 5	Specimen 6
10	4920	-	-	-	-	-
20	4920	-	-	-	-	-
30	4320	-	-	-	-	-
40	5722	1440	43200	-	-	-
50	5732	1440	300	1020	480	-
60	5742	1440	1020	300	90	120
65	60	-	-	-	-	-
70	60	1126	120	240	360	120
80	60	240	120	60	-	-
90	20	-	-	-	-	-
100	10	60	180	8381	-	-

4.3. Results and discussions

In the following, the effect of loading rates on the mechanical properties of PVC GMs will be examined. In the first subsection, mechanical insights into the effect of the loading rates on the stress-strain relationships will be discussed. Subsequently, in the second subsection, the long-term response at constant strain will be investigated through relaxation tests. This latter study aims to provide a more comprehensive understanding of the material's response, at different loading rates, contributing to an enhanced grasp of its rate-dependent behavior characteristics at long-term performance.

Additionally, time-dependency will be investigated through creep and strain recovery tests. The creep tests results aimed to assess the preloading effects on the long-term ultimate properties of the GMs, while strain recovery tests will analyze the material's ability to recover its deformation at different preloading history over extended periods. These tests are intended to provide a broader view into the time-dependent behavior of PVC GMs.

4.3.1. Rate-dependency effect at short term

The Figure 4.16 shows the force-engineering strain curves obtained from uniaxial tensile tests conducted at the specified aforementioned tensile rates. The recorded failure times span a range from approximately 20 seconds for the highest speed (500 mm/min) to nearly 11 days for the lowest speed (0.01 mm/min).

It is observed that for larger tensile rates the material strength increases. This observation highlights the significant effect of the tensile rate on the material's mechanical response, signaling inherent viscous properties (Meyers and Chawla 2008).

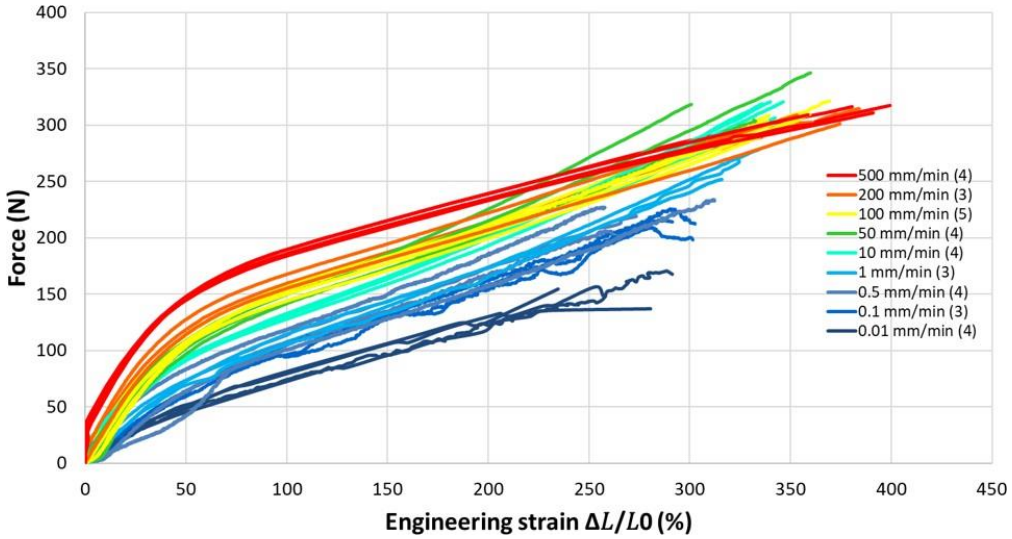


Figure 4.16: Force-engineering strain curves obtained from uniaxial tensile tests conducted at different tensile rates (mm/min). The values between brackets in the legend represent the number of repeatability tests conducted for each tensile speed. The standard laboratory test, as recommended by European standard EN12311, involves conducting a tensile test at a prescribed uniaxial displacement rate of 100 mm/min (corresponding to yellow curves).

The axial true stress-axial true strain curves for the tensile-speed-dependent tests are presented in Figure 4.17. It can be shown that the relationship changes with applied uniaxial tensile rate. Notably, the material becomes stiffer at higher tensile rates, while concurrently exhibiting a more malleable behavior at lower tensile rates. Further examination of this phenomenon is provided in the subsequent sections, which aim to properly analyze and elucidate the influence of applied speed on parameters such as tensile modulus and failure point (including stress and strain at failure).

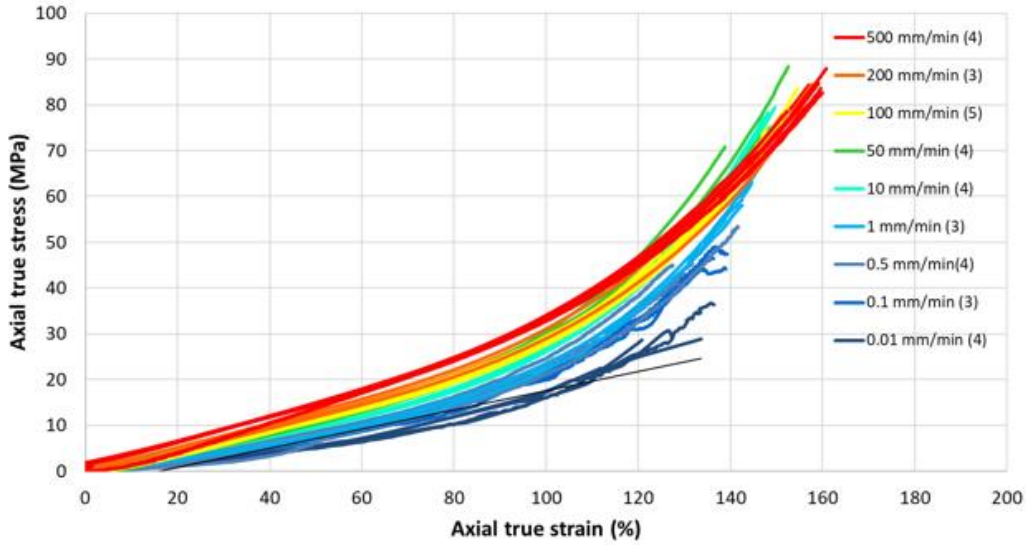


Figure 4.17: Stress-strain curves for strain-rate-dependency tests. The curves exhibit a distinctive shape compared to the force-deformation curve, which is due to the reduction in cross-sectional area. The number in parentheses mentioned in the legend indicates the repeatability test number at each tensile speed.

4.3.1.1. Rate-dependency effect on material's stiffness

In Section 4.2.1, the initial secant modulus E_{sec} is computed as an estimation of the tensile modulus. Figure 4.18 illustrates the variation in the initial secant modulus with tensile rates in logarithmic scale.

A clear dependence emerges, displaying how the material's stiffness evolves with increasing loading rates, with a coefficient of determination R^2 of 0.9442, reflecting a good agreement.

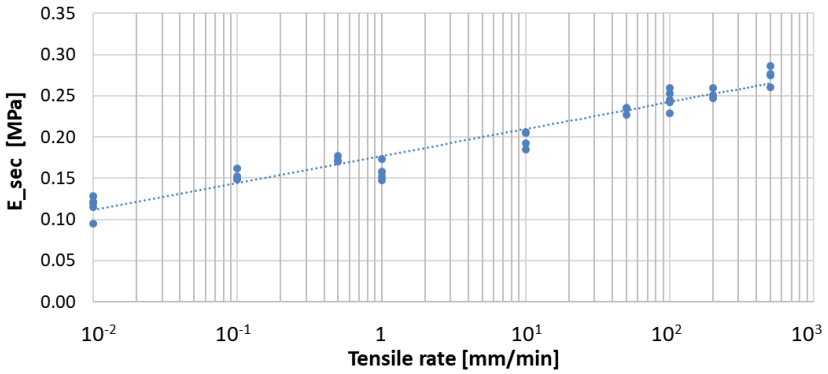


Figure 4.18: Variation of tensile modulus with tensile rate.

For further analysis, the tensile modulus (i.e., secant modulus) is represented against strain rate rather than tensile rate. The strain rate is determined by the ratio of the incremental length to the current length divided by incremental time, as expressed in Equation 4.10.

$$\dot{\varepsilon}_{(t)} = \frac{\delta L}{l\,\delta t} = \frac{\Delta L}{L\,\Delta t} \tag{4.10}$$

Figure 4.19 shows the variation in strain rate along tests. The strain rate is maximum at small deformation (i.e., at the beginning of the test). During this phase, minor fluctuations in the strain rate may occur due to initial slack or uneven tension distribution within the geomembrane, as the material adjusts to the applied load. As the test progresses, the geomembrane elongates, leading to an increase in the specimen length. This elongation results in a gradual decrease in the strain rate until failure occurs.

Figure 4.20 shows the strain rate values at the start of the test for each tensile rate. Hereinafter, the variation in tensile modulus with strain rate is presented in Figure 4.21, displaying a nearly linear upward trend (with the strain rate in log scale).

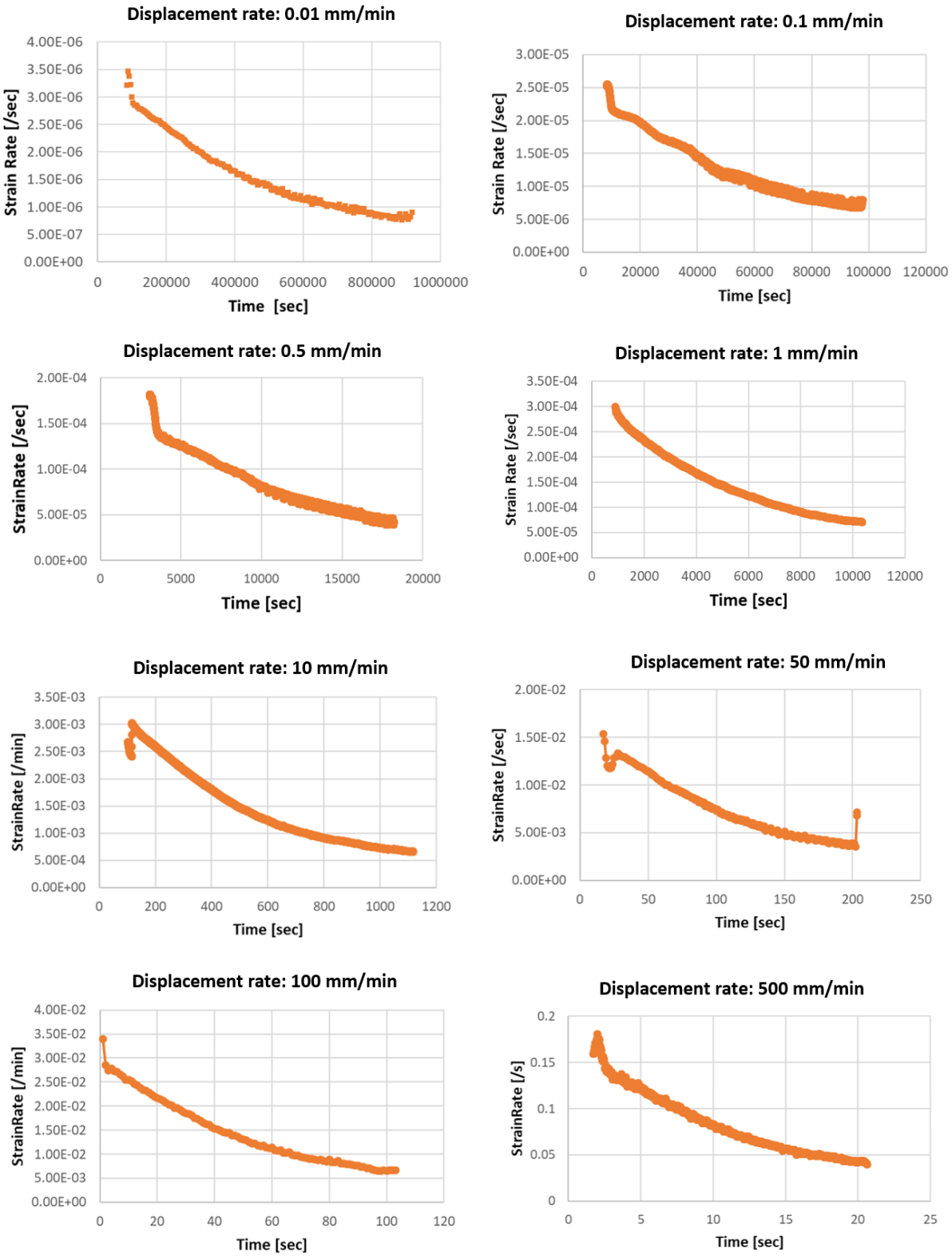


Figure 4.19: Variation of the strain rate over time during a uniaxial tensile test conducted at the various displacement rates from 0.01 to 500 mm/min.

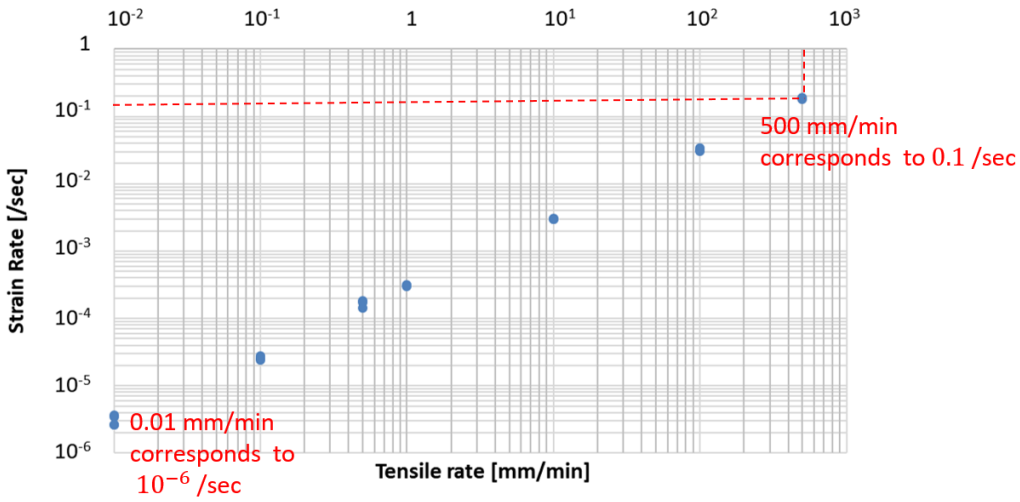


Figure 4.20: Strain rate at the beginning of the test for different tensile rates.

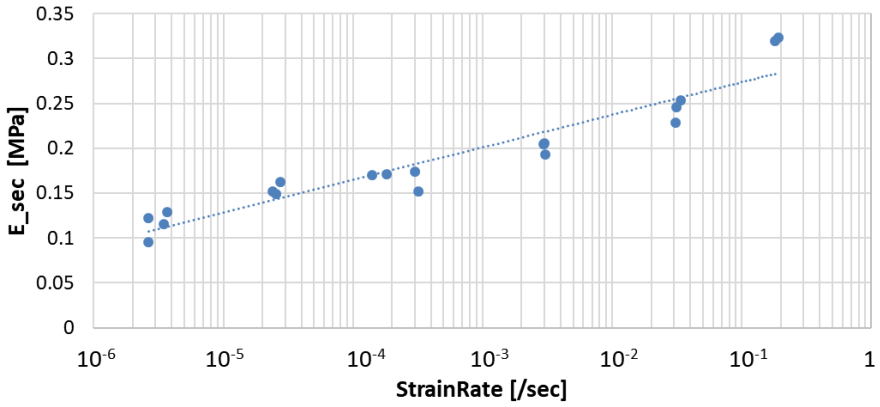


Figure 4.21: Variation in tensile modulus with strain rate.

4.3.1.2. Rate-dependency effect on the ultimate stress and strain

Examining the impact of rate dependency on the tensile strength and strain at failure is of paramount importance, as it is essential for accurately assessing the material's resistance and elongation before failure, thereby informing engineering design decisions for hydraulic projects.

Figure 4.22 shows the correlation between the tensile strength and strain at failure with the tensile rate. The corresponding strain rate for each speed at failure is presented in Figure 4.23 (determined from Figure 4.20). It is noticeable that the failure threshold in terms of stress and strain increases with strain rate, as seen in Figure 4.24. Figure 4.22(a) reveals that by increasing tensile rate from 0.01 to 500 mm/min, corresponding to strain rates of 10^{-7} to 10^{-2} /sec (refer to Figure 4.24 (a)), the tensile strength undergoes a considerable increase by approximately 214% (from 28 MPa to 88 MPa). Likewise, as observed in Figure 4.22 (b) and Figure 4.24 (b), the strain at failure experiences a higher value with a higher loading rate, reaching 161% of true strain at the highest loading rate (500 mm/min), whereas at low loading rate (0.01 mm/min) it reaches 120% of true strain. Thus, the mechanical resistance and elongation at failure of PVC GM are strongly

rate-dependent, emphasizing the importance of considering the loading rate influence in laboratory testing. Additionnaly, by considering the section's surface at the failure, it has been observed that at lower tensile speeds, it displays non-smooth features and exhibits tortuosity, contrasting sharply with the entirely smooth surface observed at failure in tests conducted at high tensile speeds. This observed non-smooth surface at lower tensile speeds highlights the generation of microcracks, that lead to a lower elongation level at failure.

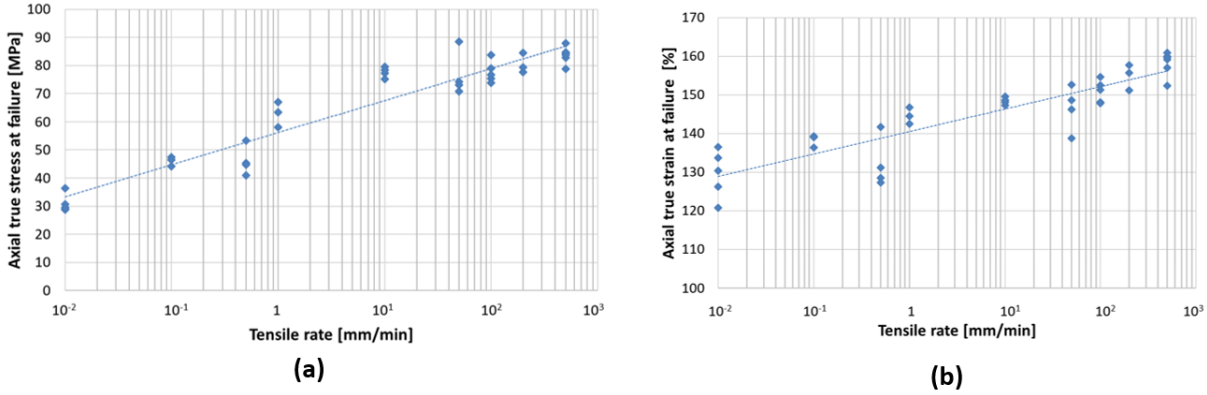


Figure 4.22: Variation of stress and strain at failure with tensile speed.

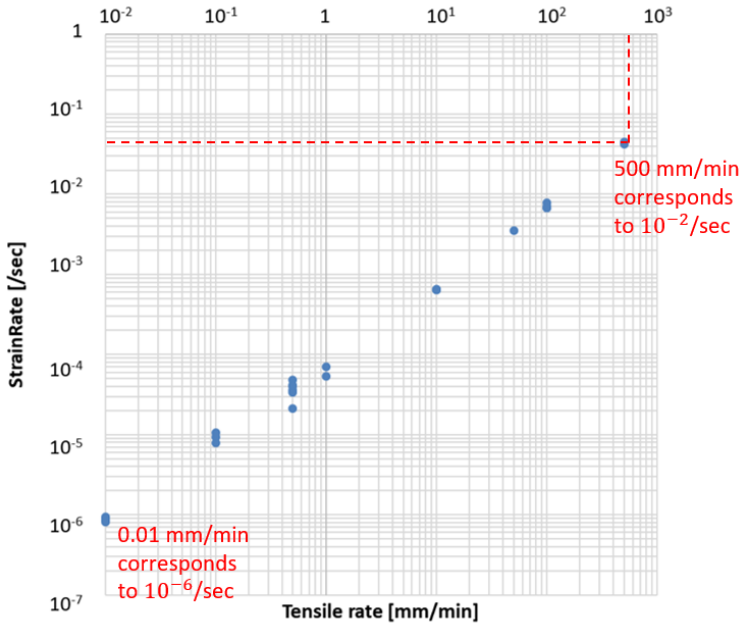


Figure 4.23: Strain rate at failure for each tensile speed.

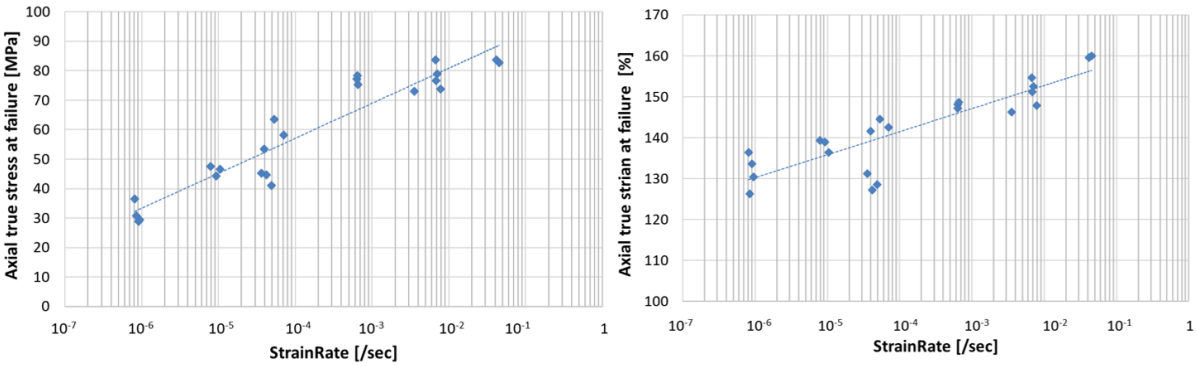


Figure 4.24: Variation of stress and strain at failure with strain rate

4.3.2. Rate-dependency effect on the long term

Figure 4.25 reports the stress-relaxation curves at different pre-relaxation tensile rates. The evolution in stress relaxation over time exhibits similar patterns across the specimens, characterized by initial quick drop followed by a progressive decrease until reaching steady regime. Depending on the tensile speeds, the curves start from different initial stress values. This initial value of stress increases with increasing loading rates, which aligns with the observation that increased loading rates lead to greater material strength, by reaching a higher value of traction forces compared to lower speeds.

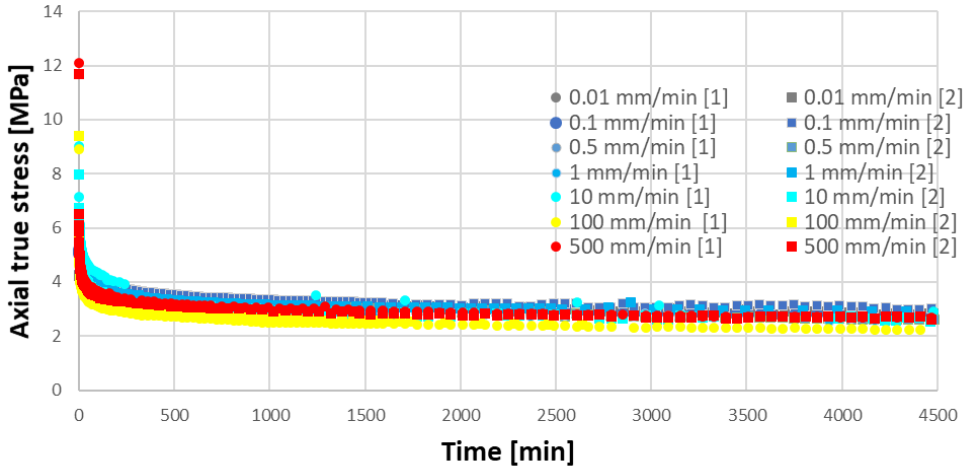


Figure 4.25: Stress relaxation curves at different tensile speeds.

4.3.2.1. Relaxation curves analysis

In order to offer a better representation of the phenomenon occurring at different time scales, Figure 4.26 shows the stress relaxation plotted against time on a logarithmic scale. Notably a consistent linear asymptotic tendency can be observed at the final stage of the relaxation behavior for different applied tensile rates, during the 4-day testing period.

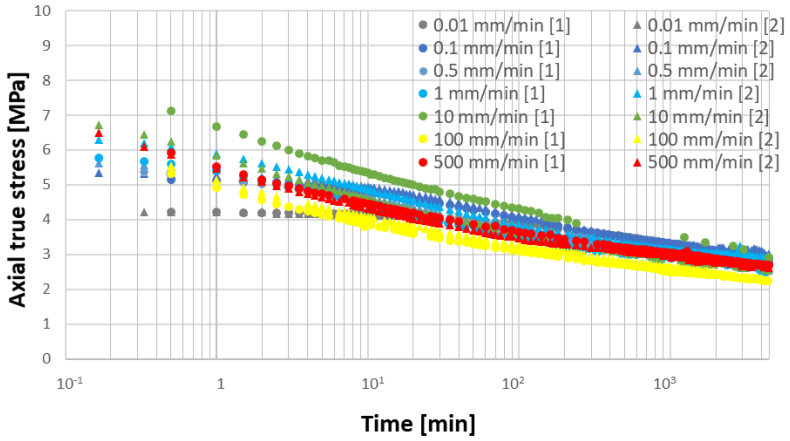


Figure 4.26: Stress relaxation curves at different tensile rates in logarithmic time scale.

Recently, the stress relaxation has been studied by Wu et al. (2023), showing a linear relationship between stress and time, both in logarithmic scale, for relaxation tests conducted at three specific tensile rates over only one order of magnitude: 2.5, 5, and 10 mm/min. Three initial strains were investigated: 40.55%, 58.79%, and 81.09%. To ensure a relevant comparison with the study of Wu et al. (2023), the results are presented in a logarithmic scale for stress and strain in Figure 4.27. The results indicate that the relationship between ln (σ) and ln (t) is not consistently linear. Particularly, as the tensile rate reduces, the curve tends to deviate, and a more horizontal trend emerges at the beginning stage of the relaxation curves for low tensile rates.

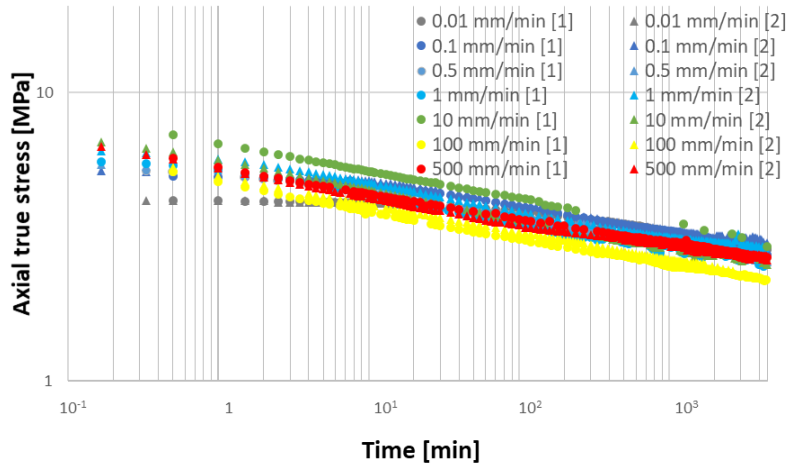


Figure 4.27: Stress relaxation curves presented in logarithmic scales for both axes at various tensile rates.

As noted by Wu et al. (2023), the initial strain significantly affects the relaxation stress. However, the specimens have not achieved the same strain level, as reported in Table 4.1. Thus, this may introduce some variability in the stress values at the onset of the relaxation. Therefore, these relaxation curves require normalization to get rid of the impact of the deformation level at the beginning of the relaxation phase.

In that way, this step ensures that the variations in the initial deformation do not affect the interpretation of stress-relaxation behavior.

In this normalization method, the asymptotic line for each test is determined. This line represents the long-term behavior of the stress-relaxation, typically modeled as:

$$\boldsymbol{\sigma = \sigma_{asymptote} + b \ln\left(\frac{t}{t_0}\right)} \qquad \textbf{(4.11)}$$

where $\sigma_{asymptote}$ is the asymptotic stress at $t_0 = 1$min, b is the slope of the asymptotic line, and t is the elapsed time in minutes.

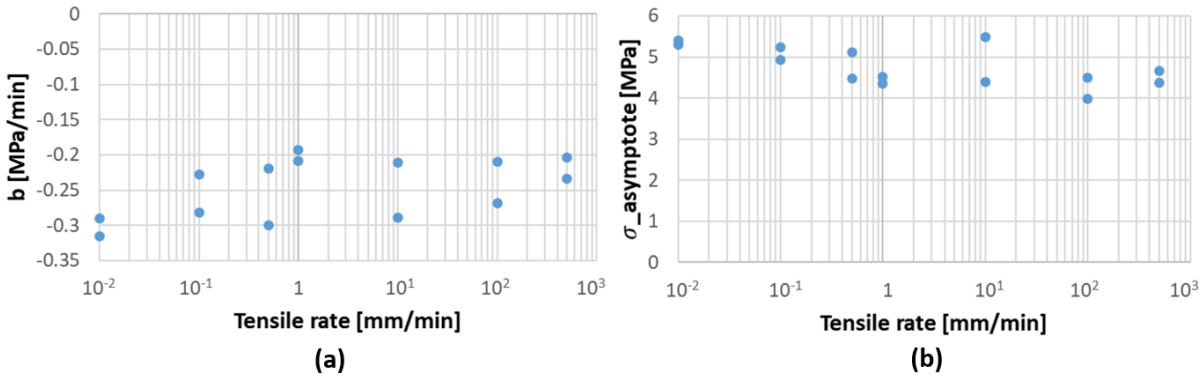


Figure 4.28: Variations of: (a) the slope b of the asymptotic line for each test, (b) $\sigma_{asymptote}$.

As seen in Figure 4.28, both the asymptotic stress and the slope of the asymptotic line are affected. This is due not only to the initial strain level but also to several additional factors such as material heterogeneity and experimental errors. The normalization step consists in reducing the effects of the initial strain as much as possible while neglecting other factors. This allows for a more direct comparison of the initial and intermediate stress relaxation stages across tests performed at different tensile rates, in order to assess their impacts on the relaxation behavior. The method consists in subtracting the asymptotic stress ($\sigma_{asymptote}$) from the observed stress values for each test, as follows:

$$\boldsymbol{\sigma_{(t)}^{corrected} = \sigma_{(t)} - \sigma_{asymptote}} \qquad \textbf{(4.12)}$$

As observed in the normalized relaxation curves in Figure 4.29, there are two distinct relaxation time characteristics. The first one is highly dependent on the applied tensile loading rate prior to relaxation, while the second one, marked by a consistent linear tendency in the final stage of the four-day relaxation test, seems not to depend on the applied tensile loading rate. This suggests that, after a certain time – approximately 240 minutes based on graphical analysis – the material exhibits the same behavior across all specimens, indicating the occurrence of a common material phenomenon. It is worth to mention that this time may vary according to environmental conditions, such as temperature and (to a smaller extent) humidity.

Accordingly, these results indicate that the loading speed no longer significantly affects long-term material behavior under constant strain, after approximately 4

hours. This suggests that the tensile speed testing may not affect the results for extended testing periods (e.g., such as in a creep test).

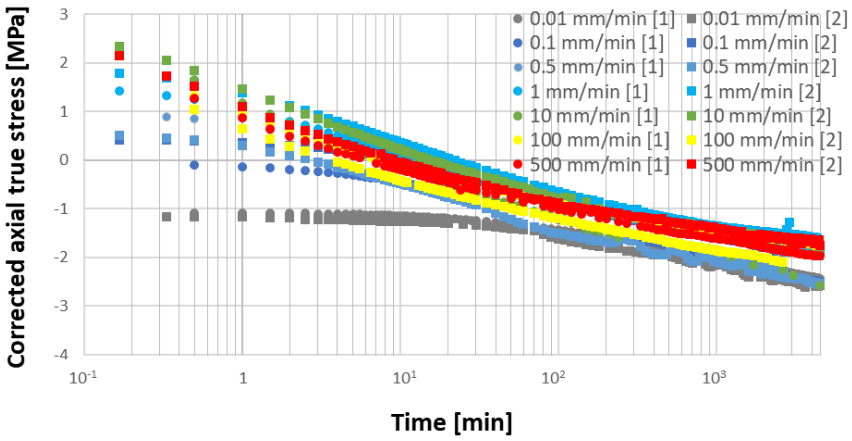


Figure 4.29: Corrected stress relaxation over time.

4.3.2.2. Rheological analysis

These results can be analyzed through constitutive models. For this purpose, Burger's model has been employed. This model consists of one-kelvin sub-model with a spring and dashpots in series, as illustrated in Figure 4.30. Two dashpot dampers have been considered in order to account for the double-time characteristics.

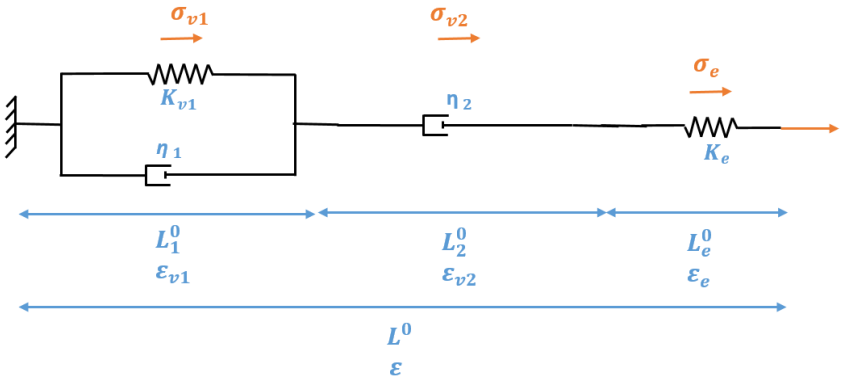


Figure 4.30: Extended, five-parameter Burger's rheological model.

The generalized constitutive equation is determined as follows:

$$\sigma + \left[\frac{\eta_1}{K_{v1}} + \frac{\eta_2}{K_{v1}} + \frac{\eta_2}{K_e}\right]\dot{\sigma} + \frac{\eta_1\eta_2}{K_e\,K_{v1}}\,\ddot{\sigma} = \eta_2\dot{\varepsilon} + \left(\frac{\eta_1\,\eta_2}{K_{v1}}\right)\ddot{\varepsilon} \tag{4.13}$$

In relaxation regime, where ε is constant, $\dot{\varepsilon}$ and $\ddot{\varepsilon}$ are both zero. Consequently, the equation describingrelaxation simplifies as:

$$\sigma_t = A\,e^{-\frac{1}{\tau_1}t} + B\,e^{-\frac{1}{\tau_2}t} \tag{4.14}$$

with:

$$\tau_1 = \frac{2\eta_1\eta_2}{\eta_1 K_e + \eta_2(K_{v1} + K_e) + \sqrt{[\eta_1 K_e - \eta_2(K_{v1} + K_e)]^2 + 4\eta_1\eta_2 K_e^2}}$$

$$\tau_2 = \frac{2\eta_1\eta_2}{\eta_1 K_e + \eta_2(K_{v1} + K_e) - \sqrt{[\eta_1 K_e - \eta_2(K_{v1} + K_e)]^2 + 4\eta_1\eta_2 K_e^2}}$$

where A and B are constants that depend on the applied tensile rate prior to relaxation, t is the time.

The results indicate a strong correlation with the 0.01 mm/min test speed, evidenced by an R^2 value of 0.98 (Table 4.3). The two characteristics times τ_1 and τ_2 are respectively 209.86 min ≃ 3.5 h and 23691 min ≃ 16.45 days, where τ_1 is close to the threshold time 240 min that separate visually the two regimes in the relaxation curve. Nevertheless, as the speed increases, Burger's model becomes less accurate to depict the entire relaxation behavior (Figure 4.31).

Therefore, it can be concluded that the double-time characteristic model works well at low speed, confirming the presence of two distinct characteristic times. However, the model endowed with constant parameters lacks of precision at high loading rate. In particular, it does not capture the linear decrease of σ with respect to log (t) over the final stage of the four-day relaxation test.

Table 4.3: Model parameters determined from test data fitting.

Tensile loading rate [mm/min]	A	B	R^2
0.01	0.6696	3.507	0.9078
0.01	0.8305	3.348	0.9889
0.1	1.346	3.477	0.9092
0.1	1.499	3.475	0.9663
1	1.779	3.258	0.8707
10	1.863	3.008	0.8135

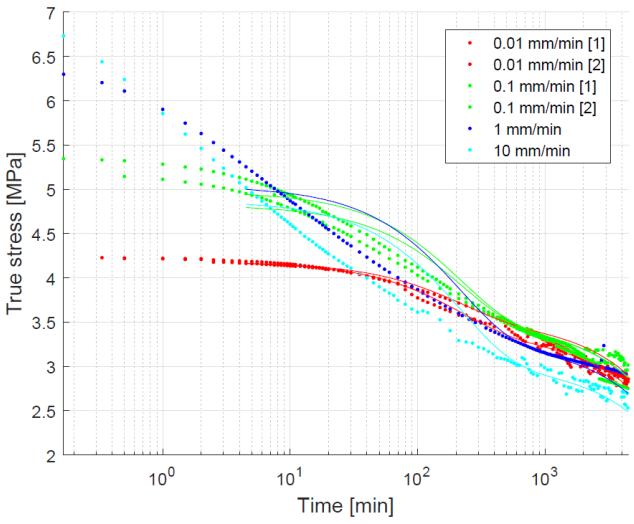


Figure 4.31: Fitting results of the relaxation curves at 0.01, 0.1, 1 and 10 mm/min.

4.3.3. Time-dependency response

The primary goal of these tests is to understand how time-dependent factors, such as the duration of loading, and preloading condition influence the material's strength and elongation at failure, as well as the material's ability to recover its original shape, notably how residual strain develops due to the hysteresis effect.

4.3.3.1. Creep behavior analysis

The creep (engineering) strain curves for testing the GM under various uniaxial tensile constant applied loads varied between 100 and 250 N and are displayed in Figure 4.32.

Graphically, these curves are typically characterized by an immediate increase in stress, which is then followed by a progressive decrease until a quasi-stable regime is reached, at which point, under large loads, the specimen splits (i.e., rupture of the specimen). Higher loads (200 N and higher) cause creep strain to grow quickly and quasi-stabilize more quickly, before failure occurs. The creep strain increases more gradually at intermediate loads (130 to 150 N), and it takes much longer (hours to days) for the strain to quasi-stabilize, followed by specimen's rupture. Lower loads (between 100 and 120 N) show a gradual increase in creep strain, taking days to months to reach a quasi-stable state.

Figure 4.33 illustrates the creep time required for PVC specimens to reach failure under various constant loads. The creep time to rupture increases as the load decreases, consistent with the correlation already observed for tensile tests between the applied load and the rate at which the material approaches failure. It should also be notices that the time to failure may vary for the same loading weight. This could be explained by the material's heterogeneity that may influence the material behavior.

Figure 4.34 shows the creep strain reached at failure at different loading weights. This graph illustrates a linear tendency between the applied force and the creep strain at failure. Therefore, the load at which the specimen splits (i.e., rupture of specimen) can be correlated with the strain observed at failure.

Consequently, based on the results illustrated in Figure 4.33 and Figure 4.34, the GM exhibits notable creep behavior under different tensile loads, with greater loads leading to larger and faster strains.

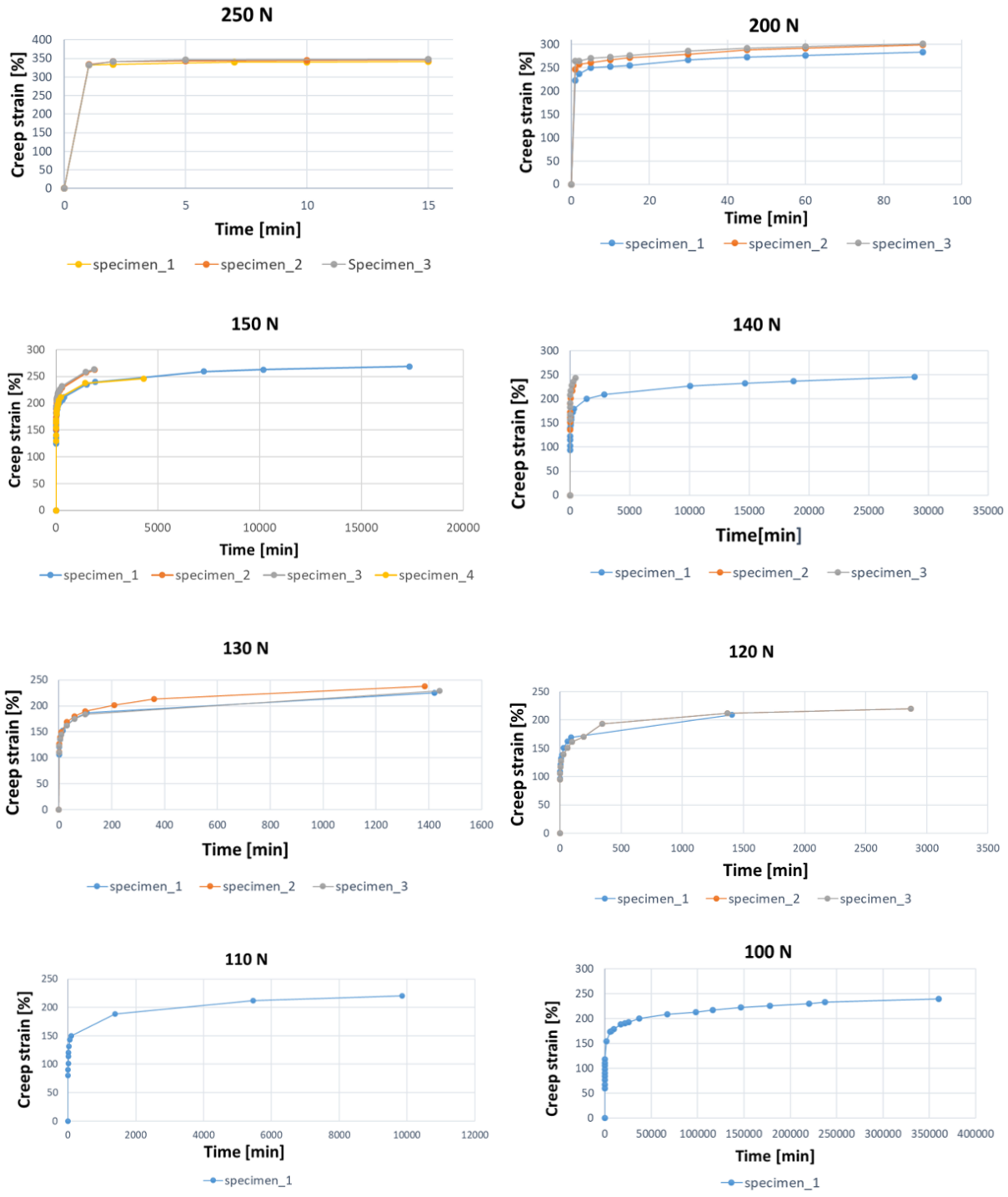


Figure 4.32: Creep (engineering) Strain Curves at Constant Stresses of 250, 200, 150, 140, 130, 120, 110, and 100 N.

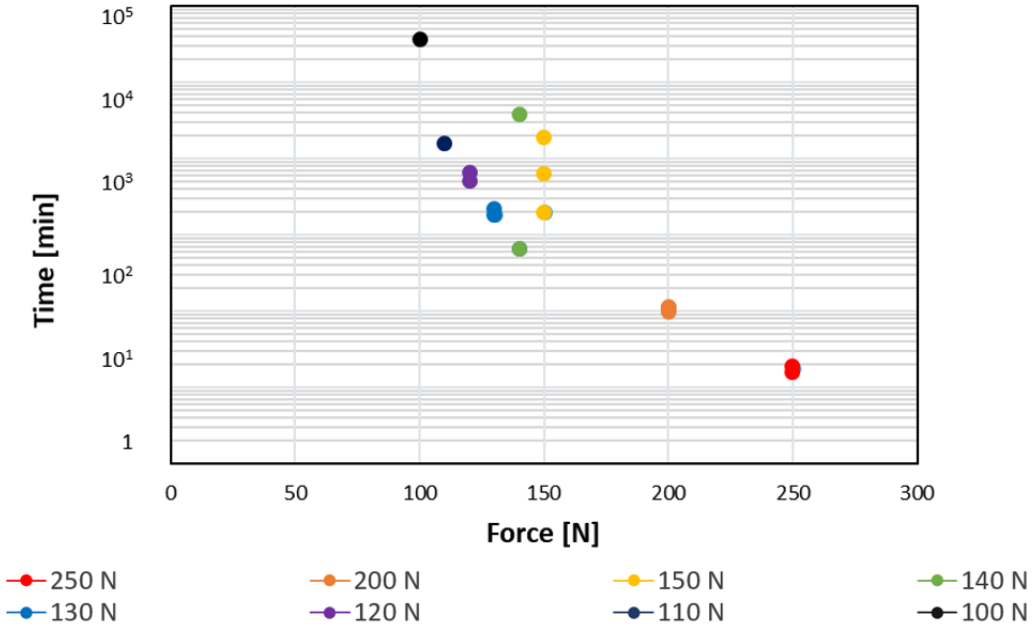


Figure 4.33: Creep failure time at different applied constant stresses.

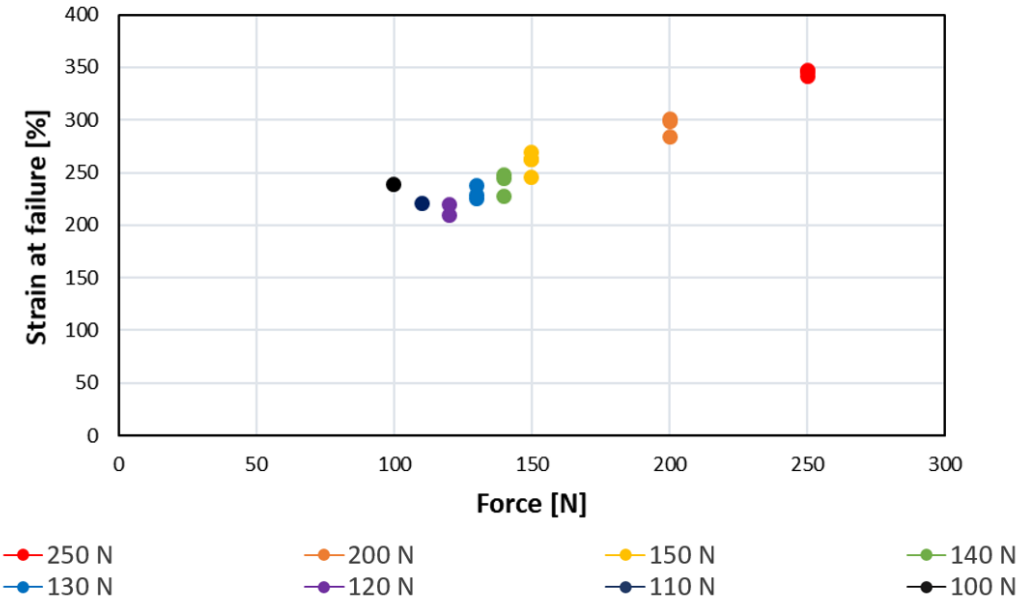


Figure 4.34: Engineering strain at failure at different applied constant stresses. Noting that no failure is observed at 100 N (at 124 days of creep).

A representation in logarithmic scale provides a better visualization of the creep behavior. As can be observed in Figure 4.35, consistent linear creep strain is typically displayed in log time scale. Additionally, it reveals that, even at a slower applied load (100N), the material continues to deform at a slower rate without entirely reaching a plateau.

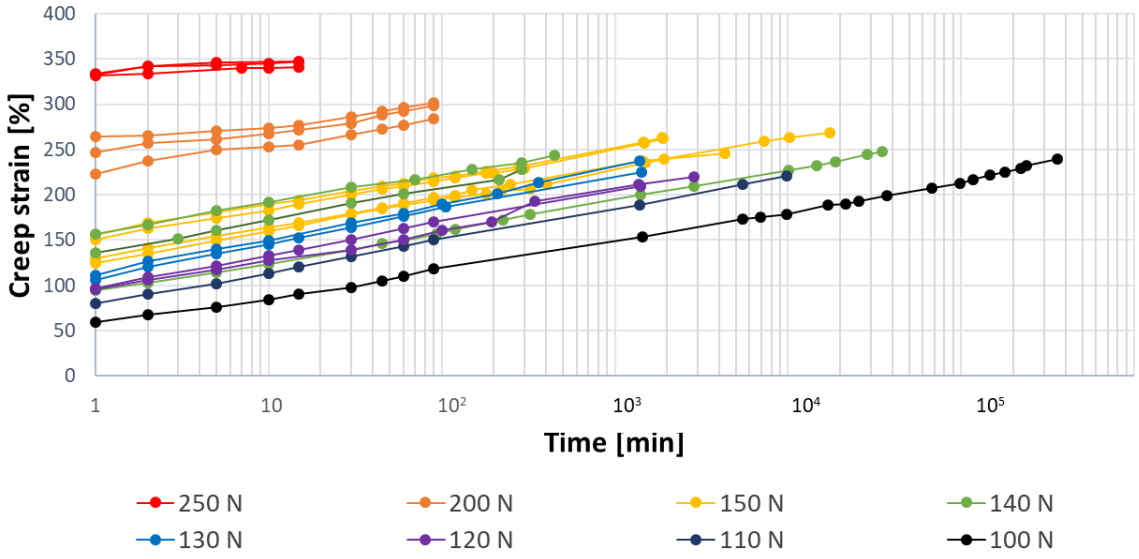


Figure 4.35: Creep (engineering) strain curves at different applied constant stresses in logarithmic time scale.

For additional inspection in evaluating the creep behavior, the (Sherby and Dorn 1958) plot is a useful way to identify the different creep stages. This plot presents the creep strain rate against the creep strain on a logarithmic scale, providing a clear visualization of how the creep rate evolves with increasing strain. According to (Koerner et al. 2014; Wang et al. 2024; Yeo and Hsuan 2010), geosynthetics creep behavior can be divided into four stages.

The initial phase, namely instantaneous strain stage, occurs immediately upon the application of the load. This is followed by primary creep strain stage, which is characterized by a decreasing creep strain rate with increasing creep strain. Subsequently, the secondary creep stage is marked by a constant/steady creep rate. Finally, in the tertiary creep stage, there is a rapid increase in creep strain, leading to material failure.

By analyzing Figure 4.36, it can be observed that at high loading weights (250-200N), a rapid decrease in creep strain rate is observed, followed by a failure. The process took approximately 14 min, indicating an instantaneous deformation that led directly to failure, without significant creep behavior.

As the load decreases (150N and below), the primary stage becomes more pronounced, highlighted by a larger period of gradual decrease in the strain rate. Interestingly, the steady-state stage (i.e., secondary creep stage) and the tertiary creep stage could not be detected. These stages may not be present at lower loads, suggesting that the material's behavior under such conditions exhibit only primary creep stage.

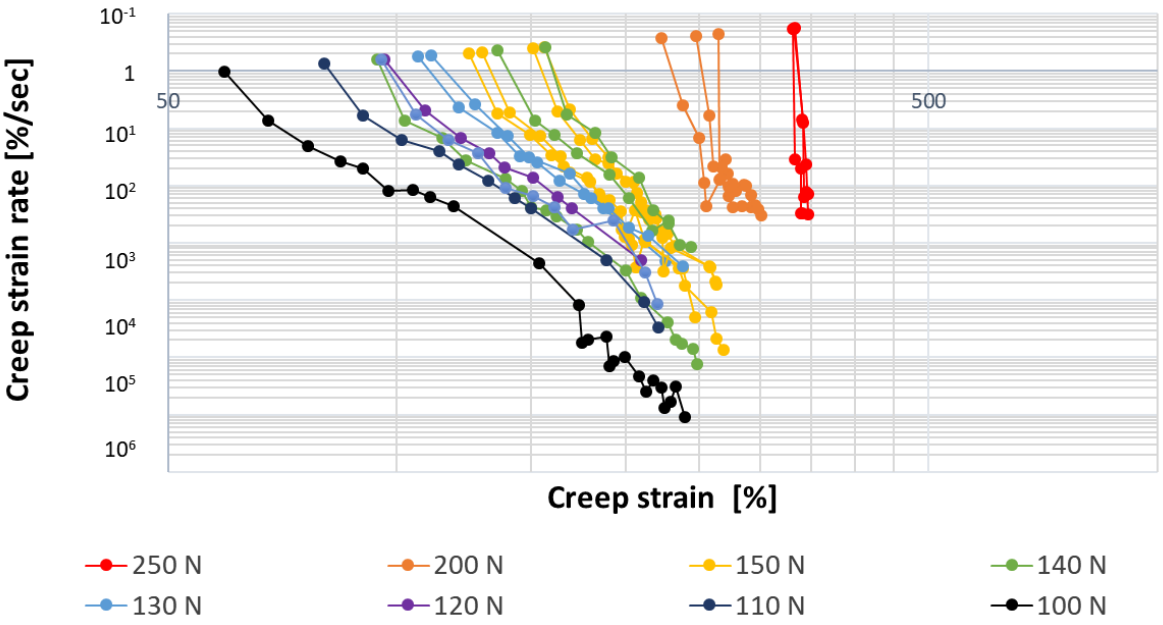


Figure 4.36: creep strain rate vs creep (engineering) strain.

These results can be analyzed through constitutive models. The four-element Burger's model, which was previously discussed and illustrated in Figure 4.30, has been employed.

Accordingly, the derived equation, describing the creep behavior under a constant Force F, is presented in Equation 4.15.

$$\varepsilon = \frac{F}{K_e} + \frac{F}{K_{v1}}\left(1 - e^{-\frac{1}{\tau}t}\right) + \frac{F}{\eta_2}t \tag{4.15}$$

Where ε is the creep strain; F is the applied constant force; K_e, K_{v1} are the elastic parameters of the model; η_1, η_2 are the viscosity parameters of the model, and τ is the characteristic time defined by η_1/K_{v1}.

The first term is related to the instantaneous elongation at time t=zero, with K_e is the linear elastic modulus. As time progresses, the creep strain increases, and for $t \to \infty$, the creep rate approaches F/η_2.

Figure 4.37 shows the fitting of creep curves under different load levels using the four-element model, with the material parameters provided in Table 4.4.

The curves highlight a good correlation with experimental creep data when the load ranges between 100 N and 150 N, where the elastic modulus K_{v1} increases with the applied load. By contrast, the viscosity coefficients η_1 and η_2 exhibit a decreasing trend with increasing loads (with some irregularities owing to material heterogeneity), indicating shorter time to failure.

However, beyond 150 N, the model fails to accurately capture the creep behavior, as the values of the viscosity coefficient η_2 are negative, which are not physically meaningful

for a viscosity coefficient. This can be explained by the fact that at higher load the behavior is limited to accelerated instantaneous deformation without any significant creep.

Consequently, the four-element model provides a reasonable approximation of the primary creep stage at intermediate loading weights [100,150] N.

Table 4.4: Creep parameters under loads in the range [100,250] N.

Loads [N]	K_{v1} [N]	η_1 [N.s]	K_e [N]	η_2 [N.s]
100	0.82178	70.255	1.8392	3.02E+05
110	1.1705	1.3597		1.38E+04
120	1.2725	7.724		4.78E+03
130	1.38644	4.75593		2.98E+03
140	1.4633927	1.3393		1.18E+03
150	1.372	4.849516		9.96E+03
200	1.1452	0.57089		-2.6E+09
250	1.199	0.40279		-2.94E+07

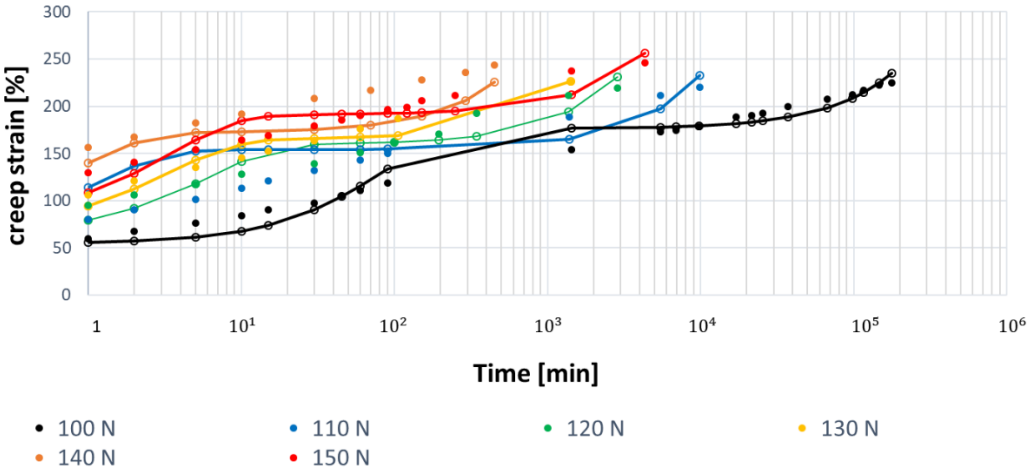


Figure 4.37: Fitting results of the creep curves at different loading rates, ranging from 100 to 150 N.

4.3.3.2. Strain recovery analysis

In many applications, geomembrane may be subjected to cyclic loading and unloading. Understanding the strain recovery behavior helps predicting how a material will perform over time under in situ conditions. This test aims to study the strain recovery properties of the material, as it is important in determining how the material will perform over time under in situ conditions, when subjected to cyclic loading and unloading.

(a) Strain recovery after short-term loading test

The main objective of this section is to evaluate the reversibility of the material's deformation after applying and subsequently removing uniaxial tensile loads, specifically to determine the strain level at which the material becomes non-recoverable. To achieve this, nineteen specimens were subjected to tensile tests at a constant displacement rate, each test being stopped at different strain levels ranging between 30 to 300 % engineering

strain, as mentioned in Section 4.2.4. Due to time limitations, this test was conducted only at the standard constant displacement rate of 100 mm/min.

Figure 4.38 presents the force-engineering strain curves for these tests. After unloading, the uniaxial engineering strain was assessed over 18-day period, with the results illustrated in Figure 4.39. The material demonstrates a rapid decrease in strain immediately after unloading, indicating immediate recovery stage. Following this, there is a gradual decrease in strain over time.

Residual engineering strain was calculated after 18 days for each specimen. A manual measurement error averaging 2% has been taken into account. Results, shown in Figure 4.40, indicate that the deformation of the material is fully recoverable below a uniaxial engineering initial strain of 80% (corresponding to a loading level of 150N). Beyond this threshold, the material experiences a residual strain, which becomes higher with greater initial strain level.

However, based on these results, it remains challenging to conclusively determine non-reversibility above 80% strain, as the material has not achieved a steady strain within 18 days, continuing to exhibit a slow strain decrease (see Figure 4.41). Extended time measurement (more than 18 days) is required to accurately define the maximum strain at which the material exhibits a purely visco-elastic behavior. Additionally, this test is conducted at a displacement rate of 100 mm/min. Further investigation into the effect of rate dependency on the material's recoverability is needed.

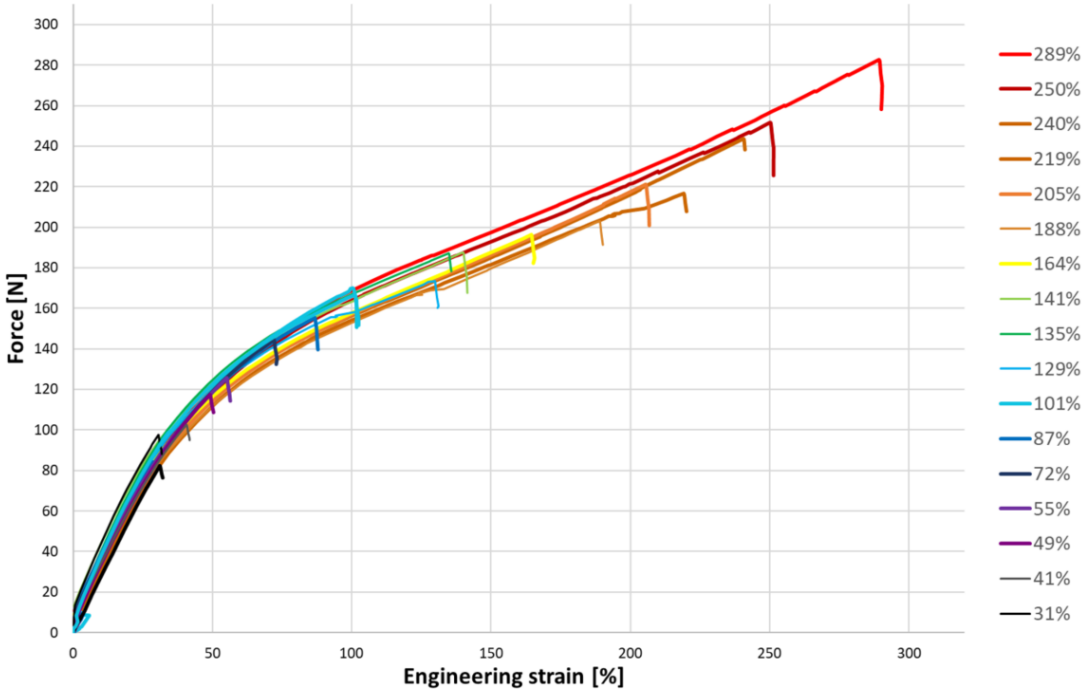


Figure 4.38: Force-engineering strain curves of conducted tensile tests at a constant displacement rate of 100 mm/min, stopped at different strain level.

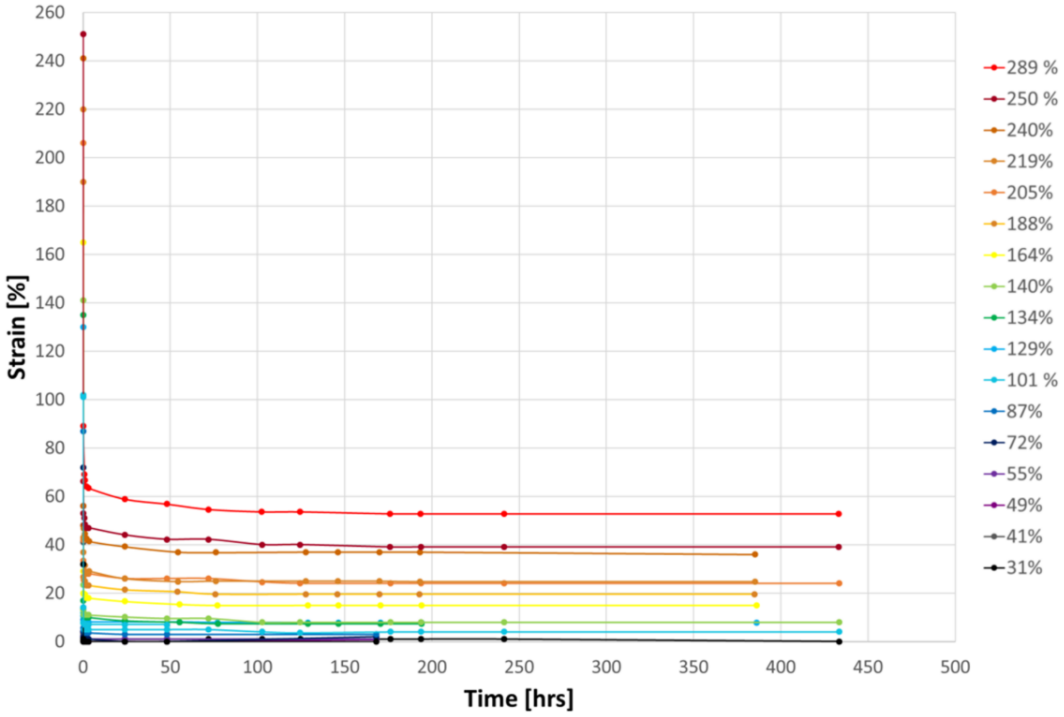


Figure 4.39: Engineering strain recovery curves following tensile testing stopped at various deformation levels. These tests are conducted at a displacement rate of 100 mm/min.

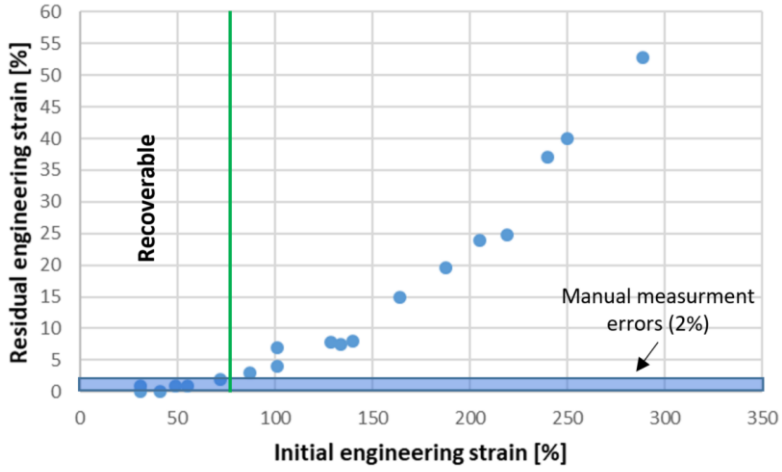


Figure 4.40: Residual engineering strain after 18 days recovery for different initial strain values.

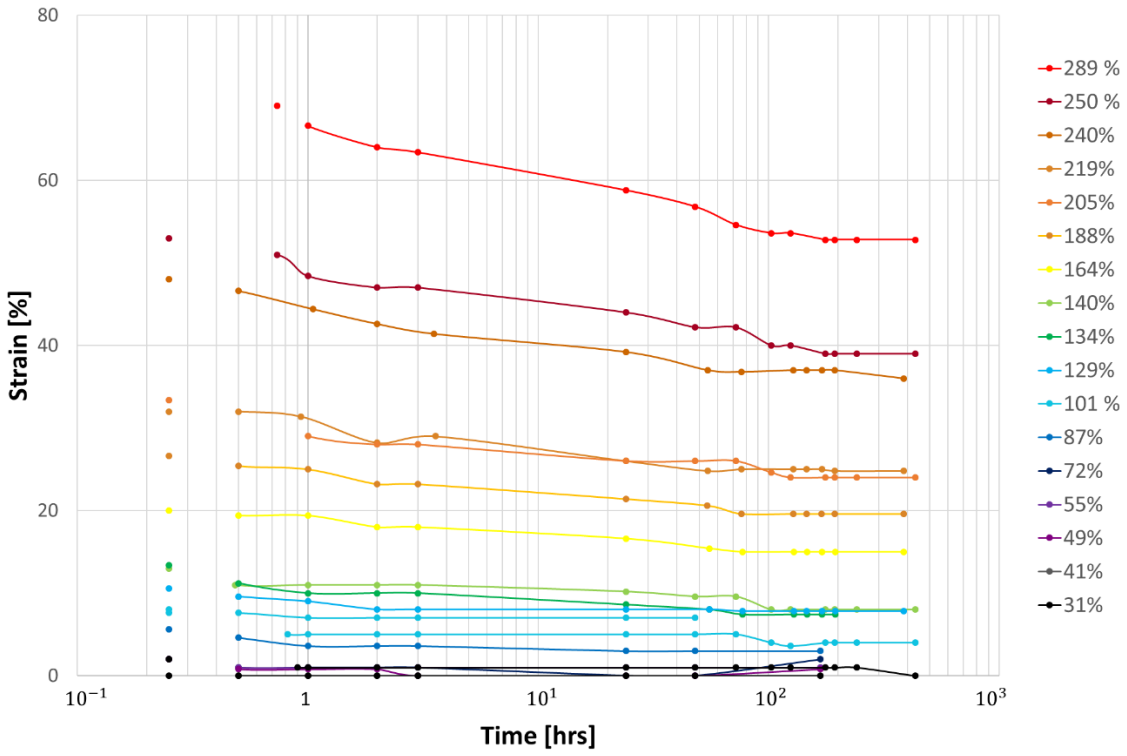


Figure 4.41: Engineering strain recovery curves following tensile testing stopped at various deformation levels, represented in logarithmic time scale.

(b) Strain recovery after long-term loading test

In this section, the strain recovery of PVC geomembranes is evaluated after extended loading under either creep or relaxation conditions. The results aim to provide a better understanding of the material's behavior and its capacity to recover strain after prolonged exposure to stress/strain. By conducting extended loading tests over distinct periods, this study seeks to investigate the time-dependent effects on strain recovery.

To assess the effect of time on strain recovery, two uniaxial tensile load tests were conducted at a displacement rate of 0.01 mm/min, each reaching the same level of strain. In the first test, the strain recovery was measured immediately after the load was removed. In the second test, the specimen was maintained under constant strain for 10 days to allow stress relaxation to occur before measuring strain recovery. Figure 4.42 provides a comparison of these two tests.

The test without the relaxation stage shows a quicker initial recovery, with the strain dropping to quasi-zero residual strain within the first 10 days, with 2 % manual measurements errors. In contract, the test with the relaxation stage exhibits a more gradual initial recovery. However, the strain continues to decrease slowly over the entire period, indicating a prolonged strain recovery process. The residual engineering strain after 49 days is 10 %.

Therefore, this comparison highlights that subjecting the GM to constant strain under real in-situ conditions affects the strain recovery behavior. Thus, a relaxation stage enables stress relaxation but does not enhance the overall recoverability of the material.

Instead, it results in a higher residual strain over time compared to the test without the relaxation stage. These results highlights the time-dependent effects on the strain recovery response of PVC GMs.

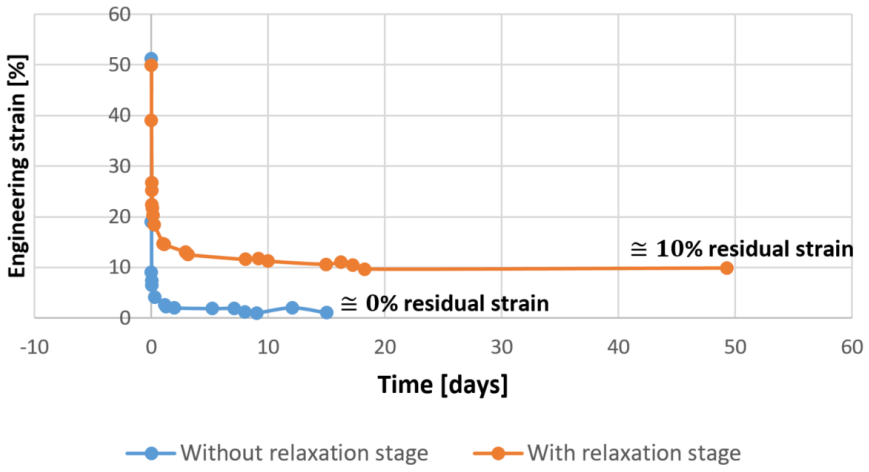


Figure 4.42: Strain recovery for two tests: With and Without Relaxation Stage.

Now, the focus is shifted to creep tests. Here, strain recovery is assessed after subjecting the material to various constant loading weights over distinct time intervals, as presented in Table 4.2.

Figure 4.43 shows the correlation between the effect of creep load time exposure and the creep loads on the strain recovery of the GM specimens. The results highlight the significant time-dependent effect on strain recovery. For instance, at 60 N, prolonged exposure generates residual strain, while exposures below 5 hours allow the material to fully recover to its original dimensions. Additionally, even at low creep loads, specimens exposed to loads for more than 2400 hours (100 days) exhibit residual strain.

The critical loading time threshold for observing residual strain decreases as the applied force increases. Higher forces reduce the time required for the material to exhibit residual strain.

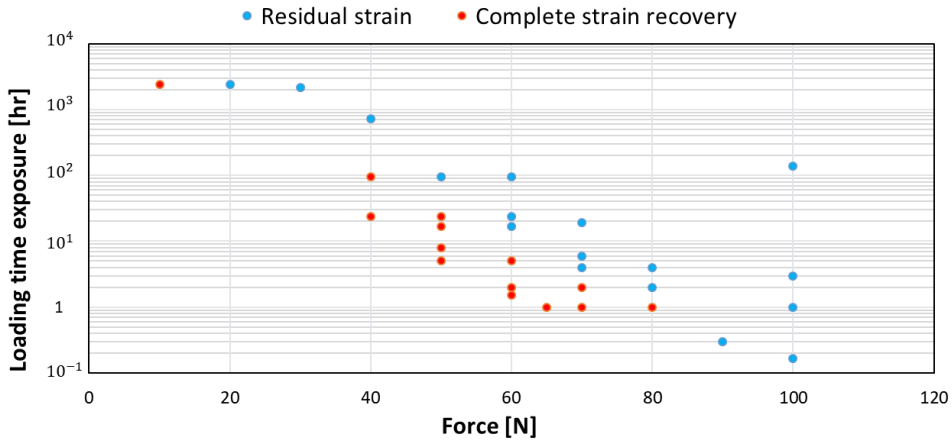


Figure 4.43: Impact of creep load and loading duration on strain recovery in PVC GMs. Specimens exhibit a residual strain is highlighted in blue, and specimens experience a complete strain recovery are marked in orange.

Moreover, it can be noted that for the same duration of loading exposure, the residual strain increases with the creep load. For instance, comparing two loads, 40 N and 50 N, applied for 96 hours under creep, the residual strain measured after 10 days of recovery is significantly higher for the 50 N load (6.42%) compared to the 40 N load (1.15%). Similarly, comparing 80 N and 70 N loads applied for 1 hour, the residual strain measured after a 120-hour recovery period is 1.34% for the 80 N load, while it is fully reversible (0%) for the 70 N load.

This indicates that higher applied constant loads (i.e., creep loads) induce more significant deformation within the material's structure, resulting in greater residual strain measured within the same recovery time once the load is removed.

Thus, the material's behavior under different creep loads and exposure times presents a dilemma, as it leads to varied recovery processes characterized by distinct recovery rates and residual strains.

For the time being, we cannot confirm whether complete recovery is achievable after an extensive recovery period for high loads. In other words, it is unclear whether the observed residual strain will eventually be fully recovered over time or if it represents a permanent (i.e., plastic) deformation.

4.3.4. Failure threshold

Based on these complementary results, a question about the intrinsic failure properties of the material—whether the failure criterion is primarily strain-based, stress-based, or a combination of both —is raised.

In order to address this inquiry, looking at Figure 4.32, it could be observed that when a creep load of 250 N is applied, the material fails at a strain of approximately 350%. The equivalent strain rate, calculated by dividing the strain at failure by the time to failure, was found to be around 5 mm/min. Comparing this with the force-engineering strain curves in Figure 4.16, we see that at a tensile speed of 1 mm/min, which is in the same

order of magnitude as the equivalent creep strain rate (5 mm/min), the stress and strain at failure were 250-270 N and within the range of 300% to 350%, respectively.

Similarly, when a constant creep stress of 200 N was applied, the material rupture occurs at a strain between 280% and 300%, with an equivalent creep strain rate of about 0.8 mm/min. This is comparable to the results of a uniaxial tensile test conducted at 0.1 mm/min, where the stress and strain at failure were nearly identical.

In summary, Figure 4.44 shows the force and engineering strain at failure corresponding to each tensile rate from tensile tests (conducted at constant tensile rate) and creep tests. The results demonstrate a good match between tests, suggesting that the material's creep performance (i.e., strength and strain) may be predictable based on its short-term response via tensile tests at constant loading rate, provided the environmental conditions remain constant (i.e., constant temperature, not exposed to UV radiation and humidity).

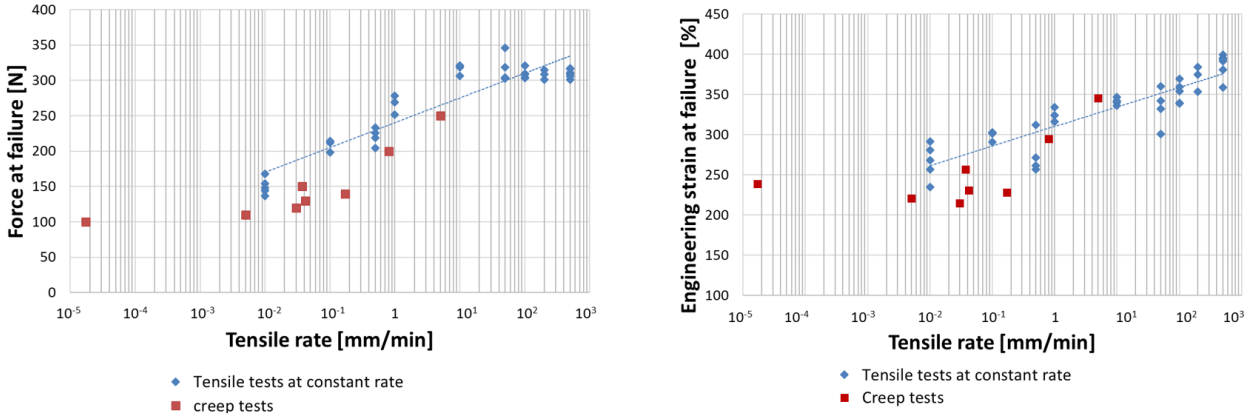


Figure 4.44: Force and engineering strain at failure for each tensile rate in long- and short-term testing.

The fact that failure occurs at consistent stress and strain values across different testing methods (creep vs. uniaxial tensile) implies that the material does not fail solely due to exceeding a particular stress (a purely stress-based criterion) or reaching a specific strain (a purely strain-based criterion). Instead, both the strength and the strain at failure decrease when decreasing the loading rate. This indicates viscous effects still persist at very slow loading rates which makes the failure criteria difficult to defined as it is not possible to isolate the elasto-plastic behavior of the material.

Driven by a quest of knowledge, a relaxation behavior was assessed at high initial engineering strain of 270 %. The test was conducted at high pre-relaxation speed of 200 mm/min to achieve high initial strain, then; the material is held at a constant high strain of 270% (close to strain failure determined at 200 mm/min (Figure 4.16)). Figure 4.45 shows the stress relaxation over time. The stress decreases over time to a residual stress of 60 N without causing failure within a measuring period of 21 days. This indicates that while strain is a key factor, the material can withstand high strain levels as long as the stress decreases.

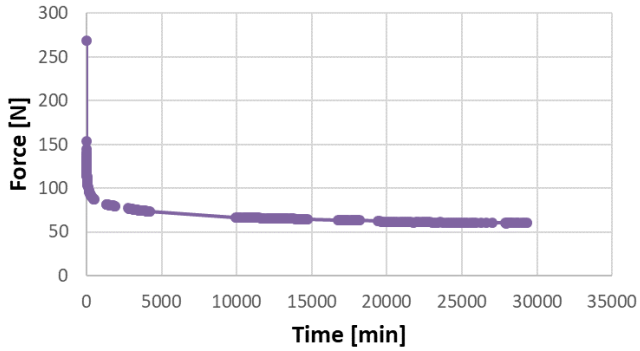


Figure 4.45: Stress relaxation curve for a specimen stretched to 270 % engineering strain at a displacement rate of 200 mm/min.

4.4. Conclusions

This research is dedicated to understand the PVC GM's response to unexpected tensile forces that may rise under various scenarii, posing challenges for engineers when designing waterproofing systems. The experimental work focused on the effect of the loading rate on the material's mechanical properties at short- and long-term tests that depict potential in situ conditions.

The results from this chapter supported the construction of the microstructural model of PVC GM presented in Chapter 3.

The study demonstrates that the material under study exhibits a rate-dependent behavior, with larger loading rates leading to an increase in rigidity modulus. In addition, as the loading rate decreases, the mechanical properties at failure (i.e., strength and elongation at failure) are reduced.

Results from relaxation tests have proven that the past loading rate no longer significantly affects measurements after few hours (approximately 4 hours). This suggests that for extended testing periods, such as in a creep test, the tensile loading speed preceding the creep test will not affect the results at long term.

Results from strain recovery tests aim to measure the immediate elastic recovery and the subsequent time-dependent recovery. They highlight the impact of preloading history, particularly loading exposure time (time-dependency), and weight. Higher loads and longer exposure times result in greater residual strain. It worth noting that these measurements were taken over a relatively extended period. However, at this stage, we cannot conclusively determine whether the residual strain is permanent or if it will dissipate gradually over several months or years.

Results from creep tests at high loads reveal that higher loads lead to greater and more rapid strain at failure. This suggests a strong correlation between the applied stress and the strain at which failure occurs.

This study proves that the creep properties can be predicted by the tensile tests at constant loading rate, provided the same environmental conditions (i.e., constant temperature, not exposed to UV radiation and humidity). Additionally, it has been proven

that the effect of viscosity on failure properties (i.e., strength and stress at failure) persists even under very slow loading rates. Typically, the failure threshold in terms of strength and strain increases with higher loading rates.

Finally, from an engineering safety standpoint, the relatively short-term laboratory testing for predicting the resistance of PVC's GM should be performed at the lower rates expected in the field, for the reason of the rate-dependency effects, in order to accurately measure intrinsic ultimate strength and deformation, and to avoid the risk of premature failure.

Relying solely on tests at 100 mm/min, the standard laboratory test - as recommended by European standard EN12311 - may not be conservative, as failure occurred sooner(i.e. both lower strain and stress) for lower speeds.

The results discussed in this research are specific to the GM being studied and should be extended carefully to other types of GMs in which other additives (such as antioxidants, fillers, carbon black, and fire retardants) may influence the mechanical behavior as well. Considering the distinctive microstructure of each GM-type, its individual response to tensile forces and long-term performance may vary accordingly.

Chapter 5: Multiscale analysis of PVC GMs: From microstructural features to macroscopic behavior

In the previous chapter, the experimental campaign highlighted the viscoelastic nature of the PVC GM under different loading conditions, which is difficult to formulate in a proper phenomenological constitutive framework. Thus, an important objective of this work is to understand the mesoscopic origin of PVC GMs macroscopic properties, through Elementary volume (EV) approach developed in Chapter 3 using DEM. The application of DEM to study elementary mechanisms within geomembranes provides a novel perspective in the GM modeling history.

By focusing on the effects of chain length, degree of crystallinity, and density of chains, this research addresses existing gaps in the literature regarding the mesoscale characteristics of PVC polymeric material. A parametric study is conducted to investigate how these factors affect the model's predictions of deformation, and failure.

The results are also compared qualitatively to the experimental data presented earlier, highlighting the key differences between the simplified numerical approach and real-world behavior.

Eventually, this chapter is organized as follows:

- Exploring a simple two-crystallite model and its response.
- Studying the effect of EV dimensions
- Presenting a parametric study on the effects of chain length, crystallinity, and amorphous region's chains density on the model's predictions
- Investigating the micro-inertial effects

As outlined in Chapter 3, the uniaxial tensile test was selected for model calibration and validation, with KUBC imposed in accordance with the material's incompressibility assumption (Equation 3.12). However, in the parametric study (Section 5.3, 5.4, 5.5, 5.6, 5.7), non-isochoric boundary conditions were (mistakenly) applied, which do not strictly satisfy the incompressibility condition (see Figure 5.1). Nevertheless, since the same boundary conditions were consistently applied across all simulations of the parametric study, the comparative analysis remains valid, even if the specimen's volume is not perfectly preserved.

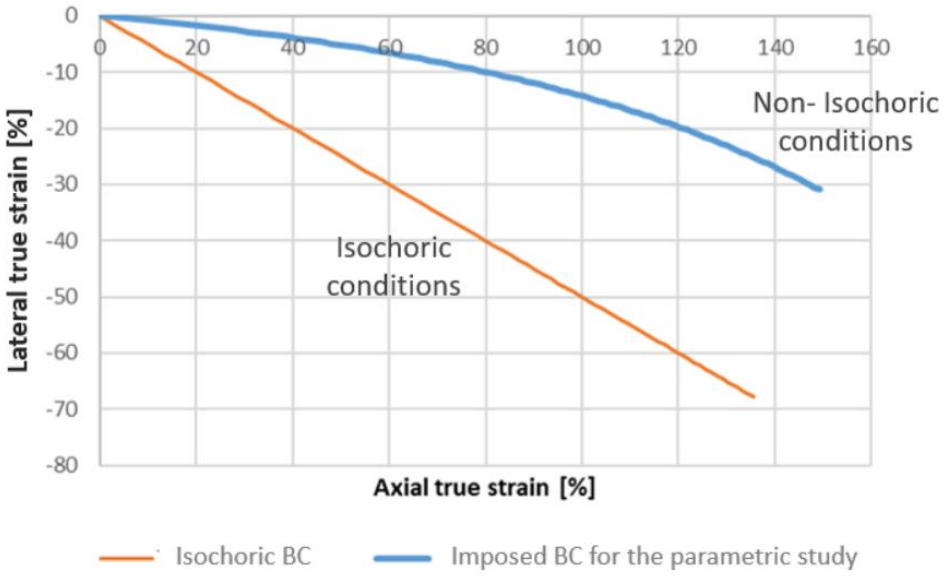


Figure 5.1: Axial vs. lateral true strain: Boundary conditions in reference simulations (orange) with isochoric conditions, and parametric study (blue) with non-isochoric conditions.

5.1. Mechanical behavior of a simple two-crystallites system

Before delving into the full-scale parametric study of an elementary volume of PVC, we investigate the behavior of a small system consisting of two crystallites linked by polymer chains, as shown in Figure 5.2 (initial state). This system is a foundational case study for understanding how specific microstructural components (i.e., the amorphous chains and the crystalline regions) respond to strain loading. No plasticizer is introduced, focusing purely on the stress distribution within the crystallites and the amorphous chains, gaining insights into the mechanisms driving deformation.

The dimensions of the system are set at **20 nm** in both width and length, with a height of **40 nm** in the loading direction. To simulate a uniaxial tensile test, we apply a constant strain rate of 4/sec to the nodes on the top boundary, while keeping the bottom boundary fixed.

In the following subsections, we investigate the microstructural distribution as well as the force distribution within the structure. This allows capturing the transition from localized microstructural changes to the macroscopic response of the two-crystallite system under load. The macroscopic behavior is determined through stress-strain curve, with stress calculated using Equation 3.18, and strain represented as the logarithmic axial strain described in Equation 4.2.

5.1.1. Microstructural evolution

Figure 5.2 shows the microstructural evolution during loading, showing the responses of crystallites and amorphous chains at various strain levels.

As the strain rate is applied, the amorphous zone stretches progressively, with chains realigning and rotating to align with the load direction. In the initial 5% of strain (Figure 5.2), both the amorphous chains and the crystallites begin to rotate to accommodate the strain without experiencing immediate failure. The adaptation and reorganization in the

microstructure play a crucial role in load transfer, preventing early failure at the crystallite-amorphous interfaces.

As the loading increases, the crystallites begin to fragment, indicating that the intermolecular connections inside the crystallites are broken. These interactions, depicted by lateral cylinders inside the crystallite structures (in pink), join the chain segments within the crystallite. The fragmentation indicates probable slide between crystalline chains, resulting in certain chains being inactive. Following this, chain scission occurs within the amorphous region, causing more chains to break and become inactive. By 30% of strain, most of the chains that originally connected the two crystallites are broken, thus dividing the system into two parts. This early stage dislocation of the crystallite justify their modeling as a network of grid nodes and connections and not merely as a rigid parallelepiped.

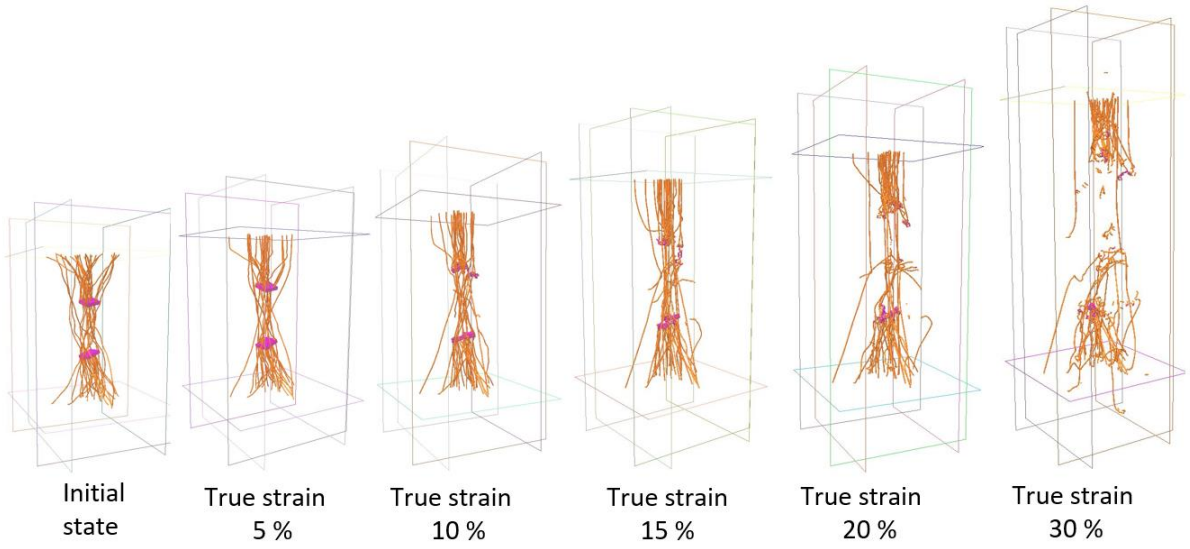


Figure 5.2: Evolution of the microstructure morphology of simple two crystallites system during uniaxial tensile test. True strain is the logarithmic strain computed following Equation 4.2.

5.1.2. Force distribution

Figure 5.3 shows a color-coded force distribution map at different deformation levels. The color-coding indicates stress concentration, with dark red representing the maximum force a cylinder can withstand.

At the beginning (1% of strain), highly-stressed regions appear mostly in the entangled areas where polymer chains interlock. These entanglements bear the initial load. At this stage, the force distribution map is non-uniform, with high stress (red) concentrated in specific interlocked chains and low stress (blue-green) distributed across the system.

As deformation approaches 5%, the forces become more uniformly distributed as polymer chains realign and rotate in both the amorphous zone and the crystallites. This adjustment, combined with chain slip in the entangled areas, enables an efficient load transfer between the amorphous chains and the crystallites, as shown by the appearance of more green and yellow regions. At this stage, some chains show orange color, indicating highly loaded chains that induce localized stress concentration in the crystallites, as we can see warmer color (orange) intensify around the crystallites.

Beyond 10% of strain, this localized stress leads to fragmentation within the crystallites, where stress exceeds the structural capacity represented notably by the resistance of the weak connections. Fragmentation here indicates that the already buildup localized stress is causing internal failure within the crystallites. At this stage, the crystallites progressively split into disconnected parts, with force increasingly concentrated on the remaining active chains in the amorphous zone, some of which approach maximum force (red). However, many amorphous chains have already become inactive due to either crystallites fragmentation or to the fact that they experience failure (shown by blue - green – yellow).

At strains beyond 30%, the force map shows nearly all chains in blue and green, indicating that the overall system has undergone structural failure, resulting in a complete loss of load-bearing connectivity.

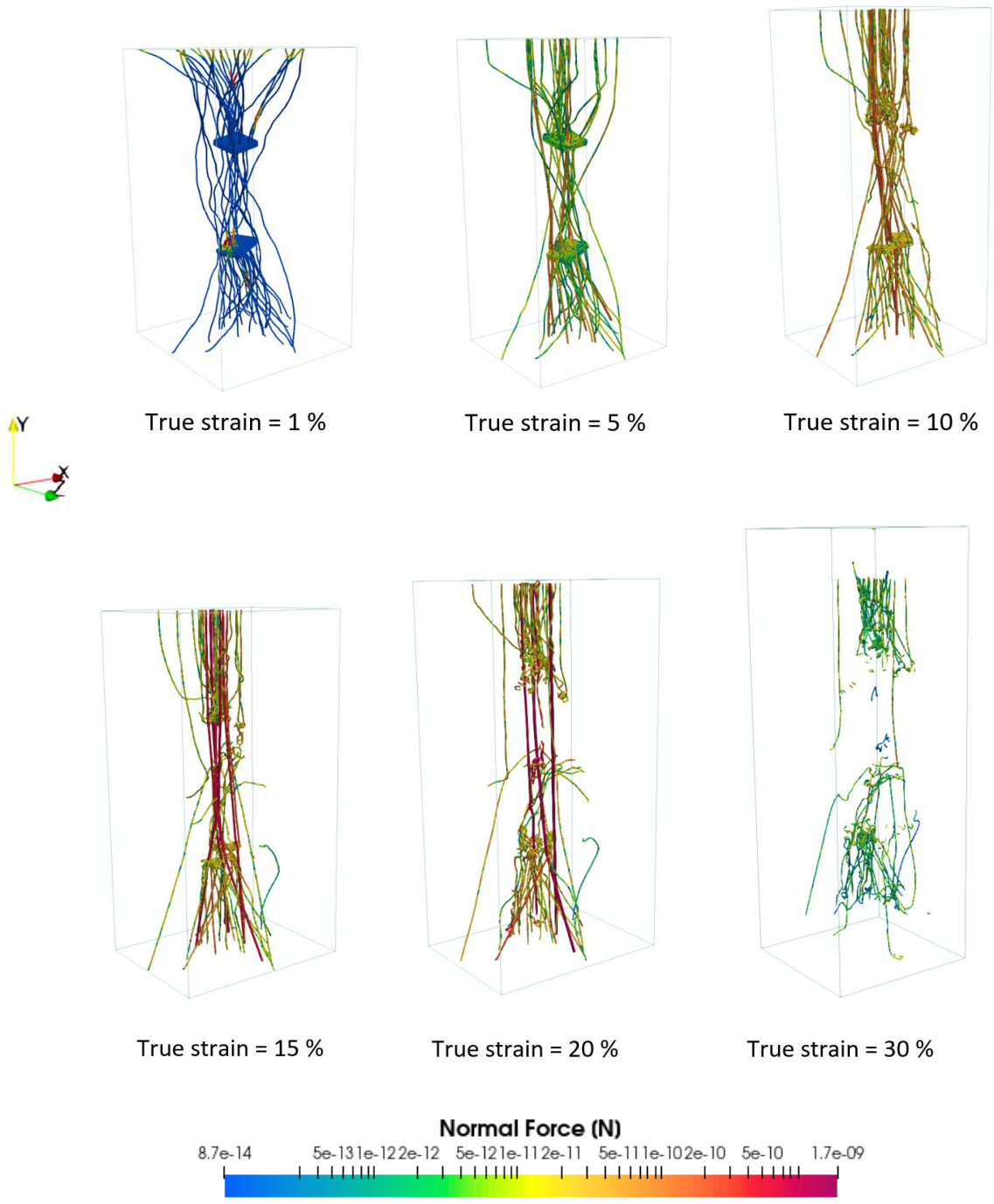


Figure 5.3: Force distribution map throughout the microstructure at different levels of deformation.

This analysis of force distribution offers critical insights into the system's load transfer mechanics. The crystallites and entanglements act as primary load-bearing structures in the early deformation stages, highlighting the importance of **crystallite interfaces** and **chain alignment**. As load increases, these crystallites bear the highest stress levels and eventually fragment, indicating that the crystallites function similarly to entanglements by resisting deformation until their structural capacity is surpassed. Finally, some crystallites are partially destroyed, leaving only the remaining active chains to bear the

load. These chains continue to support the stress until they experience breakage too, marking the point of system failure.

Note that these observations made on a simple system of two crystallites cannot be generalized directly at the material scale. Additional simulations for larger sample volumes are needed, which is the focus of the Section 5.3.

5.1.3. Stress-strain response

This section investigates the relationship between the overall mechanical response and microscale observations in the two-crystallites system.

The true stress-strain curve is shown in Figure 5.4, while the fraction of broken chains throughout the test is illustrated in Figure 5.5. Additionally, Figure 5.6 illustrates the vertical positions of chain failures (blue points) alongside the position of the top wall (red line) during the test.

Initially, the stress-strain curve exhibits a gradual, nearly horizontal trend, indicating a very slow increase in stress. This corresponds to the chain's readjustments and reorientation while no significant stress is generated within the structure. Then the stress increases gradually, until reaching a first peak at approximately 8% of strain. Subsequently, the stress drops, which is related to the splitting of the crystallites into fragments, as seen in Figure 5.2 and Figure 5.3 at 10 % deformation, while no chains exhibit failure at this stage (see Figure 5.5).

As deformation continues, the stress rises once again, as load becomes increasingly concentrated on the remaining active chains within the amorphous zone (see Figure 5.3 at 15% and 20% deformation). This linear trend ends with a stress peak that corresponds to the beginning of chain breakages (see Figure 5.4 beyond 18% of strain), where the amorphous matrix can no longer stretch linearly and starts failing incrementally beyond 18 % of strain (see Figure 5.5 and Figure 5.6).

Figure 5.6 reveals that the failure positions of chains are proximately very close, explaining that the active chains (i.e., solicited chains) experience similar mechanical stress. Additionally, this highlights how the failure of a chain can trigger the failure in neighboring chains, potentially leading to cascading failures as neighboring chains become overloaded and reach their limits of tensile strength. Therefore, the subsequent decrease in stress reflects the increase in the number of failed chains, leading to an overall reduction in the load-bearing capacity.

This behavior highlights the important role of the crystallite as well as the chain breakage in determining the material's behavior.

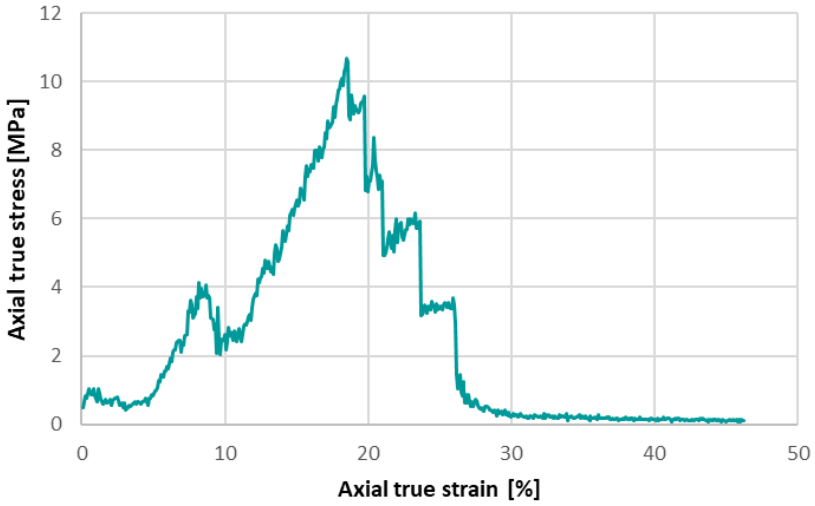


Figure 5.4: Stress-strain curve

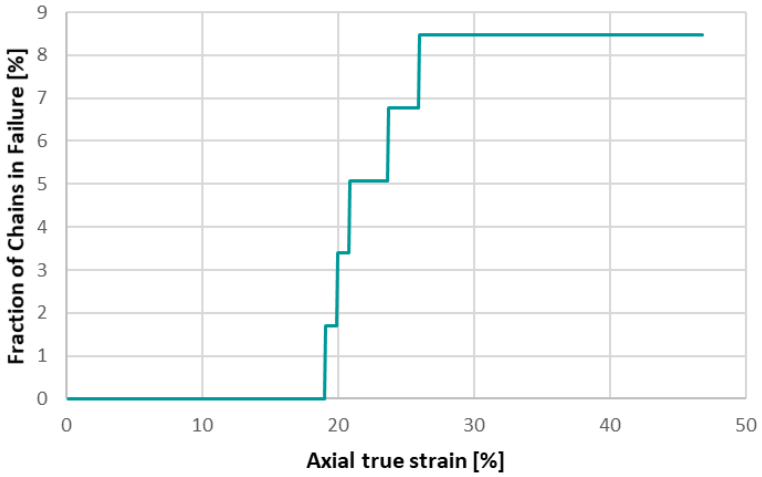


Figure 5.5: Evolution of fraction of chains in Failure during loading deformation.

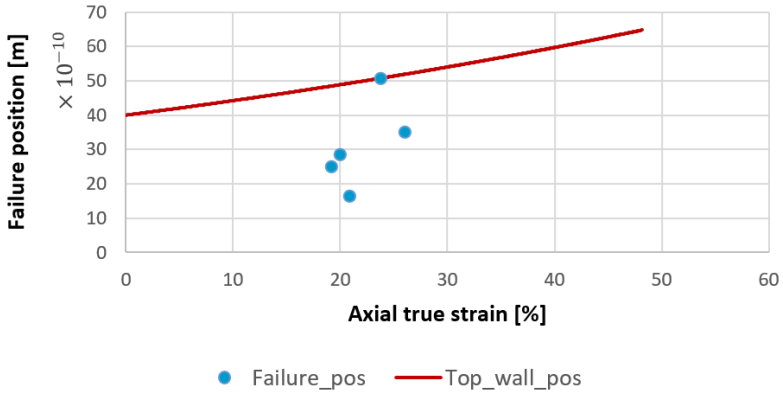


Figure 5.6: Vertical position of the failure points (blue) with respect to the top wall position (red line).

Throughout the loading process, the stress distribution remains uniform across different measured levels of the specimen, as shown in Figure 5.7. These levels, taken at 25% (Level_1), 50% (Level_2), 75% (Level_3), and 100% (Level_4) of the specimen's

current height, consistently show similar patterns of stress response. This uniformity suggests that the overall stress is well transmitted throughout the material, despite the microscale adjustments, such as chain's slip and reorientation, crystallite fragmentation, and chain breakages. This result indicates an effective load distribution across the interconnected network of amorphous chains and crystallites, and no inertial effects.

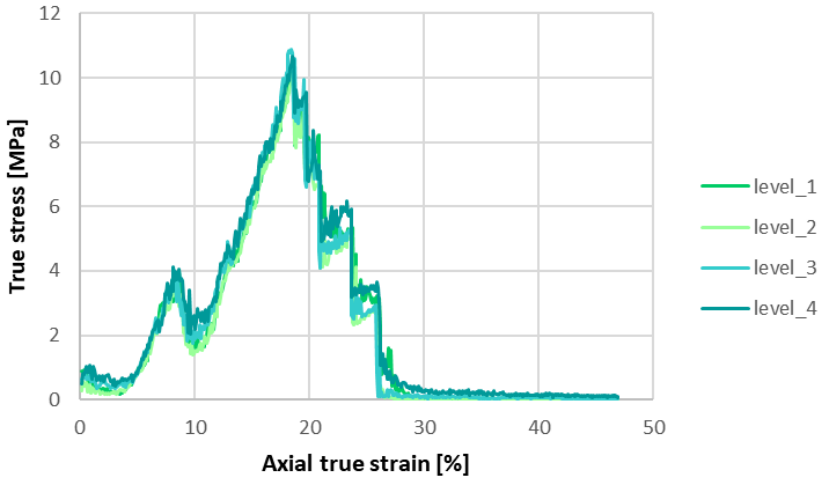


Figure 5.7: Stress distribution at four different current height levels of the specimen.

The normalized average of the maximum forces supported by the chains during loading is illustrated in Figure 5.8. The curve follows the same trend of the true stress-strain curve Figure 5.4, confirming a strong correlation between microstructural responses of individual chains and the overall macroscopic mechanical behavior. Essentially, when each chain gradually bears and eventually achieves its load-bearing limit, these microscopic changes are reflected in the macroscopic stress-strain response.

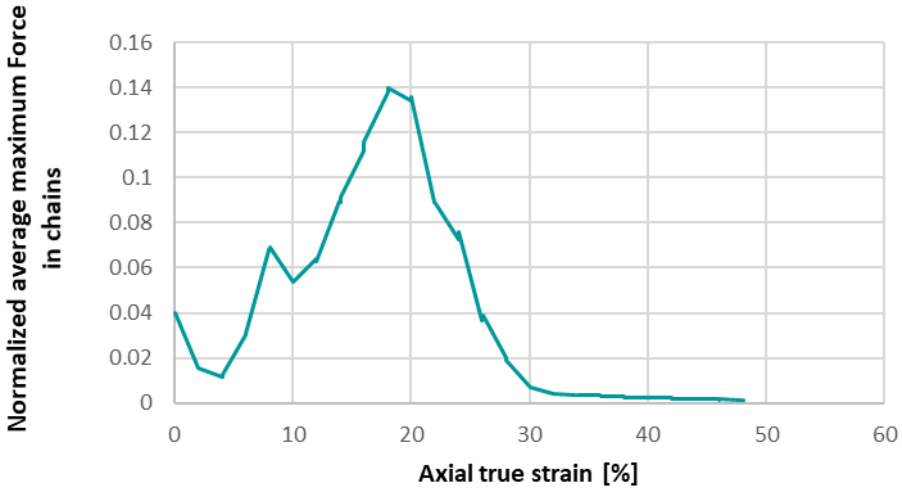


Figure 5.8: Normalized average maximum force in chains throughout the test (Relative to maximum chain's resistance).

The system's energy has been evaluated and is illustrated in Figure 5.9. Three different form of energy exist in the system: elastic energy, kinetic energy, and numerical

dissipation. The elastic energy is stored within the chain due to deformation and at contact points (e.g., entaglements), while kinetic energy accounts for the energy associated with the velocity of the chains. Dissipative energy, on the other hand, arises from the numerical damping effects when chains rearrange. It serves to stabilize the system by reducing energy from two main sources: the elastic energy stored within the chains and the kinetic energy generated as chain's nodes velocity increases. Furthermore, when a chain fails, its stored elastic energy is removed from the system. Due to a technical limitation in the YADE software, this energy is not accounted for in the dissipation calculations. As a result, when a chain fails, its stored elastic energy is numerically dissipated, and no longer contributes to the dissipation process. The elastic energy stored in the remaining chains generated unbalanced forces, which lead to its conversion into kinetic energy and eventually numerical dissipation as well.

Figure 5.9 (left) shows that a significant amount of energy is dissipated, as indicated by a sharp increase at 18% of strain. This increase can be attributed to the release of kinetic and elastic energies generated in the system.

Focusing on the elastic and kinetic energy, in Figure 5.9 (right), it could be seen a marked increase in elastic energy followed by an increase in kinetic energy. This is coinciding with slip events in the crystallites (at 8-10 % of strain) and chain scission (at 18-20 % of strain). When a failure occurs, the potential energy is transformed into kinetic energy, which will be dissipated through numerical damping.

The increase in potential energy in the system beyond 12% of strain indicates that, following the slippage of the crystallites, certain chains become highly loaded, as evidenced by the dark red regions in the configurations shown in Figure 5.3 at 15% of strain. This increased stress on the chains leads to a rapid increase in the elastic energy stored within them. As these chains are stretched further under the applied load, they accumulate potential energy, reflecting their capacity to store energy elastically. At this stage, the kinetic energy remain constant, as the nodes do not undergo acceleration, until subsequent failure happens.

The interplay between the slip of the crystallites and the increased loading of the surrounding chains, in addition to the chains scission, play a critical role in the overall energy dynamics of the material, ultimately contributing to the system's response.

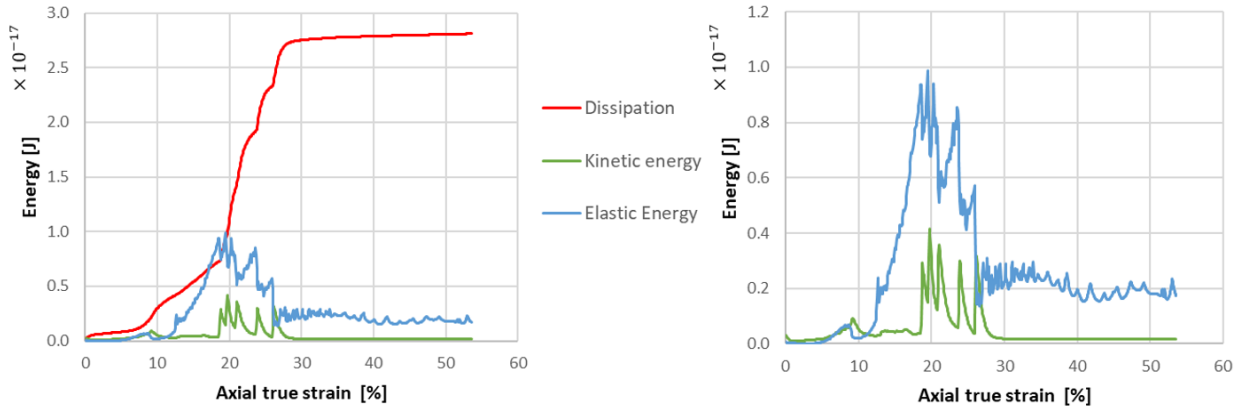


Figure 5.9: (Left) Energy balance during loading. (Right) Comparison between elastic and kinetic energy (zoom-in view).

5.2. Model calibration: defining a reference sample

5.2.1. Reference parameters

The numerical model for PVC GM relies on several geometrical and physical parameters that need to be calibrated in order to be able to simulate the mechanical response of a realistic PVC GM. For some of the parameters, the lack of experimental data prevents a proper calibration. Therefore, we selected rational values as references and we propose parametric studies in Sections 5.3, 5.4, 5.5, and 5.5.

This section details the characteristics of the reference model, including key parameters established through a series of preliminary simulations. These parameters provide a consistent basis for evaluating how variations in model parameters—such as the number of chains, tortuosity, strain rate, and REV size—affect the material's mechanical response.

According to Table 3.1, the geometrical parameters of the model include the number of polymer chains within the amorphous regions, the maximum allowed deviation angle (θ_{max}) for chain orientations, the inter-crystallites distance (D), and the dimensions of the elementary volume (EV).

The mechanical parameters considered for the reference model are simplified to three main values: the material density (ρ), the tensile strength of the chain segments (C_n) (described by Equation 3.17, with multiplication coefficient is set to 1), and the elastic modulus E as defined by Equation 3.10.

These parameters values are summarized in Table 5.1. As a result of this geometrical combination, eighteen crystallites have been created.

It is important to mention that the concept of elementary volumes (EVs) and their size on the nanometer scale, which was detailed in Section 3.3, plays a crucial role in capturing the material's macroscopic properties. As a consequence of computation costs, the simulated EVs are probably too small to fully represent the larger material behavior. Therefore, we compensate for this limitation by repeating the simulations on multiple EVs with different spatial distribution of crystallites, polymer chains and plasticizer particles. By averaging the properties of these EVs, the effective macroscopic properties of the

entire specimen can be derived. Within the time frame of the PhD, four specimens have been simulated.

Table 5.1: Parameters used for reference simulations.

Parameters	**Values**
Nb of chains per crystallite	30
Distance D [m]	150×10^{-10}
Orientation angle (θ_{max}) [rad]	$0.1\ \pi$
EV'dimensions [m^3]	$[500 \times 500 \times 500] \times 10^{-30}$
Tensile strength (C_n) [Pa]	1.95×10^{11}
Elastic modulus (E) [Pa]	6.2×10^{11}
Density (ρ) [Kg/m^3]	10^{20}
Average total nb of particles	104430
Average final porosity of the specimen	0.434
Tensile strain rate [/sec]	4
Damping coefficient	0.01

In addition to the geometrical and mechanical parameters, the damping coefficient was set to 0.01, which is found to yield an average stress-strain response closely aligning with expected material behavior under uniaxial tensile loading. The applied strain rate was set to 4 /sec, which is notably higher than the strain rates used in the corresponding experimental tests (maximum strain rate applied in the experimental tests was 0.1 /sec corresponding to 500 mm/min (see Figure 4.23). This relatively high strain rate was selected for practical runtime matter. This strain rate is applied using KUBC, ensuring the material's incompressibility. Thus, a linear strain rate is applied along the loading direction on all the boundaries nodes, while the lateral strain rate is adapted over time to mimic the non-compressible behavior observed in uniaxial tests (refer to Section 3.6.1).

5.2.2. Macroscopic stress-strain response

For the uniaxial traction test with KUBC condition presented in Section 3.6, the average stress-strain curve is shown in Figure 5.10, which demonstrates a qualitative alignment with experimental curve results, showed in Figure 4.17. The curve shows an initial quasi-linear increase in stress up to around **60 % of strain**. Then we observe a marked non-linear phase, with pronounced stress fluctuations. Ultimately, the stress significantly drops down; the structure can no longer sustain an increasing load, signaling the specimen failure.

The standard deviation (computed for the four simulations) of the stress-strain data is illustrated alongside this curve, beginning at a low value that gradually rises with deformation. This increase in standard deviation is explained by the progressive failure of chains as seen in Figure 5.11, which may introduce local perturbations that disrupt uniform force distribution across the entire specimen.

Further analysis of stress-strain behavior across different specimen heights is shown in Figure 5.12, which traces the average stress-strain curves at four height levels (i.e., 25, 50, 75, and 100 % of the current specimen height). During the initial stages of

deformation, these curves remain closely aligned, suggesting homogeneous load transfer throughout the specimens. However, above **70% of strain**, the stress is no longer homogeneous through the sample height, indicating potential stress concentrations.

This loss of stress homogeneity is probably the signature that sample volume remains a little bit limited to dilute the boundary effects related to KUBC conditions. This conjecture is supported by comparing with the two-crystallite model in Figure 5.7, where chains are primarily aligned along the loading direction and do not touch the lateral boundaries, with the more complex 3D network model in Figure 5.12. In this case, the absence of lateral boundary interactions (i.e., all the chains are aligned along the direction of loading, with no chain reaching the lateral boundary) allows for more consistent load transfer along the height, resulting in a relatively uniform stress distribution, shown in Figure 5.12. However, for a more complex 3D network, the lateral boundary effects contribute significantly to the non-uniformity of the stress.

Figure 5.13 show the failure spatial distribution in comparison with the current height of two specimens with 50 nm EV. Beyond 100% deformation, an increase in failure intensity is observed, with the failure of individual chains triggering adjacent chains to approach failure. This failure escalation effect increases the stress localization as the number of active chains capable of supporting the load decreases. Consequently, a non-uniform stress distribution develops across different deformation levels.

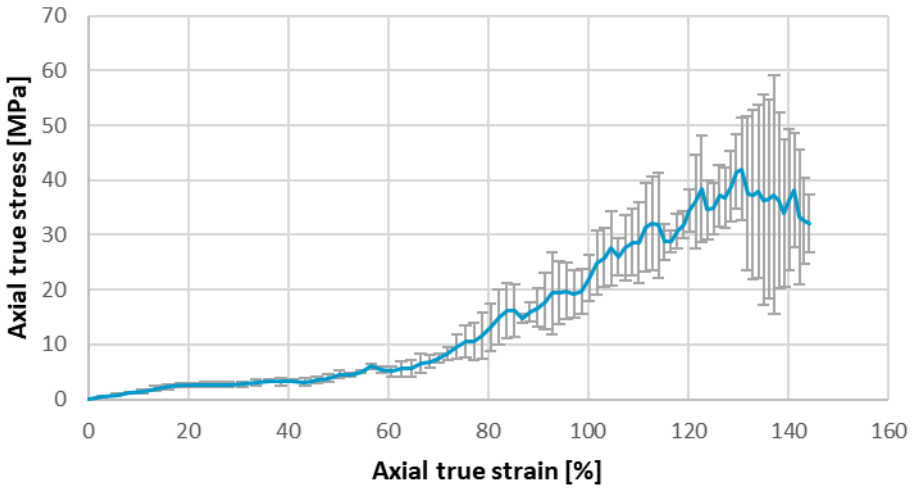


Figure 5.10: Average stress-strain curve (4 numerical tests)

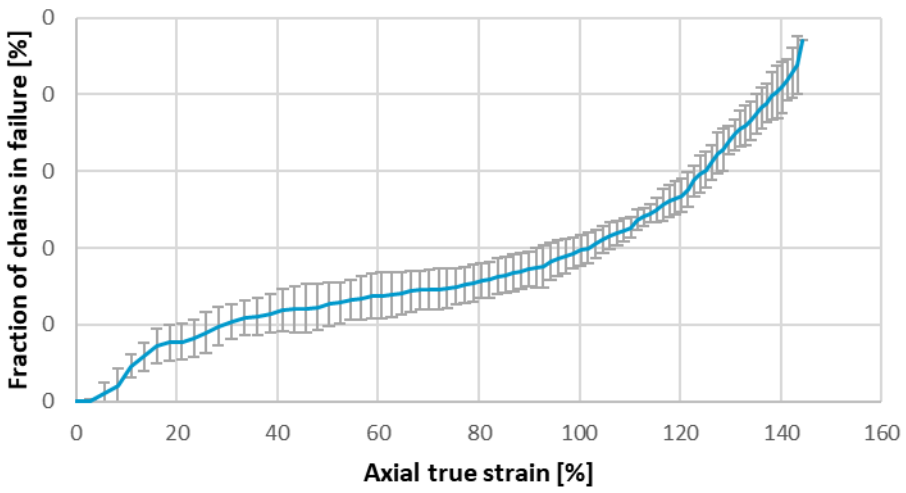


Figure 5.11: Fraction of polymer chains exhibiting failure during deformation (4 numerical tests)

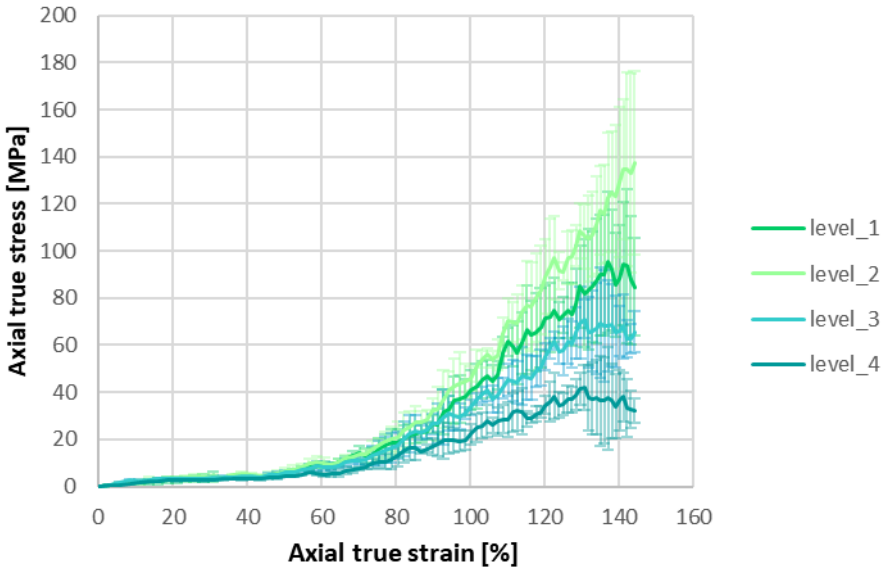


Figure 5.12: Average stress distribution (4 numerical tests) at four different height levels (respectively 25, 50, 75, and 100 % of the current specimen height from bottom to top).

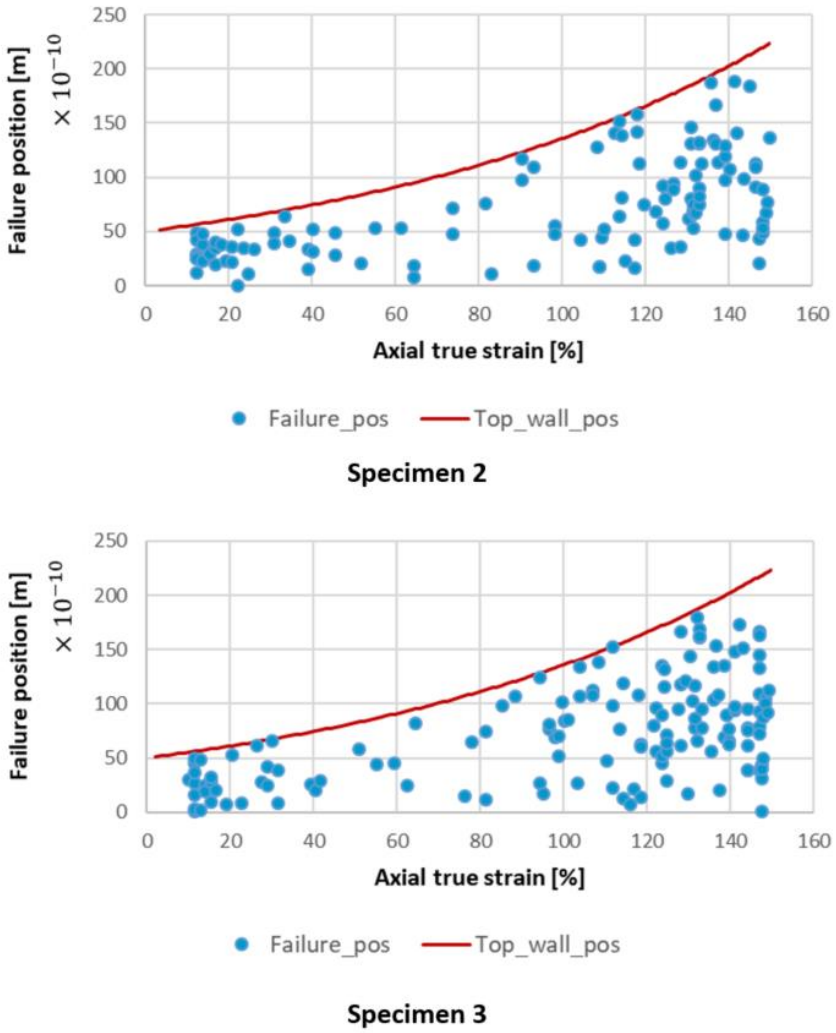


Figure 5.13: Spatial distribution of the failure point along the height of the specimen (specimens 2 and 3).

5.2.3. Stress distribution in specimen microstructure

The 3D configuration of one of the four specimens, shown in Figure 5.14, illustrates the PVC microstructure embedded within plasticizer's particles at different level of deformation. Figure 5.15 and Figure 5.16 further illustrate the force distribution across the polymer chains for two different specimens, providing insight into how load-bearing structures are arranged at the micro-level. Additionally, Figure 5.17 and Figure 5.18 show the plasticizer spheres interactions at 10 % of deformation, illustrating the important role of these particles in facilitating load transfer between polymer chains. These inter-chains plasticizer particles contribute to an interconnected load transfer network across the specimens.

At **10% of strain** (as shown in Figure 5.15 and Figure 5.16), a blue-green color mostly emerges within the chains, indicating the distribution of load within the network. This force distribution correlates with entanglement sliding, where the chains shift slightly with respect to each other without significant stress localization. As deformation continues, the load becomes uniformly distributed throughout the microstructure, with

the green color extending across the majority of chains. This suggests that the polymer chains undergo reorganization, including realignment and rotation, both within the amorphous regions and the crystallites. This structural rearrangement allows efficient load transfer, resulting in a balanced load distribution across the specimen.

To further explore this structural evolution, Figure 5.19 and Figure 5.20 provides a zoomed-in view of crystallite behavior across deformation levels for two specimens. At **20%** and **30% of strain**, the crystallites remain intact, with no visible fragmentation. During this stage, some chains exhibit a yellow coloration, indicating localized stress applied on the crystallites.

Beyond **40% of strain**, fragmentation becomes visible within some of the crystallites, particularly in the upper half of the specimen. This fragmentation marks a shift in load-bearing contribution of the crystallites to the polymer chains. Thereupon, these crystallites act as primary load-bearing structures, helping to distribute the load uniformly across the microstructure. This is in parallel with the quasi-linear response seen in Figure 5.10 up to **60% of strain**, as the intact crystallites maintain a stable load-bearing network. After further fragmentation of the crystallites (see Figure 5.21), a transition to nonlinear macroscopic behavior occurs, marking a significant shift in the system's overall response.

At **70% of strain**, yellow and red regions appear heavily, indicating more stress localization. This transition from green to yellow suggests that certain chains are now bearing more load than others are. As a result, the non-uniform stress distribution likely arises as a result of the disordered microstructural geometry. Some chains exhibit higher loads due to their orientation or position, and may fail because already broken chains are inactive and unable to bear load, which increases stress on surrounding chains.

By **90% of strain**, red zones appear in a greater number of chains, highlighting chains under high stress and approaching failure thresholds. The increasing load concentration in specific chains, while others go inactive due to failure, agrees with the growing variation and higher standard deviation observed in the stress-strain curve in Figure 5.10, and the non-uniformity of stress observed in Figure 5.12. This variation is explained by the localized perturbations in the load transfer network caused by chain failure, resulting in reduced connectivity and less uniform load distribution across the microstructure.

In summary, the load distribution across the polymer microstructure varies with increasing deformation, initially exhibiting uniform stress distribution that later shifts toward non-uniformity as localized failure sites emerge. This evolution, affected by chain failure, plasticizer interactions, and crystallite fragmentation, contributes to the observed macroscopic stress-strain behavior and highlights the material’s susceptibility to localized structural weakening under high deformation levels.

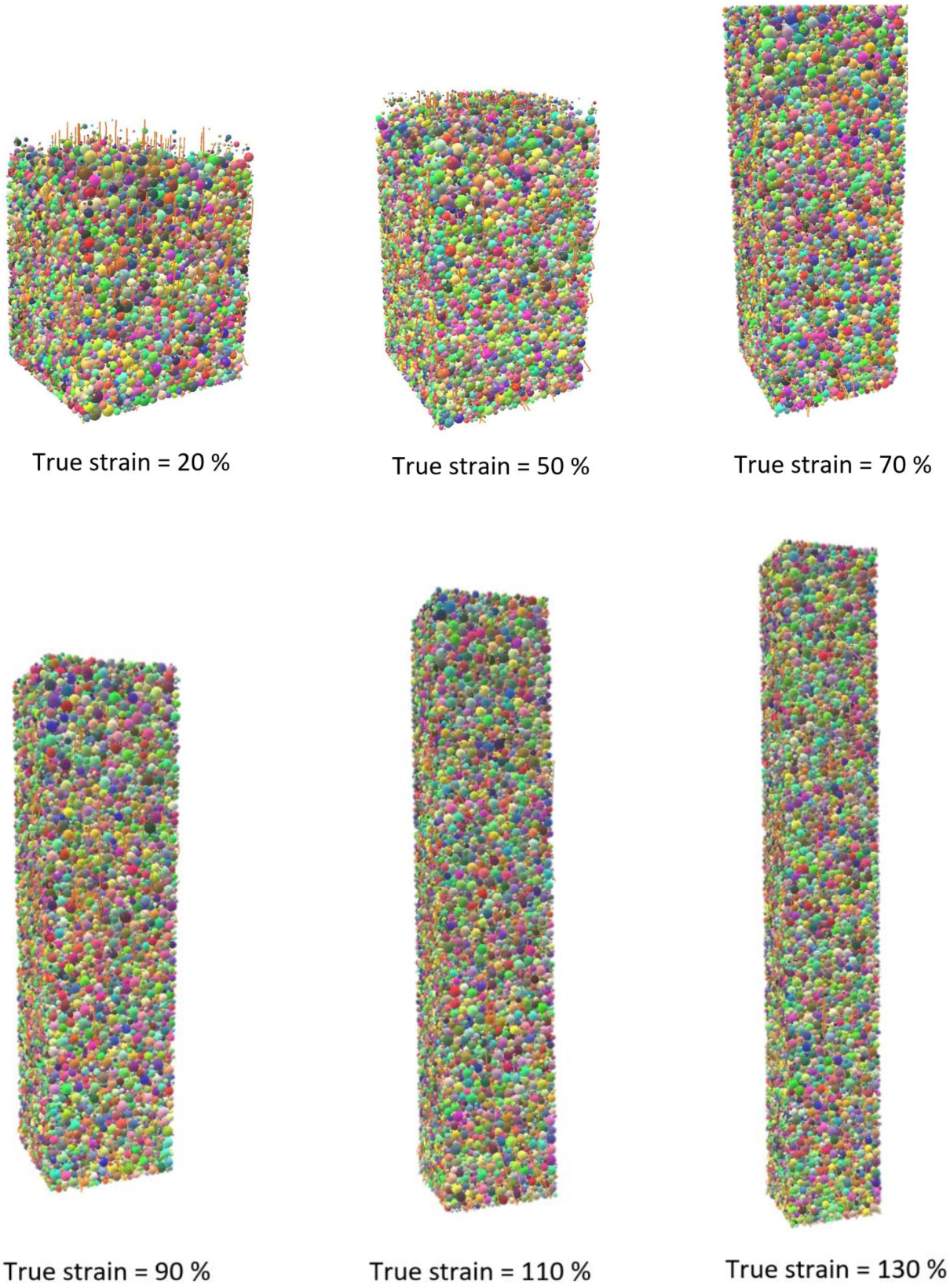


Figure 5.14: 3D configuration of the specimen (2) at different deformation levels.

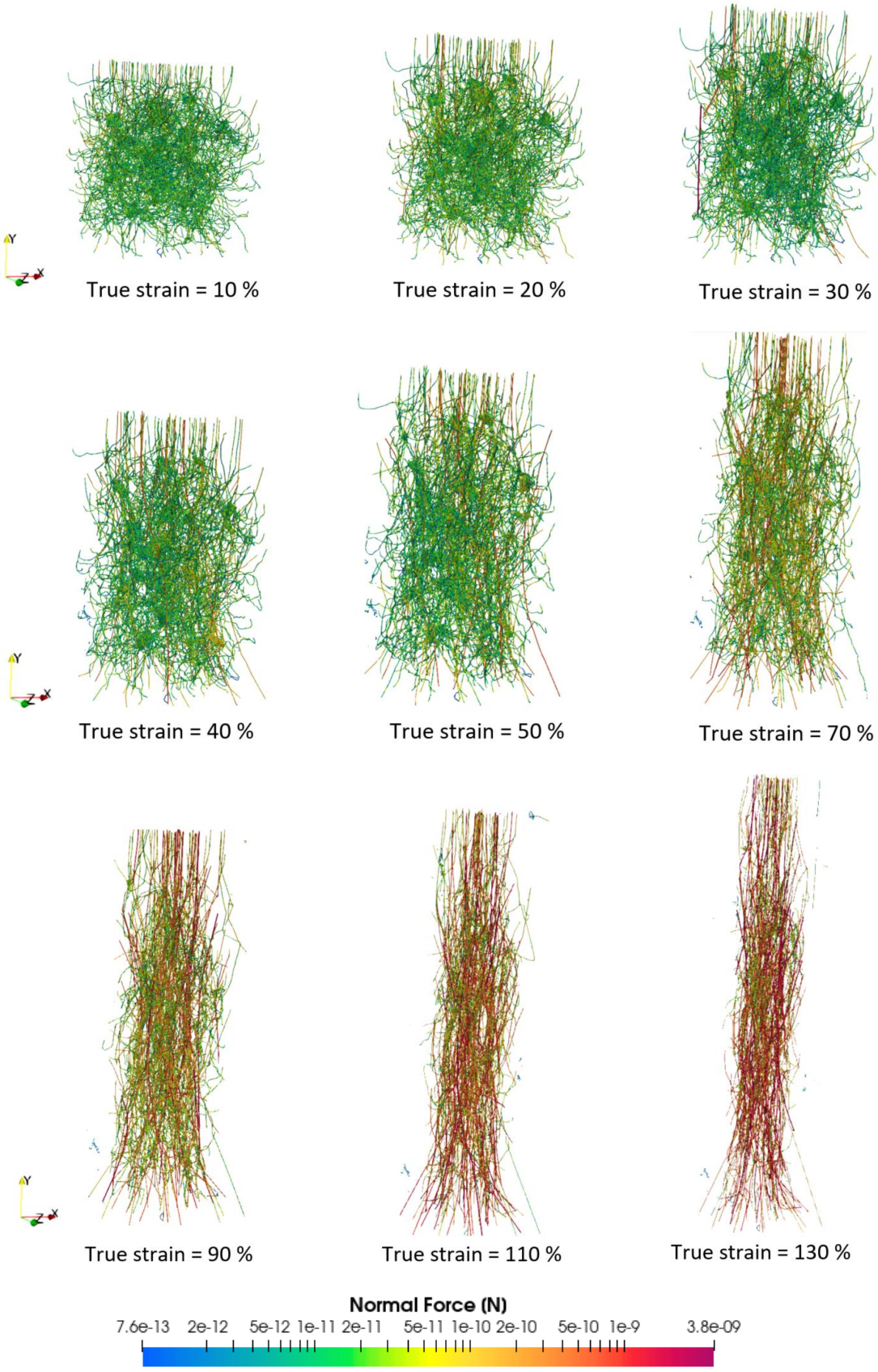


Figure 5.15: Force distribution within PVC polymer chains at different deformation levels (Specimen (2)).

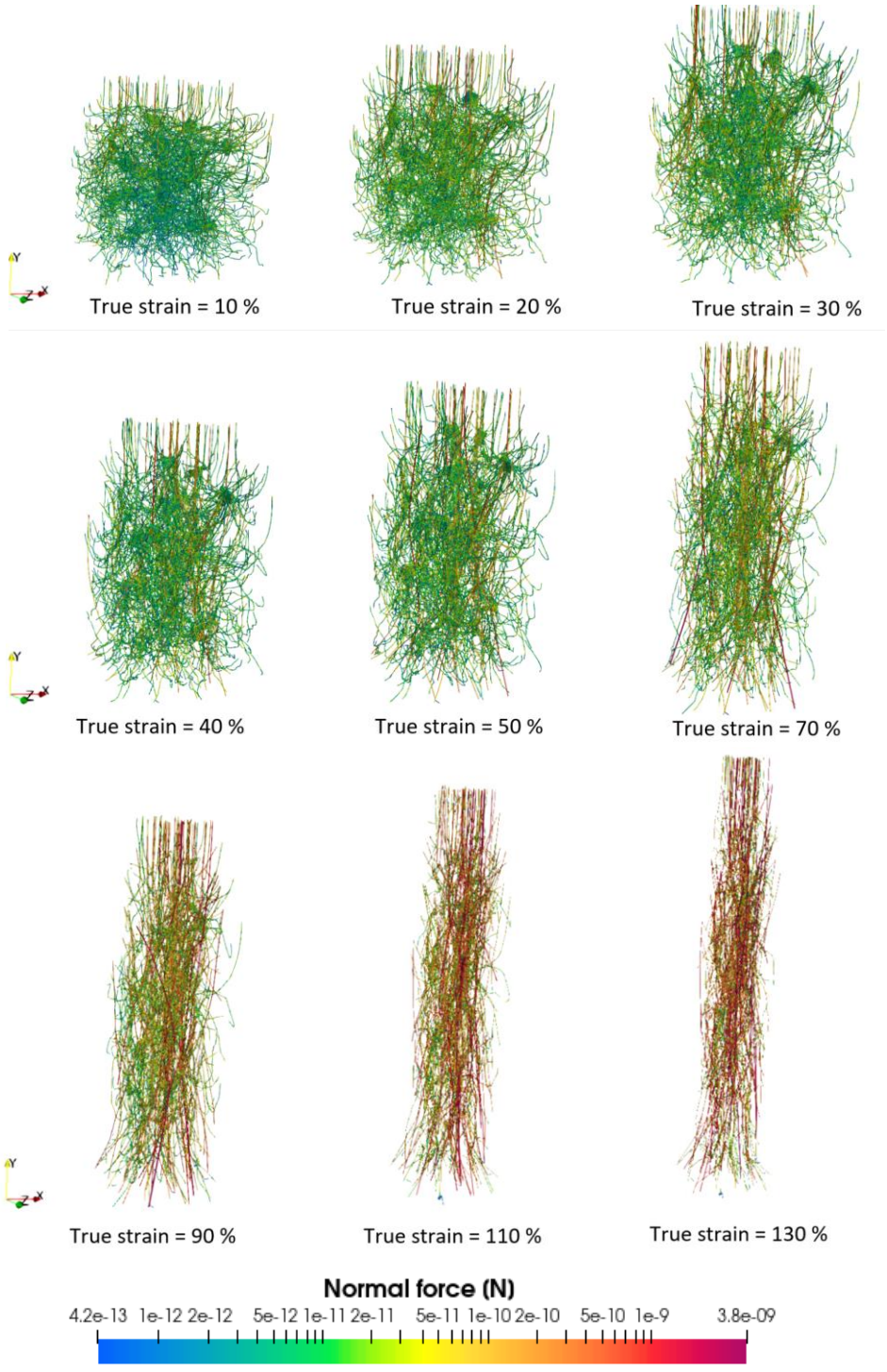


Figure 5.16: Force distribution within PVC polymer chains at different deformation levels (Specimen (3)).

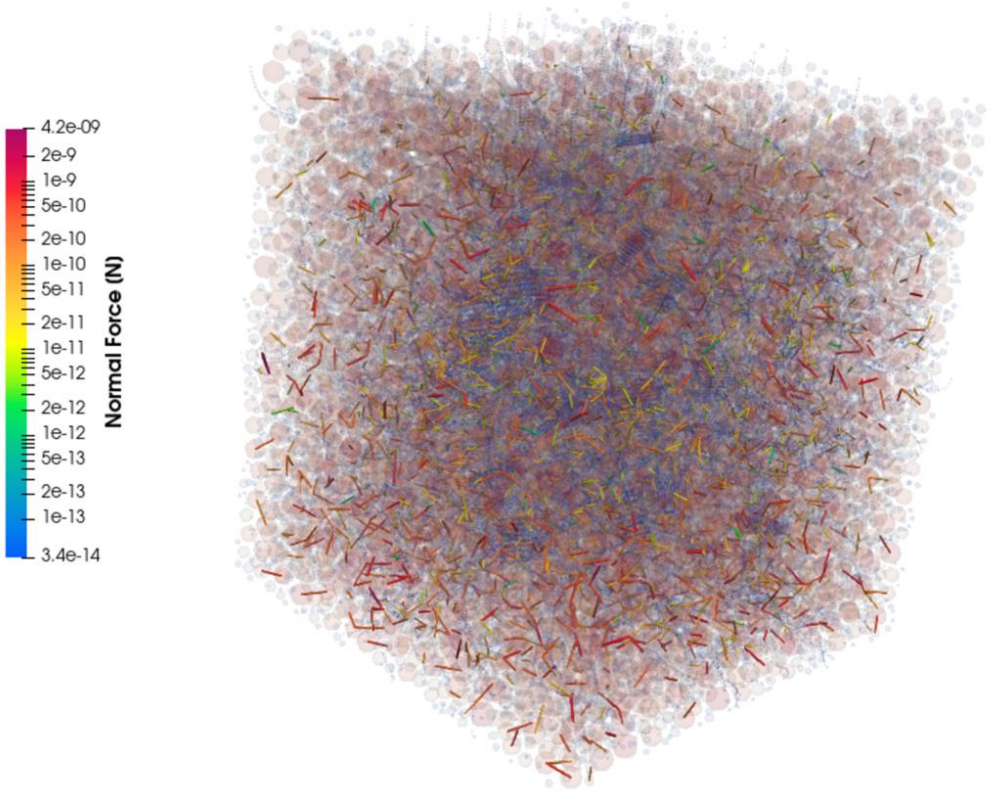


Figure 5.17: Chain-plasticizer interactions at 10% of strain (specimen (2)).

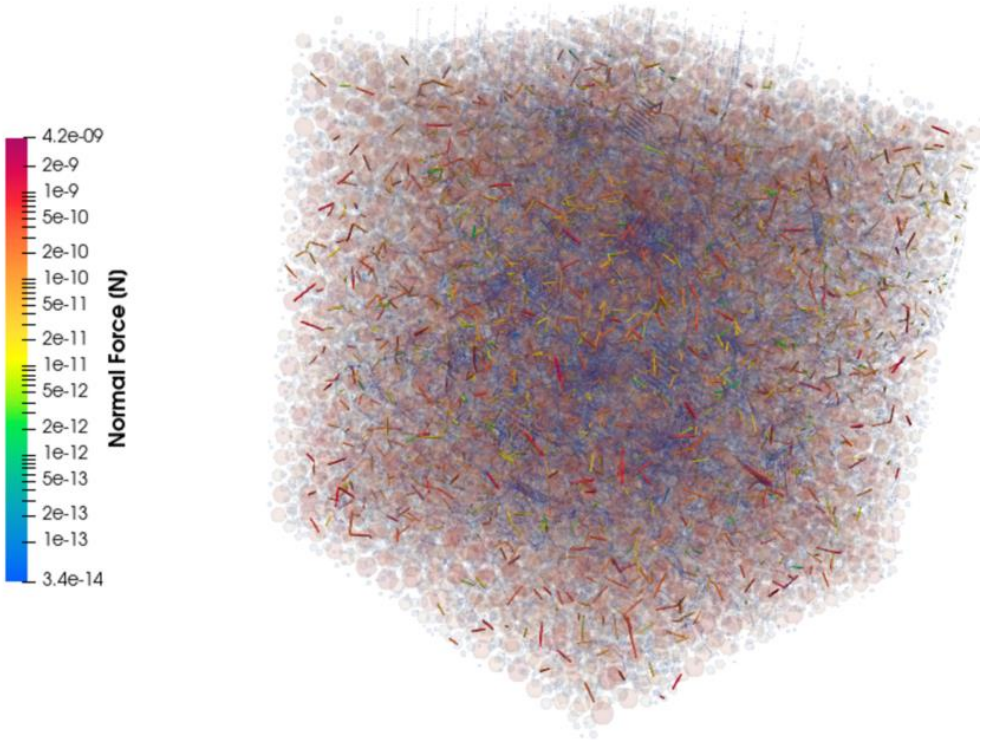
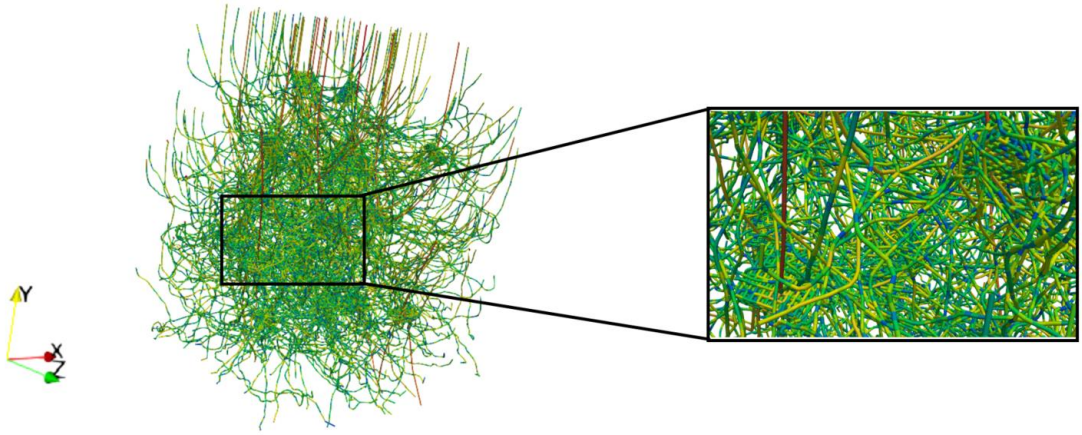
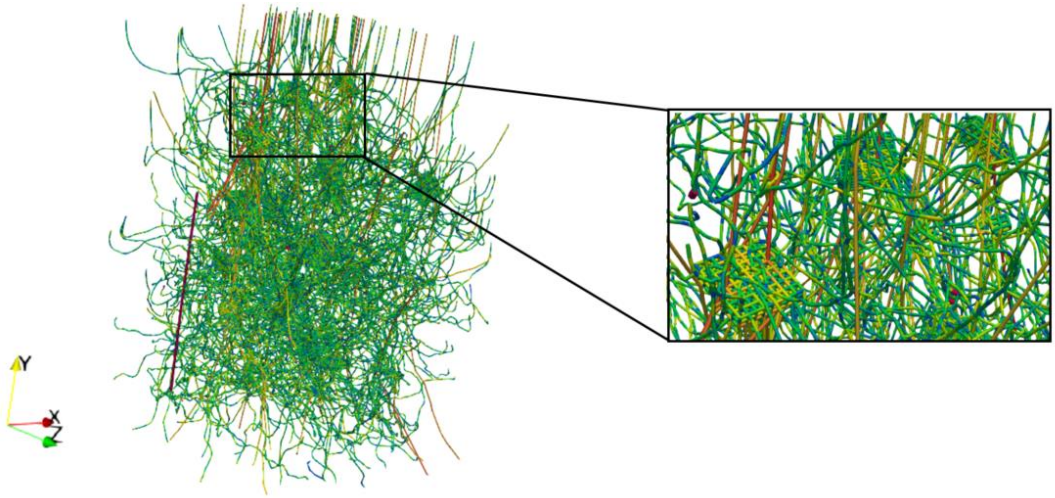


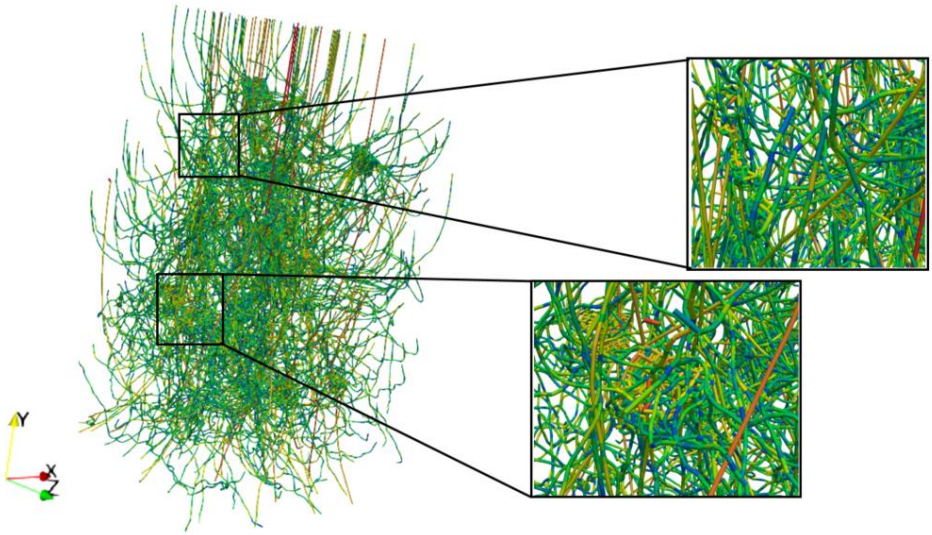
Figure 5.18: Chain-plasticizer interactions at 10% of strain (specimen (3)).



True strain = 20 %

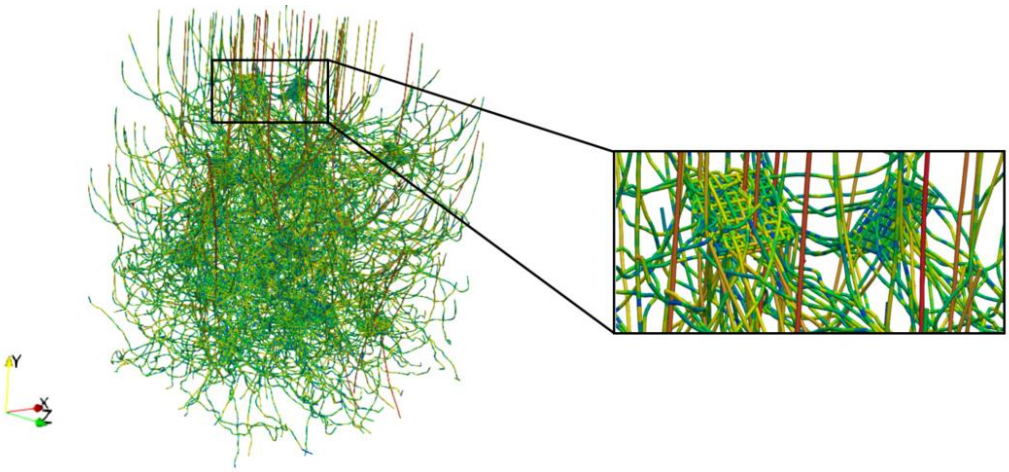


True strain = 30 %

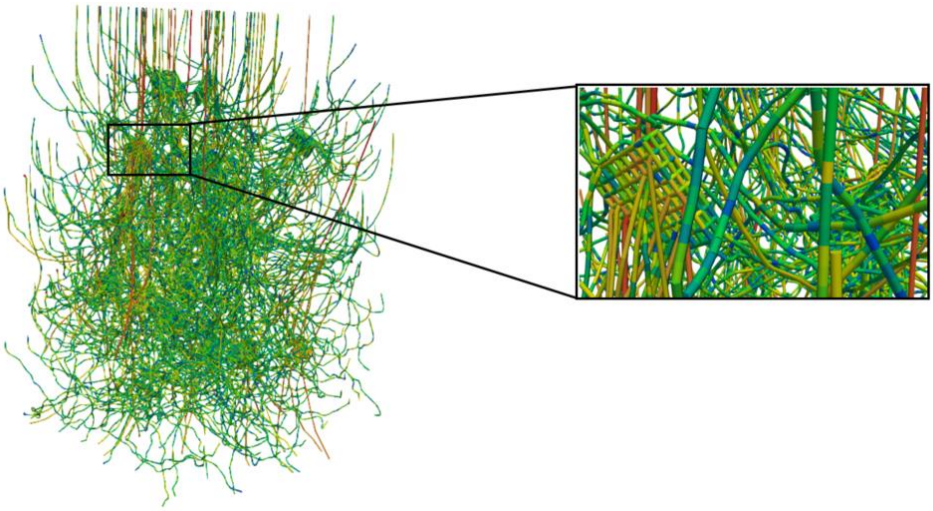


True strain = 40 %

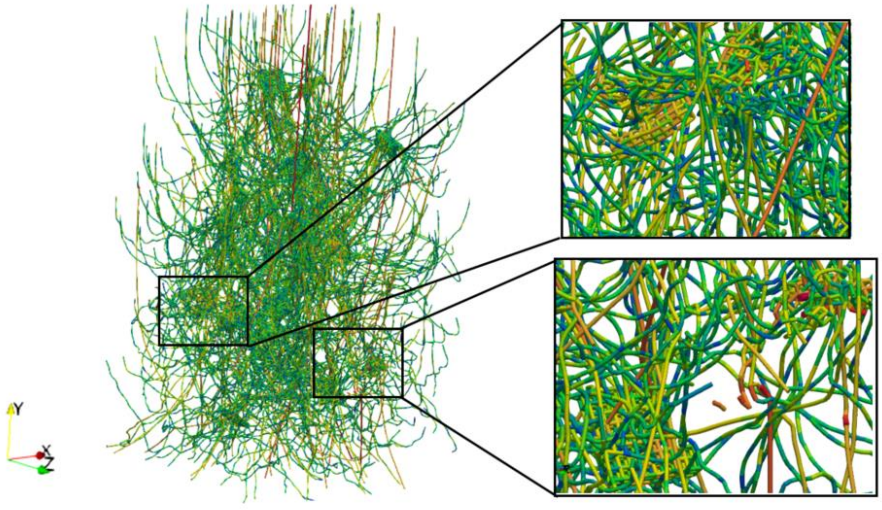
Figure 5.19: Close-up visualization of the crystallites within the microstructure at different deformation levels (specimen (2)).



True strain = 20 %



True strain = 30 %



True strain = 40 %

Figure 5.20: Close-up visualization of the crystallites within the microstructure at different deformation levels (specimen (3)).

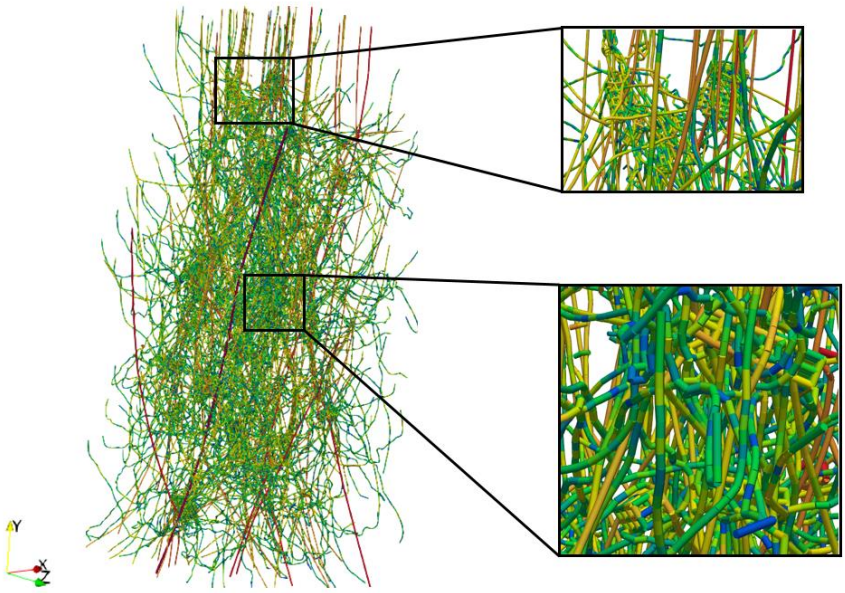


Figure 5.21: Complete crystallite fragmentation detected at 60 % of strain (specimen (3)).

5.2.4. Comparison with experimental data

In Chapter 3, we outlined that the model is based on a multiscale approach, where the microscale parameters are informed by macroscale tests (i.e., experimental tests). Accordingly, this model was calibrated using the maximum stress observed in the experimental results in order to determine a primary value of an individual chain resistance (see Equation 3.17 and Table 5.1).

Given that the maximum stress level achieved numerically is not always distinctly defined, normalization is essential for proper comparison between experimental and numerical results. Thereupon, we selected a reliably identifiable point across all experimental and numerical tests for the normalization: 40 % of deformation. This point approximately lies within the linear part of the material response. Subsequently, a secant modulus, S, is calculated at 40 % of deformation, where the normalized axial true stress is determined according to Equation 5.1.

$$\sigma_{(t)}^{Normalized} = \frac{\sigma_{(t)}}{S} \tag{5.1}$$

Figure 5.22 presents a comparison of the normalized stress-strain behavior between the experimental and model's results. The experimental results were obtained at a tensile rate of 500 mm/min, corresponding to a strain rate of 0.1 /sec (see Figure 4.23), which is the maximum tensile rate achievable with the experimental setup machine. On the other hand, the model's tests were conducted at a 4 /sec.

The results reveal that, in the experimental data, the stress-strain curve initially displays a linear response across a relatively wide range of deformation before transitioning into a nonlinear phase (80 % of strain). This later is higher than the numerical one, where **60%** of strain marks a clear transition between the linear and the non-linear behavior. This initial linear region, as observed in the microstructural analysis,

corresponds to the alignment and orientation of polymer chains and crystallites under load, where some crystallites begin to fragment. The deviation to non-linear behavior is due to several crystallites fragmentation, indicating a transfer in load-bearing contribution from the crystallites to the polymer chains. Thus, this suggests that the chain lengths are short enough for crystallite fragmentation occurring at a lower deformation level. Hereinafter, increasing **chains tortuosity**, and consequently the length of chains, could potentially increase the deformation level before multiple crystallite fragmentation. Additionally, intermolecular interactions have been somewhat approximated through micro-inertial effects, which do not precisely capture their influence. This contributes to the differences observed between numerical and experimental results.

Furthermore, outside the linear zone, the model response exhibits higher stress values compared to the experimental results. This discrepancy can be attributed to the significant effect of the boundary conditions, emphasizing that localized stress concentrations induced by individual chain failure play a significant role in shaping the material's overall behavior. This suggests that increasing the **number of chains** and/or the **EV** size in the model may help to smooth out these variations by minimizing the local perturbation impact on the global behavior.

Interestingly, this behavior can also be explained by the strong connectivity imposed by crystallites, which act as physical entanglements within the specimen. This leads to stress concentration in different regions, which, in turn, may rise the overall stress supported by the system for the same experimental and numerical deformation. This can be related to the **inter-crystallite distance D**, which plays a significant role in the system's crystallinity level, and consequently, its rigidity. An increase in this distance reduces the degree of entanglements formed by the crystallites within the microstructure, potentially leading to a decrease in the system's overall resistance.

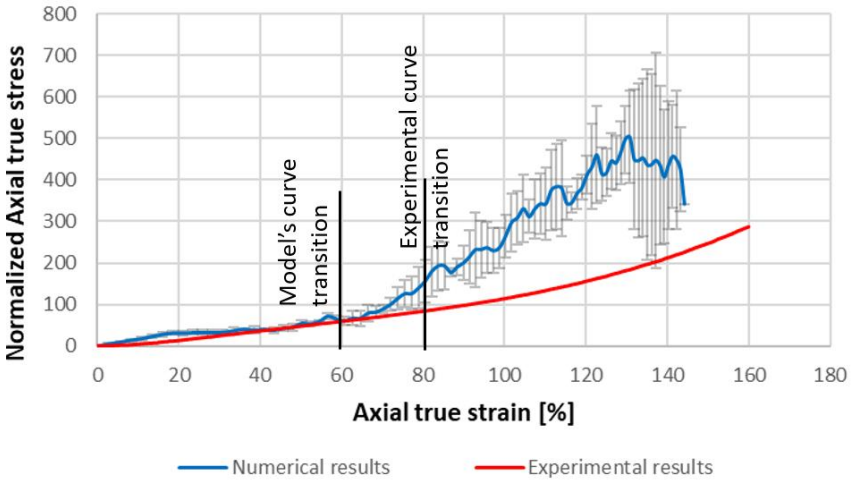


Figure 5.22: Comparison of experimental data and model results

5.3. Impact of EV sizes on the stress distribution

In this section, we investigate the effect of different elementary volume (EV) sizes – specifically 40 nm, 50 nm, and 55 nm – on the macroscopic mechanical response. This enables to specify how far we are from REV conditions and better assess how variations in the size of the analyzed volume can influence the model's performance, including local transfer mechanisms, stress localization and macroscopic response. For the 40 nm EV dimension, eight independent simulations have been conducted. For the 50 nm and 55 nm EVs, four simulations have been performed for each of them. The same geometrical and mechanical parameters, presented in Table 5.1, have been used for the three EVs. This corresponds to **26 crystallites** for 55 nm EV and **7 crystallites** for 40 nm EV. The corresponding particle count reaches 154,690 for the 55 nm sample, whereas it is notably lower at 42,608 for the 40 nm sample. Additionally this results in average final porosity of 0.453 for 55 nm, whereas it is 0.3938 for 40 nm.

Note that in this analysis, non-isochoric boundary conditions were applied, meaning the material's volume was not strictly preserved (the applied boundary conditions impose here a decrease of the volume over time). This influences the relationship between axial and lateral strains (Figure 5.1), but the comparison remains meaningful as the same boundary conditions are consistently applied across all simulations.

5.3.1. Macroscopic stress-strain behavior for different EV sizes

Looking at the average stress-strain curve, shown in Figure 5.23, the curves show a similar trend in the initial stages of deformation. However, beyond **70 % of strain**, it becomes evident that the EV sizes highly affect the macroscopic response, particularly at 40 nm. At this point, the curve for the 40 nm EV deviates significantly from the other curves, highlighting the influence of smaller EV dimensions on the macroscopic response of the material.

The curve for 55 nm show a well-defined maximum stress value approximately at **110 % of strain**, while this is not detectable when decreasing the EV dimensions. This can be explained in Figure 5.24 as well, where at 55 nm; the fraction of chains in failure increases sharply beyond 110%, indicating system approaches failure. Additionally, it could be observed that for higher EVs, the system demonstrates increased resistance, as the model reaches higher stress values.

The coefficient of variation (CV) of the stress, determined by dividing the standard deviation by the mean stress at the current deformation, is shown in Figure 5.25. This coefficient shows higher values for 40 nm EV size, indicating greater variability in the stress distribution at these smaller scales. In addition, the CV decreases when increasing the EV's size, reflecting a less effect of local perturbation on the global behavior. Thus, the fluctuations in the CV curves suggest a higher sensitivity to localized phenomenon, with the smaller EVs (i.e., 40 nm) exhibiting a more pronounced variation in their stress response.

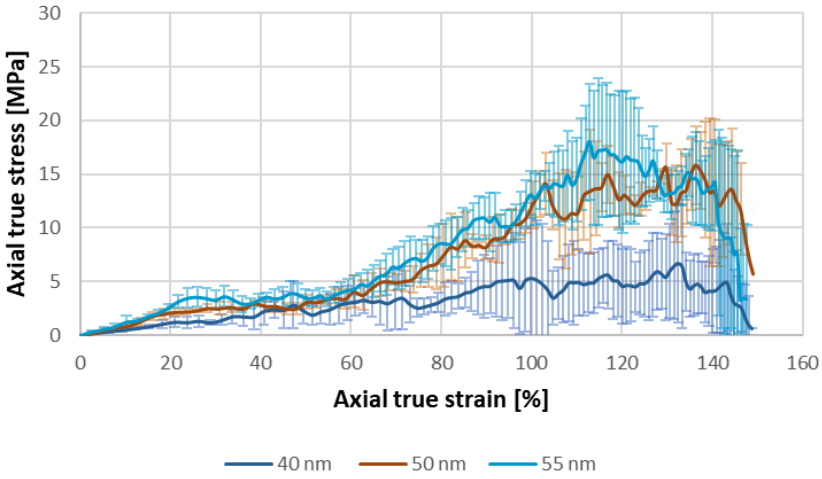


Figure 5.23: Average stress-strain curve for three different EV' sizes.

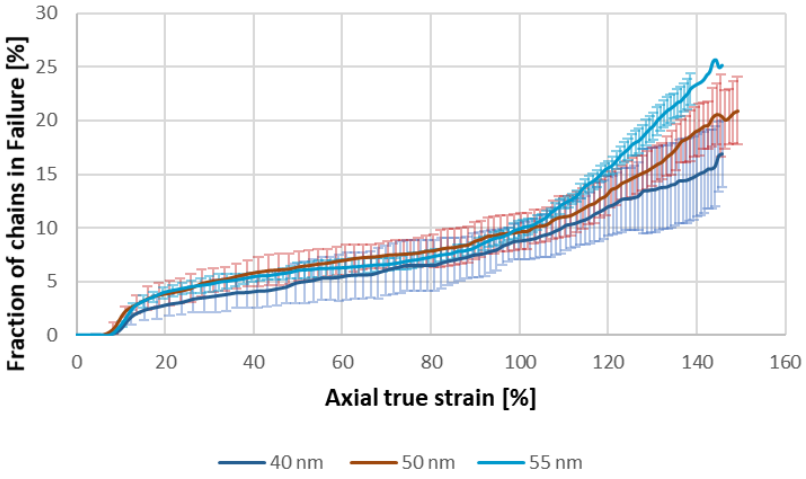


Figure 5.24: Average fraction of chains in failure for three different EV' sizes.

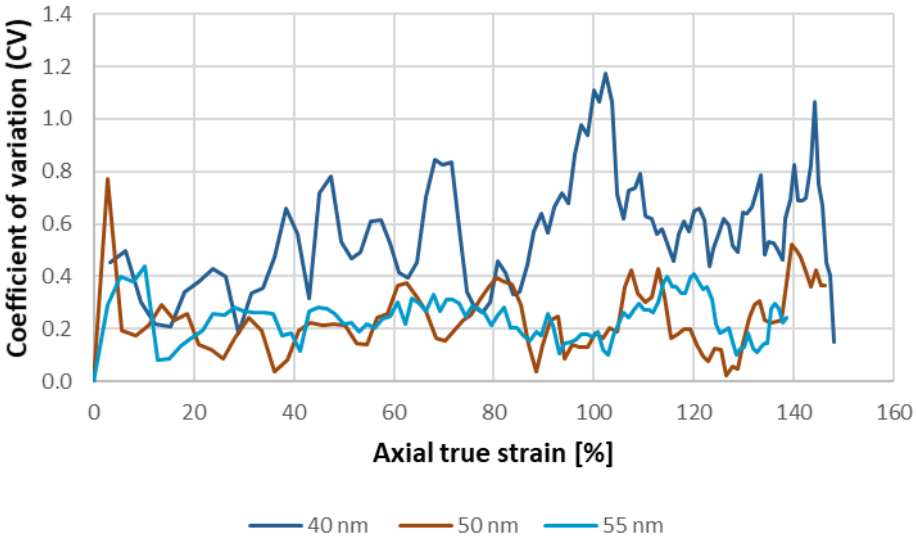


Figure 5.25: Coefficient of variation of the stress for the three EV sizes.

5.3.2. Linking macroscopic behavior to microstructural analysis

Figure 5.26 and Figure 5.27 display the microstructural morphology and force distribution within polymer chains (shown without plasticizer particles for clarity) for specimens with 40 nm, 50 nm and 55 nm EVs at different deformation levels.

At higher EV sizes (55 nm), the chains form a more connected and denser network, as shown by the **denser spatial arrangement and wider distribution of forces**. As deformation progresses, this larger, denser network indicates a higher capacity to distribute and balance load across chains, as a uniform color spreads within approximately all the specimen. This leads to less stress variations and lower standard deviation determined through different microstructure morphologies. In the other hand, smaller EVs (i.e., 40 nm) have fewer chains involved, thus, the force localization in individual chains becomes more pronounced, as the force color is not homogeneously distributed in all the chains. Hence, the loss of any individual chain due to failure has a noticeable effect on the structure, leading to more pronounced **individual chain failure effect**.

The spatial distribution of failure points along the height of the specimen highlights this feature. For the 55 nm EV (Figure 5.31), failure sites become highly concentrated and the occurrence of failure is accelerated beyond 100 % of strain, where one chain's failure triggers surrounding chains to approach failure by taking on additional load. This reflects the load transfer interconnectivity between the chains. However, for smaller EVs (40 nm) (Figure 5.30), the distribution of failure is more dispersed throughout the deformation. This indicates the lack of chain-to-chain load transfer, which is consistent the non-uniformity of stress distribution.

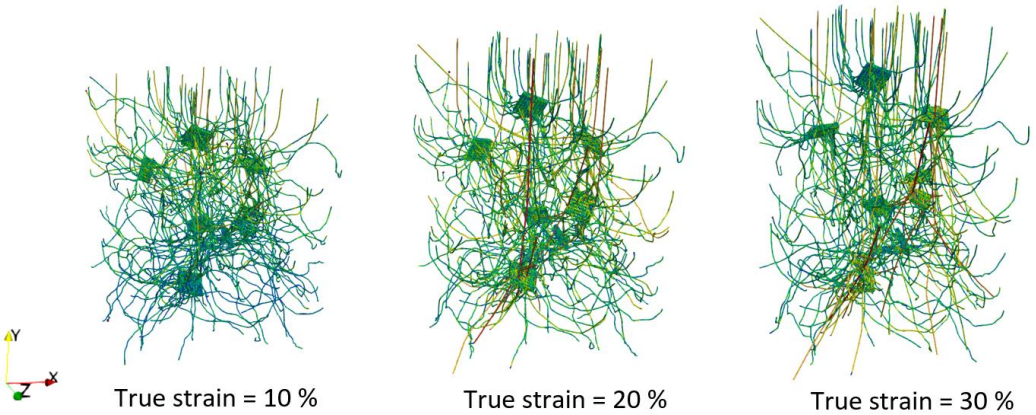
Furthermore, the lack of a clear maximum stress for smaller EVs could be attributed to local damage accumulation that is more prominent and has a greater effect on the material's overall stress response. These local failures contribute to the increasing variability in the stress-strain curve and in the CV. Additionally, the higher stress observed at larger EVs is primarily due to the well-connected, complex structure.

By zooming-into the crystallites in Figure 5.28, crystallite fragmentation happens prematurely, starting as early as 30% of strain, for smaller EVs (40 nm). In contrast, for the 55 nm EV, the crystallites remain intact at similar deformation levels (i.e., 30%), as seen in Figure 5.29, demonstrating that larger EVs help distribute the local stresses more effectively, with reduced boundary effect**.** Smaller EV, on the other hand, lack this structural support, making crystallites more susceptible to stress localization, caused by boundary effect, and consequently leads to early failure. This highlights that individual chain failure or crystallite fragmentation can significantly impact the overall response in smaller EV, due to boundary effects.

The stress strain distribution at four different heights of the specimen is shown in Figure 5.32, Figure 5.12 and Figure 5.33 for 40, 50, 55 nm respectively. Figure 5.32 (40 nm) shows higher variation and fluctuations, although it indicates a more uniform-stress distribution as the curves closely superimpose. This uniformity across height levels is somewhat misleading as it results from limited individual chains, lacking interconnectivity, and **withstanding the load individually**. By contrast, for higher EV

(50 and 55 nm), less fluctuation emerged, with pronounced non-uniformity of stress beyond 100 % of strain across height. This is mainly related to the interconnected network that leads to **localized stress accumulation in different regions**. Consequently, this indicates that even at a 55 nm EV, boundary effects contribute to non-uniformity across the specimen.

This result highlights a key observation: in smaller EVs, with fewer chains, the response is highly dependent of individual chains, resulting in greater variability and fluctuations in stress-strain behavior. In contrast, larger EVs demonstrate a more interconnected network leading to reduced stress variability with less sensitivity to individual chains. However, for the examples considered, even for the 55 nm EV, the boundary effects and the stress localization effects on the macroscopic uniformity of the stress across the specimen are not fully mitigated, although they are less pronounced at lower deformations levels. This highlights that the EV sizes used may not be large enough to completely avoid these effects. Nonetheless, due to computational time limitations related to the number of particles, the next simulations are conducted with a 50 nm EV. But, it is worth to keep in mind that while this choice helps reduce computational demands, the boundary effects cannot be fully avoided at higher deformation levels.



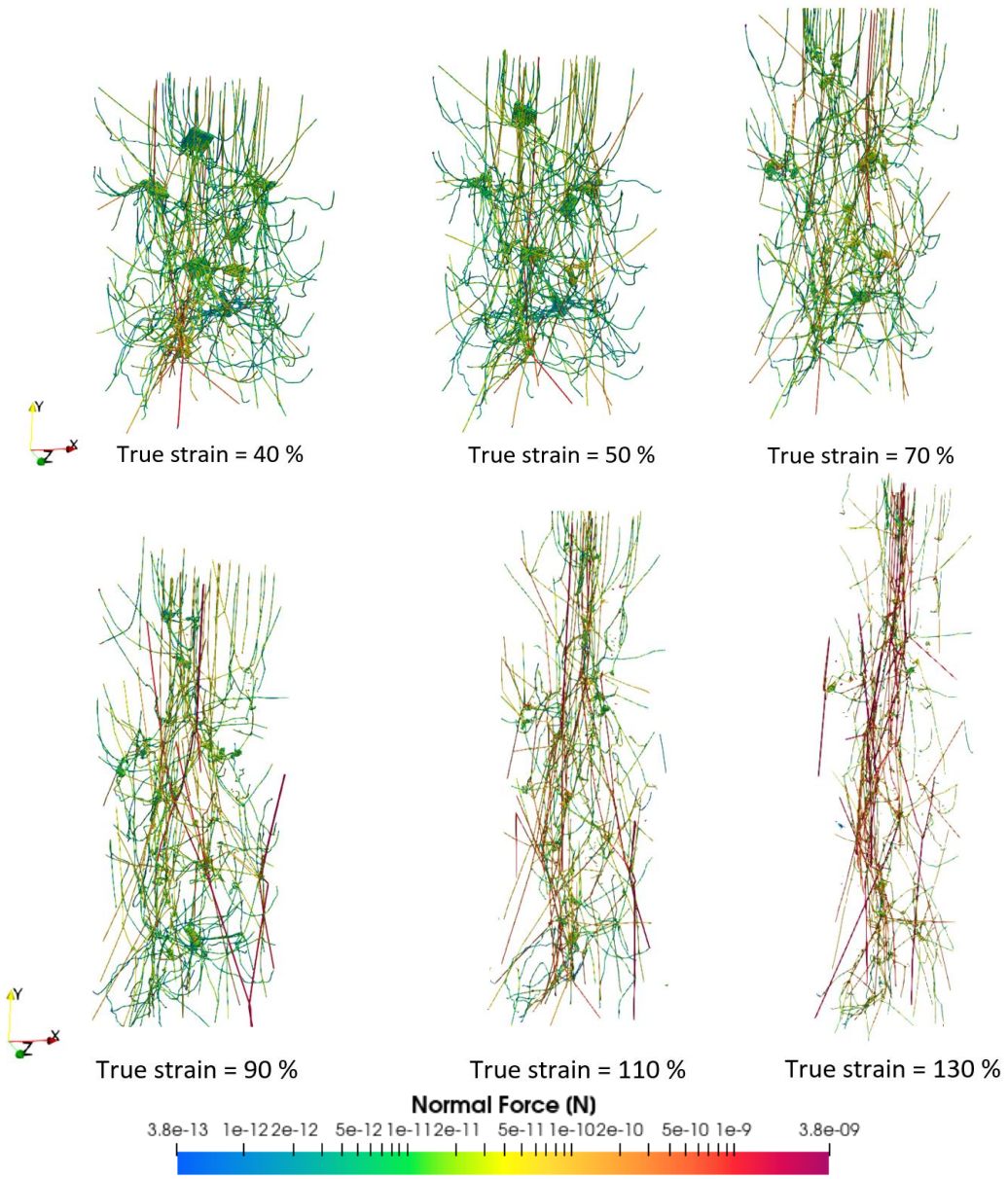
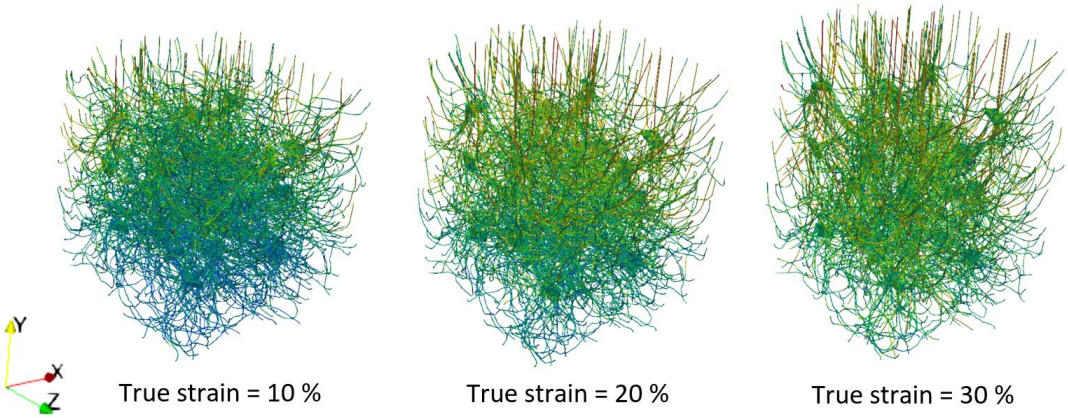


Figure 5.26: Force distribution map within the chains for 40 nm EV sizes (Specimen (1)).



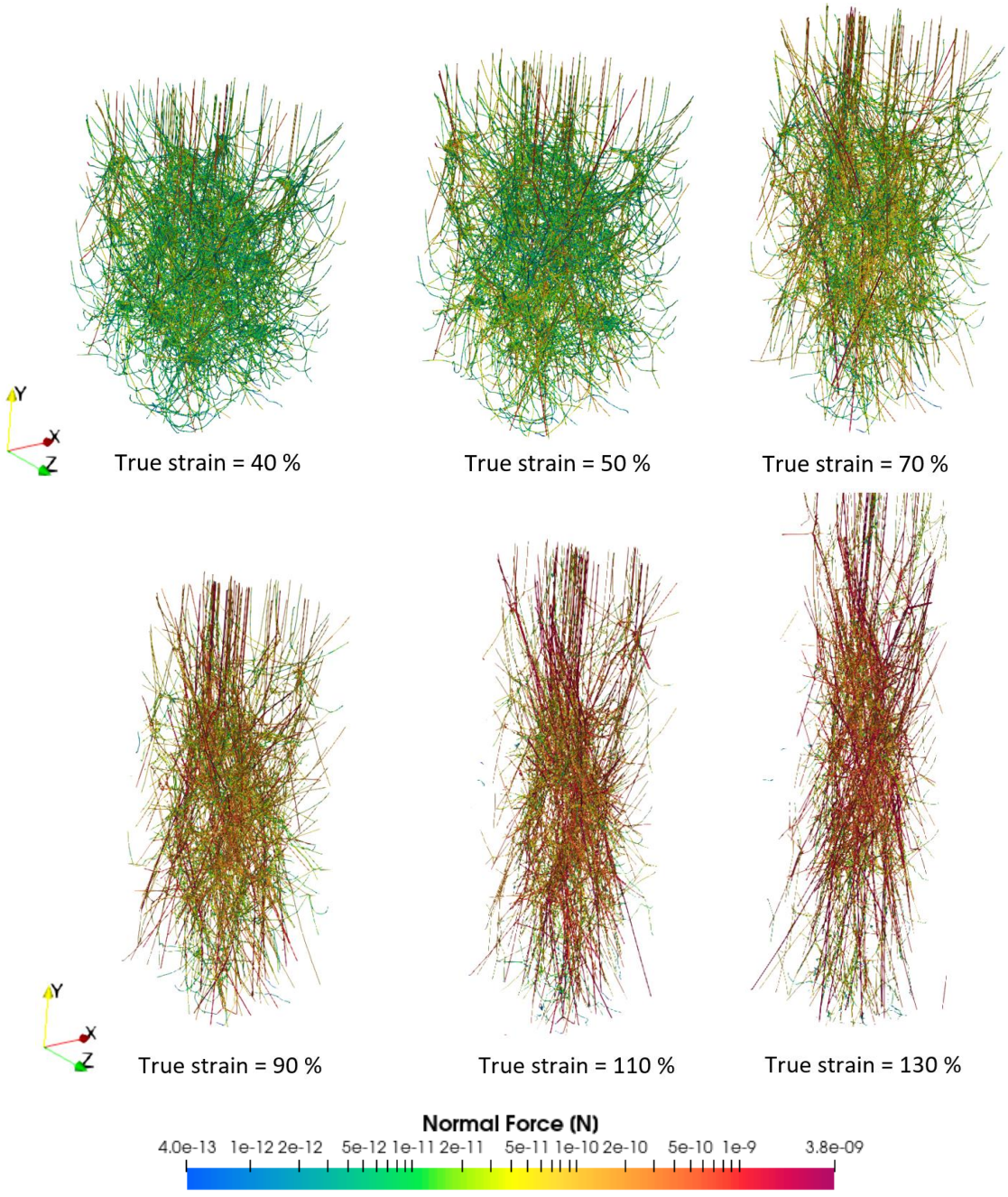


Figure 5.27: Force distribution map within the chains for 55 nm EV sizes (Specimen (1)).

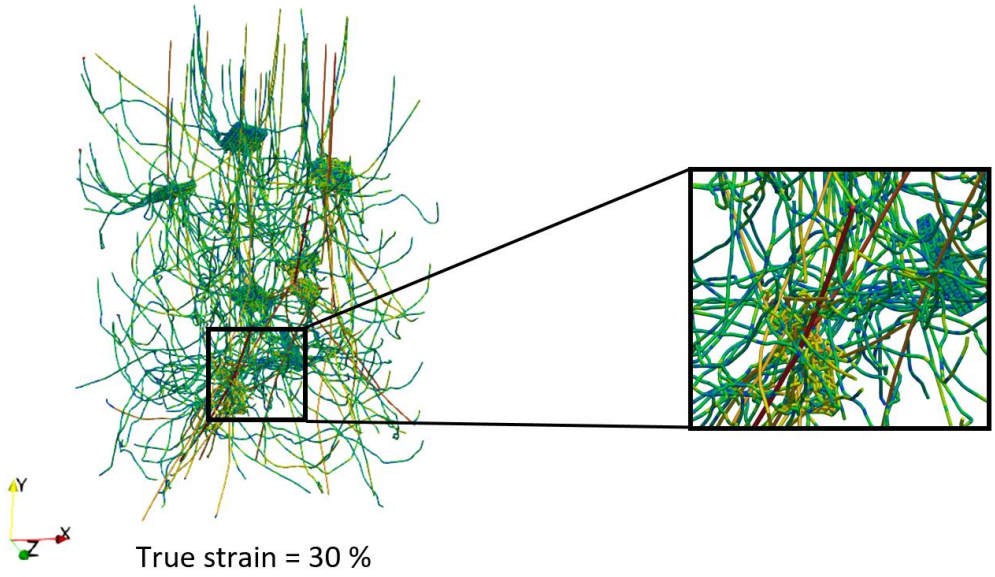


Figure 5.28: Close-up visualization of the crystallites within the microstructure at 30% of deformation level for a **40 nm** EV sizes (specimen (1)).

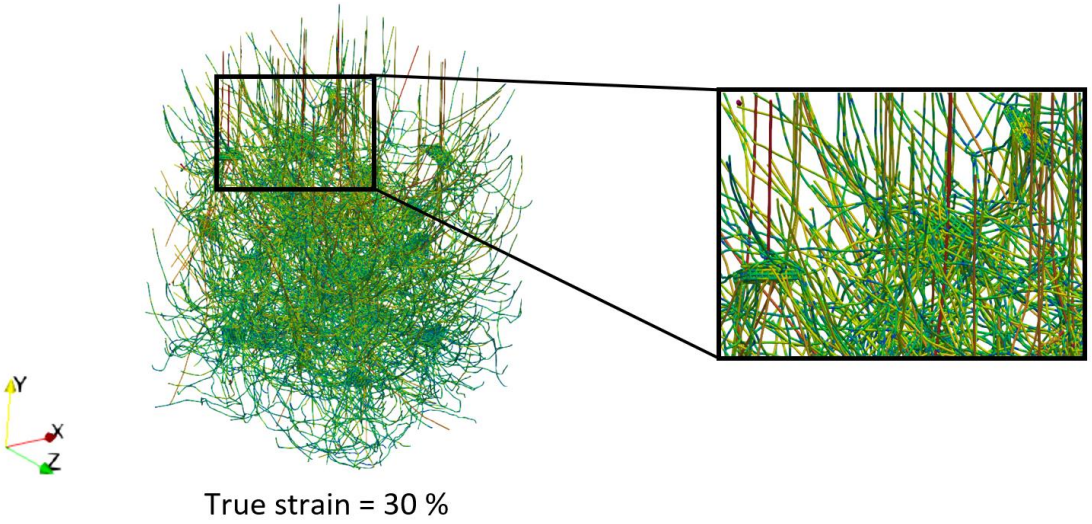


Figure 5.29: Close-up visualization of the crystallites within the microstructure at 30% of deformation level for a **55 nm** EV sizes (specimen (1)).

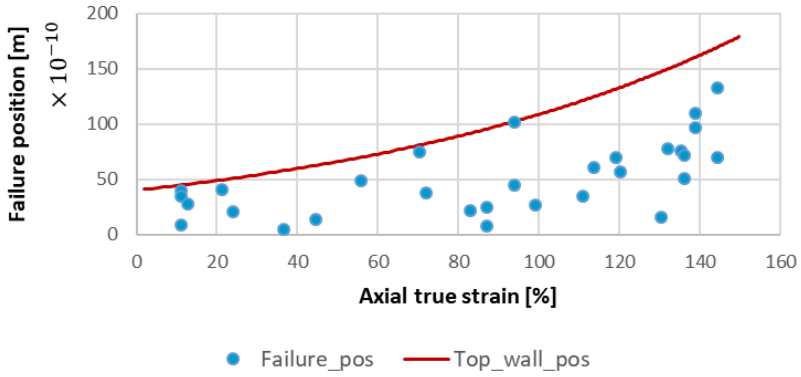


Figure 5.30: Spatial distribution of the failure point along the height of the specimen (1) with **40 nm** EV sizes.

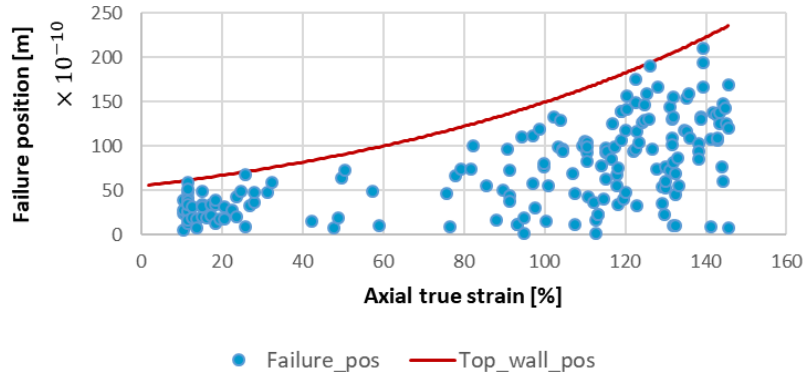


Figure 5.31: Spatial distribution of the failure point along the height of the specimen (1) with **55 nm** EV sizes.

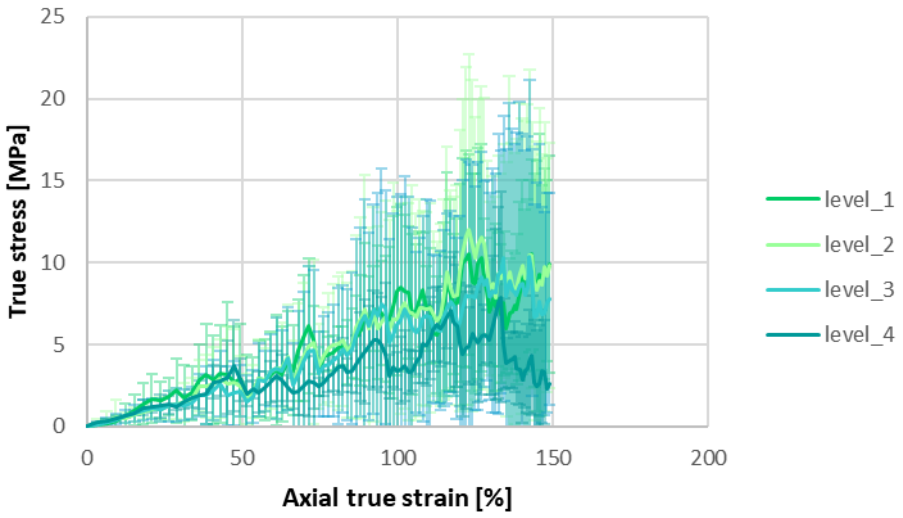


Figure 5.32: Average stress distribution at four different height levels (i.e., 25, 50, 75, and 100 % of the current specimen height) for specimen with **40 nm** EV sizes.

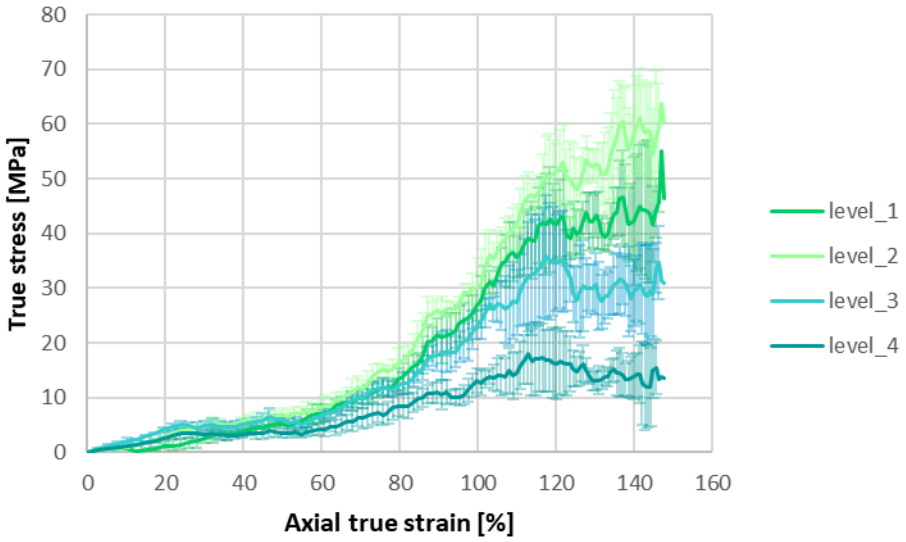


Figure 5.33: Average stress distribution at four different height levels (i.e., 25, 50, 75, and 100 % of the current specimen height) for specimen with **55 nm** EV sizes.

5.3.3. Comparison with experimental data

In Chapter 3, we outlined that the model is based on a multiscale approach, where the microscale parameters are informed by macroscale tests (i.e., experimental tests). Accordingly, this model was calibrated using the maximum stress observed in the experimental results in order to determine a primary value of an individual chain resistance (see Equation 3.17 and Table 5.1).

Given that the maximum stress level achieved numerically is not always distinctly defined, normalization is essential for proper comparison between experimental and numerical results. Thereupon, we selected a reliably identifiable point across all experimental and numerical tests for the normalization: 40 % of deformation. This point approximately lies within the linear part of the material response. Subsequently, a secant modulus, S, is calculated at 40 % of deformation, where the normalized axial true stress is determined according to Equation 5.1.

$$\sigma_{(t)}^{Normalized} = \frac{\sigma_{(t)}}{S} \tag{5.1}$$

Figure 5.34 presents a comparison of the normalized stress-strain behavior between the experimental and model's results. The experimental results were obtained at a tensile rate of 500 mm/min, corresponding to a strain rate of 0.1 /sec (see Figure 4.23), which is the maximum tensile rate achievable with the experimental setup machine. On the other hand, the model's tests were conducted for three EV sizes at a 4 /sec.

The results reveal that, in the experimental data, the stress-strain curve initially displays a linear response across a relatively wide range of deformation before transitioning into a nonlinear phase (80 % of strain). This later is higher than the numerical one, where **60%** of strain marks a clear transition between the linear and the non-linear behavior. This initial linear region, as observed in the microstructural analysis, corresponds to the alignment and orientation of polymer chains and crystallites under load, where some crystallites begin to fragment. The deviation to non-linear behavior is

due to several crystallites fragmentation, indicating a transfer in load-bearing contribution from the crystallites to the polymer chains. Thus, this suggests that the chain lengths are short enough for crystallite fragmentation occurring at a lower deformation level. Hereinafter, increasing **chains tortuosity**, and consequently the length of chains, could potentially increase the deformation level before multiple crystallite fragmentation. Additionally, intermolecular interactions have been somewhat approximated through micro-inertial effects, which do not precisely capture their influence. This contributes to the differences observed between numerical and experimental results.

Furthermore, outside the linear zone, the model response varies with EV sizes. Smaller EV sizes result in larger stress variations, highlighting that localized stress concentrations caused by individual chain failure have a major impact on material behavior. This suggests that increasing the **number of chains** and/or the **EV** size in the model may help to smooth out these variations by minimizing the local perturbation impact on the global behavior.

Interestingly, when comparing the EV sizes, the curves for the 50 nm and 40 nm sizes do not show a well-defined peak stress, whereas the curve for the 55 nm EV dimension reveals a peak at around 110% of strain —significantly lower than the failure strain, which occurs at 159%. This further supports the idea that the model's chain lengths may be insufficiently long to achieve a higher deformation level. Additionally, the model's curve for high EV sizes (e.g., 50, 55 nm) shows higher stress values compared to the experimental results. This is explained by the strong connectivity imposed by the crystallites that play the role of entanglements within the specimen. This leads to stress concentration in different regions, which, in turn, may rise the overall stress supported by the system. In addition, this can be related to the **inter-crystallite distance D**, which plays a significant role in the system's crystallinity level, and consequently, its rigidity. An increase in this distance reduces the degree of entanglements formed by the crystallites within the microstructure, potentially leading to a decrease in the system's overall resistance.

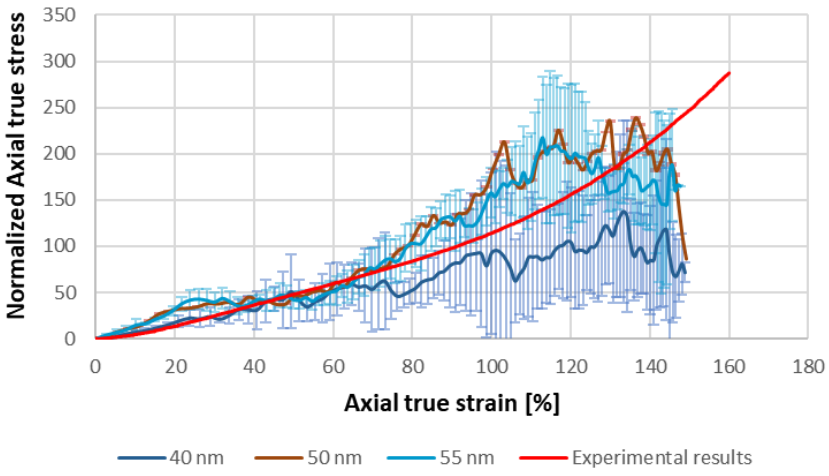


Figure 5.34: Comparison of experimental data and model results for different EV sizes (40 nm, 50 nm, 55 nm).

5.4. Impact of the number of chains per crystallite

In the reference simulation, the amorphous region is characterized by a chain density of 30 chains per crystallite. In this section, we will explore the impact of varying this density on the stress distribution and failure mechanisms, by considering two different values of the chain number parameter—one higher (40 chains per crystallite) and one lower (20 chains per crystallite) than the reference parameter. All other geometrical parameters remain consistent with the reference configuration, presented in Table 5.1, in order to assess specifically the effects of chain density on the model's macroscopic response. Due to time constraints, a single simulation was performed for each of these values. Table 5.2 presents the number of particles, the number of chains, and the final porosity for each simulation.

Note that in this analysis, non-isochoric boundary conditions were applied, meaning the material's volume was not strictly preserved (the applied boundary conditions impose here a decrease of the volume over time). This influences the relationship between axial and lateral strains (Figure 5.1), but the comparison remains meaningful as the same boundary conditions are consistently applied across all simulations.

Table 5.2: Impact of Chain Density on Particle Count and Specimen Porosity.

Parameters	**20 chains/crystallite**	**30 chains/crystallite**	**40 chains/crystallite**
Total chains number	360	540	720
Total nb of particles	84434	104430	123919
Average final porosity of the specimen	0.397	0.434	0.462

5.4.1. Stress-strain curves at different chain number per crystallite

Figure 5.35 shows the stress-strain response for varying chain densities per crystallite, highlighting a notable difference in the macroscopic response. The curves exhibit a linear trend up to approximately 60% of strain, which becomes more evident as the chain density increases. This increase in chain density within the amorphous region results in a greater load-bearing capacity.

Additionally, at low-to-moderate deformation (i.e., <80%), the higher chain density results in a smoother stress-strain response with reduced fluctuation compared to the lower density value. Beyond 80%, the failure rate of chains is sharply increased for higher density configuration (40 per crystallite), as seen in Figure 5.36. This escalation in failure leads to a lack of a well-defined maximum stress, as large-scale chain breakage disrupts the system's stability, creating irregularities and fluctuations in the stress-strain curve.

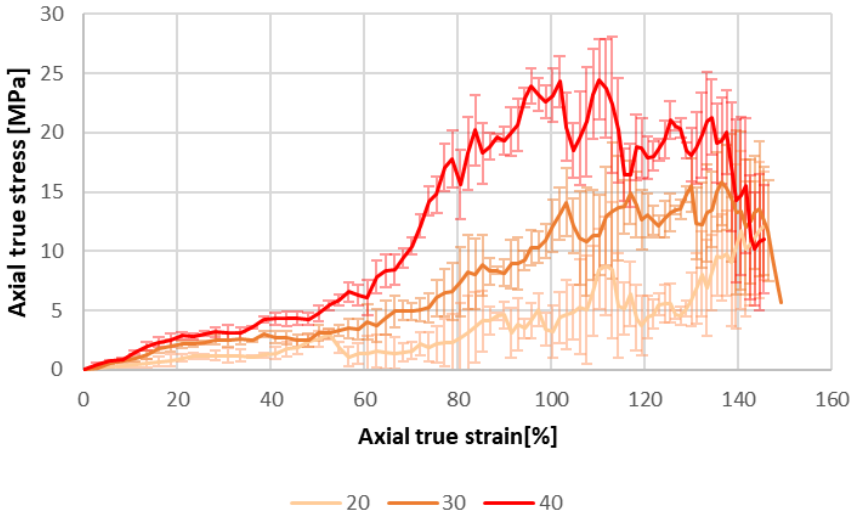


Figure 5.35: Stress-strain response at different chain densities per crystallite.

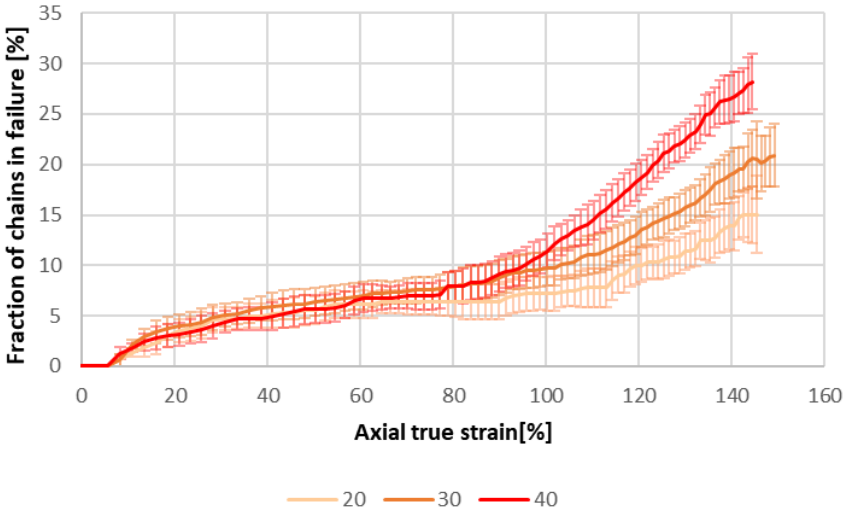


Figure 5.36: Fraction of chains in failure at different chain densities per crystallite.

5.4.2. Force distribution maps at different chain density

Figure 5.37 and Figure 5.38 show the force distribution color maps at different chain densities per crystallite, highlighting the influence of chain density on stress distribution across the specimen.

The force distribution color maps show that, in both specimens, there is a quasi-uniform distribution of color across the material, with chains marked in red indicating that they are highly stressed and approaching failure. However, in the specimen with a higher number of chains per crystallite, the impact of these **individual chain failures** on the overall material behavior is less pronounced. Despite some chains reach failure (indicated by the red color), the global stress distribution remains relatively stable because the higher density of chains allows for better load redistribution across the network.

Additionally, as shown in Figure 5.38, higher chain density contributes to improved system connectivity, resulting in increased resistance and the ability to sustain higher

stress values. This denser network reduces the impact of individual chain failures on the global material behavior.

As the deformation progresses beyond 70%, the specimen with higher chain density exhibits significant perturbations in the force distribution, evidenced by the spread of red areas indicating chains nearing failure. While the network is denser, leading to greater load-bearing capacity, the higher number of chains also results in a more rapid accumulation of localized failures, as the failure of one chain triggers the surrounding chains' failure. These failures cause noticeable fluctuations and perturbations in the system, disrupting the overall material response.

The presence of a higher number of chains in the amorphous region creates more points of stress concentration, leading to early failure in the crystalline regions. For the specimen with 40 chains per crystallite, crystallite fragmentation occurs at 30% of deformation (see Figure 5.40) while for the specimen with 20 chains per crystallite, the first crystallite fragmentation is observed at 40% of strain (see Figure 5.39).

However, this premature failure does not show a big variation in the stress strain curve, as the curve remains linear until 60 % of deformation for higher number of chains. However, after further crystallite fragmentation, as seen in Figure 5.41, the load-bearing contribution is switched from the crystallites to the polymer chains and the deviation of the curve becomes evident at 60 % of strain.

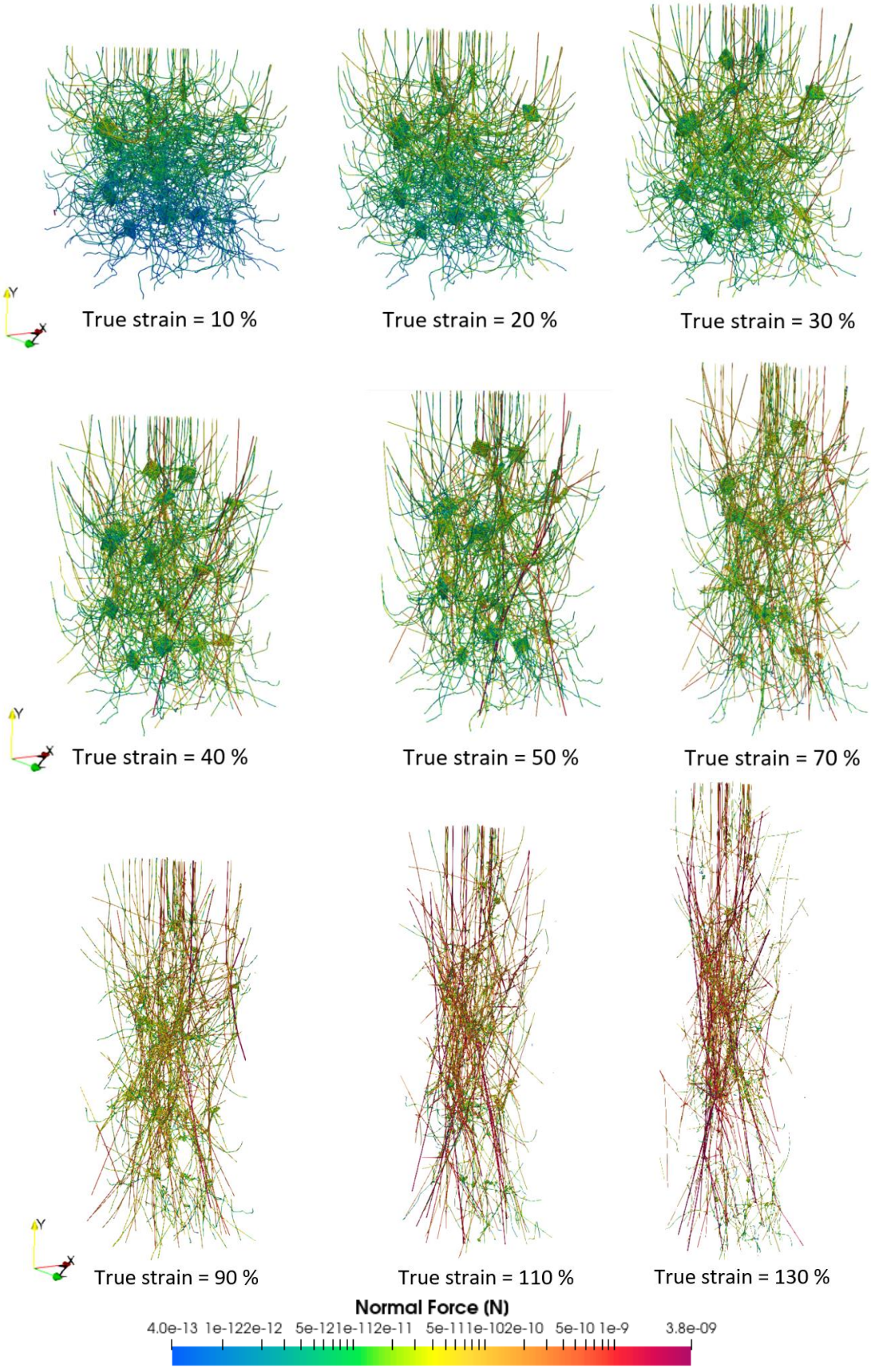


Figure 5.37: Force distribution for a specimen with 20 chains per crystallite.

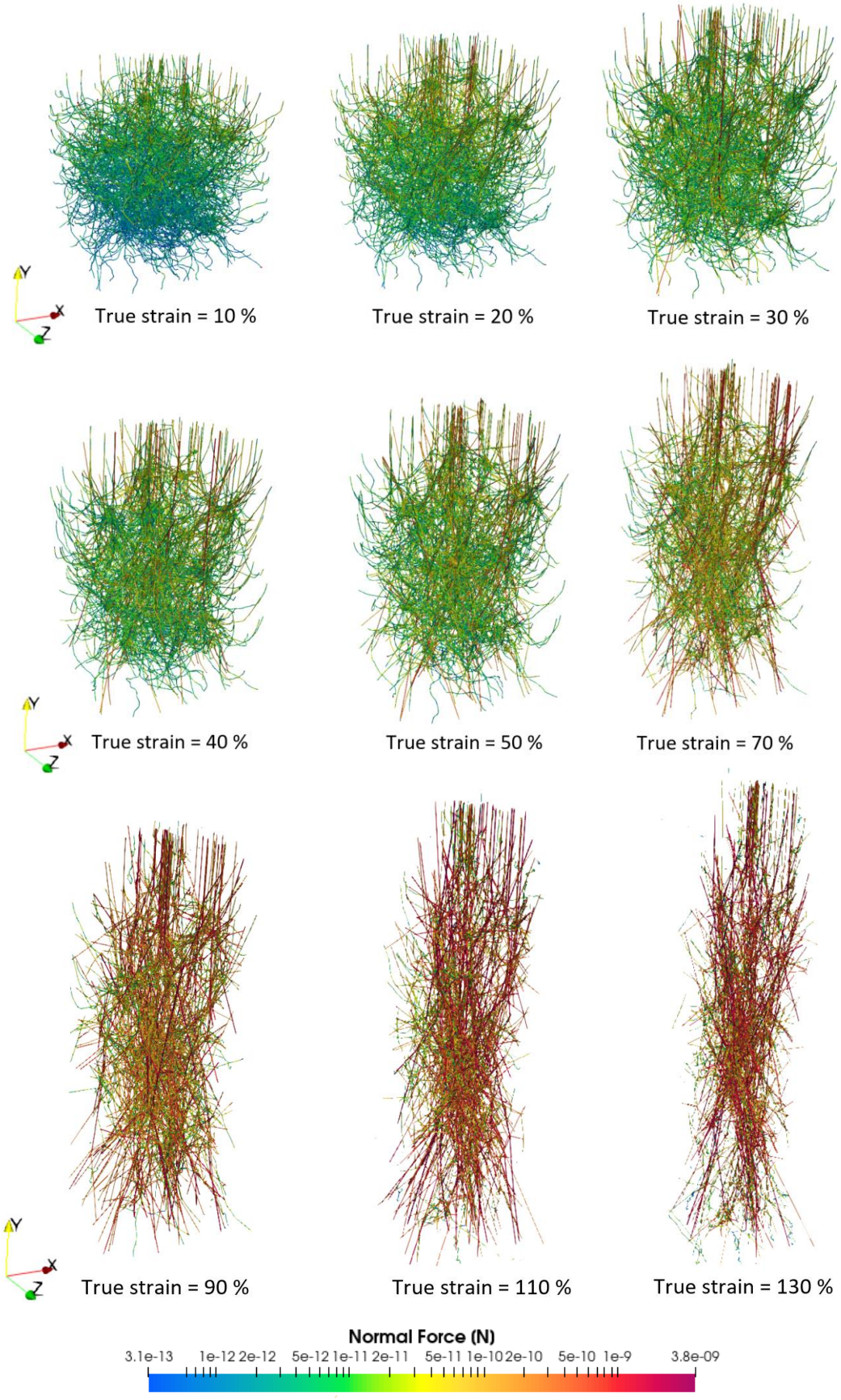


Figure 5.38: Force distribution for a specimen with 40 chains per crystallite.

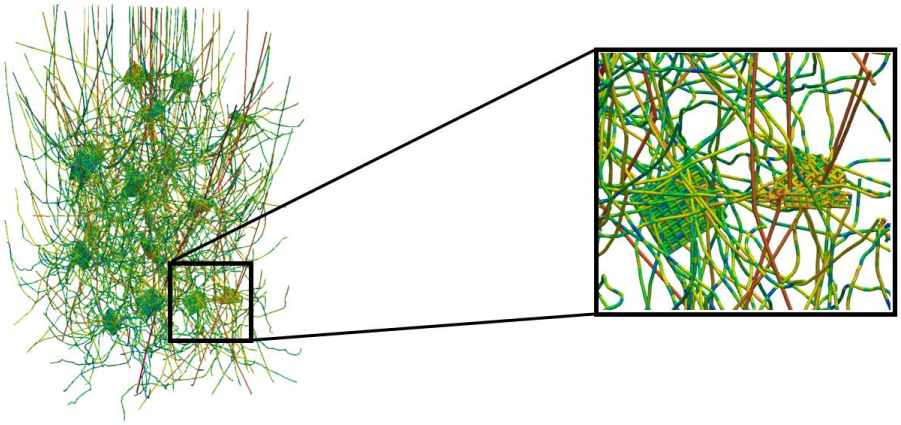


Figure 5.39: First appearance of crystallite fragmentation for specimen with 20 chains per crystallite.

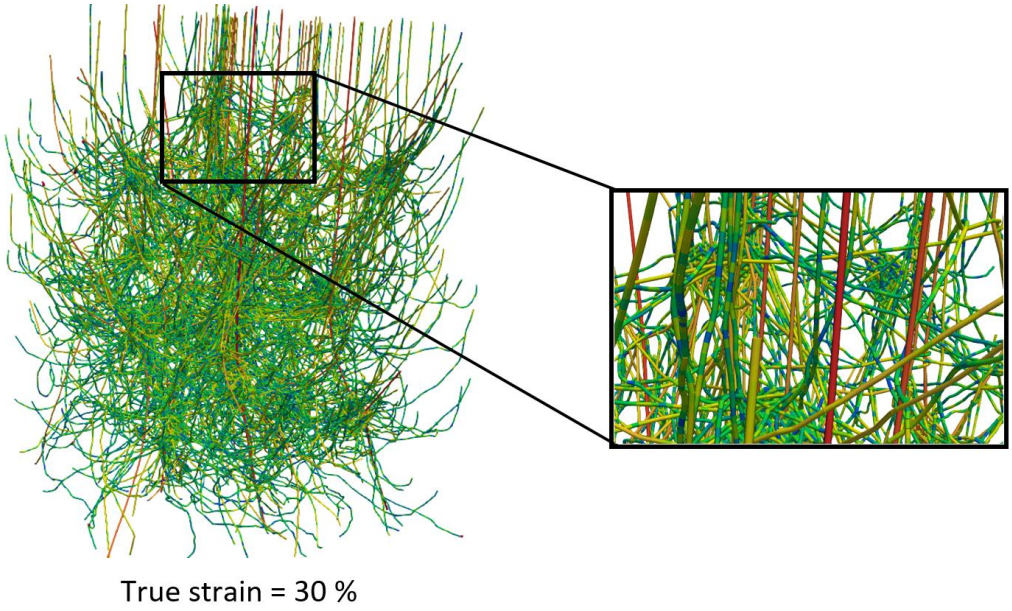


Figure 5.40: First appearance of crystallite fragmentation for specimen with 40 chains per crystallite.

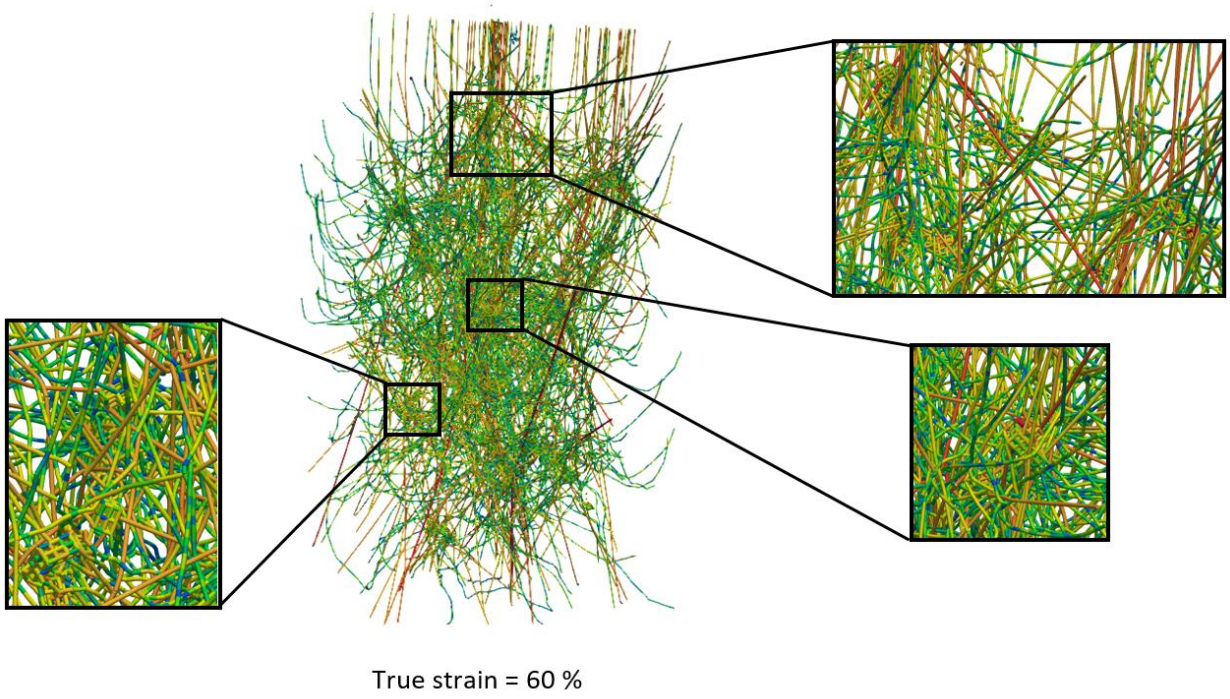


Figure 5.41: Complete fragmentation of crystallites in specimen with 40 chains per crystallite at 60% of strain.

5.4.3. Stress uniformity across the specimen

The stress distribution across the specimen, observed in Figure 5.43, reveals that for higher chain densities, the stress-strain curves at various specimen heights remain closely aligned up to 70% of strain.

In contrast, specimen with fewer chains shows noticeable differences in stress distribution even at lower deformation levels (i.e., 40% strain), as shown in Figure 5.42. This could be explained by the fact that with smaller number of chains, the boundary effect plays a significant role. Additionally, the local failures induced by individual chains rupture have a considerable impact on the overall stress distribution.

Beyond 70 % of strain, specimen with higher number of chains, that exhibits a complex network, results in stress perturbations and a non-uniform stress distribution across the specimen.

Consequently, this suggests that the number of chains used presents a dilemma, where increasing the number of chains reduces the effect of individual local chains failure, and enhances the force distribution throughout the specimen at low-to-moderate deformation. However, at high deformations, the intricate network with localized failures in high-stress regions may lead to a non-uniform stress distribution across the specimen.

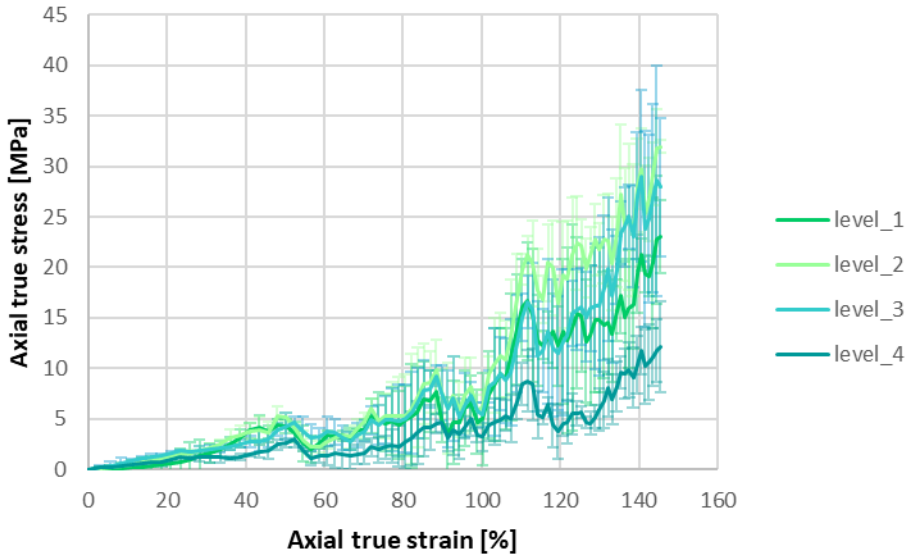


Figure 5.42: Stress distribution at four different height levels (i.e., 25, 50, 75, and 100 % of the current specimen height) for a specimen with **20 chains** per crystallite.

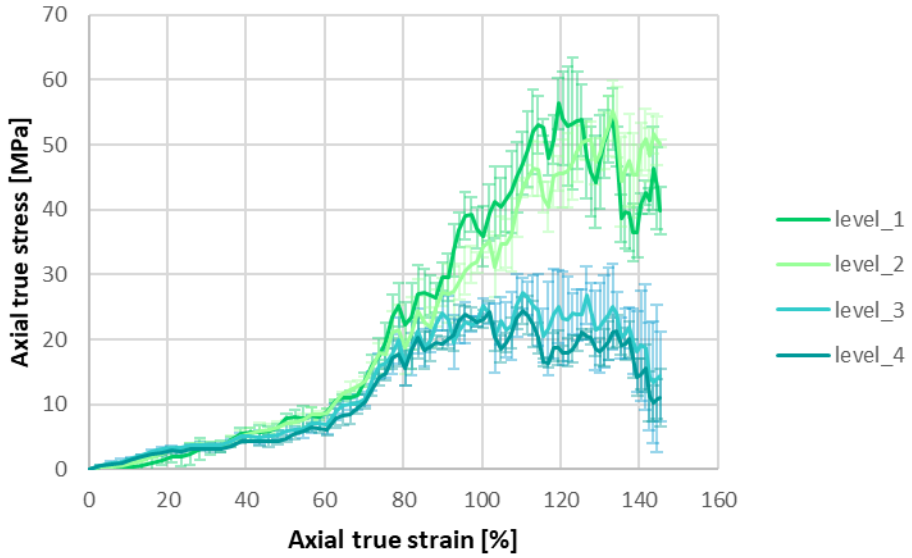


Figure 5.43: Stress distribution at four different height levels (i.e., 25, 50, 75, and 100 % of the current specimen height) for a specimen with **40 chains** per crystallite.

5.5. Impact of the chain's length on the model results

The chain's tortuosity plays a significant role in defining the density of the amorphous region, greater tortuosity results in longer chains, which subsequently impacts how crystallites are interconnected within the 3D network. This property is controlled by the maximum deviation angle θ_{max} used for the generation of the chains within the amorphous region, through random walk algorithm discussed in Chapter 3 (refer to Section 3.1.3). In this section, we will investigate the impact of chain length on the model's mechanical behavior and failure mechanisms, providing insight into how chain tortuosity shapes overall performance.

To reach our goal, three values of θ_{max} have been considered $[0.08\,\pi, 0.1\,\pi, 0.12\,\pi]$ rad, with $0.1\,\pi$ rad serving as the reference parameter used in the reference simulation. All other parameters remain unchanged (Table 5.1). This combination of geometric parameters results in the number of particles and porosity values shown in Note that in this analysis, non-isochoric boundary conditions were applied, meaning the material's volume was not strictly preserved (the applied boundary conditions impose here a decrease of the volume over time). This influences the relationship between axial and lateral strains (Figure 5.1), but the comparison remains meaningful as the same boundary conditions are consistently applied across all simulations.

Table 5.3. Figure 5.44 shows the distribution of chain lengths for each θ_{max} value.

Note that in this analysis, non-isochoric boundary conditions were applied, meaning the material's volume was not strictly preserved (the applied boundary conditions impose here a decrease of the volume over time). This influences the relationship between axial and lateral strains (Figure 5.1), but the comparison remains meaningful as the same boundary conditions are consistently applied across all simulations.

Table 5.3: Impact of chain length on particle count and specimen's porosity.

Parameters	$\theta_{max} = 0.08\,\pi$	$\theta_{max} = 0.1\,\pi$	$\theta_{max} = 0.12\,\pi$
Total chains number	540	540	540
Total nb of particles	96938	104435	115771
Average final porosity of the specimen	0.465	0.434	0.513

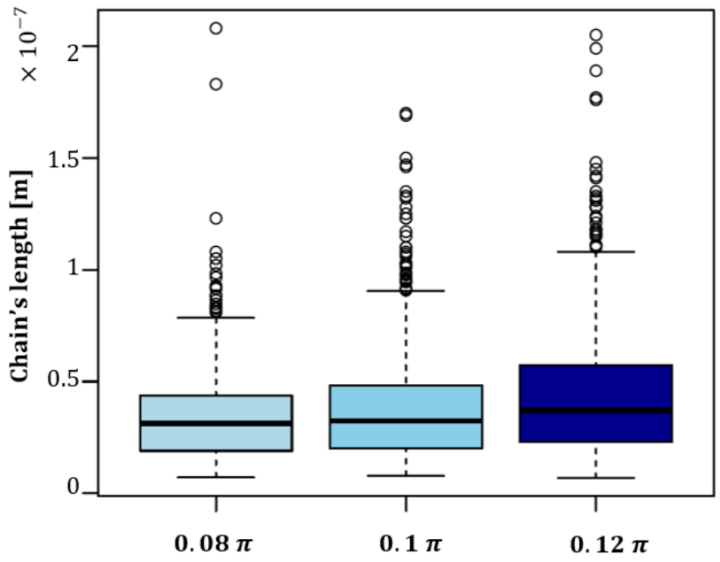


Figure 5.44: Chain length distribution in function of the orientation angle θ_{max} (rad).

5.5.1. Impact of chain's length on the stress-strain curve

The stress-strain curve, shown in Figure 5.45, reveals that when the chains length is increased, the curve becomes smoother, exhibiting fewer fluctuation compared to shorter

chains. Additionally, the quasi-linear part of the curve becomes more pronounced with longer chains, reaching higher level of deformation before transitioning to non-linear part (70-80% of strain). In contrast, the transition to non-linear behavior is less detectable for lower chains length, due to high stress fluctuation.

Correspondingly, Figure 5.46 shows the fraction of chains failed, which noticeably decreases with increasing chain length, suggesting an improved structural stability. This reduction in chain failure fraction aligns with the observed smoother stress-strain response in Figure 5.45, emphasizing the role of longer chains in distributing stress more effectively.

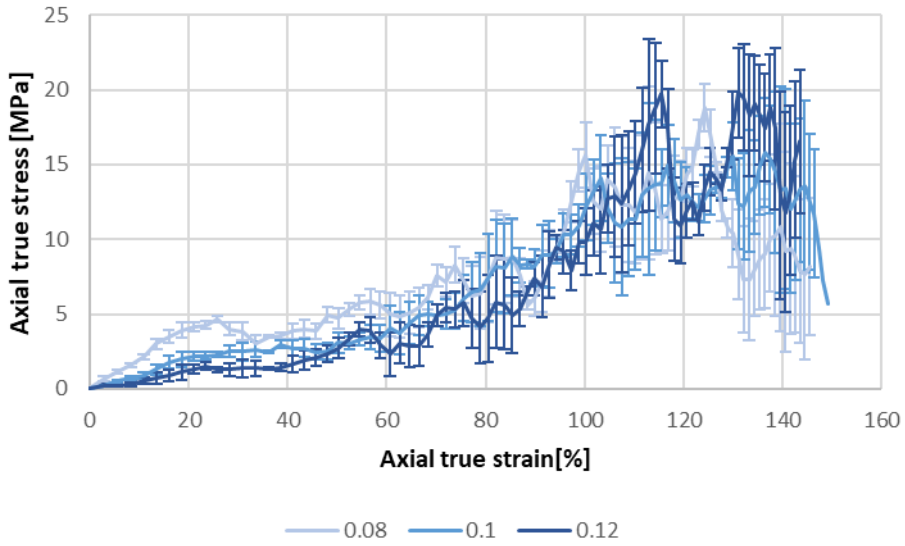


Figure 5.45: Stress-strain with different chain's length represented by different θ_{max} (in radians).

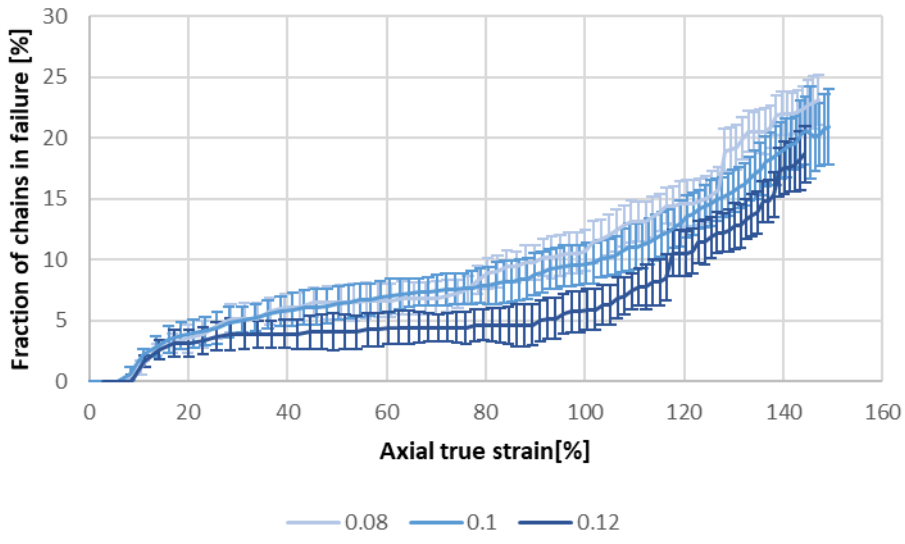


Figure 5.46: Fraction of chains in failure with different chain's length represented by different θ_{max} (in radians).

5.5.2. Microstructural analysis and force distribution

Comparing the force distribution colored-map between longer and shorter chains, as seen in Figure 5.47 and Figure 5.48, reveals distinct constitutive trends under loading. At the early deformation (**<10% of strain**), chains with greater lengths experience a smaller stress level, as indicated by the widespread presence of cold colors (blue and green) across the specimen. As deformation increases, the cold colors persist and spread throughout the specimen, even up to 50% of strain in longer chains. This highlights a well-distributed and uniform stress distribution within the material, minimizing stress localization in critical regions such as crystallites and chain entanglements.

In contrast, shorter chains, shown in Figure 5.47, exhibit non-uniform force distribution much earlier, with stress localization becoming apparent beyond 20% deformation. This is visualized by the appearance of warmer colors (yellow and red), indicating regions of higher stress concentration. Such localized forces lead to premature failure within the crystallite for specimen with shorter chains, as evidenced by the first crystallite fragmentation occurring at only 20% of strain (Figure 5.49). For the specimen with longer chains, however, the beginning of crystallite fragmentation is delayed until 60% of strain (Figure 5.50).

The non-uniform force distribution in shorter chains results in higher stress variability and perturbations in the stress-strain curve, as the load is not uniformly distributed and is significantly affected by localized stress concentrations. Additionally, upon closer analysis, complete crystallite fragmentation occurs at 50% deformation for shorter chains (see Figure 5.51), while for longer chains, this happens at 80% of deformation (see Figure 5.52). This delay correlates with the transition to nonlinear behavior observed in the stress-strain curve (Figure 5.45), further illustrating the structural benefits of longer chains in delaying mechanical failure.

Beyond **80% of strain** in specimens with longer chains, fluctuations in the stress-strain response become more noticeable, as chains exhibit red color, indicating that they approach failure. Thus, these fluctuations reflect the global impact of individual chain failures as the chains approach the ultimate stress limit. This fluctuation is merely attributed to the number of chains and the elementary volume (EV) used. Previous analysis showed that, i) increasing the number of chains decreases the impact of individual chain failures on the global stress-strain response and ii) increasing the EV reduces the influence of boundary conditions. Therefore, these factors are largely responsible for the stress variability observed in specimens with longer chains specimen that exceed 80% of strain. This demonstrates how material and structural characteristics interact at high deformation levels.

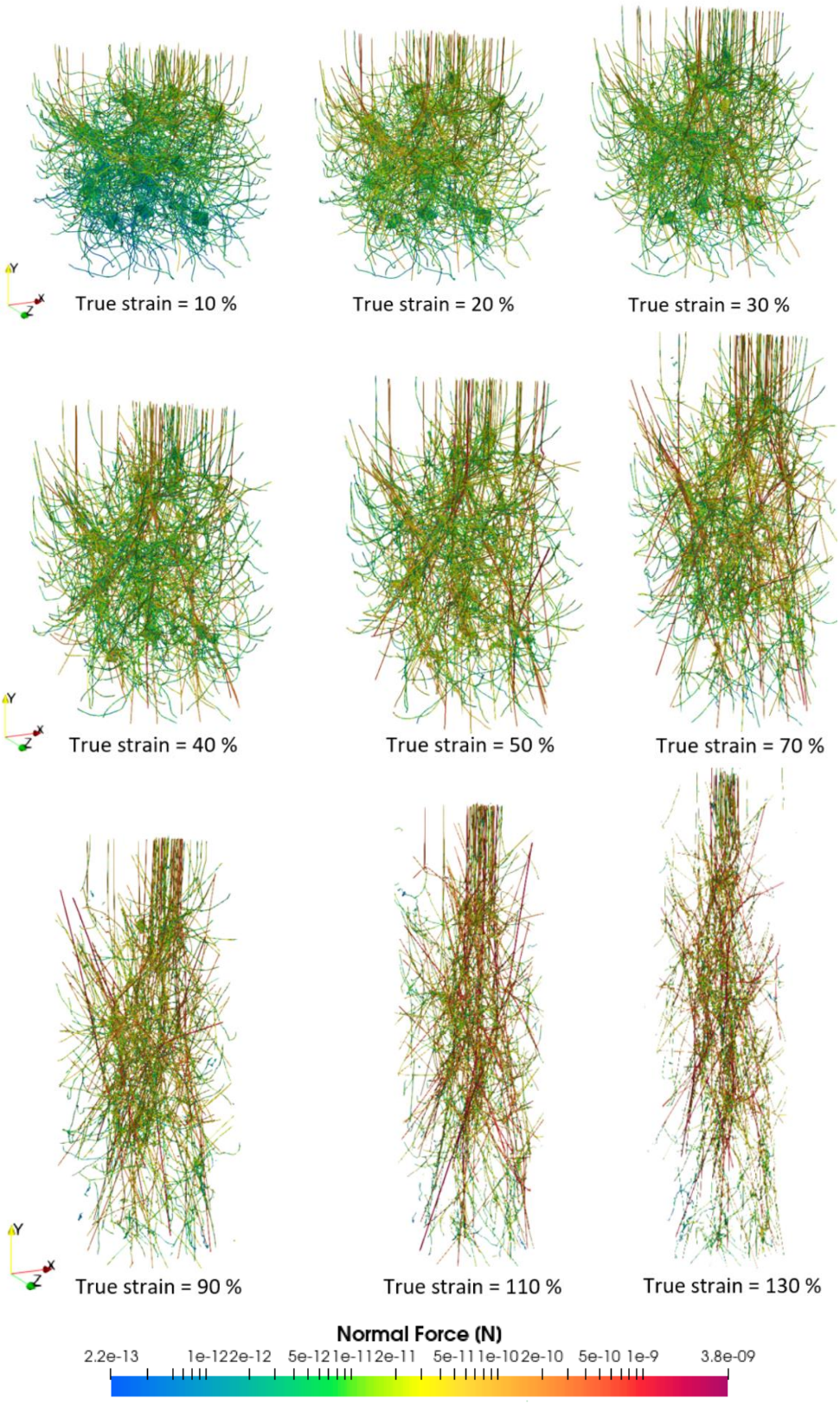


Figure 5.47: Force distribution for a specimen with $\theta_{max} = 0.08\,\pi$ rad.

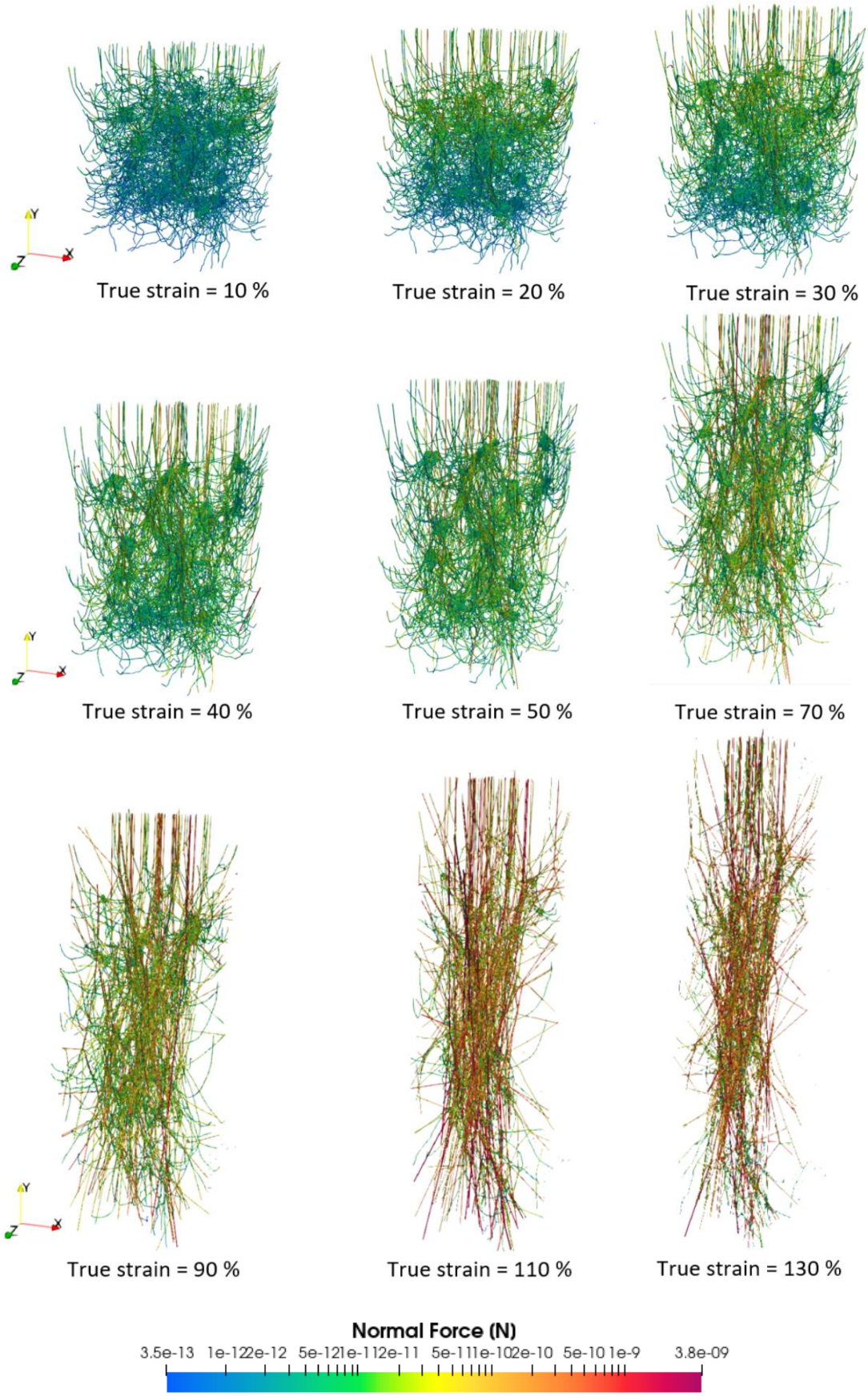
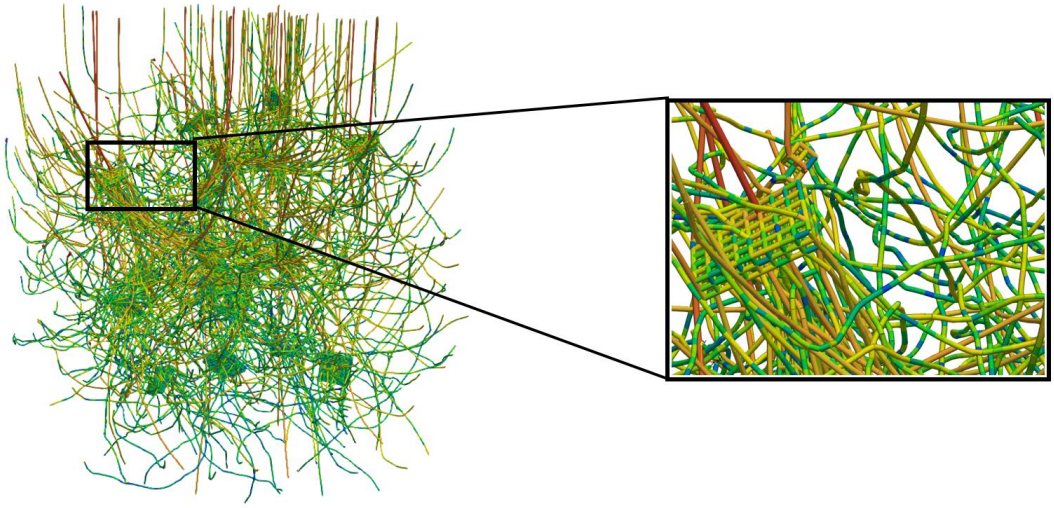
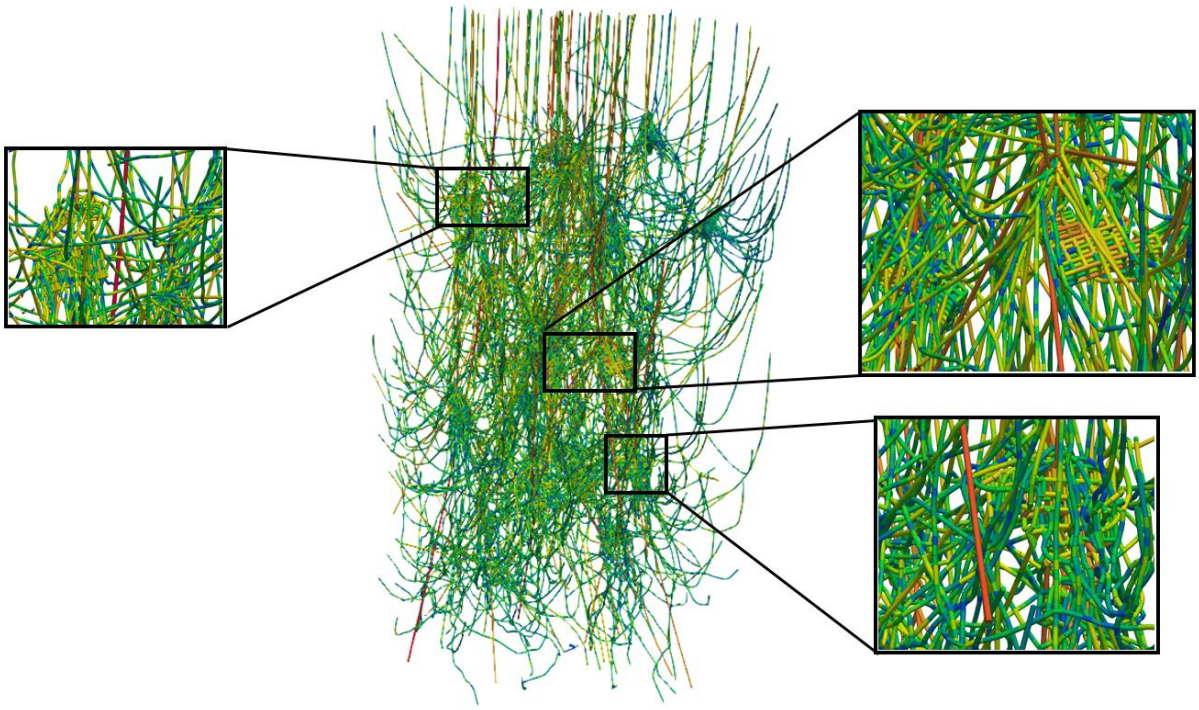


Figure 5.48: Force distribution for a specimen with $\theta_{max} = 0.12\ \pi$ rad.



True strain = 20 %

Figure 5.49: First appearance of crystallite fragmentation for specimen with shorter chains and less tortuosity ($\theta_{max} = 0.08\ \pi$).



True strain = 60 %

Figure 5.50: First appearance of crystallite fragmentation for specimen with longer chains and higher tortuosity ($\theta_{max} = 0.12\ \pi$).

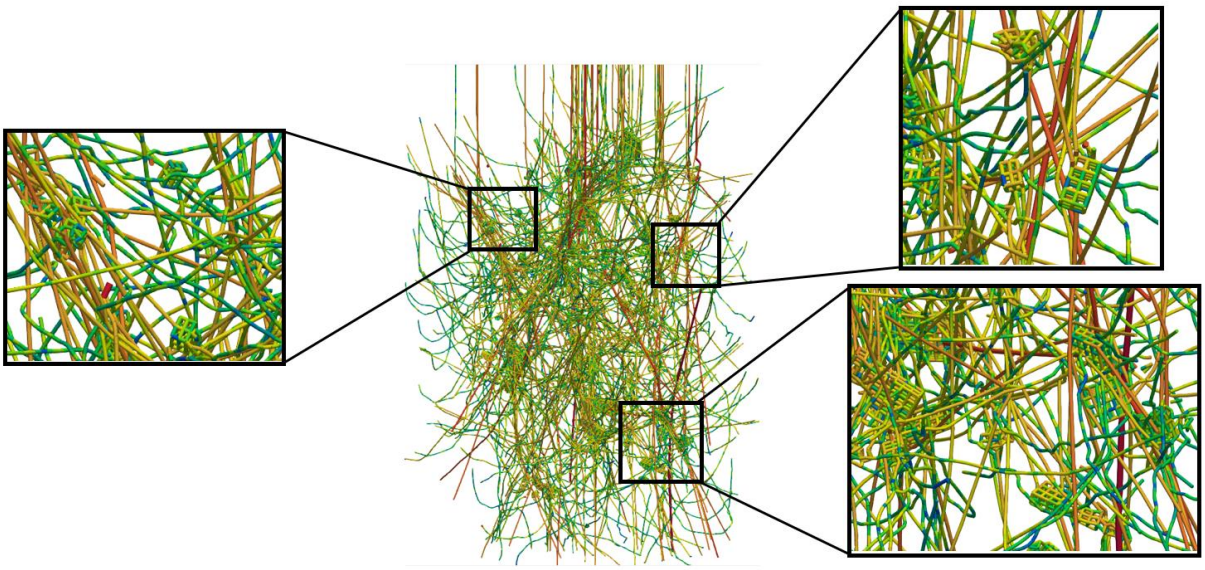


Figure 5.51: Complete fragmentation of crystallites in specimen with shorter chains and less tortuosity ($\theta_{max} = 0.08\ \pi$).

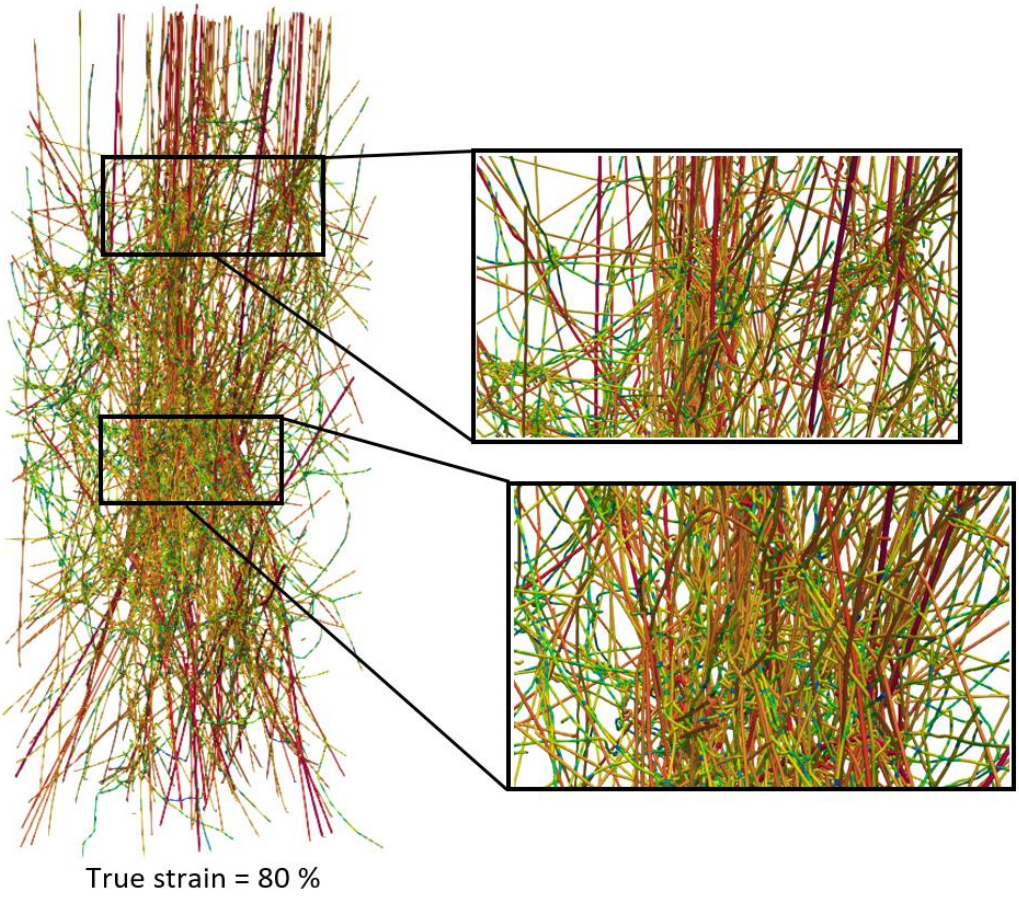


Figure 5.52: Complete fragmentation of crystallites in specimen with longer chains and higher tortuosity ($\theta_{max} = 0.12\ \pi$).

5.5.3. Stress uniformity across the specimen

As observed in Figure 5.53, Figure 5.12, and Figure 5.54, stress uniformity has been improved significantly with increasing chain length. This behavior can be attributed to more uniform force distribution observed in Figure 5.48. Additionally, for longer polymer chains, failure is predominantly concentrated beyond 100% of strain, as observed in Figure 5.56. This observation indicates that under lower strain levels, these longer chains remain largely intact. Few chains exhibit failure, highlighting less variability of stress. In contrast, with shorter chains (see Figure 5.55), the chain's failure position locates randomly during the test, creating high local variation of stress and stress concentration in different regions across the specimen.

By comparing the interactions between the plasticizer and the chains, it is evident that these interactions are more uniformly distributed across the material when the chains are longer (Figure 5.58). In contrast, with shorter chains (Figure 5.57), the plasticizer interactions become more concentrated in the upper part of the specimen, highlighting significant stress localization in this region.

Longer chains effectively distribute the applied load uniformly throughout the material, minimizing the occurrence of localized stress concentrations. There is less brittle failure in specific regions, as the uniform stress distribution prevents the formation of critical stress spots. Consequently, longer chains enhance the **overall structural integrity** and **mechanical stability** of the specimen under deformation.

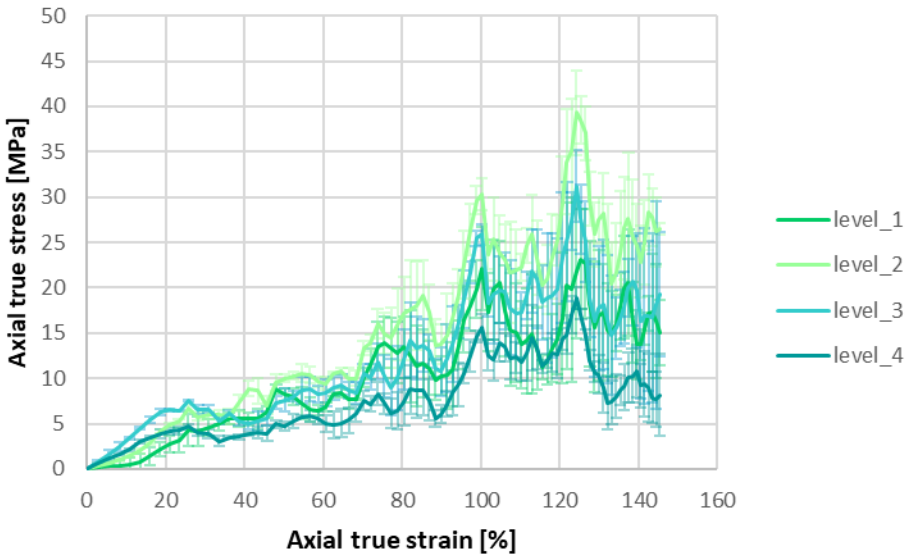


Figure 5.53: Stress distribution at four different height levels (i.e., 25, 50, 75, and 100 % of the current specimen height) for a specimen with $\theta_{max} = 0.08\ \pi$ rad.

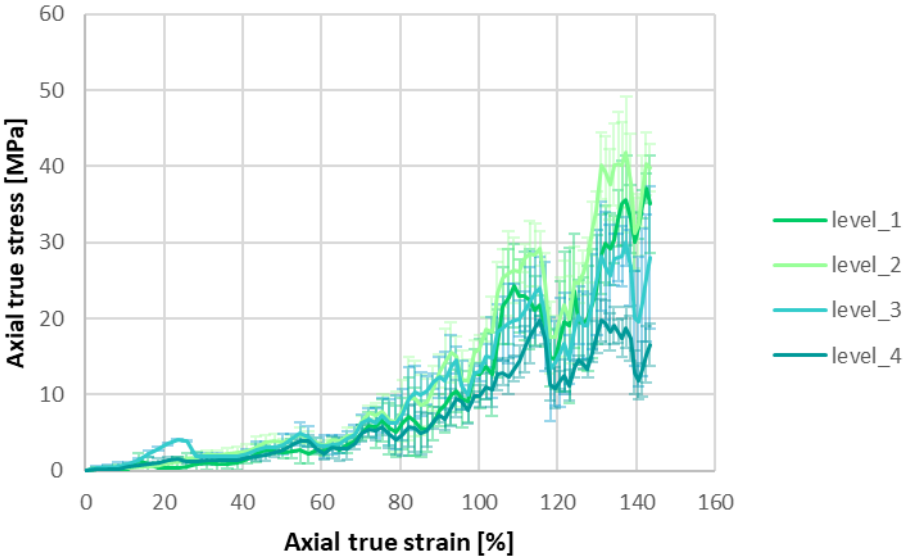


Figure 5.54: Stress distribution at four different height levels (i.e., 25, 50, 75, and 100 % of the current specimen height) for a specimen with $\theta_{max} = 0.12\ \pi$ rad.

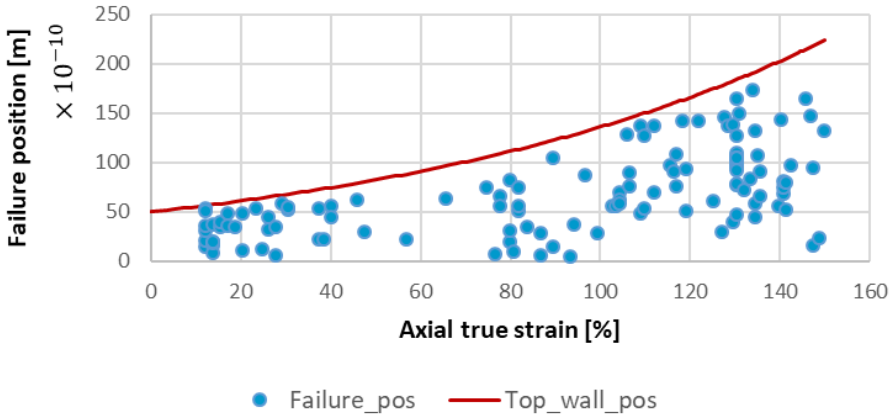


Figure 5.55: Spatial distribution of the failure point along the height of the specimen with shorter chains ($\theta_{max} = 0.08\ \pi$ rad)

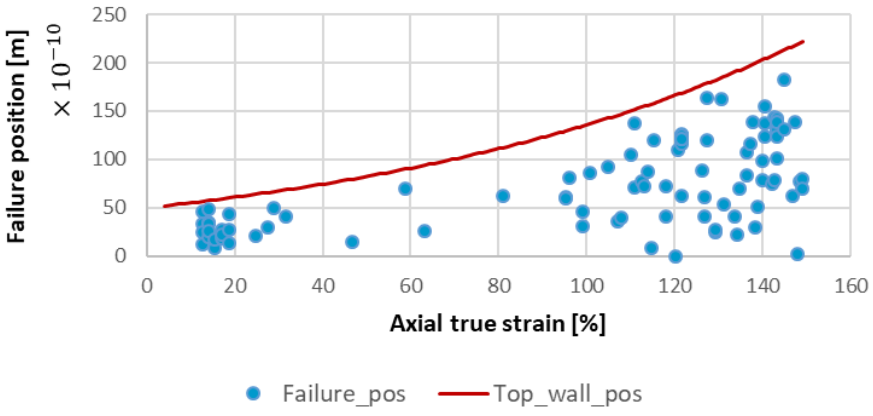


Figure 5.56: Spatial distribution of the failure point along the height of the specimen with longer chains ($\theta_{max} = 0.12\ \pi$ rad)

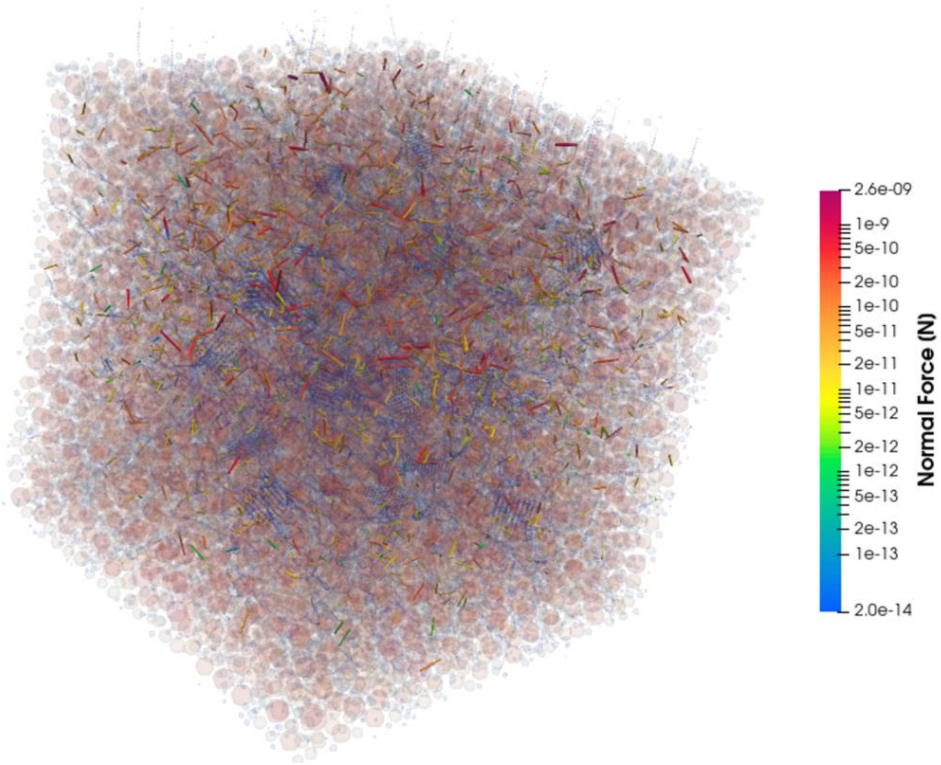


Figure 5.57: Plasticizer-chains interactions for specimen with shorter chains ($\theta_{max} = 0.08\ \pi$ rad) at 10 % of stress.

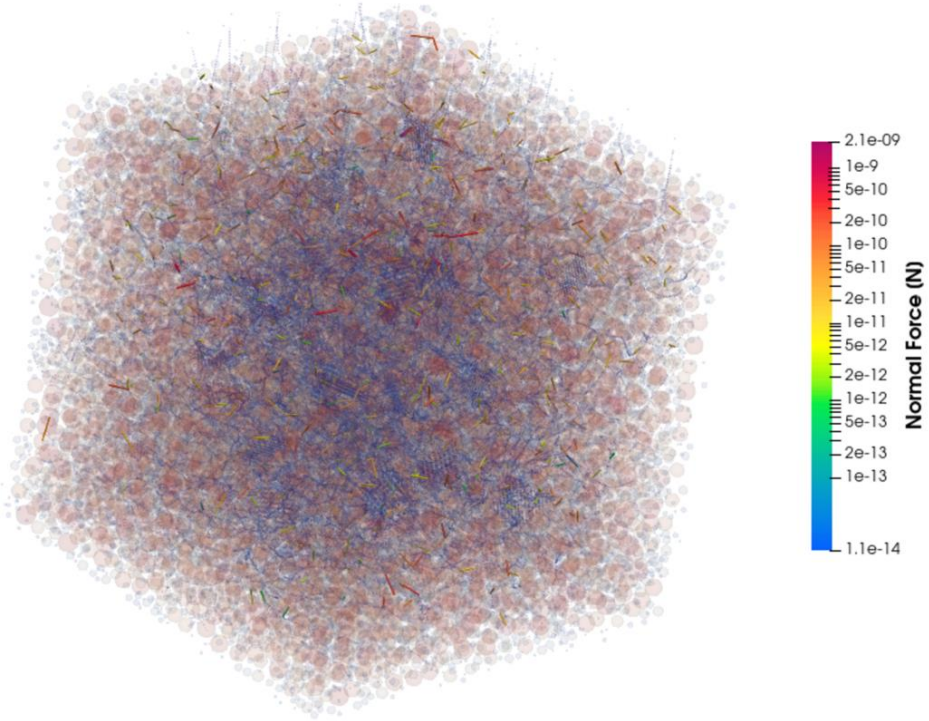


Figure 5.58: Plasticizer-chains interactions for specimen with longer chains ($\theta_{max} = 0.12\ \pi$ rad) at 10 % of stress.

5.6. Tensile strain rate and micro-inertial dynamics effects

Capturing the complex intermolecular interactions within a numerical model poses significant challenges, particularly due to the computational cost and difficulty of directly simulating long-range molecular forces such as van der Waals interactions or dipole-dipole interactions. Thus, to account for the lack of direct intermolecular interactions that generate these resisting forces, micro-inertial effects are introduced as a surrogate for molecular resistance to motion. These micro-inertial dynamics is accompanied with numerical dissipation, to account for molecular rearrangements and heat production.

In this section, the influence of micro-inertial dynamics on system behavior is investigated by conducting simulations on identical microstructure configurations under two different tensile strain rates: 4/s and 0.4/sec. Additionally, the energy balance during loading is analyzed, in order to assess the effect of the tensile rate on the energy distribution and dissipation within the system.

Note that in this analysis, non-isochoric boundary conditions were applied, meaning the material's volume was not strictly preserved (the applied boundary conditions impose here a decrease of the volume over time). This influences the relationship between axial and lateral strains (Figure 5.1), but the comparison remains meaningful as the same boundary conditions are consistently applied across all simulations.

5.6.1. Stress-strain response with different tensile rates

Figure 5.59 presents the stress-strain curves for a specimen subjected to two tensile strain rates: 4/sec (blue curve) and 0.4 /sec (orange curve). The comparison concerns the response up to 78% of strain. The curve at 4/sec is steeper initially, indicating a higher resistance to deformation. In contrast, the curve at 0.4 /sec begins more horizontally, indicating a very slow increase in stress within the system. Beyond 30 %, the system subjected to 0.4/sec shows an increased resistance with noticeable important fluctuation, indicating the high effect of individual chains failure on the global response (see Figure 5.60).

When examining the fraction of failed chains at the two strain rates, as shown in Figure 5.60, it is evident that the same chains experience failure at both rates, as the corresponding curves are superimposed. This suggests that **the chain's failure mechanism is mainly rate-independent**.

Force distribution colored-map provides further insight. Figure 5.61, which shows the force distribution for the test conducted at 0.4/sec, reveals a predominance of blue regions (indicating low forces) even at 40% of strain. In contrast, Figure 5.11, representing the 4/s test, shows a transition to green regions (indicating higher forces) at 20% of strain. This indicates a greater resistance of the system at higher strain rates.

Interestingly, when a test is conducted at 4/sec using the same polymeric chain morphological configuration, but without the inclusion of plasticizer grains, the stress-strain response (gray curve shown in Figure 5.59) is closely similar to that of the test conducted at 0.4/s. This observation highlights the important role of plasticizer grains in load transfer during deformation.

Plasticizer-chain interactions provide additional evidence. At 10% of strain, the simulation conducted at 4/s (previously shown in Figure 5.17) demonstrates highly significant and widespread interactions across the specimen. However, in the simulation conducted at 4/sec (see Figure 5.17), these interactions are less important. Thereupon, this suggests that at a lower tensile strain rate of 0.4 /sec, the polymer chains have sufficient time to rearrange, reducing the load transfer to the plasticizer grains. However, at faster loading, the chains do not have time enough to adjust, resulting in the plasticizer grains playing a more prominent role in transferring the load. This is why the material's resistance increases with increasing tensile rates.

The stress distribution at different heights of the specimen is presented in Figure 5.63 (4/sec) and Figure 5.64 (at 0.4/sec). As shown, the stress is more uniformly distributed at higher strain rate (4/sec), while it exhibits significant variability, even during the early stages of deformation at 0.4/sec. This again highlights the important role of the plasticizer grains in transferring loading at higher strain rate.

Consequently, at faster loading, the micro-inertial effects play a significant role, resulting in an additional resistance of the system. In fact, the stress-strain curve is steeper at the beginning because the chains are moving quickly, and the micro-inertial effects damp this motion, effectively increasing the system's apparent stiffness. In contrast, at lower strain rates, micro-inertial effects are less pronounced, and the load is transferred more gradually to the plasticizer, where the plasticizer grains are able to move more easily in response to the slower deformation (as seen in Figure 5.61). This results in a **more gradual increase in stress** during the early stages of deformation.

Eventually, a significant portion of the **overall system resistance** comes from the **plasticizer's resistance forces**, which limit the polymer chains to rearrange and rotate quickly. Plasticizer's resistance forces become important when increasing the loading rates. Additionally, the superimposed curves of the fraction of failed chains at different tensile rates highlights that the mechanism governing the failure is not affected by the strain rates, demonstrating that the micro-inertial effects do not fundamentally alter the nature of failure.

Globally, this observation qualitatively explains why the material's resistance increases with higher loading rates in the experimental tests. As the plasticizer contributes significantly to the force resistance of the material, this effect becomes more pronounced at higher strain rates, highlighting what mechanisms govern the macroscopic viscous properties of the material. However, at lower tensile rates, the load transfer to the plasticizer is less significant, and consequently, the resistance forces of the plasticizer acting on the chains, are less important, which reduces the overall resistance. This emphasizes the underlying macroscopic viscous properties of the material, which are more prominent at higher strain rates.

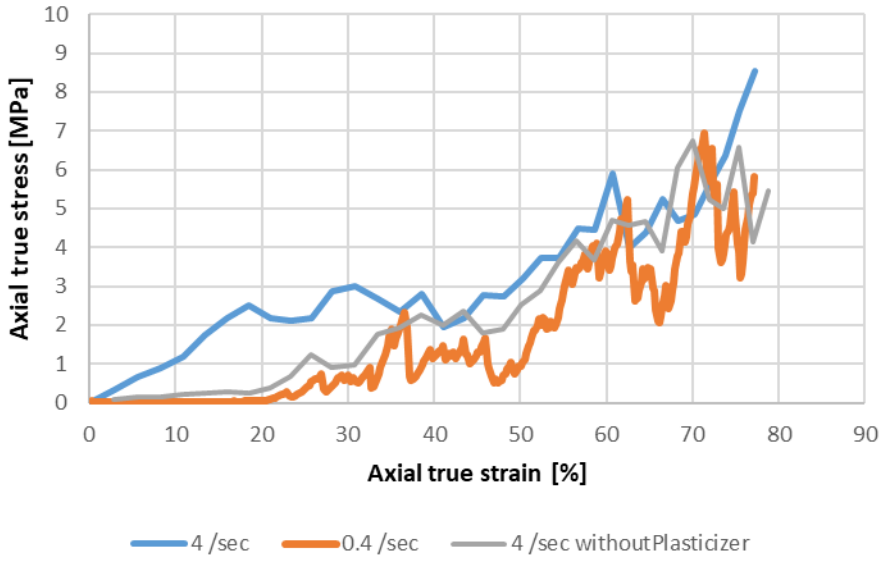


Figure 5.59: Stress-strain curve of two specimens conducted at two different tensile rates **4** and **0.4 /sec**.

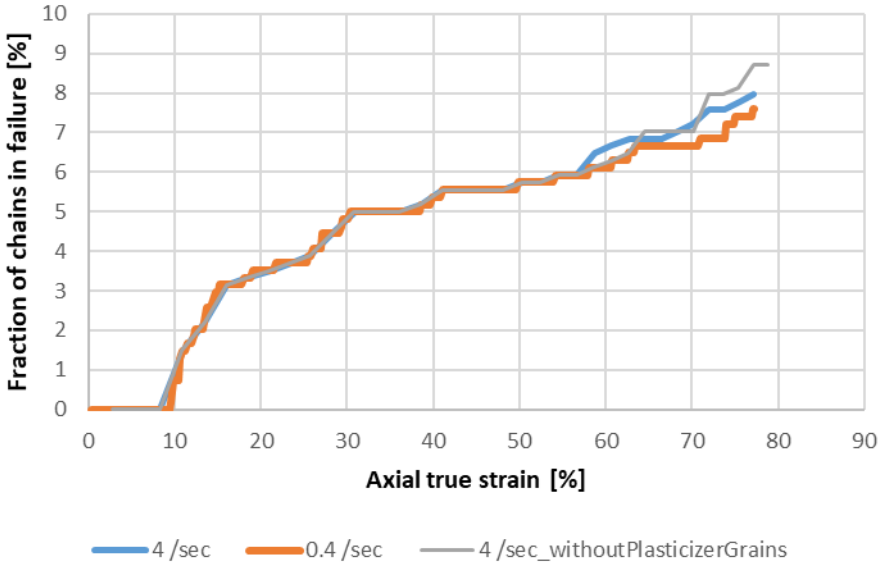


Figure 5.60: Fraction of chains in failure for tests conducted at two different tensile rates **4** and **0.4 /sec**.

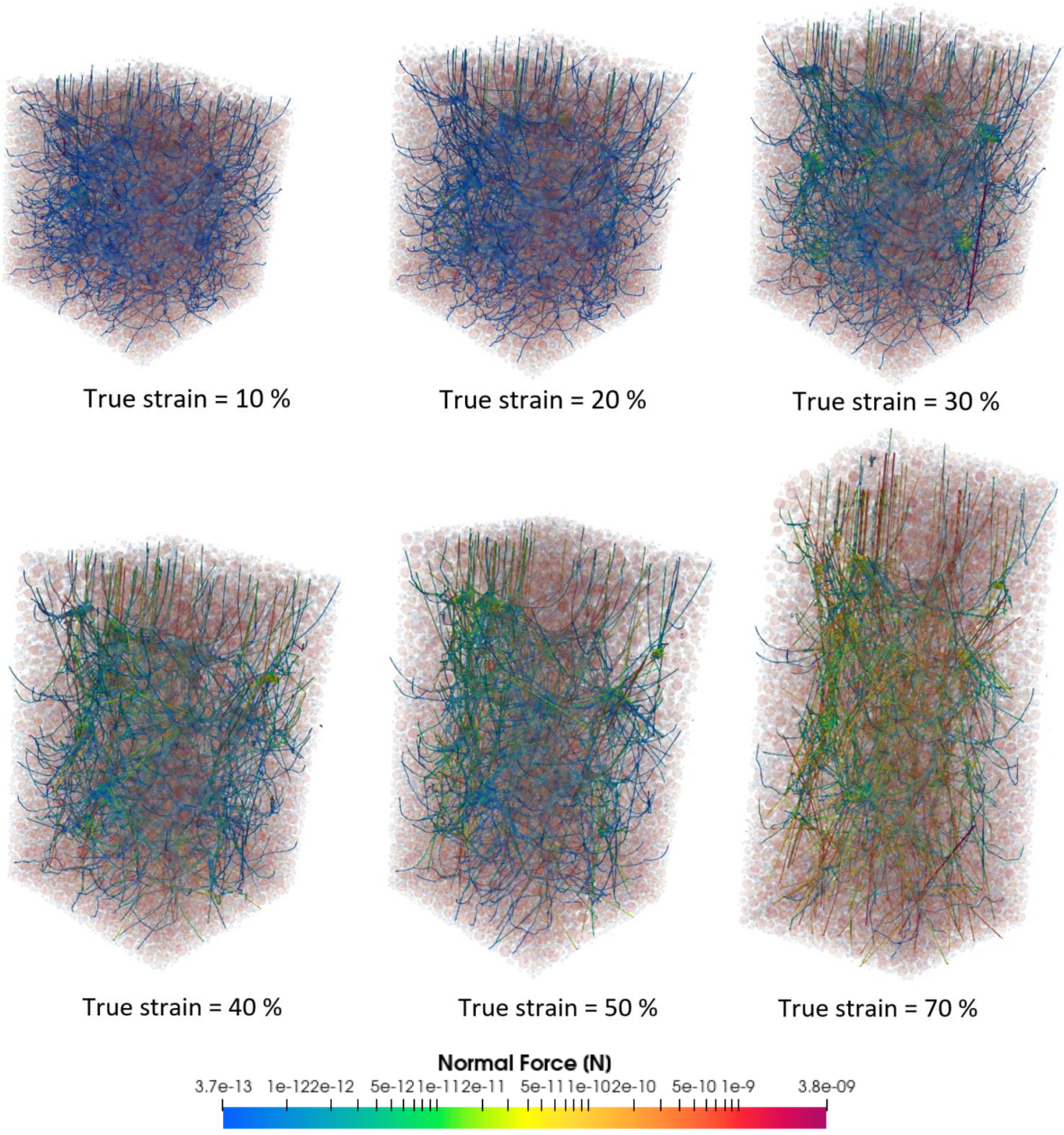


Figure 5.61: Force distribution for a specimen subjected to uniaxial tensile rate of 0.4 /sec. Visualization includes sphere arrangement during loading, in order to see how the plasticizer's grains adjust with deformation at low tensile rate.

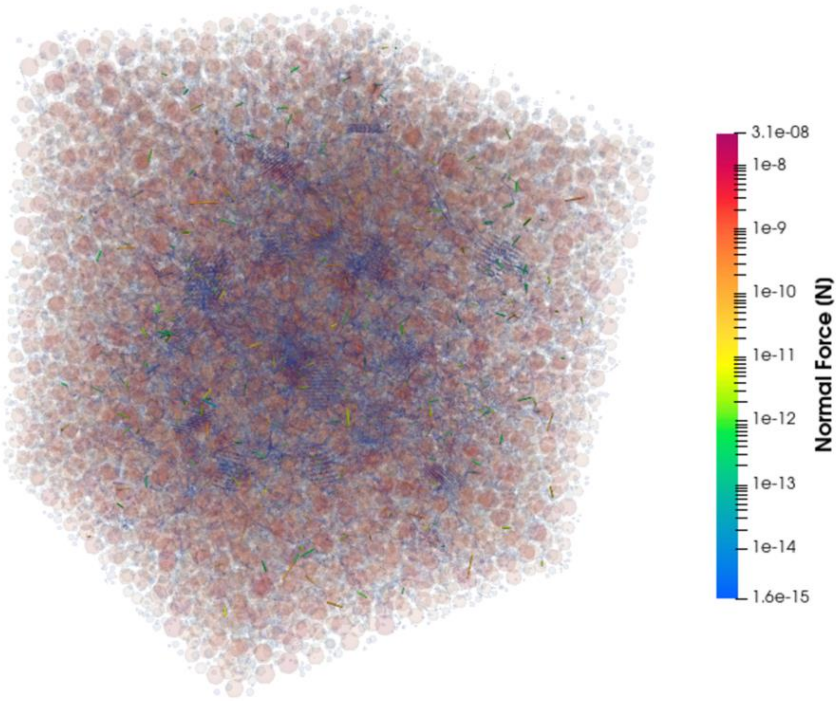


Figure 5.62: Plasticizer-chains interactions at 10% of strain for a specimen subjected to uniaxial tensile rate of 0.4 /sec.

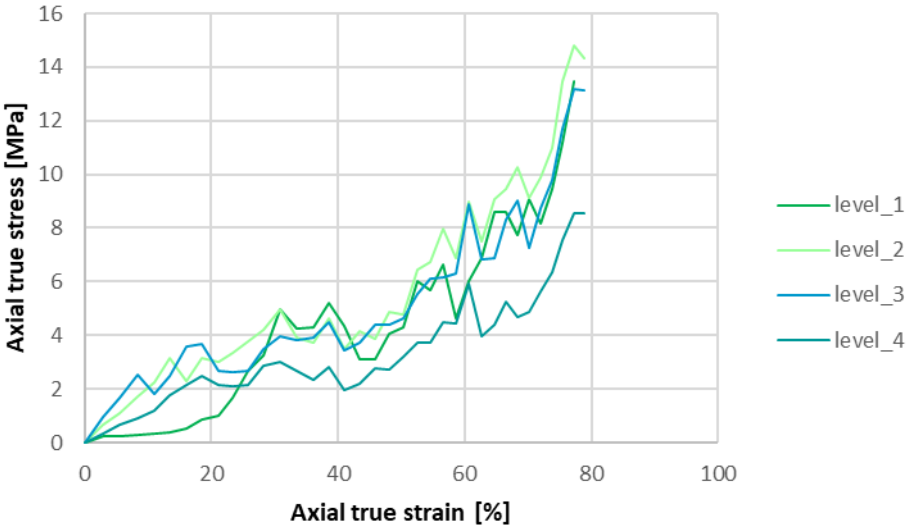


Figure 5.63: Stress distribution at four different heights of the specimen (i.e., 25, 50, 75, and 100 % of the current specimen height) for a specimen, subjected to tensile strain rate equals to **4 /sec**.

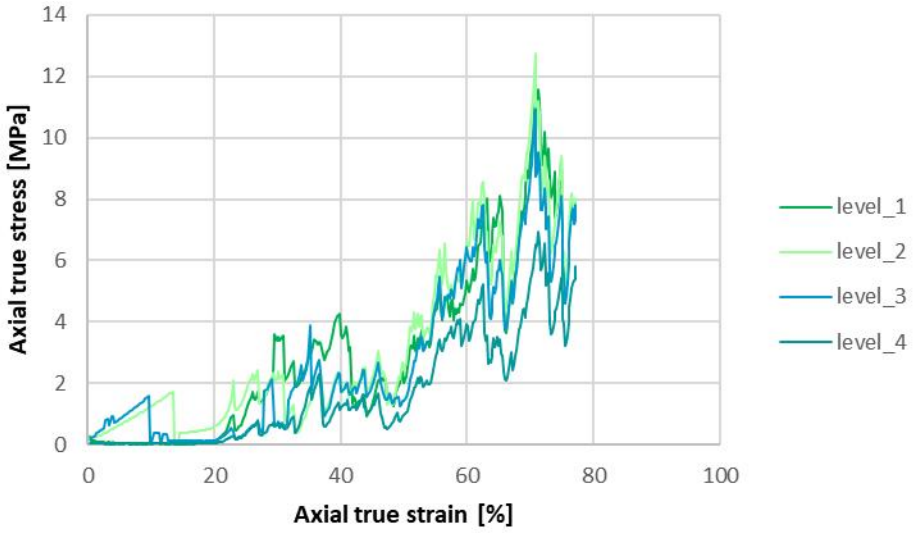


Figure 5.64: Stress distribution at four different heights of the specimen (i.e., 25, 50, 75, and 100 % of the current specimen height) for a specimen, subjected to tensile strain rate equals to **0.4 /sec.**

5.6.2. Energy balance

Figure 5.65 presents the energy distribution during loading at tensile strain rates of respectively 0.4 and 4/sec.

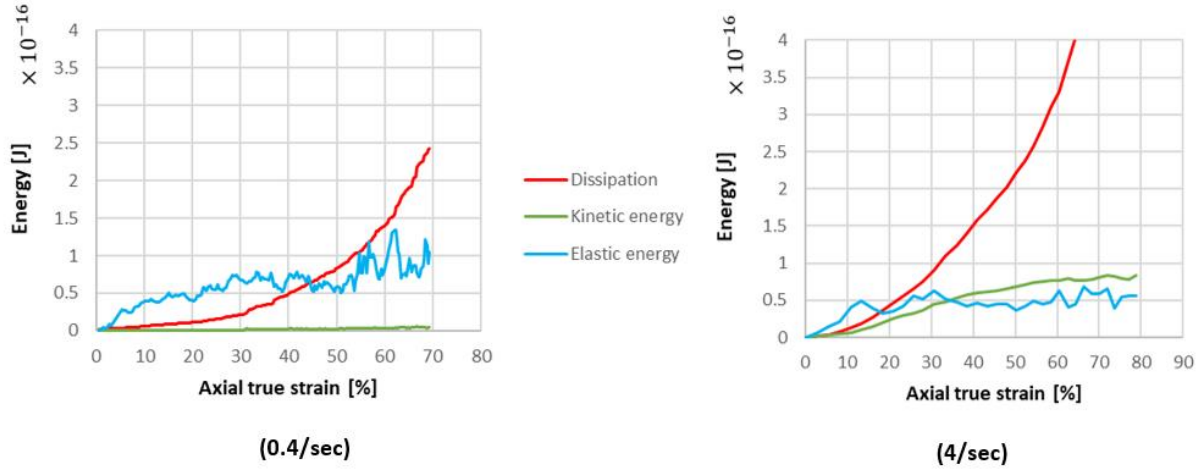


Figure 5.65: Energy balance during loading at tensile strain rates of 0.4 /sec and 4/sec.

The kinetic energy is higher at higher strain rate (4/sec). This can be explained by the fact that the chains and plasticizer grains are forced to respond more rapidly, leading to higher particles velocities, and larger inertial effects. In contrast, the kinetic energy is relatively negligible at lower strain rate (0.4/sec), indicating that the system approaches a quasi-static regime. Here, the system distributes and stores energy in the form of potential energy.

Indifferently, the numerical dissipation contributes in a large amount of the system energy at high loading rate (4/sec). This, as specified previously, is related to the unbalanced forces generated when a chain is cropped. These forces are initially converted into kinetic energy, which subsequently dissipates as numerical dissipation. Additionally

at higher loading speeds, the dissipation caused by resistive damping increases, as the kinetic energy within the system is higher.

5.7. Simulation of non-plasticized PVC material

It is also insightful to investigate the mechanical response of non-plasticized PVC, which exhibits distinct structural characteristics. According to the literature (refer to Section 2.1.3), non-plasticized PVC is characterized by a higher degree of crystallinity, with crystallites typically spaced about 10 nm each other. To simulate such a crystallized specimen, the same geometrical parameters used for the reference simulation were employed with only changing the crystallite spacing, ensuring a consistent basis for comparison. The resulting configuration consists of **42 crystallites**, comprising a total of 145061 particles and 1260 polymer chains.

Note that in this analysis, non-isochoric boundary conditions were applied, meaning the material's volume was not strictly preserved (the applied boundary conditions impose here a decrease of the volume over time). This influences the relationship between axial and lateral strains (Figure 5.1), but the comparison remains meaningful as the same boundary conditions are consistently applied across all simulations.

The results, shown in Figure 5.66, demonstrate higher resistance in the non-plasticized PVC material, which is primarily attributed to the complex crystalline network.

To further illustrate this behavior, a force distribution map could visualize how stress is transferred through the chains. A quasi-uniform color emerges within the specimen, as shown in Figure 5.68. Figure 5.67 shows a more consistent uniformity of the stress at different specimen's heights until 100 % of strain corresponding to the peak stress. Beyond this strain, the non-uniformity of the stress is remarkable and correlates with the observed stress decrease in Figure 5.66, suggesting localized large scale failure regions, as evidenced in Figure 5.68 at 110 % of strain.

Consequently, these crystallites effectively act as entanglements, redistributing the stress more uniformly across the specimen and reducing the localized effects of individual chain failure and localized failure region over the mechanical response. Additionally, this supports the hypothesis that their presence enhances the material's resistance and uniformity in stress propagation.

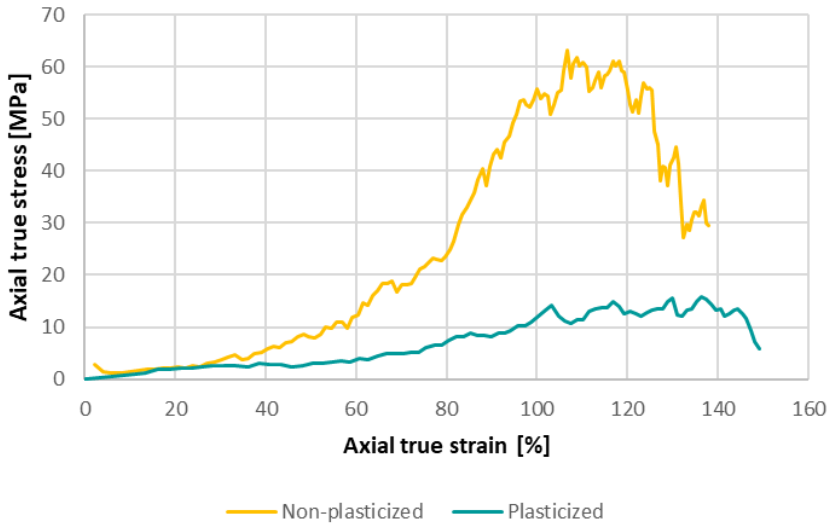


Figure 5.66: Comparison of the stress-strain curve for plasticized and non-plasticized PVC material.

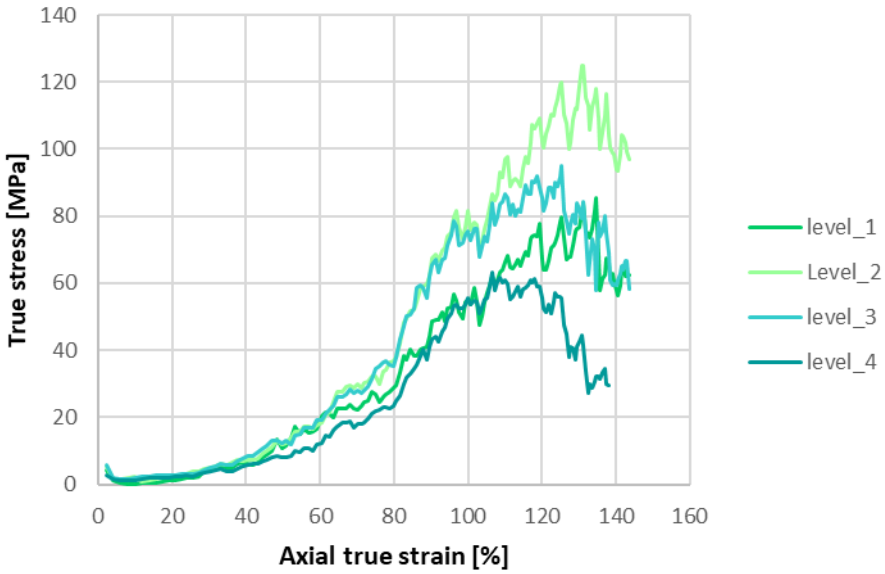


Figure 5.67: Stress distribution at four different height levels (respectively 25, 50, 75, and 100 % of the current specimen height from bottom to top) for **non-plasticized PVC** specimen.

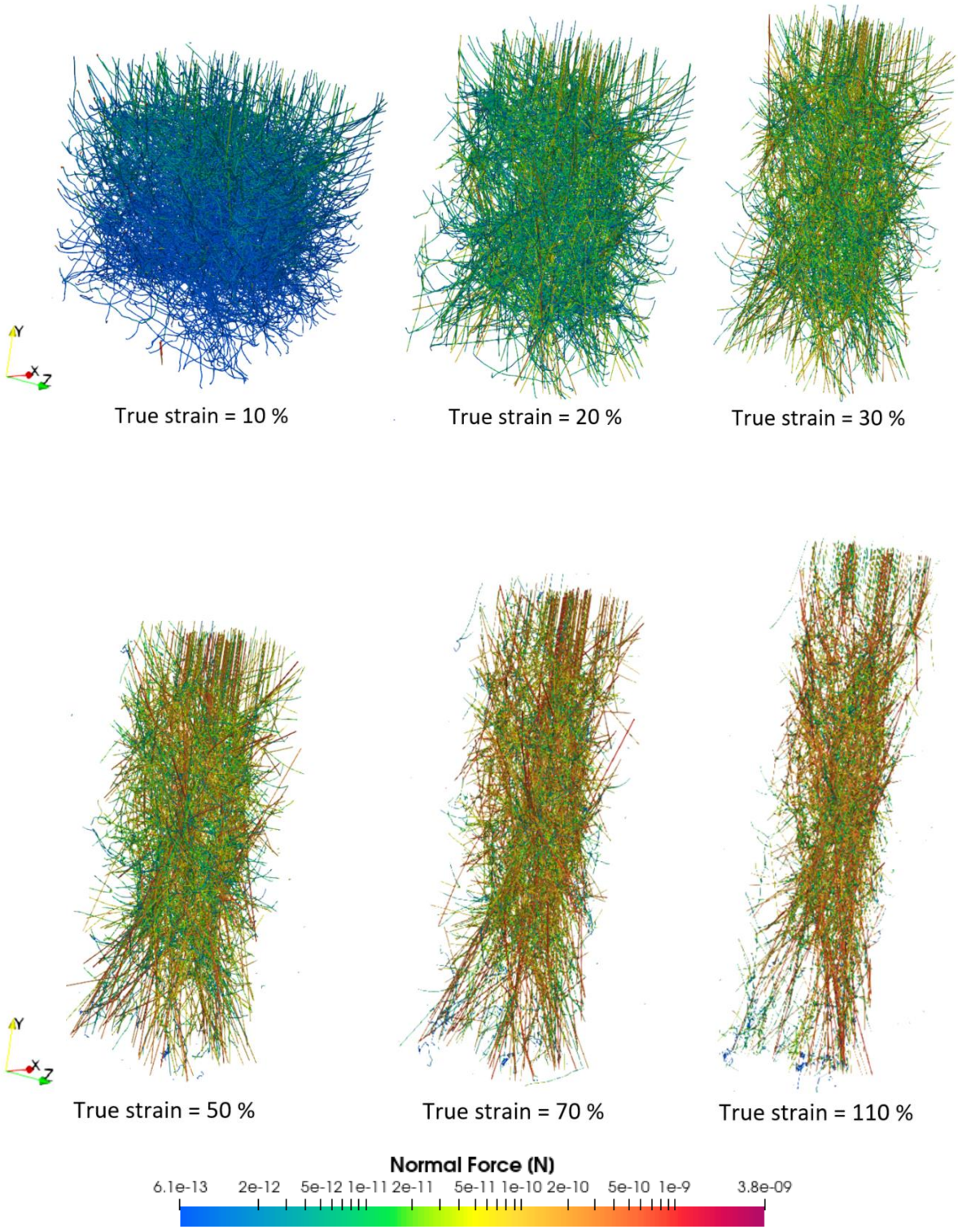


Figure 5.68: Force distribution colored-map of a **non-plasticized** specimen.

5.8. Main findings

This chapter provides a detailed multiscale analysis of the mechanical behavior of PVC geomembranes under uniaxial tensile loading, successfully linking mesoscopic elementary mechanisms to macroscopic responses.

In the model, micro-inertial effects combined with numerical dissipation have been used as a proxy of the so-called viscous effects. While this latter is difficult to model directly at the mesoscale level, the use of these proxies allows the model to replicate key aspects of the material's response to varying strain rates.

The model demonstrates the capability to predict macroscopic behavior by tracking mesoscale deformation and analyzing force distribution maps across the network microstructure.

A key contribution of this work lies in the ability to relate mesoscale behavior to the macroscale mechanical response, offering a deeper understanding of the elementary deformation mechanisms:

- **Linear Stress-Strain Behavior** ($\leq 60\%$ of strain): The linear regime of the stress-strain curve is primarily attributed to the rearrangement and reorientation of polymer chains and crystallites. During this phase, some crystallites begin to fragment; even this does not significantly disrupt the overall behavior.
- **Transition to Nonlinear Behavior** ($\geq 60\%$ of strain): Once all crystallites are fragmented, the material's response transitions to a nonlinear regime. This indicates a transfer in the load-bearing contribution from the crystallites to the individual chains.

In Chapter 3, the geometrical sensitivity of the morphological structure was discussed. In this chapter, the impact of these geometrical parameters on the mechanical responses and stress distribution was investigated, revealing their distinct roles in the material's mechanical response and model's reliability:

- **Effect of EV size:** The non-uniformity observed at high strain levels is primarily attributed to the Elementary volume used. With increasing EV, the response is less dependent on local-individual chain failure, as the volume demonstrates a more interconnected network that leads to a more uniform stress distribution and less inertial effects.
- **Effect of amorphous region chain density** (represented by the number of chains per crystallite): The results reveal that higher chain density improves the system connectivity, and consequently reduces the effect of local-individual chain failure on the system's behavior, and decreasing as a result the stress variability and fluctuation. However, at higher deformation levels, the complex network induced by higher chain density led to a large-scale chains breakage, that disrupts the system's stability, creates a non-uniform stress distribution and makes the maximum resistance not so clearly marked.

- **Effect of chain length**: The results demonstrate that increasing tortuosity, associated with longer chains, facilitate effective distribution of forces across the network. This delays crystallite fragmentation, reducing stress localization. Thus, with an increase in the chains tortuosity using $\theta_{max} = 0.12\,\pi$ rad, the transition to the non-linear behavior was detected at 80 % of strain. This is in accordance with the experimental results, which shows a transition to a non-linear behavior at 80 % of strain.
- **Strain rate sensitivity:** The results show higher resistance with higher strain rate. Interestingly, it was observed that the chain failure rate at the microscale is rate-independent. The increased resistance is largely due to the plasticizer's role in **distributing the stress** throughout the material. At higher strain rates, this plasticizer grains limiting chain rearrangement under microinertial effects, thereby increasing the overall resistance of the material.

The model was also used for simulating a non-plasticized PVC material, which exhibits significantly higher resistance, highlighting the role of crystallites as entanglement-based load-bearing structures that enhance the system's resistance.

Chapter 6: General conclusions and perspectives

6.1. Objective of this work

This PhD work originated from an engineering need to uncover the underlying mechanisms behind the response of PVC GMs, particularly when subjected to tensile forces. In fact, tensile stresses are the primary cause of many mechanical failure occurrences within geomembranes, involving tearing, puncturing, and bursting, which can result from factors such as gravity, waves, earthquakes, direct contact with angular solids,... . Therefore, the objective of this research was to gain a deeper understanding of how PVC GMs behave under these tensile forces using an extensive experimental campaign, coupled with a multiscale modeling DEM-based approach to bridge the gap between microscale material properties, and macroscopic performance.

6.2. Major contributions of this work

This work provides extensive complementary insights at different scales. Experimental tests significantly contribute to understanding the GM's behavior under different tensile modes, using both short- and long-term tests to evaluate the ultimate tensile properties of the geomembrane. In parallel, in the numerical approach used, the full complexity of the microstructure geometry is accounted for, offering a deeper understanding of how tensile forces are distributed within the geomembrane, and linking the elementary molecular mechanisms to the observed macroscopic behavior. The results prove the capacity of DEM modeling over a cascade of scales in predicting and visualizing macroscopic performance from microscale phenomena in the geomembrane applications. These findings are crucial for assisting engineers in designing a long-lasting waterproofing system that should protect the environment and public health.

The major conclusions of this work are listed below:

6.2.1. Rate-dependent behavior

The results demonstrate that the material under study exhibits a rate-dependent behavior, particularly in the short term. At higher strain rates, the material shows an increase in rigidity modulus and enhanced mechanical properties at failure; specifically, greater resistance and higher elongation at failure are achieved.

The **developed model** demonstrates that the increased resistance observed at higher tensile rates is largely attributed to the presence of plasticizer. At higher tensile rates, the plasticizer grains act as resistance points, transmitting and bearing a significant fraction of the load. This inability of the polymer chains to reorganize quickly under high strain rates results in an increased overall resistance. At lower tensile rates, the plasticizer

grains have more time to move and allow some rearrangement of polymer chains, leading to less resisting force acting on the polymer chain, and consequently, lower overall material's resistance. This reflects the macroscopic viscous property of the material.

6.2.2. Time-dependent response

The study highlights the impact of preloading history, particularly loading exposure time (time-dependency), and weight on the strain recovery and creep behaviors. Results from creep tests at high loads reveal that higher loads lead to a premature failure occurring at high strains. This is important in determining how the material will perform over time when subjected to cyclic loading and unloading.

6.2.3. Failure criteria under tensile forces

One can ask about the intrinsic ultimate properties of this material, a major challenge that the engineers have to take on in ensuring its long-term functionality. The results demonstrate that the material's ultimate properties (i.e., strength and strain) during long-term loading creep may be predictable based on its short-term response (standardize lab mechanical tests), provided the environmental conditions remain constant (i.e., constant temperature, not exposed to UV radiation and humidity). This predictability can significantly help in the design and lifespan assessment of geomembranes used in critical applications. It was also evidenced that the failure threshold (including, strength and strain at failure) is highly rate-dependent, emphasizing the need for carefully taking the loading rates into account in design protocols.

6.2.4. Relation between mesoscale deformation and macroscale behavior

The model shows the capacity to track deformation and stress distribution at the mesoscale, and relate them to the macroscopic behavior. Interestingly, the model demonstrates that the linear regime of the stress strain response arises primarily from the microstructural adaptation of components (i.e., crystallites, amorphous region, and plasticizer) to the deformation. During this phase, some crystallites undergo fragmentation due to localized stress concentration; however, this localized failure does not significantly impact the global response. These crystallites act as entanglements, effectively distributing and bearing the load. After several crystallite fragmentations due to localized stress concentrations (nearly all crystallites eventually fragment), the response exhibits a transition to a nonlinear regime in the stress-strain curve, where the load-bearing responsibility shifts predominantly to the polymer chains. At this stage, the model captures individual chain failures alongside localized large-scale failure, offering critical insights into the deformation mechanisms at play.

6.3. Perspectives and future work

This PhD opens promising perspectives in both experimental and modeling domains, paving the way for future advancements in the PVC GM engineering field:

6.3.1. Future studies on REV size and selection

In this study, the largest elementary volume (EV) achieved with DEM employing CPU processors was 55 nm, which included around 155,000 particles. This simulation needed 7 computing days using 4 out of 24 available cores on an Intel® Xeon® E5-4617 CPU @2.90 GHz, chosen by an optimal balance of computation and communication overhead.

However, the simulation's most time-consuming component is the **insertion sort collider**, which detects particle contacts and is implemented on a single thread. The computing cost of the collider grows considerably with the number of particles. This demonstrates the difficulty of scaling the simulation to bigger EVs, as the non-parallelized collider remains a performance barrier. Despite the computational effort, the achieved EV still exhibits noticeable stress variability at high deformation levels. This highlights the effect of localized stress concentration and localized failure on the material's overall behavior, indicating that larger volumes are necessary to capture objective representative elementary volume (REV) characteristics.

This could be improved by using a CPU-GPU hybrid approach, and executing parallelized tasks using GPU.

6.3.2. Towards more exploration and model enhancements

The developed DEM-based model in this study has revealed different possibilities for further exploration and improvement. Several simulations have been unexplored due to the constraints of the PhD time frame. Below, key areas of interest for future research are listed.

6.3.2.1. Effect of inter-crystallite distance

The inter-crystallite distance, influenced by the amount of plasticizer added during manufacturing, is a key factor in determining the material's mechanical behavior. As highlighted by Summers (1981), the plasticizer molecules penetrate between the crystallites, inducing the swilling of the amorphous region and increasing this distance.

It would be interested to investigate the effect of varying plasticizer amounts by adjusting the inter-crystallite distance D, to access its impact on the mechanical performance.

6.3.2.2. Including long-range intermolecular interactions

In the present model, viscous effects are proxied through the activation of micro-inertial dynamics and numerical dissipation. However, a more refined approach could incorporate more rational intermolecular interactions, by imposing forces acting at distance for each particle. This would lead to predict viscous effects quantitatively, allowing for a more accurate assessment of the rate dependent material behavior.

6.3.2.3. Increasing the number of chains while increasing the chain length

The chain length could be increased by increasing chain tortuosity, or inter-crystallite distance (i.e., reducing the crystallinity level). Using an increased chain length has shown a delay (relatively to the reference simulation) in the transition to nonlinear behavior at

80% of strain , which is consistent with experimental findings. However, it was impossible to detect a well-defined maximum stress due to significant stress variation, caused by local perturbation. To address this, future simulations incorporating longer chains alongside a higher number of chains could be explored. This consideration may help reduce stress variability, mitigate the impact of large-scale failure, and improve the stability of the material's response in complex systems. In such a way, the elongation at failure could be more precisely determined and compared with experimental results.

6.3.3. Evaluation of material behavior through cyclic loading-unloading-reloading tests

As seen in the relaxation and creep tests conducted in this study, the material may exhibit irreversible strain that depends on the exposure time and loads (i.e., constant strain in case of relaxation, and constant stress in case of creep). Interestingly, it would be highly beneficial to perform cycles of loading-unloading-reloading, that permits to assess whether the material's mechanical properties, such as stiffness and stress-strain response, are altered by the recovery time and irreversible deformation.
The process involves two methodology:

- Applying tensile loading → unloading and allowing the specimen to recover its strain → reloading
- Applying tensile loading → holding the specimen for creep or relaxation → unloading and allowing the specimen to recover its strain for different period → reloading

By comparing stress-strain behavior across cycles, the study aims to determine if loading time and strain recovery influence material performance. Such an investigation would provide an enhanced understanding of the material's performance throughout repeated loading cycles, closely representing in-situ scenarios where materials are subjected to continuous loading and unloading.

References

Abdelaal, F. B., R. K. Rowe, and R. W. I. Brachman. 2014. "Brittle rupture of an aged HPDE geomembrane at local gravel indentations under simulated field conditions." *Geosynth. Int.*, 21 (1): 1–23. https://doi.org/10.1680/gein.13.00031.

Adema, K. N. S., H. Makki, E. A. J. F. Peters, J. Laven, L. G. J. van der Ven, R. A. T. M. van Benthem, and G. de With. 2015. "Kinetic Monte Carlo simulation of the photodegradation process of polyester-urethane coatings." *Phys. Chem. Chem. Phys.*, 17 (30): 19962–19976. The Royal Society of Chemistry. https://doi.org/10.1039/C5CP01581B.

AFNOR. 2000. "NF EN 1931. Flexible sheets for waterproofing - Bitumen, plastic and rubber sheets for roof waterproofing - Determination of water vapour transmission properties." *Afnor Ed.*

AFNOR. 2010. "NF EN 14151. Géosynthétiques - Détermination de la résistance à l'éclatement." *Afnor Ed.*

AFNOR. 2013. "NF EN 12311-2. Flexible sheets for waterproofing - Determination of tensile properties - Part 2 : plastic and rubber sheets for roof waterproofing." *Afnor Ed.*

AFNOR. 2014. "NF EN ISO 6427. Plastics - Determination of matter extractable by organic solvents (conventional methods)." *Afnor Ed.*

AFNOR. 2018. "NF EN ISO 527-3. Plastiques - Détermination des propriétés en traction - Partie 3 : conditions d'essai pour films et feuilles." *Afnor Ed.*

AFNOR. 2019a. "NF EN ISO 527-1. Plastiques - Détermination des propriétés en traction - Partie 1 : principes généraux." *Afnor Ed.*

AFNOR. 2019b. "NF EN 1849-2. Flexible sheets for waterproofing - Determination of thickness and mass per unit area - Part 2 : plastics and rubber sheets for roof waterproofing." *Afnor Ed.*

AFNOR. 2019c. "NF EN ISO 1183-1; Plastics - Methods for determining the density of non-cellular plastics - Part 1 : immersion method, liquid pycnometer method and titration method." *Afnor Ed.*

AFNOR. 2023. "NF EN ISO 527-4. Plastiques - Détermination des propriétés en traction - Partie 4 : conditions d'essai pour les composites plastiques renforcés de fibres isotropes..." *Afnor Ed.*

Akel, N., G. Stoltz, A. Wautier, F. Nicot, and N. Touze. 2025. "Rate-dependent tensile response of Polyvinyl Chloride geomembranes." *Geotext. Geomembr.*, 53 (1): 445–456. https://doi.org/10.1016/j.geotexmem.2024.11.004.

Almeida, M., I. Hosseinpour, and M. Riccio. 2013. "Performance of a geosynthetic-encased column (GEC) in soft ground: Numerical and analytical studies." *Geosynth. Int.*, 20: 252–262. https://doi.org/10.1680/gein.13.00015.

ASTM D4885. 2018. "ASTM D 4885-88 Standard Test Method For Determining Performance Streght of Geomembranes by The Wide Strip Tensile Method | PDF | Strength Of Materials | Ultimate Tensile Strength." *Scribd*.

Balani, K., V. Verma, A. Agarwal, and R. Narayan. 2014. *Biosurfaces: A Materials Science and Engineering Perspective*. Wiley.

Bekoin, F. 2016. “Etude analytique, numérique et expérimentale du comportement mécanique des systèmes géosynthétiques : application au cas des barrières de sécurité des extensions d’ISDND.” phdthesis. Université Grenoble Alpes.

Bhandari, A., and J. Han. 2010. “Investigation of geotextile–soil interaction under a cyclic vertical load using the discrete element method.” *Geotext. Geomembr.*, 28 (1): 33–43. https://doi.org/10.1016/j.geotexmem.2009.09.005.

Blanco, M. 2006. “- BLANCO, M.; CASTILLO, F. y AGUIAR, E.- "Comportamiento de los plastificantes utilizados como aditivos del poli(cloruro de vinilo) plastificado usado como geomembrana en obras hidráulicas” . Rev. Plast. Modernos 92 (603), 246-250 (2.006).” *Rev. Plásticos Mod.*, 92: 246–250.

Blanco, M., B. Mateo, D. Cazzuffi, and M. A. Crespo. 2017. *Lining of reservoirs with synthetic geomembranes*.

Blanco, M., G. Rico, L. Pargada, F. Castillo, and M. A. Crespo. 2010. “Influence of plasticizer type in PVC-P geomembranes durability.” *III Natl. Waterproofing Congr. Build. Public Works Reserv. Barc.*, 347–357.

Blanco, M., N. Touze-Foltz, M. Pérez Sánchez, M. Redon-Santafe, F. J. Sánchez Romero, J. B. Torregrosa Soler, and F. A. Zapata Raboso. 2018. “Durability of reinforced PVC-P geomembranes installed in reservoirs in eastern Spain.” *Geosynth. Int.*, 25 (1): 85–97. ICE Publishing. https://doi.org/10.1680/jgein.17.00035.

Bourrier, F., F. Kneib, B. Chareyre, and T. Fourcaud. 2013. “Discrete modeling of granular soils reinforcement by plant roots.” *Ecol. Eng.*, 61: 646–657. https://doi.org/10.1016/j.ecoleng.2013.05.002.

Bouvard, J. L., D. K. Ward, D. Hossain, S. Nouranian, E. B. Marin, and M. F. Horstemeyer. 2009. “Review of Hierarchical Multiscale Modeling to Describe the Mechanical Behavior of Amorphous Polymers.” *J. Eng. Mater. Technol.*, 131 (4): 041206. https://doi.org/10.1115/1.3183779.

Brinson, H. F., and L. C. Brinson. 2008. *Polymer engineering science and viscoelasticity: an introduction*. New York: Springer.

Brooks, C. L. 1989. “Computer simulation of liquids.” *J. Solut. Chem.*, 18 (1): 99–99. https://doi.org/10.1007/BF00646086.

Broughton, J. Q., F. F. Abraham, N. Bernstein, and E. Kaxiras. 1999. “Concurrent coupling of length scales: Methodology and application.” *Phys. Rev. B*, 60 (4): 2391–2403. American Physical Society. https://doi.org/10.1103/PhysRevB.60.2391.

Cazzuffi, D., and D. Gioffrè. 2018. “Long-time behavior of exposed geomembranes used for the upstream face rehabilitation of concrete and masonry dams.”

Cazzuffi, D., and D. Gioffrè. 2020. “Lifetime assessment of exposed PVC-P geomembranes installed on Italian dams.” *Geotext. Geomembr.*, Special issue on Geosynthetics for Hydraulic and Environmental Applications, 48 (2): 130–136. https://doi.org/10.1016/j.geotexmem.2019.11.015.

Cazzuffi, D., and D. Gioffrè. 2023. “Geomembrane barrier systems for construction and rehabilitation of embankment dams.” 164–179.

Cazzuffi, D., D. Gioffrè, and A. Luciani. 2023. “Geosynthetics in tunnels and underground structures applications.” *E3S Web Conf.*, (O. M. Amer and R. El-Sherbiny, eds.), 368: 01005. https://doi.org/10.1051/e3sconf/202336801005.

Cazzuffi, D., J.-P. Giroud, A. Scuero, and G. Vaschetti. 2011. “EMPLOI DES GÉOMEMBRANES DANS LES BARRAGES : 50 ANS DE DIFFÉRENTES APPLICATIONS DANS LE MONDE.”

Cen, W. J., H. Wang, D. J. Li, and L. S. Wen. 2018. “Large-strain tensile behaviour of geomembranes with defects using 3D digital image correlation.” *Geosynth. Int.*, 25 (6): 644–655. https://doi.org/10.1680/jgein.18.00031.

Chareyre, B., and P. Villard. 2005. “DEM modelling of soil structures reinforced with geosynthetics.”

Chen, C., G. R. McDowell, and N. H. Thom. 2012. “Discrete element modelling of cyclic loads of geogrid-reinforced ballast under confined and unconfined conditions.” *Geotext. Geomembr.*, 35: 76–86. https://doi.org/10.1016/j.geotexmem.2012.07.004.

Chen, W.-B., T. Xu, and W.-H. Zhou. 2021. “Microanalysis of smooth Geomembrane–Sand interface using FDM–DEM coupling simulation.” *Geotext. Geomembr.*, 49 (1): 276–288. https://doi.org/10.1016/j.geotexmem.2020.10.022.

Cundall, P. 1971. “A computer model for simulating progressive, large-scale movements in blocky rock systems.”

Cundall, P. A., and O. D. L. Strack. 1979. “A discrete numerical model for granular assemblies.” *Géotechnique*, 29 (1): 47–65. https://doi.org/10.1680/geot.1979.29.1.47.

Dammyr, Ø., B. Nilsen, K. Thuro, and J. H. Grøndal. 2014. “Possible Concepts for Waterproofing of Norwegian TBM Railway Tunnels.” *Rock Mech. Rock Eng.*, 47. https://doi.org/10.1007/s00603-013-0388-5.

Dixon, N., G. Fowmes, and M. Frost. 2017. “Global challenges, geosynthetic solutions and counting carbon.” *Geosynth. Int.*, 24 (5): 451–464. https://doi.org/10.1680/jgein.17.00014.

Dubois, F., V. Acary, and M. Jean. 2018. “The Contact Dynamics method: A nonsmooth story.” *Comptes Rendus Mécanique*, The legacy of Jean-Jacques Moreau in mechanics / L’héritage de Jean-Jacques Moreau en mécanique, 346 (3): 247–262. https://doi.org/10.1016/j.crme.2017.12.009.

Effeindzourou, A., B. Chareyre, K. Thoeni, A. Giacomini, and F. Kneib. 2016. “Modelling of deformable structures in the general framework of the discrete element method.” *Geotext. Geomembr.*, 44 (2): 143–156. https://doi.org/10.1016/j.geotexmem.2015.07.015.

Eldesouky, H. M. G., and R. W. I. Brachman. 2020. “Viscoplastic modelling of HDPE geomembrane local stresses and strains.” *Geotext. Geomembr.*, 48 (1): 41–51. https://doi.org/10.1016/j.geotexmem.2019.103503.

Ellero, M., P. Español, and E. G. Flekkøy. 2003. “Thermodynamically consistent fluid particle model for viscoelastic flows.” *Phys. Rev. E*, 68 (4): 041504. American Physical Society. https://doi.org/10.1103/PhysRevE.68.041504.

Feng, S.-J., X. Liu, H.-X. Chen, and T. Zhao. 2018. “Micro-mechanical analysis of geomembrane-sand interactions using DEM.” *Comput. Geotech.*, 94: 58–71. https://doi.org/10.1016/j.compgeo.2017.08.019.

Fillot, L., P. Hajji, C. Gauthier, and K. Masenelli-Varlot. 2006. “U-PVC gelation level assessment, part 1: Comparison of different techniques.” *J. Vinyl Addit. Technol.*, 12 (3): 98–107. https://doi.org/10.1002/vnl.20077.

Fincham, D. 1992. “Leapfrog Rotational Algorithms.” *Mol. Simul.*, 8 (3–5): 165–178. Taylor & Francis. https://doi.org/10.1080/08927029208022474.

Frost, J. D., D. Kim, and S.-W. Lee. 2012. “Microscale geomembrane-granular material interactions.” *KSCE J. Civ. Eng.*, 16 (1): 79–92. https://doi.org/10.1007/s12205-012-1476-x.

de Gennes, P. G. 1971. “Reptation of a Polymer Chain in the Presence of Fixed Obstacles.” *J. Chem. Phys.*, 55 (2): 572–579. https://doi.org/10.1063/1.1675789.

Ghafar Chehab, A., and I. D. Moore. 2006. “Constitutive Model for High Density Polyethylene to Capture Strain Reversal.” *Pipelines 2006*, 1–8. Chicago, Illinois, United States: American Society of Civil Engineers.

Gilbert, M. 1994. “Crystallinity in Poly(vinyl Chloride).” *J. Macromol. Sci. Part C Polym. Rev.*, 34 (1): 77–135. https://doi.org/10.1080/15321799408009633.

Giroud, J. 2021. “Discussion on ‘Lifetime assessment of exposed PVC-P geomembranes installed on Italian dams’ by D. Cazzuffi and D. Gioffrè.” *Geotext. Geomembr.*, 49. https://doi.org/10.1016/j.geotexmem.2021.02.002.

Giroud, J. P. 1984. “Aging of PVC geomembranes in uranium mine tailing ponds.” *Proc. Int. Conf. Geomembr.*, 311–316.

Giroud, J. P. 1994. “Mathematical model of geomembrane stress-strain curves with a yield peak.” *Geotext. Geomembr.*, 13 (1): 1–22. https://doi.org/10.1016/0266-1144(94)90054-X.

Giroud, J. P. 2006. “Geosynthetics engineering: successes, failures and lessons learned.”

Gooneie, A., S. Schuschnigg, and C. Holzer. 2016. “Dissipative Particle Dynamics Models of Orientation of Weakly-Interacting Anisometric Silicate Particles in Polymer Melts under Shear Flow: Comparison with the Standard Orientation Models.” *Macromol. Theory Simul.*, 25. https://doi.org/10.1002/mats.201500086.

Gooneie, A., S. Schuschnigg, and C. Holzer. 2017. “A Review of Multiscale Computational Methods in Polymeric Materials.” *Polymers*, 9 (1): 16. https://doi.org/10.3390/polym9010016.

Hageman, J. C. L., R. J. Meier, M. Heinemann, and R. A. de Groot. 1997. “Young Modulus of Crystalline Polyethylene from ab Initio Molecular Dynamics.” *Macromolecules*, 30 (19): 5953–5957. American Chemical Society. https://doi.org/10.1021/ma9703721.

Hamad, F., P. Vermeer, and C. Moormann. 2014. “Geotextile-soil modelling using the material point method (MPM).”

Hoogerbrugge, P. J., and J. M. V. A. Koelman. 1992. “Simulating Microscopic Hydrodynamic Phenomena with Dissipative Particle Dynamics.” *Europhys. Lett.*, 19 (3): 155. https://doi.org/10.1209/0295-5075/19/3/001.

Hornsey, W. P., and D. M. Wishaw. 2012. “Development of a methodology for the evaluation of geomembrane strain and relative performance of cushion geotextiles.” *Geotext. Geomembr.*, 35: 87–99. https://doi.org/10.1016/j.geotexmem.2012.05.002.

Hou, J., H. Li, L. Liu, S. Wang, Y. Teng, and S. Bao. 2021. “A DEM analysis of geomembrane-lined landfill subject to vertical loading.” *Geotext. Geomembr.*, 49 (2): 369–375. https://doi.org/10.1016/j.geotexmem.2020.10.008.

Hsuan, G., H. Schroeder, R. Rowe, W. Mller, J. Greenwood, D. Cazzuffi, and R. Koerner. 2008. “Long-term performace and lifetime prediction of geosynthetics.” *EuroGeo4*, 1–40.

ISO/DIS 10318-1,. 2015. “Geosynthetics — Part 1: Vocabulary.”

Karademir, T., and J. D. Frost. 2021. “Elevated Temperature Effects on Geotextile–Geomembrane Interface Shear Behavior.” *J. Geotech. Geoenvironmental Eng.*, 147 (12): 04021148. American Society of Civil Engineers. https://doi.org/10.1061/(ASCE)GT.1943-5606.0002698.

Koerner, R., G. Hsuan, and G. Koerner. 2016. “Lifetime predictions of exposed geotextiles and geomembranes.” *Geosynth. Int.*, 24: 1–15. https://doi.org/10.1680/jgein.16.00026.

Koerner, R. M. 1998. *Designing with geosynthetics*. Upper Saddle River, NJ: Prentice Hall.

Koerner, R. M., G. Koerner, and Y. Hsuan. 2014. “Creep tension testing of geosynthetics.” *GSI White Pap.*, 29.

Kohn, W., and L. J. Sham. 1965. “Self-Consistent Equations Including Exchange and Correlation Effects.” *Phys. Rev.*, 140 (4A): A1133–A1138. https://doi.org/10.1103/PhysRev.140.A1133.

Kongkitkul, W., T. Chantachot, and F. Tatsuoka. 2014. “Simulation of geosynthetic load–strain–time behaviour by the non-linear three-component model.” *Geosynth. Int.*, 21 (4): 244–255. https://doi.org/10.1680/gein.14.00012.

Krauskopf, L. G. 1993. “Plasticizer structure/performance relationships.” *J. Vinyl Technol.*, 15 (3): 140–147. https://doi.org/10.1002/vnl.730150306.

Kuhl, A., P. Muñoz-Rojas, R. Barbieri, and I. Benvenutti. 2016. “A procedure for modeling the nonlinear viscoelastoplastic creep of HDPE at small strains: POLYMER ENGINEERING AND SCIENCE-2016.” *Polym. Eng. Sci.*, 57. https://doi.org/10.1002/pen.24395.

Lamri, A., M. Shirinbayan, M. Pereira, L. Truffault, J. Fitoussi, S. Lamouri, F. Bakir, and A. Tcharkhtchi. 2020. “Effects of strain rate and temperature on the mechanical behavior of high-density polyethylene.” *J. Appl. Polym. Sci.*, 137 (23): 48778. https://doi.org/10.1002/app.48778.

Landel, R. F., and L. E. Nielsen. 1993. *Mechanical Properties of Polymers and Composites, Second Edition*. CRC Press.

Lebedev, V. P., V. I. Zegel’man, D. Ya. Tsvankin, and Ye. N. Zil’berman. 1972. “The conformational composition of and structure formation in polyvinylchloride over a wide range of molecular weights.” *Polym. Sci. USSR*, 14 (9): 2119–2131. https://doi.org/10.1016/0032-3950(72)90002-0.

Leelaprachakul, T., A. Kubo, and Y. Umeno. 2023. “Coarse-Grained Molecular Dynamics Simulation of Polycarbonate Deformation: Dependence of Mechanical Performance by the Effect of Spatial Distribution and Topological Constraints.” *Polymers*, 15 (1): 43. Multidisciplinary Digital Publishing Institute. https://doi.org/10.3390/polym15010043.

Lin, Q., Q.-G. Cheng, Y. Xie, F. Zhang, K. Li, Y. Wang, and Y. Zhou. 2021. “Simulation of the fragmentation and propagation of jointed rock masses in rockslides: DEM modeling and physical experimental verification.” *Landslides*, 18 (3): 993–1009. https://doi.org/10.1007/s10346-020-01542-z.

Lodi, P., B. Bueno, and J. Zornberg. 2008. “Degradation of Geomembrane after Weathering Exposure.”

Lodi, P. C., B. de S. Bueno, J. Hamada, E. L. de Oliveira, and G. H. R. da Silva. 2013. “Evaluation of mechanical and thermal properties after chemical degradation of PVC and HDPE geomembranes.” *EJGE - Electron. J. Geotech. Eng.*, 18 (F): 1227–1236.

Lodi, P. C., B. S. Bueno, J. Kuwano, and J. Koseki. 2006. “Thermal degradation of geomembranes after exposure to heat.” Millpress Science Publishers.

Luciani, A., and D. Peila. 2019. “Tunnel Waterproofing: Available Technologies and Evaluation Through Risk Analysis.” *Int. J. Civ. Eng.*, 17 (1): 45–59. https://doi.org/10.1007/s40999-018-0328-6.

Luding, S. 2008. “Introduction to discrete element methods: Basic of contact force models and how to perform the micro-macro transition to continuum theory.” *Eur. J. Environ. Civ. Eng.*, 12 (7–8): 785–826. Taylor & Francis. https://doi.org/10.1080/19648189.2008.9693050.

Makki, H., K. Adema, E. A. J. F. Peters, J. Laven, L. Ven, R. Benthem, and G. With. 2014. "A Simulation approach to Study Photo-degradation Processes of Polymeric Coatings." *Polym. Degrad. Stab.*, 105. https://doi.org/10.1016/j.polymdegradstab.2014.03.040.

Marcotte, B. A., and I. R. Fleming. 2019. "The role of undrained clay soil subgrade properties in controlling deformations in geomembranes." *Geotext. Geomembr.*, Geosynthetics for Transportation and Environmental Applications, 47 (3): 327–335. https://doi.org/10.1016/j.geotexmem.2019.02.001.

Marcotte, B. A., and I. R. Fleming. 2021. "Direct measurement of geomembrane strain from aggregate indentations." *Geosynth. Int.*, 28 (5): 464–478. ICE Publishing. https://doi.org/10.1680/jgein.21.00027.

Mavrantzas, V. G. 2021. "Using Monte Carlo to Simulate Complex Polymer Systems: Recent Progress and Outlook." *Front. Phys.*, 9: 661367. https://doi.org/10.3389/fphy.2021.661367.

Mavrantzas, V. G., and H. C. Öttinger. 2002. "Atomistic Monte Carlo Simulations of Polymer Melt Elasticity: Their Nonequilibrium Thermodynamics GENERIC Formulation in a Generalized Canonical Ensemble." *Macromolecules*, 35 (3): 960–975. American Chemical Society. https://doi.org/10.1021/ma010688f.

Meidani, M., M. A. Meguid, and L. E. Chouinard. 2016. "A Calibration Procedure for Modeling HDPE Geomembrane Using Discrete Element Method."

Meidani, M., M. A. Meguid, and L. E. Chouinard. 2017. "Finite-Discrete Element Analysis of Interface Shear Damage to HDPE Geomembrane in Contact with Gravel Drainage Layer." *Proc. 7th Int. Conf. Discrete Elem. Methods*, Springer Proceedings in Physics, X. Li, Y. Feng, and G. Mustoe, eds., 351–359. Singapore: Springer Singapore.

Merry, S. M., and J. D. Bray. 1997. "Time-Dependent Mechanical Response of HDPE Geomembranes." *J. Geotech. Geoenvironmental Eng.*, 123 (1): 57–65. https://doi.org/10.1061/(ASCE)1090-0241(1997)123:1(57).

Meyers, M. A., and K. K. Chawla. 2008. *Mechanical behavior of materials*. Cambridge university press.

Müller, W. W. 2006. *HDPE Geomembranes in Geotechnics*. Springer.

Müller, W. W., and A. Wöhlecke. 2019. "Zero leakage? Landfill liner and capping systems in Germany." *Environ. Geotech.*, 6 (3): 162–170. https://doi.org/10.1680/jenge.16.00031.

Nakano, A., M. Bachlechner, R. K. Kalia, E. Lidorikis, P. Vashishta, G. Voyiadjis, T. J. Campbell, S. Ogata, and F. Shimojo. 2001. "Multiscale Simulation of Nanosystems." *Comput. Sci. Eng.*, 3: 56–66. https://doi.org/10.1109/5992.931904.

Neyertz, S., and D. Brown. 2013. "Molecular Dynamics Study of Carbon Dioxide Sorption and Plasticization at the Interface of a Glassy Polymer Membrane." *Macromolecules*, 46: 2433–2449. https://doi.org/10.1021/ma302073u.

Nicot, F., F. Darve, and RNVO Group: Natural Hazards and Vulnerability of Structures. 2005. "A multi-scale approach to granular materials." *Mech. Mater.*, 37 (9): 980–1006. https://doi.org/10.1016/j.mechmat.2004.11.002.

Niklausa, F., G. Stemme, S. Lu, and R. J. Gutmann. 2006. "APPLIED PHYSICS REVIEWS-FOCUSED REVIEW."

de Pablo, J. J., and W. A. Curtin. 2011. "Multiscale Modeling in Advanced Materials Research: Challenges, Novel Methods, and Emerging Applications." *MRS Bull.*, 32: 905–911. https://doi.org/10.1557/mrs2007.187.

Patterson, K. G., S. J. Padgett, and N. A. Peppas. 1982. “Microcrystalline and three-dimensional network structure of plasticized poly(vinyl chloride).” *Colloid Polym. Sci.*, 260 (9): 851–858. https://doi.org/10.1007/BF01419095.

Plimpton, S. 1995. “Fast Parallel Algorithms for Short-Range Molecular Dynamics.” *J. Comput. Phys.*, 117 (1): 1–19. https://doi.org/10.1006/jcph.1995.1039.

Radjai, F., and F. Dubois. 2011. *Discrete-element modeling of granular materials*. Wiley-Iste.

Reddy, D. V., and B. Butul. 1999. “A comprehensive literature review of liner failures and longevity.” *Submitt. Fla. Cent. Solid Hazard. Waste Manag. Univ. Fla.*

Rollin, A. L., S. Lambert, and P. Pierson. 2002. *Géomembranes: guide de choix sous l’angle des matériaux*. Presses Internationales Polytechnique.

Rowe, R. K. 1998. “Geosynthetics and the minimization of contaminant migration through barrier systems beneath solid waste.” University of Western Ontario, Department of Civil Engineering, Faculty of ….

Rowe, R. K., F. B. Barakat, D. Patch, and K. Weber. 2023. “Diffusion and partitioning of different PFAS compounds through thermoplastic polyurethane and three different PVC-EIA liners.” *Sci. Total Environ.*, 892: 164229. https://doi.org/10.1016/j.scitotenv.2023.164229.

Rowe, R. K., M. S. Morsy, and A. M. R. Ewais. 2019. “Representative stress crack resistance of polyolefin geomembranes used in waste management.” *Waste Manag.*, 100: 18–27. https://doi.org/10.1016/j.wasman.2019.08.028.

Rowe, R. K., S. Rimal, and H. Sangam. 2009. “Ageing of HDPE geomembrane exposed to air, water and leachate at different temperatures☆.” *Geotext. Geomembr.*, 27 (2): 137–151. https://doi.org/10.1016/j.geotexmem.2008.09.007.

Rudd, R. e., and J. q. Broughton. 2000. “Concurrent Coupling of Length Scales in Solid State Systems.” *Phys. Status Solidi B*, 217 (1): 251–291. https://doi.org/10.1002/(SICI)1521-3951(200001)217:1<251::AID-PSSB251>3.0.CO;2-A.

Scholtès, L., P. -Y. Hicher, F. Nicot, B. Chareyre, and F. Darve. 2009. “On the capillary stress tensor in wet granular materials.” *Int. J. Numer. Anal. Methods Geomech.*, 33 (10): 1289–1313. https://doi.org/10.1002/nag.767.

Schomaker, V., and D. P. Stevenson. 1941. “Some Revisions of the Covalent Radii and the Additivity Rule for the Lengths of Partially Ionic Single Covalent Bonds*.” *J. Am. Chem. Soc.*, 63 (1): 37–40. American Chemical Society. https://doi.org/10.1021/ja01846a007.

Scuero, A., and G. Vaschetti. 2017. “Geomembrane sealing systems for dams: ICOLD Bulletin 135.” *Innov. Infrastruct. Solut.*, 2 (1): 29. https://doi.org/10.1007/s41062-017-0089-0.

Serra, S., S. Iarlori, E. Tosatti, S. Scandolo, and G. Santoro. 2000. “Dynamical and thermal properties of polyethylene by ab initio simulation.” *Chem. Phys. Lett.*, 331 (2): 339–345. https://doi.org/10.1016/S0009-2614(00)00881-2.

Sherby, O. D., and J. E. Dorn. 1958. “Anelastic creep of polymethyl methacrylate.” *J. Mech. Phys. Solids*, 6 (2): 145–162. https://doi.org/10.1016/0022-5096(58)90022-X.

Shi, Z., T. Jiang, M. Jiang, F. Liu, and N. Zhang. 2015. “DEM investigation of weathered rocks using a novel bond contact model.” *J. Rock Mech. Geotech. Eng.*, 7 (3): 327–336. https://doi.org/10.1016/j.jrmge.2015.01.005.

Shilkrot, L. E., W. A. Curtin, and R. E. Miller. 2002. “A coupled atomistic/continuum model of defects in solids.” *J. Mech. Phys. Solids*, 50 (10): 2085–2106. https://doi.org/10.1016/S0022-5096(02)00017-0.

Smilauer, V., E. Catalano, B. Chareyre, S. Dorofeenko, J. Duriez, N. Dyck, J. Elias, B. Er, A. Eulitz, A. Gladky, N. Guo, C. Jakob, F. Kneib, J. Kozicki, D. Marzougui, R. Maurin, C. Modenese, L. Scholtes, L. Sibille, J. Stransky, T. Sweijen, K. Thoeni, and C. Yuan. 2011. "Yade Documentation."

Sperling, L. H. 1986. "Introduction to Physical Polymer Science."

Stark, T. D., H. Choi, and P. W. Diebel. 2004. "PLASTICIZER MOLECULAR WEIGHT AND PLASTICIZER RETENTION IN PVC GEOMEMBRANES."

Summers, J. W. 1981. "The nature of poly (vinyl chloride) crystallinity—the microdomain structure." *J. Vinyl Technol.*, 3 (2): 107–110. https://doi.org/10.1002/vnl.730030204.

Suter, J. L., D. Groen, and P. V. Coveney*. 2015. "Chemically Specific Multiscale Modeling of Clay–Polymer Nanocomposites Reveals Intercalation Dynamics, Tactoid Self-Assembly and Emergent Materials Properties." *Adv. Mater. Deerfield Beach Fla*, 27 (6): 966–984. https://doi.org/10.1002/adma.201403361.

Tadmor, E. B., M. Ortiz, and R. Phillips. 1996. "Quasicontinuum analysis of defects in solids." *Philos. Mag. A*, 73 (6): 1529–1563. Taylor & Francis. https://doi.org/10.1080/01418619608243000.

Talamini, B., Y. Mao, and L. Anand. 2017. "Progressive damage and rupture in polymers." *J. Mech. Phys. Solids*, 111. https://doi.org/10.1016/j.jmps.2017.11.013.

"The Nobel Prize in Physics 1991." 1991. *NobelPrize.org*. Accessed July 3, 2024. https://www.nobelprize.org/prizes/physics/1991/9905-what-do-they-look-like/.

Thusyanthan, N. I., S. P. G. Madabhushi, and S. Singh. 2012. "Seismic Performance of Geomembrane Placed on a Slope in MSW Landfill Cell: A Centrifuge Study." 1–12. American Society of Civil Engineers. https://doi.org/10.1061/40787(166)19.

Touze, N., G. Stoltz, and L. Peyras. 2021. "Containment ponds, reservoirs and canals." *ICE Handb. Geosynth. Eng.*, ICE Handbooks, 311–341. ICE Publishing.

Touze-Foltz, N., H. Xie, and G. Stoltz. 2021. "Performance issues of barrier systems for landfills: A review." *Geotext. Geomembr.*, Special issue on "Application of geosynthetics in geoenvironmental engineering," 49 (2): 475–488. https://doi.org/10.1016/j.geotexmem.2020.10.016.

Tschöp, W., K. Kremer, J. Batoulis, T. Bürger, and O. Hahn. 1998. "Simulation of polymer melts. I. Coarse-graining procedure for polycarbonates." *Acta Polym.*, 49 (2–3): 61–74. https://doi.org/10.1002/(SICI)1521-4044(199802)49:2/3<61::AID-APOL61>3.0.CO;2-V.

Usman, M., and R. Galler. 2014. "Ageing and Degradation of PVC Geomembrane Liners in Tunnels." *Int. Conf. Chem. Civ. Environ. Eng. CCEE2014*, 69–76.

Vasiluta, P., N. F. Cofaru, and I. I. Cofaru. 2017. "Studies on predictive virtual models based on finite element analysis of the behaviour of geomembranes." *MATEC Web Conf.*, (N. Balc, ed.), 137: 06006. https://doi.org/10.1051/matecconf/201713706006.

Vázquez-Quesada, A., M. Ellero, and P. Español. 2009. "Smoothed particle hydrodynamic model for viscoelastic fluids with thermal fluctuations." *Phys. Rev. E*, 79 (5): 056707. American Physical Society. https://doi.org/10.1103/PhysRevE.79.056707.

Verlet, L. 1967. "Computer 'Experiments' on Classical Fluids. I. Thermodynamical Properties of Lennard-Jones Molecules." *Phys. Rev.*, 159: 98–103. APS. https://doi.org/10.1103/PhysRev.159.98.

Vivek G. Bhartu. 2017. “Microstructural Investigation of UV-Degraded Geotextiles/Geomembranes through Scanned Electron Microscopic Study.” *J. Geol. Resour. Eng.*, 5 (2). https://doi.org/10.17265/2328-2193/2017.02.002.

Wang, L., W. Cen, E. Bauer, J. Wei, Z. Wen, and J. Yan. 2024. “Creep Failure Characteristics and Mathematical Modeling of High-Density Polyethylene Geomembranes under High Stress Levels.” *Polymers*, 16 (14): 2019. https://doi.org/10.3390/polym16142019.

Wautier, A., S. Bonelli, and F. Nicot. 2019. “DEM investigations of internal erosion: Grain transport in the light of micromechanics.” *Int. J. Numer. Anal. Methods Geomech.*, 43 (1): 339–352. https://doi.org/10.1002/nag.2866.

Wenig, W. 1978. “The microstructure of poly(vinyl chloride) as revealed by x-ray and light scattering.” *J. Polym. Sci. Polym. Phys. Ed.*, 16 (9): 1635–1649. https://doi.org/10.1002/pol.1978.180160908.

Wesseloo, J., A. T. Visser, and E. Rust. 2004. “A mathematical model for the strain-rate dependent stress–strain response of HDPE geomembranes.” *Geotext. Geomembr.*, 22 (4): 273–295. https://doi.org/10.1016/j.geotexmem.2004.02.002.

Wilson, A. S. 1995. *Plasticisers : principles and practice*. London : Institute of Materials.

Wu, Y., C. Yin, X. Zhang, and X. Gu. 2023. “Fractional Order Viscoelastic Model for Stress Relaxation of Polyvinyl Chloride Geomembranes.” *Appl. Sci.*, 13 (3): 1582. https://doi.org/10.3390/app13031582.

Yeo, S.-S., and Y. G. Hsuan. 2010. “Evaluation of creep behavior of high density polyethylene and polyethylene-terephthalate geogrids.” *Geotext. Geomembr.*, 28 (5): 409–421. https://doi.org/10.1016/j.geotexmem.2009.12.003.

Yin, Y. L., Z. H. Yang, and M. L. Shi. 2019. “Complex plane analysis of fractional derivative model and its use for parameter determination of viscoelastic material.” *IOP Conf. Ser. Mater. Sci. Eng. Online*, 592 (1): 8. United Kingdom.

Zhang, J., B. Koo, Y. Liu, J. Zou, A. Chattopadhyay, and L. Dai. 2015. “A novel statistical spring-bead based network model for self-sensing smart polymer materials.” *Smart Mater. Struct.*, 24 (8): 085022. https://doi.org/10.1088/0964-1726/24/8/085022.

Zhang, X., Z. Ma, Y. Wu, and J. Liu. 2021. “Response of Mechanical Properties of Polyvinyl Chloride Geomembrane to Ambient Temperature in Axial Tension.” *Appl. Sci.*, 11 (22): 10864. https://doi.org/10.3390/app112210864.

Zhang, X., Y. Wu, Z. Ma, and C. Yin. 2022. “Mechanical properties of PVC geomembrane based on non-contact measurement.” *Geosynth. Int.*, 30: 1–15. https://doi.org/10.1680/jgein.21.00104.

List of figures

Figure 1.1: Traction forces generated inside improperly installed geomembrane under water loading. 15
Figure 1.2: Direct contact of the geomembrane with drainage layer. 16
Figure 2.1 : The micro-domain structure of PVC. (Right) Average crystallite size of PVC. Inspired from Summers (1981). 20
Figure 2.2 : Gelation process described by Summers's model. Disappearance of the PVC primary particle structure and development of a macromolecular network (Illustration taken from (Fillot et al. 2006)) 21
Figure 2.3 : PVC GM manufacturing. Inspired from (Rollin et al. 2002). 21
Figure 2.4 : Two crystallinity-types are shown here. (a) The crystals is made up of a series of parallel polymer chains. (b) The lamella-shaped crystal is being formed by molecular chains that fold onto themselves. Adapted from (Gilbert 1994). 22
Figure 2.5 : Integration of plasticizer between the polymer chains (Personal communication from Alexis Roulet). 23
Figure 2.6 : The polymer and the CO2 penetrants displayed along the x-direction in space-filling models with the VMD software. Extracted from (Neyertz and Brown 2013). 29
Figure 2.7 : A polycarbonate chain was represented using a two beadspring coarse-grain model, where the interaction potentials were derived from distribution functions proportional to the Boltzmann factors of generalized intrachain interactions. Subsequently, a standard molecular dynamics simulation scheme was applied for each considered temperature. Adapted from (Tschöp et al. 1998). 30
Figure 2.8 : Four semi-flexible silicate embedded between polymer chains (Gooneie et al. 2016) 31
Figure 2.9 : A schematic of the reptation model. In a crowded and entangled polymer environment, a long and linear polymer chain (red) is located in a virtual tube (red), which traces the chain trajectory. Surrounding polymers are shown in gray. Extracted from (de Gennes 1971; "The Nobel Prize in Physics 1991" 1991). 32
Figure 2.10 : The Kuhn segment in the unstretched state is b. Upon stretching, the polymer chain deformed under two types: alignment of the Kuhn segments, then, stretching due to the deformation of the consistent molecular bonds, with $\lambda b$is dimensionless stretch constant referred to the bond deformation stretch. Referred to (Leelaprachakul et al. 2023; Talamini et al. 2017). 33
Figure 2.11 : Multiscale modeling of epoxy material. Extracted from (Zhang et al. 2015). 34
Figure 2.12 : Maxwell's model. (a) Rheological model, (b) the creep behavior, and (c) the relaxation behavior. 36

Figure 2.13 : Kelvin's model. (a) Rheological model, (b) the creep behavior, and (c) the relaxation behavior.... 37
Figure 2.14 : (a) Top view of the GM specimen made of particles arranged in a dumbbell-shape. (b) A 3D view of the specimen. Extracted from (Meidani et al. 2016).... 39
Figure 2.15 : Modeling the GM using bounded particles with overlap to reasonably simulate the surface characteristics of the geomembrane. Extracted from (Feng et al. 2018). 39
Figure 2.16 : Geomembrane modeling. (a) Membrane view. (b) Membrane modeling using cylinders and nodes indicating the mesh. Derived from (Effeindzourou et al. 2016). 40
Figure 2.17 : The sequence of typical DEM simulation. 41
Figure 2.18 : Simplified representation of the elasto-frictional law used in DEM simulations.... 43
Figure 2.19 : Illustration of incremental update of the shear displacement 44
Figure 2.20: Cylinder Element created by employing the Minkowski sum. 46
Figure 2.21: Schematic views of external interactions. (a) Sphere-cylinder interaction. (b) Cylinder-cylinder interaction. 49
Figure 2.22 : Leapfrog integration. Velocities are known at time $t + \Delta t2$, while positions and accelerations are known at time t. 50
Figure 3.1 : Polymer chains modeling using connected cylinders, where each cylinder element is made up of two GridNodes joined by a GridConnection. The deformation of the cylinder is governed by the relative displacement between the two nodes. 55
Figure 3.2 : A typical crystallite model. 56
Figure 3.3 : Numerical procedure to control intercrystallite distance thanks to periodic isotropic compression. In such auxiliary simulations, each crystallite is represented by a virtual sphere with radius D. 58
Figure 3.4 : Random walk algorithm to initialize the polymer chains between crystallites. 58
Figure 3.5 : Intersection cross-check of chains in amorphous regions via spatial partitioning of crystallites in cells. Potential crystallite neighbours for the chains' nodes are only searched for in its own cell and in the neighboring cells (light orange and green zones). 59
Figure 3.6 : Separation of overlapped cylinders by repulsive forces. 59
Figure 3.7 : Final 3D configuration of the microstructure of PVC with a characteristic size of 40 nm and $\theta max = 0.1\ \pi$. 60
Figure 3.8 : Process of integrating plasticizers using spherical particles. (1) Creation of a randomly distributed sphere pack. (2) Removal of the overlapped spheres with chains' cylinders. (3): Spheres expansion to fill voids between the chains. (4) Zoom-in view of polymer chains embedded between the plasticizer's particles.... 62
Figure 3.9 : Particle size distribution of spheres according to diameter, with $D60/D10$ equal to 62
Figure 3.10 : comparative analysis of 3D configurations: impact of θmax.... 63

Figure 3.11 : Comparative analysis of 3D configurations: impact of different chain number per crystallite. 64
Figure 3.12 : Comparative analysis of 3D configurations: impact of inter-crystallites distance D (For the same elementary volume, 18 Crystallites at D=10 nm vs. 7 Crystallites at D=15 nm). 65
Figure 3.13: Applied velocity distribution on the GridNodes's boundaries with respect to the KUBC approach, with $\varepsilon = 121 + \varepsilon\nu - 1$. 69
Figure 3.14 : Set of velocities applied on the wall 70
Figure 3.15: Summary of the model's build-up steps. 72
Figure 4.1: Uniaxial tensile test setup. 75
Figure 4.2: (a) Specimen mounted between the clumps of the two grips. (b) Template used for marking the two reference points. (c) The cutter machine and the template used to crop specimens in the form of dumbbell-shape. 75
Figure 4.3: Creep Test Frame where several creep tests can be conducted simultaneously. 76
Figure 4.4: Dimensions (in millimeters) of Dumbbell-shaped specimen. 76
Figure 4.5: Typical force-engineering strain curve in uniaxial tensile tests. 77
Figure 4.6: Lateral true strain vs. axial true strain in machine (MD) and cross directions (CD) at a uniaxial tensile speed of 0.5mm/min: Slopes of -0.49 (Thickness) and -0.5 (Width) in MD, and -0.5 (Thickness) and -0.51 (Width) in CD. 79
Figure 4.7: Schematic view of the image processing method employed to determine the width and relative longitudinal length during uniaxial tensile testing. The spatial-temporal evolution of both width and length is determined by monitoring pixel values along the width and length using a horizontal and vertical red line, respectively. 80
Figure 4.8: Lateral true strain vs. axial true strain at uniaxial tensile speeds of 0.5, 100, and 200 mm/min. 80
Figure 4.9: Typical axial true stress - axial true strain curves in uniaxial tensile tests. The tensile modulus $\boldsymbol{Esec}$ is determined from the initial secant drawn between 10 % and 50 % true strain. 81
Figure 4.10: Pre-Relaxation Test Procedure: the sample is stretched until it reaches a 50% deformation level. Once this level is reached, the specimen is held in this configuration, and the stress-relaxation phase starts. 83
Figure 4.11: Relaxation Test: measuring stress over time at a fixed Deformation level. 83
Figure 4.12: Spatial-temporal evolution of width during stress relaxation determined by monitoring pixel values along the width. 83
Figure 4.13: Measuring displacement over time at a fixed load level. 84
Figure 4.14: Loading and unloading tests conducted on two specimens randomly chosen from the GM sample. 85
Figure 4.15: strain Recovery Test Procedure: Measuring the length between the two marked points over time. 86
Figure 4.16: Force-engineering strain curves obtained from uniaxial tensile tests conducted at different tensile rates (mm/min). The values between brackets in the legend

represent the number of repeatability tests conducted for each tensile speed. The standard laboratory test, as recommended by European standard EN12311, involves conducting a tensile test at a prescribed uniaxial displacement rate of 100 mm/min (corresponding to yellow curves). 88
Figure 4.17: Stress-strain curves for strain-rate-dependency tests. The curves exhibit a distinctive shape compared to the force-deformation curve, which is due to the reduction in cross-sectional area. The number in parentheses mentioned in the legend indicates the repeatability test number at each tensile speed. 88
Figure 4.18: Variation of tensile modulus with tensile rate. 89
Figure 4.19: Variation of the strain rate over time during a uniaxial tensile test conducted at the various displacement rates from 0.01 to 500 mm/min. 90
Figure 4.20: Strain rate at the beginning of the test for different tensile rates. 91
Figure 4.21: Variation in tensile modulus with strain rate. 91
Figure 4.22: Variation of stress and strain at failure with tensile speed. 92
Figure 4.23: Strain rate at failure for each tensile speed. 92
Figure 4.24: Variation of stress and strain at failure with strain rate 93
Figure 4.25: Stress relaxation curves at different tensile speeds. 93
Figure 4.26: Stress relaxation curves at different tensile rates in logarithmic time scale. 94
Figure 4.27: Stress relaxation curves presented in logarithmic scales for both axes at various tensile rates. 94
Figure 4.28: Variations of: (a) the slope b of the asymptotic line for each test, (b) $\sigma asymptote$ 95
Figure 4.29: Corrected stress relaxation over time. 96
Figure 4.30: Extended, five-parameter Burger's rheological model. 96
Figure 4.31: Fitting results of the relaxation curves at 0.01, 0.1, 1 and 10 mm/min. 97
Figure 4.32: Creep (engineering) Strain Curves at Constant Stresses of 250, 200, 150, 140, 130, 120, 110, and 100 N. 99
Figure 4.33: Creep failure time at different applied constant stresses. 100
Figure 4.34: Engineering strain at failure at different applied constant stresses. Noting that no failure is observed at 100 N (at 124 days of creep). 100
Figure 4.35: Creep (engineering) strain curves at different applied constant stresses in logarithmic time scale. 101
Figure 4.36: creep strain rate vs creep (engineering) strain. 102
Figure 4.37: Fitting results of the creep curves at different loading rates, ranging from 100 to 150 N. 103
Figure 4.38: Force-engineering strain curves of conducted tensile tests at a constant displacement rate of 100 mm/min, stopped at different strain level. 104
Figure 4.39: Engineering strain recovery curves following tensile testing stopped at various deformation levels. These tests are conducted at a displacement rate of 100 mm/min. 105
Figure 4.40: Residual engineering strain after 18 days recovery for different initial strain values. 105

Figure 4.41: Engineering strain recovery curves following tensile testing stopped at various deformation levels, represented in logarithmic time scale. 106
Figure 4.42: Strain Recovery for Two Tests: With and Without Relaxation Stage.....107
Figure 4.43: Impact of creep load and loading duration on strain recovery in PVC GMs. Specimens exhibit a residual strain is highlighted in blue, and specimens experience a complete strain recovery are marked in orange. 108
Figure 4.44: Force and engineering strain at failure for each tensile rate in long- and short-term testing. 109
Figure 4.45: Stress relaxation curve for a specimen stretched to 270 % engineering strain at a displacement rate of 200 mm/min. 110
Figure 5.1: Evolution of the microstructure morphology of simple two crystallites system during uniaxial tensile test. True strain is the logarithmic strain computed following Equation 4.2....114
Figure 5.2: Force distribution map throughout the microstructure at different levels of deformation. 116
Figure 5.3: Stress-strain curve....118
Figure 5.4: Evolution of fraction of chains in Failure during loading deformation.....118
Figure 5.5: Vertical position of the failure points (blue) with respect to the top wall position (red line). 118
Figure 5.6: Stress distribution at four different current height levels of the specimen. 119
Figure 5.7: Normalized average maximum force in chains throughout the test (Relative to maximum chain's resistance). 119
Figure 5.8: (Left) Energy balance during loading. (Right) Comparison between elastic and kinetic energy (zoom-in view)....121
Figure 5.9: Average stress-strain curve 123
Figure 5.10: Fraction of polymer chains exhibiting failure during deformation 124
Figure 5.11: Average stress distribution at four different height levels (respectively 25, 50, 75, and 100 % of the current specimen height from bottom to top). 124
Figure 5.12: Spatial distribution of the failure point along the height of the specimen (specimens 2 and 3). 125
Figure 5.13: 3D configuration of the specimen (2) at different deformation levels...127
Figure 5.14: Force distribution within PVC polymer chains at different deformation levels (Specimen (2)). 128
Figure 5.15: Force distribution within PVC polymer chains at different deformation levels (Specimen (3)). 129
Figure 5.16: Chain-plasticizer interactions at 10% of stress (specimen (2)). 130
Figure 5.17: Chain-plasticizer interactions at 10% of stress (specimen (3)). 130
Figure 5.18: Close-up visualization of the crystallites within the microstructure at different deformation levels (specimen (2)). 131
Figure 5.19: Close-up visualization of the crystallites within the microstructure at different deformation levels (specimen (3)). 132

Figure 5.20: Complete crystallite fragmentation detected at 60 % of strain (specimen (2)). 133
Figure 5.21: Average stress-strain curve for three different EV' sizes. 136
Figure 5.22: Average fraction of chains in failure for three different EV' sizes. 136
Figure 5.23: Coefficient of variation of the stress for the three EV sizes. 136
Figure 5.24: Force distribution map within the chains for 40 nm EV sizes (Specimen (1)). 139
Figure 5.25: Force distribution map within the chains for 55 nm EV sizes (Specimen (1)). 140
Figure 5.26: Close-up visualization of the crystallites within the microstructure at 30% of deformation level for a **40 nm** EV sizes (specimen (1)). 141
Figure 5.27: Close-up visualization of the crystallites within the microstructure at 30% of deformation level for a **55 nm** EV sizes (specimen (1)). 141
Figure 5.28: Spatial distribution of the failure point along the height of the specimen (1) with **40 nm** EV sizes. 142
Figure 5.29: Spatial distribution of the failure point along the height of the specimen (1) with **55 nm** EV sizes. 142
Figure 5.30: Average stress distribution at four different height levels (i.e., 25, 50, 75, and 100 % of the current specimen height) for specimen with **40 nm** EV sizes. 142
Figure 5.31: Average stress distribution at four different height levels (i.e., 25, 50, 75, and 100 % of the current specimen height) for specimen with **55 nm** EV sizes. 143
Figure 5.32: Comparison of experimental data and model results for different EV sizes (40 nm, 50 nm, 55 nm). 144
Figure 5.33: Stress-strain response at different chain densities per crystallite. 146
Figure 5.34: Fraction of chains in failure at different chain densities per crystallite. 146
Figure 5.35: Force distribution for a specimen with 20 chains per crystallite. 148
Figure 5.36: Force distribution for a specimen with 40 chains per crystallite. 149
Figure 5.37: First appearance of crystallite fragmentation for specimen with 20 chains per crystallite. 150
Figure 5.38: First appearance of crystallite fragmentation for specimen with 40 chains per crystallite. 150
Figure 5.39: Complete fragmentation of crystallites in specimen with 40 chains per crystallite at 60% of strain. 151
Figure 5.40: Stress distribution at four different height levels (i.e., 25, 50, 75, and 100 % of the current specimen height) for a specimen with **20 chains** per crystallite. 152
Figure 5.41: Stress distribution at four different height levels (i.e., 25, 50, 75, and 100 % of the current specimen height) for a specimen with **40 chains** per crystallite. 152
Figure 5.42: Chain length distribution in function of the orientation angle θmax (rad). 153
Figure 5.43: Stress-strain with different chain's length represented by different θmax (in radians). 154

Figure 5.44: Fraction of chains in failure with different chain's length represented by different θmax (in radians).....154
Figure 5.45: Force distribution for a specimen with $\theta max = 0.08\ \pi$ rad. 156
Figure 5.46: Force distribution for a specimen with $\theta max = 0.12\ \pi$ rad. 157
Figure 5.47: First appearance of crystallite fragmentation for specimen with shorter chains and less tortuosity ($\theta max = 0.08\ \pi$).....158
Figure 5.48: First appearance of crystallite fragmentation for specimen with longer chains and higher tortuosity ($\theta max = 0.12\ \pi$). 158
Figure 5.49: Complete fragmentation of crystallites in specimen with shorter chains and less tortuosity ($\theta max = 0.08\ \pi$).....159
Figure 5.50: Complete fragmentation of crystallites in specimen with longer chains and higher tortuosity ($\theta max = 0.12\ \pi$).....159
Figure 5.51: Stress distribution at four different height levels (i.e., 25, 50, 75, and 100 % of the current specimen height) for a specimen with $\theta max = 0.08\ \pi$ rad.....160
Figure 5.52: Stress distribution at four different height levels (i.e., 25, 50, 75, and 100 % of the current specimen height) for a specimen with $\theta max = 0.12\ \pi$ rad.....161
Figure 5.53: Spatial distribution of the failure point along the height of the specimen with shorter chains ($\theta max = 0.08\ \pi$ rad) 161
Figure 5.54: Spatial distribution of the failure point along the height of the specimen with longer chains ($\theta max = 0.12\ \pi$ rad) 161
Figure 5.55: Plasticizer-chains interactions for specimen with shorter chains ($\theta max = 0.08\ \pi$ rad) at 10 % of stress. 162
Figure 5.56: Plasticizer-chains interactions for specimen with longer chains ($\theta max = 0.12\ \pi$ rad) at 10 % of stress. 162
Figure 5.57: Stress-strain curve of two specimens conducted at two different tensile rates **4** and **0.4 /sec**. 165
Figure 5.58: Fraction of chains in failure for tests conducted at two different tensile rates **4** and **0.4 /sec**. 165
Figure 5.59: Force distribution for a specimen subjected to uniaxial tensile rate of 0.4 /sec. Visualization includes sphere arrangement during loading, in order to see how the plasticizer's grains adjust with deformation at low tensile rate.....166
Figure 5.60: Plasticizer-chains interactions at 10% of strain for a specimen subjected to uniaxial tensile rate of 0.4 /sec. 167
Figure 5.61: Stress distribution at four different heights of the specimen (i.e., 25, 50, 75, and 100 % of the current specimen height) for a specimen, subjected to tensile strain rate equals to **4 /sec**.....167
Figure 5.62: Stress distribution at four different heights of the specimen (i.e., 25, 50, 75, and 100 % of the current specimen height) for a specimen, subjected to tensile strain rate equals to **0.4 /sec.**.....168
Figure 5.63: Energy balance during loading at tensile strain rates of 0.4 /sec and 4/sec. 168
Figure 5.64: Comparison of the stress-strain curve for plasticized and non-plasticized PVC material. 170

Figure 5.65: Stress distribution at four different height levels (respectively 25, 50, 75, and 100 % of the current specimen height from bottom to top) for **non-plasticized PVC** specimen. 170
Figure 5.66: Force distribution colored-map of a **non-plasticized** specimen. 171

List des tables

Table 3.1: Model's parameters influencing global behavior. 66
Table 4.1: Level of maximal engineering strain achieved during each relaxation test. 82
Table 4.2: Extended Loading Durations for Different Applied Weights in Creep Tests. 87
Table 4.3: Model parameters determined from test data fitting. 97
Table 4.4: Creep parameters under loads in the range [100,250] N. 103
Table 5.1: Parameters used for reference simulations. 122
Table 5.2: Impact of Chain Density on Particle Count and Specimen Porosity. 145
Table 5.3: Impact of Chain length on Particle Count and Specimen Porosity. 153

APPENDIX A

A. Key Concepts of DEM Formulation in YADE

a. YADE code structure

The code structure benefits from the conception of classes and objects using C++ programming language. Therefore, it distinguishes between two class families.

The first class family, known as data components, involves all the data related to the bodies, including their shapes (e.g., Sphere, GridNode, Wall), materials, states (e.g., position, acceleration, linear and angular velocity), bounds (i.e., approximating volume for collision detection step), as well as their interactions, and generalized forces. In YADE, each interaction has two components: the geometrical component (IGeom), which includes geometrical interaction, such as inter-penetration and relative velocity between a pair of bodies, and the physical component (IPhys), which includes physical interaction, such as normal and shear contact forces.

The second class family consists of engines that operate on the data. There are three types of engines in YADE:

- GlobalEngines, which operate on the whole simulation (e.g., ForceResetter, GravityEngine, and InsertionsSortCollider).
- PartialEngine, which operate only on some pre-selected bodies (e.g., ForceEngine to apply constant forces on preselected bodies).
- Dispatchers aim to activate other functions, called Functors, specified for each object type and scenario.

b. Collision detection between bodies in YADE

To reduce computation time, the contact detection process is carried out in two stages: potential and exact collisions. The first stage is a fast collision detection using the sweep-and-prune algorithm, which employs axis-aligned bounding boxes using BoundFunctor to identify potential collisions between elements. This can result in two scenarios: either the bounding boxes are in contact without the bodies actually touching, or both the bounding boxes and the bodies are in contact. The second stage is to filter out impossible collisions and calculate the exact collision calculation. This latter is executed during strain evaluation explained in the followed section.

c. Interaction detection and computation in YADE

The interaction geometry computation process involves the IGeomDispatcher, which selects the appropriate IGeomFunctor based on the combination of two shapes (see Figure A.1). These functors return an IGeom instance (e.g., ScGeom, ScGridCoGeom, and

GridCoGridCoGeom) with an Ig2 prefix, using specific geometry parameters corresponding to the shape (e.g., radius for spheres, position of nodes for GridConnections[1]). These parameters can be queried to obtain various geometrical characteristics, such as penetration distance or shear strain.

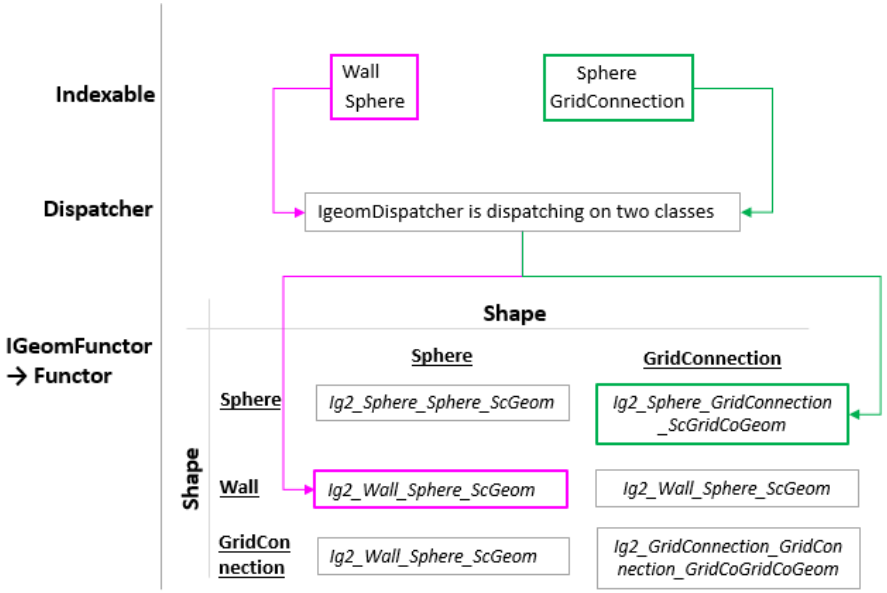


Figure A.1: Schematic view of the interaction geometry computation between a pair of bodies with different shapes.

IPhysDispatcher is used to determine the physical properties of the contact between two bodies. It uses IPhysFunctors based on the combination of the materials of the bodies in contact and returns an IPhys instance (e.g., FrictPhys, FrictViscoPhys, CohFrictPhys) with an Ip2 prefix (see Figure A.2). Some of the output physical contact parameters are computed using some averaging algorithm (such as contact stiffness from Young's moduli of material's particles); others might be internal variables like damage.

The contact laws are determined by the LawDispatcher, which dispatches to a third set of functors based on the combinations of IGeom and IPhys (hence the 2 in their name) for each particular interaction (see Figure A.3). The Law2 functors represent the "constitutive law," resolving the interaction by computing forces on the interacting bodies, or by updating interaction state variables.

[1] GridConnections are the result of the Minkowski sum of a line and a sphere. This specific type of body will be used and comprehensively elucidated in this research

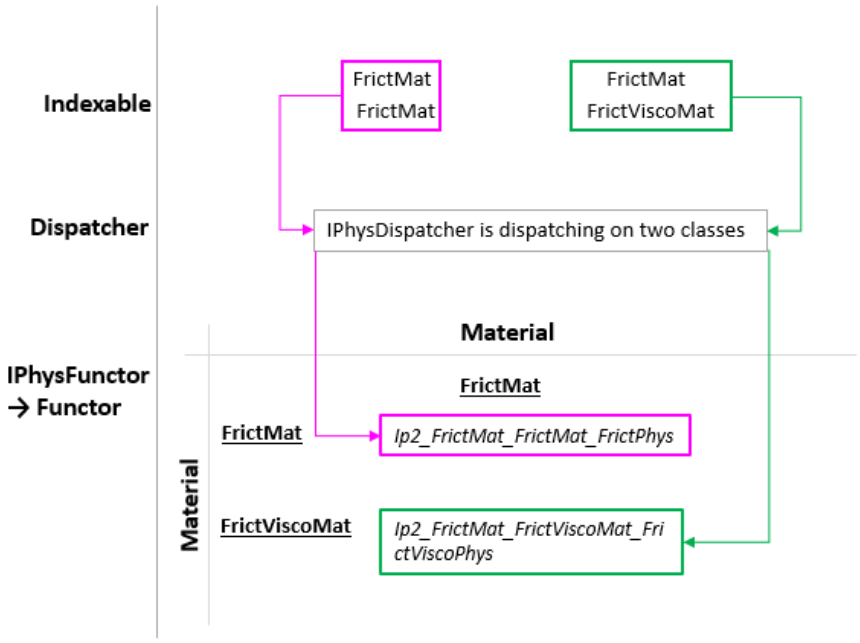


Figure A.2: Physical interaction computation schematics: Contact determination between Frictional and Frictional-Viscoelastic Materials.

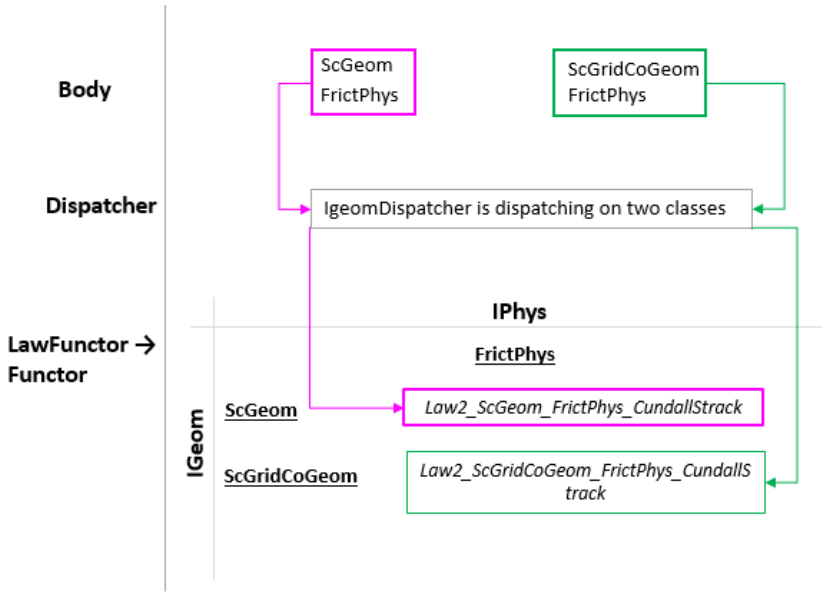


Figure A.3: Schematic View of Two Distinct Constitutive Laws for Different Contact Parameters. Each Law Functor Calculates Contact Forces Based on the Selected Constitutive Law.